

Characterisation of ferroptosis response in small cell lung cancer neuroendocrine subtypes

Inaugural-Dissertation
zur
Erlangung des Doktorgrades
der Mathematisch-Naturwissenschaftlichen Fakultät
der Universität zu Köln



vorgelegt von
Christina Maria Bebber
aus Bergisch Gladbach

Köln, 2021

Berichtersteller/in: Prof. Dr. Silvia von Karstedt

Prof. Dr. Günter Schwarz

Dr. Marcus Conrad

Prof. Dr. Ana J. García-Sáez

Tag der mündlichen Prüfung: 14.12.2021

Table of content

Table of content	i
List of Figures	vi
List of tables	viii
Abbreviations	ix
Zusammenfassung	xv
Abstract	xvi
1 Introduction	1
1.1 Programmed cell death	1
1.1.1 Intrinsic apoptosis	1
1.1.2 Extrinsic apoptosis	2
1.1.3 Necroptosis	4
1.1.4 Ferroptosis (adapted from Bebbber et al., Cancers, 2020)	5
1.1.4.1 Thioredoxin redox system	10
1.1.4.2 Cancer metabolism and ferroptosis	12
1.2 Lung Cancer	14
1.2.1 Small Cell Lung Cancer (SCLC)	14
1.2.1.1 Genomic profile of SCLC	16
1.2.1.2 Cell of origin and SCLC subtypes	18
1.2.1.3 The RP mouse model of SCLC	20
1.3 Aim of the study	21
2 Results	23
2.1 Treatment naïve SCLC presents with inactivation of important regulated cell death pathways	23
2.1.1 Treatment-naïve SCLC presents with inactivation of the extrinsic apoptosis pathway	24
2.1.2 Treatment-naïve SCLC presents with inactivation of the necroptosis pathway	25
2.2 SCLC presents with high vulnerability for ferroptosis	26

2.2.1	Treatment-naïve SCLC presents with upregulation of ferroptosis protective genes	26
2.2.2	SCLC is more sensitive to ferroptosis induction than NSCLC.....	28
2.2.3	Human and mouse SCLC cell lines are vulnerable to ferroptotic cell death	30
2.2.4	Gpx4 expression is sufficient to protect SCLC cells from ferroptosis.....	31
2.3	SCLC cell lines are segregated by ferroptosis response	33
2.4	SCLC ferroptosis response and neuroendocrine subtypes.....	35
2.4.1	SCLC ferroptosis response separates neuroendocrine subtypes	35
2.4.2	Mouse SCLC cell lines segregate by ferroptosis response.....	37
2.4.3	Neuroendocrine subtypes do not segregate by chemotherapy response	38
2.4.4	Cells with acquired ferroptosis resistance are more sensitive to chemotherapy.....	39
2.4.5	MYC and YAP1 overexpression increases ferroptosis sensitivity	39
2.5	Ferroptosis responders are characterised by a ferroptosis-prone lipidome.....	43
2.5.1	Ferroptosis sensitive SCLC presents with increased fatty acid metabolism.....	43
2.5.2	Ferroptosis sensitive SCLC presents with increased basal levels of peroxidised lipids.....	44
2.5.3	Ferroptosis sensitive SCLC presents with increased ether-linked phospholipid synthesis	45
2.5.4	SCLC patient data confirm altered lipid metabolism in ASCL1-low patients.....	48
2.6	SCLC subtypes divide by two distinct redox pathway dependencies.....	49
2.6.1	Non-NE SCLC is dependent on the GSH-based anti-oxidant redox pathway.....	49
2.6.2	Neuroendocrine SCLC is characterised by TRX pathway addiction	52
2.6.3	TXNRD1 inhibition does not induce ferroptotic cell.....	54
2.7	SCLC subtype plasticity is defined by redox pathway compensation.....	55
2.8	<i>In vivo</i> treatment response	59
2.8.1	Combined inhibition of GCL and TXNRD1 reduces SCLC tumour growth <i>in vivo</i>	59
2.9	Combined inhibition of GCL and TXNRD1 kills chemo-naive and relapse SCLC CDXs <i>ex vivo</i>	65

2.10	Low expression of GPX4 and TXNRD1 is a marker for improved outcome in SCLC patients.....	66
2.11	Data contribution.....	68
3	Discussion.....	69
3.1	Cell death pathways in SCLC.....	69
3.2	Ferroptosis sensitivity in ASCL1-low non-NE SCLC.....	70
3.3	TRX pathway dependency in ASCL1-high NE SCLC.....	75
3.4	Combined ferroptosis induction and TRX pathway inhibition targets SCLC subtype plasticity.....	78
3.5	Concluding remarks.....	80
4	Material and Methods.....	82
4.1	Materials used in this study.....	82
4.2	Molecular biological techniques.....	83
4.2.1	Nucleic acid techniques.....	83
4.2.1.1	Preparation of Plasmid DNA.....	83
4.2.1.2	Preparation of genomic DNA for genotyping.....	84
4.2.1.3	Polymerase chain reaction (PCR).....	84
4.2.1.4	Detection and purification of nucleic acids by agarose gel electrophoresis.....	85
4.2.1.4.1	RNA Isolation and cDNA synthesis.....	85
4.2.1.4.2	Determination of nucleic acid concentration.....	85
4.2.1.4.3	Quantitative real-time PCR analysis.....	86
4.2.2	Cell culture techniques.....	87
4.2.2.1	Generation of mouse SCLC cell lines.....	88
4.2.2.2	Cell lines and culture conditions.....	89
4.2.2.3	Generation of human SCLC CDXs.....	89
4.2.2.4	PBMC isolation.....	89
4.2.2.5	Plasmid construction for CRISPR sgRNAs.....	89
4.2.2.5.1	Phosphorylation and Annealing of oligonucleotide duplexes.....	89
4.2.2.5.2	Backbone digest and ligation of DNA (Golden Gate reaction) for sgRNA.....	90
4.2.2.5.3	Sanger sequencing.....	90
4.2.2.5.4	Preparation of chemo competent <i>E. coli</i>	90

4.2.2.5.5 Transformation of <i>E. coli</i>	91
4.2.2.6 Production of viral vectors	91
4.2.2.6.1 Production of lentiviral particles in HEK293T cells	91
4.2.2.6.2 Production of retroviral particles in HEK Phoenix Eco cells.....	92
4.2.2.6.3 Transduction of target cells.....	92
4.2.2.6.4 Generation of inducible Ascl1 overexpressing cells	93
4.2.2.7 Transfection of target cells.....	93
4.2.3 Protein analysis techniques.....	94
4.2.3.1 Protein extraction from cultured cells.....	94
4.2.3.2 Protein extraction from fresh frozen tissue.....	95
4.2.3.3 Western Blot analysis	95
4.2.4 Redox shift assays.....	96
4.2.5 Quantification of oxidised glycerophospholipids via lipidomics	97
4.2.6 Quantification of Glycerophospholipid via lipidomics	98
4.2.7 Fluorescence activated Cell Sorting (FACS)	98
4.2.7.1 ASCL1-staining for Flow Cytometry.....	98
4.2.7.2 Lipid ROS quantification by BODIPY C11 staining.....	99
4.2.7.3 General ROS quantification by H2DCFDA staining.....	99
4.2.7.4 Labile iron quantification by Calcein-AM staining.....	99
4.2.7.5 Cellular GSH quantification.....	99
4.2.8 Cell viability and cell death assays.....	100
4.2.8.1 Cell Titer Blue assay.....	100
4.2.8.2 IncuCyte cell imaging.....	100
4.2.8.3 PI staining in FACS	100
4.2.8.4 Clonogenic survival assay	100
4.2.9 Mouse experiments.....	100
4.2.9.1 Autochthonous SCLC Mouse Model.....	101
4.2.9.2 MRI analysis.....	101
4.2.9.3 Tumour xenograft studies.....	101
4.2.9.4 Tumour allograft studies	102
4.2.10 Staining.....	102
4.2.10.1 ASCL1-staining for immunofluorescence microscopy	102
4.2.10.2 Immunohistochemistry.....	103
4.2.10.3 ASCL1 histology scoring.....	103

4.2.11	Human SCLC RNA-seq data ethical approval	103
4.2.12	Analysis software and bioinformatic analysis.....	104
4.2.13	Data presentation and statistical analysis.....	104
5	References.....	105
6	Publications.....	135
7	Acknowledgments	136
8	Eidesstattliche Erklärung	137
9	Appendix.....	138

List of Figures

Figure 1 Extrinsic and intrinsic apoptosis pathways.	3
Figure 2 Necroptosis pathway.	4
Figure 3 Schematic view of the ferroptosis pathway.	9
Figure 4 Schematic overview of the thioredoxin pathway.	11
Figure 5 Schematic overview of SCLC subtypes.	20
Figure 6 Schematic overview of the SCLC mouse model.	21
Figure 7 Extrinsic and intrinsic apoptosis pathways are downregulated in treatment-naïve SCLC.	24
Figure 8 The necroptosis pathway is downregulated in treatment-naïve SCLC.	26
Figure 9 Ferroptosis pathway components are upregulated in treatment-naïve SCLC.	27
Figure 10 SCLC cells are more susceptible to ferroptosis induction than NSCLC cells.	29
Figure 11 Human and mouse SCLC cell lines are sensitive to ferroptosis induction.	31
Figure 12 GPX4 expression is sufficient to protect SCLC from ferroptosis.	32
Figure 13 SCLC cell lines segregate by ferroptosis response.	34
Figure 14 SCLC neuroendocrine subtypes segregate by ferroptosis response.	36
Figure 15 Murine SCLC neuroendocrine subtypes segregate by ferroptosis response.	37
Figure 16 SCLC neuroendocrine subtypes do not segregate by chemotherapy response.	39
Figure 17 RSL3 resistant made cell lines are more sensitive to cisplatin treatment.	39
Figure 18 Non-ne SCLC cells are more sensitive to ferroptosis.	41
Figure 19 NE marker expression in human and mouse SCLC cell lines.	42
Figure 20 non-NE SCLC presents with increased levels of ACSL4 and upregulated lipid metabolism.	44
Figure 21 non-NE/NE SCLC subtypes undergo lipid metabolism remodelling.	45
Figure 22 Non-NE SCLC subtype presents with increased ether-lipid synthesis.	47

Figure 23 ASCL1^{low} SCLC express higher levels of lipid ether metabolism genes.	48
Figure 24 SCLC-A cells presents with low GSH levels.	50
Figure 25 ASCL1-low expressing SCLC cells are sensitive to GSH depletion.	51
Figure 26 SCLC-A cells present with increased TRX pathway activity.	53
Figure 27 Neuroendocrine SCLC presents with TRX pathway addiction.	54
Figure 28 Auranofin induced cell death is not rescued with Fer-1 co-incubation.	55
Figure 29 Single treatment regime selectively depletes ASCL1-low or ASCL1-high population.	56
Figure 30 Single treatment regime promotes subtype plasticity.	57
Figure 31 BSO/Auranofin-induced cell death is partially ferroptotic and partially dependent on ROS.	58
Figure 32 Dose titration.	60
Figure 33 Combined ferroptosis induction and TRX pathway inhibition demonstrates broad anti-tumour activity in human SCLC xenograft model <i>in vivo</i>.	61
Figure 34 Combined ferroptosis induction and TRX pathway inhibition demonstrates broad anti-tumour activity murine SCLC allograft model for subtype heterogeneity <i>in vivo</i>.	63
Figure 35 Combined ferroptosis induction and TRX pathway inhibition demonstrates broad anti-tumour in a SCLC GEMM <i>in vivo</i>.	65
Figure 36 Combined inhibition of GCL and TXNRD1 kills chemo-naive and relapse SCLC CDXs <i>ex vivo</i>.	66
Figure 37 Low expression of GPX4 and TXNRD1 serves as prognostic marker set for improved survival in SCLC patients.	67
Figure 38 ASCL1-low non-NE SCLC is characterised by ferroptosis sensitivity due to a ferroptosis-prone lipidome.	75
Figure 39 ASCL1-high NE SCLC is characterised by TRX pathway dependency.	78
Figure 40 SCLC non-NE/NE subtypes segregate by lipid ROS/ROS vulnerability.	80
Figure 41 GSEA analysis.	138

List of tables

Table 4-1 Reagents used in this study	82
Table 4-2 Chemicals used in this study.....	83
Table 4-3 Primers used in genotyping.....	84
Table 4-4 Components used for PCR.	85
Table 4-5 PCR program for amplification of DNA fragments using Red Taq polymerase.....	85
Table-4-6 qPCR components.....	86
Table 4-7 Primer sequences used for qPCR analysis.....	86
Table 4-8 Cell lines used in this work.....	87
Table 4-9 Cell culture reagents.	88
Table 4-10 Antibiotics used in cell culture	88
Table 4-11 CRISPR gRNA sequences.....	90
Table-4-12 Components used for Golden Gate reaction.....	90
Table 4-13 Plasmids.....	92
Table 4-14 siRNA sequences.....	93
Table 4-15 SDS Page composition.....	94
Table 4-16 Primary antibodies used for Western Blot analysis	95
Table 4-17 Secondary antibodies used for Western Blot analysis	96

Abbreviations

4-HNE	4-hydroxynonenal
AA	Arachidonic acid
ACD	Accidental cell death
ACSL4	Acyl-CoA synthetase long-chain family member 4
AdA	Adrenic acid
Adeno-Cre	Adenoviral particles expressing the Cre recombinase
AGP	1-O-alkyl-glycerol-3-phosphate
AGPAT	1-Acylglycerol-3-Phosphate O-Acyltransferase
AGPS	Alkylglycerone phosphate synthase
AIFM2	Apoptosis-inducing factor mitochondrial 2
AKT	Protein kinase B
ALK	Anaplastic lymphoma kinase
APAF1	Apoptosis promoting factor 1
APC	Antigen presenting cell
ARE	Antioxidant response element
ASCL1	Achaete-scute family bHLH transcription factor 1
ATOH1	Atonal BHLH Transcription Factor 1
ATP	Adenosine triphosphate
AUC	Area under the curve
BAK	BCL-2 homogenous antagonist/killer
BAX	Bcl-2 associated X protein
BCA	Bicinchoninic acid
BCL-2	B-cell lymphoma 2
BCL-XL	BCL2 like 1
BH3	Bcl-2 Homology 3
bHLH	Basic helix-loop-helix
BHT	Butylated hydroxytoluene
BID	BH3-interacting domain death agonist
BIM	BCL2-interacting mediator of cell death
Bp	base pairs
BSA	Bovine Serum Albumin
BSO	Buthionine sulfoximine
c-FOS	Fos proto-oncogene
c-JUN	Jun proto-oncogene
CASP	Caspase
CBS	Cystathionine β -synthase
CD	Cluster of Differentiation
cDNA	Complementary DNA
CDX	CTC-derived explant models
CHGA	Chromogranin A
ciAP1/2	Cellular inhibitor of apoptosis protein 1/2

CoA	Coenzyme A
COX2	Cyclooxygenase 2
Cre	Causes recombination
CREBBP	CREB binding protein
CRISPR	Clustered Regularly Interspaced Short Palindromic Repeats
CSE	Cystathionine γ -lyase
CTC	Circulating tumour cell
CYLD	Cylindromatosis
Da	Dalton
DAG	Diacylglycerol
DBZ	Dibenzazepine
DFO	Deferoxamine
DISC	Death-inducing signalling complex
DLL	Delta Like Canonical Notch Ligand
DMPC	1,2-dimyristoyl- <i>sn</i> -glycero-3-phosphocholine
DMPE	1,2-dimyristoyl- <i>sn</i> -glycero-3-phosphoethanolamine
DMSO	Dimethyl sulfoxide
DMT1	Divalent metal transporter 1
DNA	Deoxyribonucleic acid
DOX	Doxycycline
DTPA	Diethylenetriaminepentaacetic acid
DTT	Dithiothreitol
E. coli	<i>Escherichia coli</i>
EDTA	Ethylenediaminetetraacetic acid
EGFR	Epidermal Growth Factor Receptor
EMA	European medicines agency
EMT	Epithelial to mesenchymal transition
EP300	E1A binding protein p300
ER	Endoplasmatic reticulum
Erastin	Eradicator of RAS and ST-expressing cells
ESI-MS/MS	Electrospray Ionisation Tandem Mass Spectrometry
EtOH	Ethanol
ETS	Environmental tobacco smoke
EZH2	Enhancer of zeste homolog 2
FACS	Fluorescence-activated cell sorting
FADD	Fas-associated protein with death domain
FAR1	Fatty acyl-CoA reductase 1
FasL	Fas receptor and Fas ligand
FCS	Fetal Calf Serum
FDA	Food and drug administration
Fer-1	Ferrostatin-1
FPKM	Fragments Per Kilobase of transcript per Million mapped reads
FSP1	Ferroptosis supressor protein 1
FW	Forward

GAPDH	Glyceraldehyde 3-phosphate dehydrogenase
GCL	Glutamate-cysteine ligase
GCLC	Glutamate-cysteine ligase catalytic subunit
GCLM	Glutamate-cysteine ligase modifier subunit
GEMM	Genetically engineered mouse models
GNPAT	Glyceronephosphate O-acyltransferase
GPX4	Glutathione peroxidase 4
GR	Glutathione reductase
GSEA	Gene set enrichment analysis
GSH	Glutathione
GSR	Glutathione reductase
GSS	Glutathione synthetase
GSSG	Glutathione disulfide
H&E	Hematoxylin and eosin
H2DCFDA	2',7'-dichlorodihydrofluoresceindiacetate
HCC	Hepatocellular carcinoma
HEK	Human embryonic kidney 293 cells
HES1	Hairy and enhancer of split-1
Het	Heterozygous
HRAS	Harvey rat sarcoma viral oncogene homolog
HRP	Horseradish peroxidase
IACUC	Institutional Animal Care and Use Committee
IHC	Immunohistochemistry
IRP1	Iron responsive protein 1
ISC	Iron-sulfur cluster
IVC	Individually ventilated cages
Iz	Isoleucine zipper
KEAP1	Kelch-associated protein 1
KO	Knockout
KRAS	Kirsten rat sarcoma viral oncogene homolog
LANUV	Landesamt für Natur, Umwelt und Verbraucherschutz Nordrhein-Westfalen
LB	Lysogeny broth
LC	Liquid Chromatography
LD	Lipid droplet
LDLR	Low-density lipoprotein receptor
LOX	Lipoxygenase
LoxP	Locus of X-over P1
LOXs	Lipoxygenases
LPC	Lysophospholipid
LPCAT3	Lysophosphatidylcholine acyltransferase 3
LUAD	Lung adenocarcinoma
M. musculus	<i>Mus musculus</i>
MCB	Monochlorobimane

MCL	Myeloid leukemia cell differentiation protein
MCL-1	MCL1, BCL2 family apoptosis regulator
MDA	Malondialdehyde
MEF	Mouse Embryonic Fibroblasts
MEK5/ERK5	Mitogen-activated protein kinase kinase 5-extracellular signal-regulated kinase 5
MeOH	Methanol
MgCl₂	Magnesium chloride
MHC	Major histocompatibility complex
MLKL	Mixed-lineage kinase domain like
MOMP	Mitochondrial outer membrane permeabilization
mPTP	Mitochondrial permeability transition pore
MRI	Magnetic resonance imaging
MRM	Multiple Reaction Monitoring
mRNA	Messenger RNA
MYC	MYC proto-oncogene bHLH transcription factor
MYCL	MYCL proto-oncogene, bHLH transcription factor
MYCN	MYCN proto-oncogene, bHLH transcription factor
NAC	N-acetylcysteine
NADH	Nicotinamide adenine dinucleotide
NADPH	Nicotinamide adenine dinucleotide phosphate
NCAM1	Neural adhesion molecule 1
NE	Neuroendocrine
NEB	Neuroepithelial bodies
Nec-1	Necrostatin-1
NEUROD1	Neurogenic differentiation factor 1
NFIB	Nuclear factor I/B
NFS1	Nitrogen-Fixing Bacteria S-Like Protein
NGS	Normal goat serum
NICD	Notch intracellular domain
NOX	NADPH oxidase
NOXA	Phorbol-12-myristate-13-acetateinduced protein 1
NRF2	Nuclear factor erythroid 2-related factor 2, also called <i>NFE2L2</i>
NSCLC	Non-small cell lung cancer
OXPHOS	Oxidative phosphorylation
PBMC	Peripheral blood monocytes
PBS	Phosphate Buffered Saline
PBST	Phosphate-buffered saline-Tween 20
PC	Phosphatidylcholine
PCD	Programmed cell death
PCR	Polymerase chain reaction
PD-1	Programmed cell death protein 1
PE	Phosphatidylethanolamine
PEDS1	Plasmanylethanolamine desaturase 1
PFA	Paraformaldehyde

PI	Propidium iodide
PI3	phosphoinositide 3 kinase
PNEC	Pulmonary neuroendocrine cell
POU2F3	POU class 2 homeobox 3
PRDX	Peroxireductase
PS	Penicillin-Streptomycin
PTEN	Phosphatase and tensin homolog
PUFA	Polyunsaturated fatty acid
PUFA-ePL	Polyunsaturated ether-linked phospholipid
PUMA	Pro-apoptotic factors BCL2 binding component 3
qRT-PCR	Quantitative reverse transcription PCR
RAS	Rat Sarcoma
RB1	Retinoblastoma-associated protein 1
REST1	RE1 Silencing Transcription Factor, also called NRSF
RET	Rearranged during transfection
RIPK	Receptor-interacting serine-threonine protein kinase
RNA	Ribonucleic acid
RNA-seq	RNA-sequencing
ROI	Region of interest
ROS	Reactive oxygen species
ROS1	ROS proto-oncogene 1
RP	Rb1; Trp53 knockout mouse
RPM	Rounds per minute
RSL3	RAS-selective lethal 3
RT	Room temperature
RV	Reverse
SCLC	Small Cell Lung Cancer
SDS	Sodium dodecyl sulfate
SEM	Standard error of the mean
sgRNA	Single guide RNA
shRNA	Small hairpin RNA
siRNA	Small interfering RNA
SLC3A2	Solute carrier family 3 member 2, protein name: 4F2
SLC7A11	Solute carrier family 7 member 11, protein name: xCT
SLFN11	Schlafen family member 11
SMAC	Second mitochondria derived
SNP	Single nucleotide polymorphism
SOD	Superoxide dismutases
SPF	Specific pathogen free
STEAP3	Six-transmembrane epithelial antigen of prostate 3
SYP	Synaptophysin
tBID	Truncated BID
TBS-T	Tween 20 in Tris-buffered saline
TCA	Tricarboxylic acid cycle

TCR	T cell receptor
TE	Tris EDTA buffer
TEMED	N,N,N',N' Tetra Methylenediamine
TFR1/CD71	Transferrin receptor 1
TKI	Tyrosine-kinase inhibitor
TMB	Tumor mutational burden
TNF	Tumour necrosis factor
TP53	Tumor protein p53
TP73	Tumor protein p73
TPM	Transcript per million
TRADD	TNFR-associated death domain
TRAF	TNF receptor-associated factor
TRAIL	TNF-related apoptosis-inducing ligand
Trp53	Transformation related protein 53 (<i>M. musculus</i>)
TSE	Turbo-spin echo
TXN	Thioredoxin, protein name: TRX
TXNIP	Thioredoxin interacting protein 1
TXNRD	Thioredoxin reductase, protein name: TRXR
TZS	TNF (T)/z-VAD-fmk (Z)/SMAC mimetic (S)
VIM	Vimentin
WT	Wildtype
XIAP	X-linked inhibitor of apoptosis
YAP1	Yes-associated protein 1
ZBP1	Z-DNA-binding protein 1

Zusammenfassung

Die Behandlung des kleinzelligen Bronchialkarzinoms (SCLC) blieb in den letzten 30 Jahren eine große klinische Herausforderung mit nur wenigen neuen Behandlungsstrategien. Nach anfänglich erfolgreicher Chemotherapie kommt es fast immer zu Rückfällen des SCLC mit intratumoraler neuroendokriner (NE) Subtyp-Heterogenität als Ergebnis unterschiedlicher Herkunftszellen und Subtyp-Plastizität. SCLC wird durch den Verlust der Tumorsuppressor-Gene TP53 und RB1 sowie durch eine hohe Tumormutationslast (TML) definiert, was auf einen selektiven Druck zur Inaktivierung von Zelltod-Signalwegen vor der Therapie hindeutet. Eine umfassende Analyse der Verfügbarkeit von Zelltod-Signalwegen bei SCLC wurde jedoch bisher noch nicht durchgeführt. In dieser Studie zeigen wir durch systematische Charakterisierung der Verfügbarkeit von regulierten Zelltod-Signalwegen in RNA-Sequenzierungsdaten humaner, therapie-naiver SCLC-Patientengewebe eine Inaktivierung von extrinsischen Apoptose- und Nekroptose-Signalweg-Komponenten und eine hohe Expression von Ferroptose-protectiven Genen. Ferroptose ist eine kürzlich beschriebene Form des regulierten Zelltods, die durch eine eisenabhängige Akkumulation von tödlichen Lipidperoxiden induziert wird, was zu einer Destabilisierung und somit zu Schäden der Lipiddoppelschicht führt. In dieser Studie haben wir festgestellt, dass non-NE-SCLC-Zellen der Maus und des Menschen, die durch eine niedrige Achaete-Scute Homolog 1 (ASCL1)-Expression gekennzeichnet sind, besonders empfindlich für Ferroptose sind, während NE-SCLC-Zellen hingegen sehr anfällig für die Hemmung des Thioredoxin (TRX)-Signalwegs sind. Non-NE-SCLC sind durch eine Erhöhung des oxidierten Lipidspiegels sehr anfällig für eine genetische oder pharmakologische Induktion von Ferroptose. Wir zeigen, dass Ferroptose-Resistenz in SCLC durch NE-Differenzierung und Expression des NE-Linien-definierenden Transkriptionsfaktors ASCL1 gekennzeichnet ist. ASCL1 unterdrückt die Glutathion-Synthese im NE-SCLC-Subtyp, der eine Abhängigkeit vom Thioredoxin (TRX)-Antioxidans-Weg erwirbt. In Co-Kulturen, die intratumorale non-NE/NE-Heterogenität replizieren, tötet Ferroptose-Induktion die non-NE-Populationen, während die NE-Zellpopulationen durch Hemmung des TRX-Wegs eliminiert wird. Wenn nur einer der beiden Redox-Signalwege inhibiert wird, besteht die Möglichkeit, dass durch NE/non-NE-Plastizität SCLC Zellen der Behandlung entgehen. Nur durch kombinierte Ferroptose-Induktion und Hemmung des TRX-Signalwegs werden etablierte non-NE- und NE-Tumore in SCLC-Xenotransplantaten und Mausmodellen erfolgreich behandelt. Zusammengefasst zeigen diese Ergebnisse, dass durch gezielte Kombinationstherapien die NE/non-NE-Heterogenität und Plastizität des SCLC behandelt werden kann.

Abstract

Small cell lung cancer (SCLC) treatment has remained a major clinical challenge with very few newly approved treatment strategies in the last 30 years. After initial chemotherapy response SCLC almost invariably relapses presenting with intratumoural neuroendocrine (NE) subtype heterogeneity as a result of different cells-of-origin and subtype plasticity. SCLC is defined by loss of function mutations in tumour suppressor genes TP53 and RB1 as well as a significant tumour mutational burden (TMB), suggesting selective pressure to inactivate cell death pathways prior to therapy. However, a comprehensive analysis of cell death pathway availability in SCLC has not been pursued yet. In this study, through systematic characterisation of regulated cell death pathway availability in RNA-sequencing data of human treatment-naïve SCLC patient tissue, we find broad inactivation of the extrinsic apoptosis and necroptosis pathway components and high expression of genes preventing from ferroptosis. Ferroptosis is a recently described form of regulated cell death induced by iron-dependent accumulation of fatal lipid-peroxides resulting in destabilisation of the lipid bilayer and membrane rupture. In this study, we identified that non-NE mouse and human SCLC cells marked by low Achaete-Scute Homolog 1 (ASCL1) expression are uniquely primed for ferroptosis, while NE SCLC cells instead are highly vulnerable to thioredoxin (TRX) pathway inhibition. Non-NE SCLC presents with an elevated oxygenated lipidome and is selectively vulnerable to genetic or pharmacological induction of ferroptosis. We identified NE-differentiation marked by the NE lineage-defining transcription factor ASCL1 expression to determine ferroptosis resistance. ASCL1 suppresses glutathione synthesis in the NE SCLC subtype which acquires addiction to the thioredoxin (TRX) anti-oxidant pathway. Co-cultures replicating non-NE/NE intratumoural heterogeneity selectively deplete non-NE populations upon ferroptosis induction, while only TRX pathway inhibition eliminates NE cell populations. Importantly, single redox-pathway targeting induces NE/non-NE plasticity enabling treatment escape in SCLC. Hence, combined ferroptosis induction and inhibition of the TRX pathway kills established non-NE and NE tumours in xenografts, genetically engineered mouse models of SCLC and patient-derived treatment-naïve and refractory NE SCLC models. In SCLC but not lung adenocarcinoma, combined low expression of GPX4 and TRX reductase 1 (TXNRD1) identified a patient subset with significantly improved overall survival. Taken together, these findings reveal that informed cell death pathway mining in treatment-naïve SCLC can identify rational combination therapies which address SCLC NE/non-NE heterogeneity and plasticity under treatment.

1 Introduction

1.1 Programmed cell death

Cells die via two different types of cell death, accidental cell death (ACD), an uncontrolled process induced instantaneously by very harsh environmental factors and programmed cell death (PCD) ¹. PCD is an important, regulated mechanism controlling physiological processes such as development, immunity and tissue homeostasis ^{2,3}. PCD can be triggered by intracellular or extracellular perturbations surpassing stress response mechanisms which subsequently activate a “programmed” molecular cascade in cells ultimately resulting in cell death ⁴. Originally, PCD is divided into three main types based on their morphological features namely 1) apoptosis (plasma membrane blebbing), 2) autophagy (cellular vacuolisation) and 3) necrosis (no characteristic features of 1 and 2), but to date, many novel signalling pathways that coordinate regulated cell death have been described ^{2,5}.

Over the past decades, the role of cell death in human diseases has been studied, including immunological disorders, organ failure, neurodegeneration and cancer. One of the most important hallmarks of cancer is the efficient evasion of PCD ⁶. Hence, targeting key molecules of cell death pathways was reported to inhibit cancer growth by inducing PCD ⁷⁻¹⁰. Moreover, the recent advent of immunotherapy has exploited the fact that also immune effector cells can be re-activated to effectively trigger PCD in tumour cells ¹¹. Herein, binding of death ligands expressed by immune effector cells to their cognate receptor on tumour cells induces extrinsic apoptosis and/or necroptotic cell death ^{12,13}.

1.1.1 Intrinsic apoptosis

The first described and best characterised PCD to date is apoptosis ¹⁴. In contrast to necrosis, apoptosis results in membrane blebbing and controlled cellular degradation ¹⁵. Apoptosis can be induced extrinsically by the binding of death ligands to their cognate receptors and intrinsically by intracellular triggers such as DNA damage or stress signals ¹⁶. These cell damage signals can be sensed and further enhanced by various control mechanisms such as tumour protein p53 (TP53) ^{16,17}. Stress signals further result in an activation of pro-apoptotic factors BCL2 binding component 3 (BBC3; best known as p53-upregulated modulator of apoptosis, **PUMA**) ¹⁸, phorbol-12-myristate-13-acetate-induced protein 1 (PMAIP1; also known as **NOXA**) ¹⁹ and BCL2 like 11 (BCL2L11; also known as BCL2-interacting mediator of cell death, **BIM**) ²⁰ and BH3 interacting domain

death agonist (**BID**)²¹ over anti-apoptotic BCL-2 family members, such as B-cell-lymphoma-2 (**BCL-2**)²², BCL2 like 1 (BCL2L1, also known as **BCL-XL**)²³ and MCL1, BCL2 family apoptosis regulator (**MCL-1**) resulting in induction of apoptosis via the mitochondria²⁴. This ultimately leads to multimerisation of BCL-2 family members BCL-2 associated X protein (**BAX**) and BCL-2 homogenous antagonist/killer (**BAK**) in the mitochondrial outer membrane²⁵⁻²⁷. This allows for irreversible mitochondria outer membrane permeabilisation (MOMP) through BAX/BAK pores^{28,29}. Cytochrome C released from mitochondria caused by MOMP binds apoptosis promoting factor 1 (APAF1) and procaspase 9 in the cytosol and they assemble forming the apoptosome (oligomerisation of cytochrome C/APAF1 complexes)³⁰. The apoptosome then activates the intrinsic caspase (CASP) cascade consisting of initiator CASP8/9/10 and effector CASP3/6/7) driving cleavage of a variety of cellular protein substrates ultimately resulting in DNA fragmentation and apoptosis³¹.

1.1.2 Extrinsic apoptosis

Extrinsic apoptosis is initiated upon binding of death ligands belonging to the tumour necrosis factor (TNF) superfamily (TNF-related apoptosis-inducing ligand (TRAIL)) or CD95L to their respective death receptors on the cell surface belonging to the TNF receptor superfamily (Fas or CD95)^{13,32}. Binding of ligands to their cognate receptors results in either direct recruitment of Fas-associated protein with death domain (FADD) to membrane complexes or in the formation of intracellular secondary complexes driving death-inducing signalling complex (DISC) assembly by recruiting procaspase 8³³. In **type 1** cells, which are predominantly thymocytes and mature lymphocytes, the initiator CASP8 is activated via ubiquitination by cullin 3 and then activates effector caspases (mainly CASP3) resulting in DNA fragmentation and apoptosis preventing uncontrolled membrane rupture and cell content release³⁴. In **type 2** cells, most prominently hepatocytes, pancreatic β cells and the majority of cancer cells, effector caspase (CASP3) activation is inhibited by X-linked inhibitor of apoptosis (XIAP)^{34,35}. Instead, CASP8 cleaves BID, which translocates to mitochondria in its truncated form (tBID) and activates pro-apoptotic protein BAX and BAK to cause MOMP³⁶. MOMP induces the release of second mitochondria-derived activator of caspase (SMAC) from mitochondria, a natural antagonist for XIAP, which thereby counteracts CASP3 inhibition³⁵. Cytochrome c released from mitochondria binds the adaptor molecule APAF1 to assemble the apoptosome inducing apoptosis as described in 1.1.1³⁰.

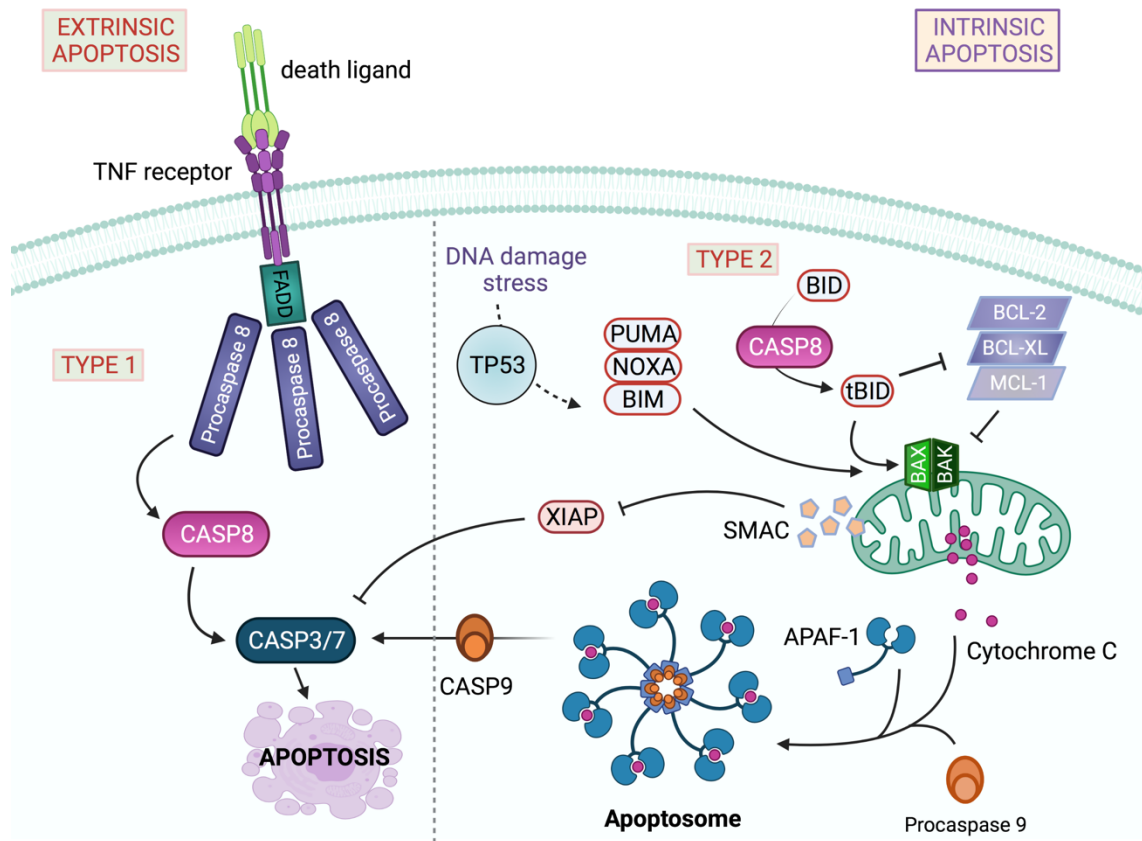


Figure 1 Extrinsic and intrinsic apoptosis pathways.

Extrinsic apoptosis is induced upon death ligand binding to their cognate receptors (TNF receptor superfamily). In type 1 extrinsic apoptosis this is followed by FADD recruitment to the receptor. FADD in turn recruits procaspase 8 which is then activated to caspase 8 (CASP8). CASP8 further activates effector caspases 3 and 7 (CASP3/7) inducing apoptosis. In type 2 cells, x-linked inhibitor of apoptosis (XIAP) inhibits cleavage of CASP3 by CASP8. This can be circumvented by XIAP binding of the natural XIAP-agonist second mitochondria-derived activator of caspase (SMAC). SMAC is released from mitochondria upon mitochondrial outer membrane permeabilisation (MOMP). CASP8 cleaves the BH3-interacting domain death agonist (BID) into tBID, which then translocates to mitochondria activating BCL-2 associated X protein (BAX) and Bcl-2 homologous antagonist/killer (BAK). BAX and BAK are responsible to induce MOMP which is accompanied by cytochrome c release from mitochondria which binds apoptotic protease activating factor 1 (APAF-1) in the cytosol. APAF-1, cytochrome c and procaspase 9 assemble the apoptosome resulting in activation of caspase 9 (CASP9) activating executioner caspases 3 and 7 resulting in apoptosis. Intrinsic apoptosis is induced upon cellular stress, such as DNA damage, which can be sensed by tumour-suppressor protein p53 (TP53) resulting in activation of pro-apoptotic factors BCL2 binding component 3 (BBC3; best known as p53-upregulated modulator of apoptosis, PUMA), phorbol-12-myristate-13-acetate-induced protein 1 (PMAIP1; also known as NOXA) and BCL2 like 11 (BCL2L11; also known as BCL2-interacting mediator of cell death, BIM) and BH3 interacting domain death agonist (BID) over anti-apoptotic BCL-2 family members, such as BCL-2, BCL2 like 1 (BCL2L1, also known as BCL-XL) and MCL1, BCL2 family apoptosis regulator (MCL-1). Activation of BCL-2 associated X protein (BAX) and BCL-2 homogenous antagonist/killer (BAK) is followed by irreversible mitochondria outer membrane permeabilisation (MOMP). Cytochrome C released by MOMP binds apoptosis promoting factor 1 (APAF1) and they assemble the apoptosome. The apoptosome then activates the caspase (CASP) cascade consisting of initiator CASP8/9/10 and

effector CASP3/7 ultimately resulting in DNA fragmentation and apoptosis. The scheme was drawn using fully licensed biorender.com.

1.1.3 Necroptosis

In contrast to apoptotic cell death, necrotic PCDs such as necroptosis phenotypically result in membrane rupture accompanied by release of cellular content to the extracellular space^{37,38}. Necroptosis is critically dependent on receptor interacting serine/threonine kinase (RIPK3) and mixed lineage kinase domain like pseudokinase (MLKL)^{12,37}. Upon extra- or intracellular stimulation detected by death receptors including TNFR, complex 1 is formed at the membrane³⁹. Complex I is a multiprotein complex consisting of TNFR-associated death domain (TRADD), ubiquitinated RIPK1, cellular inhibitor of apoptosis protein 1/2 (cIAP) and TNF receptor-associated factor (TRAF) 2 and TRAF5³⁹. In a CASP8-deficient scenario or upon SMAC-mediated inhibition of cIAPs, necroptosis is induced and RIPK1 is activated by deubiquitination by cylindromatosis (CYLD)⁴⁰. RIPK1 activates RIPK3 which is not only activated by RIPK1 but also by other RHIM-domain containing proteins like Z-DNA-binding protein 1 (ZBP1)^{41,42}. RIPK3 catalyses the phosphorylation of MLKL forming the necrosome (also named complex III) which triggers membrane permeabilisation and thereby necroptosis⁴³.

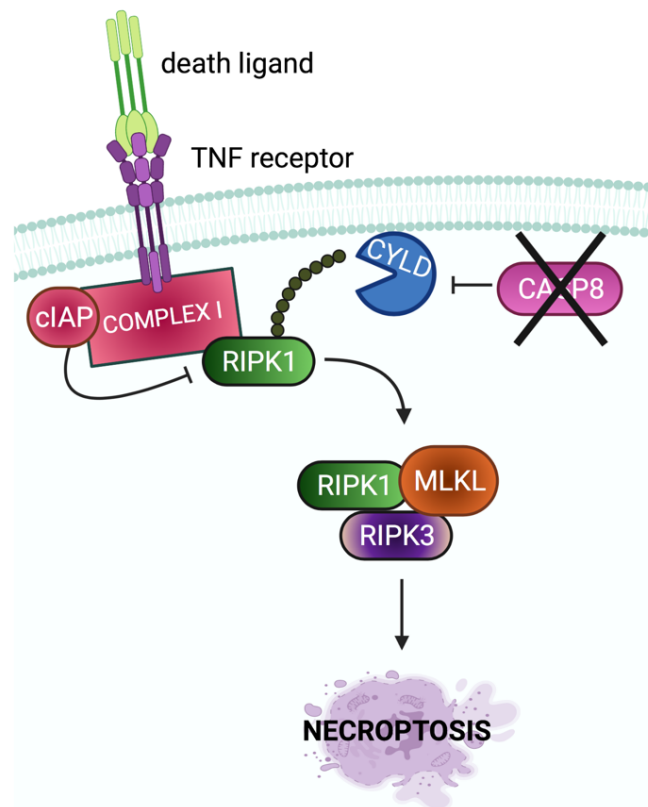


Figure 2 Necroptosis pathway.

Upon binding of death ligands to their cognate receptor, complex 1 is formed consisting of TNFR-associated death domain (TRADD), ubiquitinated receptor interacting serine/threonine kinase (RIPK)1,

cellular inhibitor of apoptosis protein 1/2 (cIAP) and TNF receptor-associated factor (TRAF) 2 and TRAF5. In a caspase 8 (CASP8) deficient scenario or upon SMAC mediated inhibition of cIAPs, RIPK1 is deubiquitinated by cylindromatosis (CYLD) and activated. RIPK1 activates RIPK3. RIPK3 in turn catalyses the phosphorylation of MLKL. Together they form the necrosome which triggers membrane permeabilisation and induces necroptosis. The scheme was drawn using fully licensed biorender.com.

1.1.4 Ferroptosis (adapted from Bebbler et al., *Cancers*, 2020)

Although not named at the time, ferroptosis was first discovered as part of a synthetic lethality screen for small-molecules selectively targeting rat sarcoma (*RAS*)-mutant cells⁴⁴. The small molecules eradicator of *RAS* and *ST*-expressing cells (erastin)⁴⁵ and *RAS*-selective lethal 3 (RSL3)⁴⁶ were first described to induce a *RAS*-specific oxidative type of cell death independently of caspases with a necrotic phenotype.

The name-giving hallmark of ferroptosis is the requirement of divalent iron (Fe^{2+}) as chelation of iron by deferoxamine (DFO) rescues experimental induction of ferroptosis⁴⁷. Constitutive cellular iron import is mediated by transferrin which binds free ferric iron (Fe^{3+}), the formed complex binds the transferrin receptor (TFR1/CD71) and is then shuttled into the cell via endocytosis. Consequently, transferrin was shown to be required for MEF cells to undergo ferroptosis⁴⁸. Yet, our laboratory has recently shown that dynamin 1 and 2-mediated endocytosis of transferrin receptor is dispensable for ferroptosis induced in non-small cell lung cancer cell lines⁴⁹. Once Fe^{3+} is imported, endosomal six-transmembrane epithelial antigen of prostate 3 (STEAP3) catalyses the reduction to divalent Fe^{2+} and releases it to the cellular labile iron pool by divalent metal transporter 1 (DMT1)⁵⁰. Interestingly, *DMT1* has been shown to be up-regulated upon ferroptosis-induction⁵¹. Furthermore, depletion of Nitrogen-Fixing Bacteria S-Like Protein (NFS1) sensitises lung adenocarcinoma to ferroptosis⁵². NFS1 is a cysteine desulfurase harvesting sulfur from cysteine essential for biosynthesis of iron-sulfur cluster (ISC). ISCs serve as protein cofactors for many cellular proteins predominantly involved in oxidative phosphorylation (OXPHOS). Upon suppression of NFS1 causing inhibition of ISC biosynthesis the iron responsive protein 1 (IRP1) is activated and stabilises TFR1 mRNA and promoting iron uptake and intracellular release⁵³ which can then sensitise cancer cells to ferroptosis⁵².

The other important hallmark of ferroptosis is the characteristic accumulation of reactive oxygen species (ROS) especially membrane lipid peroxides⁴⁷. Lipid peroxides were recently modelled to destabilise the lipid bilayer resulting in disintegration of cellular membranes^{54,55}. Using lipidomics, arachidonic acid (AA)- and adrenic acid (AdA)-containing phospholipids, specifically phosphatidylethanolamine (PE) species were identified as the main *in vivo* lipid products of ferroptosis⁵⁶. Moreover, recently ether-linked phospholipids have been identified as specific lipid peroxidation targets during ferroptosis⁵⁷. Lipid

peroxidation can take place spontaneously in the presence of free redox active Fe^{2+} to promote a Fenton reaction generating hydroxyl radicals ($\text{HO}\cdot$) from hydrogen peroxide (H_2O_2)⁵⁸. These radicals then react directly with polyunsaturated fatty acids (PUFAs) in membrane phospholipids. Alternatively, divalent iron can serve as a cofactor for lipoxygenase (LOX) to catalyse PUFA peroxidation enzymatically⁵⁹. Lipid peroxidation within membranes can then trigger a chain reaction of lipid ROS attacking proximal PUFAs. PUFAs are especially sensitive to lipid peroxidation due to highly reactive hydrogen atoms within methylene bridges^{60,61}. Interestingly, 4-hydroxynonenal (4-HNE) and malondialdehyde (MDA) are aldehyde secondary products of lipid peroxidation which combined with TFR1/CD71 and cyclooxygenase 2 (COX2) upregulation⁶² can serve as ferroptosis markers in tissues⁶³.

The main source of ROS in cells is OXPHOS⁶⁴. OXPHOS generates cellular energy in the form of adenosine triphosphate (ATP) at the expense of atmospheric oxygen. Here, protein complexes belonging to the electron transport chain are located in the inner mitochondrial membrane where they transport electrons derived from nicotinamide adenine dinucleotide (NADH) via redox reduction to the terminal electron acceptor oxygen (O_2) which is thereby reduced to water (H_2O). NADH is one of the major products of the tricarboxylic acid (TCA) cycle within the mitochondrial lumen driven by metabolites as Acetyl-CoA from glycolysis and β -oxidation⁶⁴. During electron transport, a small proportion of electrons leak out of the transport chain at complex I and III and react with oxygen molecules to generate highly reactive superoxide ($\text{O}\cdot^-$)⁶⁵. Superoxides can be transported into the cytosol using the mitochondrial permeability transition pore (mPTP) in the outer mitochondrial membrane. Thereby, OXPHOS is a major source of reactive oxygen species (ROS) in aerobic cells which initiated the need to adapt and evolve a complex cellular anti-oxidant defence system.

To cater to this need, superoxide dismutases (SOD) localised either in the cytoplasm (SOD1) or in the mitochondrial matrix (SOD2) catalyse the dismutation of $\text{O}\cdot^-$ into slightly less reactive hydrogen peroxide (H_2O_2)⁶⁵. To further protect cells from H_2O_2 -oxydative damage, it is reduced to water (H_2O) by cellular antioxidant enzymes such as catalases, glutathione peroxidases (GPXs) or peroxireductases (PRDXs)⁶⁶. The majority of antioxidant defence proteins such as SLC7A11, GCLC, GCLM and GPX4 are transcriptionally induced by the master antioxidant transcription factor nuclear factor erythroid 2-related factor 2 (NRF2, also called NFE2L2)⁶⁷. NRF2 is activated upon oxidative-stress induced degradation of its negative regulator kelch-associated protein 1 (KEAP1), translocates to the nucleus and induces the expression of antioxidant response element (ARE)-containing antioxidant genes⁶⁷⁻⁶⁹. Yet, high levels of ROS can overwhelm the cellular anti-oxidant defence system resulting in oxidative stress in the form of free radicals directly

oxidising cysteines within proteins, lipids and DNA. This process is fuelled by redox-active metals. Hence, limiting availability of free divalent redox-active metals via keeping them sequestered within metal-binding proteins is part of the cellular antioxidant defence machinery⁷⁰.

Acyl-CoA synthetase long-chain family member 4 (*ACSL4*) was identified as a first cellular protein genetically required for ferroptosis by generating the lipid target pool for peroxidation^{71,72}. *ACSL4* mediates esterification of AA and AdA with CoA forming Acyl-CoA which can then undergo either catabolic fatty acid oxidation (β -oxidation) or anabolic PUFA biosynthesis⁷²⁻⁷⁴. In a similar manner, lysophosphatidylcholine acyltransferase 3 (*LPCAT3*) contributes to ferroptosis by incorporation of Acyl-AA into phospholipids of cellular membranes thereby providing the pool of PUFAs targeted by peroxidation^{72,75,76}. Recently, important peroxisomal genes have been identified in a genome-wide CRISPR-Cas9 suppressor screen to contribute to ferroptosis⁵⁷. Polyunsaturated ether-linked phospholipids (PUFA-ePLs) synthesised in the peroxisome and endoplasmic reticulum (ER) are specifically peroxidised during ferroptosis⁵⁷. Together, these findings demonstrate that PUFA synthesis and peroxidation are essential prerequisites for cells to die via ferroptosis.

Counteracting this axis of lethal lipid peroxidation in cells, glutathione peroxidase 4 (*GPX4*), the only GPX family member capable of reducing lipid hydroperoxides (L-OOH) to their respective lipid alcohols (L-OH) and thereby prevent ferroptosis⁶². In humans, eight GPX family members exist, *GPX1-4* and *GPX6* are selenoproteins containing a redox-active selenocysteine residue⁷⁷. GPXs act as antioxidant enzymes capable of reducing different ROS species in cells⁶². Importantly, inhibition of *GPX4* using the small molecule inhibitor RSL3, ML210 or ML162 led to efficient induction of ferroptosis^{47,62,78,79}. *GPX4* requires glutathione (GSH) as a redox equivalent to reduce lipid hydroperoxides. GSH, a thiol-containing tripeptide consisting of glycine, glutamate and cysteine is the most abundant cellular non-protein antioxidant⁸⁰. GSH synthesis is coupled to the availability of intracellular cysteine generated from cystine imported from the extracellular space via the sodium-independent cystine/glutamate antiporter System xc-. System xc- is a heterodimer consisting of a heavy (4F2, gene name: solute carrier family 3 member 2 (*SLC3A2*)) and a light chain (xCT, gene name: solute carrier family 7 member 11 (*SLC7A11*))⁸¹. Interestingly, *SLC7A11*, the subunit decisive for specific amino acid antiport was shown to be a molecular target of erastin and the resulting cystine depletion was responsible for the induction of ferroptosis^{82,83}. Moreover, depletion of cysteine from cell culture media can induce ferroptosis, avoiding the use of pharmacological inhibitors

Furthermore, Wang et al. described in 2020, that immunotherapy activated CD8⁺ T cells sensitise cancer cells for ferroptosis. IFN- γ released by CD8⁺ T cells mediates decreased expression of *SLC3A2* and *SLC7A11* in target cells which leads to impaired cysteine import and thereby reduced GSH levels. This resulted in higher levels of lipid peroxidation promoting ferroptosis in target cells⁸⁴.

An alternative source for intracellular cysteine used for GSH synthesis can be the trans-sulfuration pathway in certain cells potentially compensating for cysteine-deprivation⁸⁵. Here, homocysteine is generated from methionine in an ATP-dependent manner by the cystathionine beta-synthase (CBS) and converted into cysteine, which is catalysed by the cystathionine γ -lyase (CSE)⁸⁶. Interestingly, a newly developed CBS inhibitor has been identified to induce ferroptosis in different cancer cell lines⁸⁷. During GSH synthesis, glutamate and cysteine are ligated by the glutamate-cysteine ligase (GCL) forming the GSH precursor γ -glutamylcysteine. GCL is a heterodimer consisting of the catalytic subunit Glutamate-Cysteine Ligase Catalytic Subunit (GCLC) and the regulatory subunit Glutamate-Cysteine Ligase Modifier Subunit (GCLM)⁸⁸. One ferroptosis inducer, which is applicable for *in vitro* and *in vivo* treatment to date is buthionine sulfoximine (BSO). BSO binds GCL and thereby inhibits GSH synthesis indirectly inhibiting reduction of lipid peroxides through GPX4.

Recently, the ferroptosis suppressor protein 1 (FSP1, also called apoptosis-inducing factor mitochondrial 2 (AIFM2)) as another ferroptosis regulating factor has been identified in a synthetic lethal CRISPR-Cas9 knockout (KO) screen in RSL3 treated cancer cells⁸⁹ and a cDNA overexpression screen complementing for *GPX4* loss⁹⁰. Doll et al. and Bersuker et al. report that FSP1 is recruited to the plasma membrane by N-terminal myristoylation, where it acts as an oxidoreductase reducing ubiquinone (=Coenzyme Q10) to the lipophilic radical scavenger ubiquinol limiting plasma membrane lipid peroxidation in the absence of GPX4. Hence, ubiquinol generated by FSP1 acts similar to the described small-molecule lipophilic radical scavenger Ferrostatin-1 (Fer-1) and liproxstatin-1 inhibiting ferroptosis^{47,91}. Other antioxidants such as alpha-tocopherol, butylated hydroxytoluene and β -carotene have also been shown to suppress erastin-induced cell death⁴⁵.

Imbalance in the levels of iron, cysteine and GSH in cells are decisive for the execution of ferroptotic cell death. Since its discovery in 2012, many genes have been identified to be involved in ferroptosis regulation, however the exact molecular mechanism of ferroptosis and its execution remains to be fully elucidated.

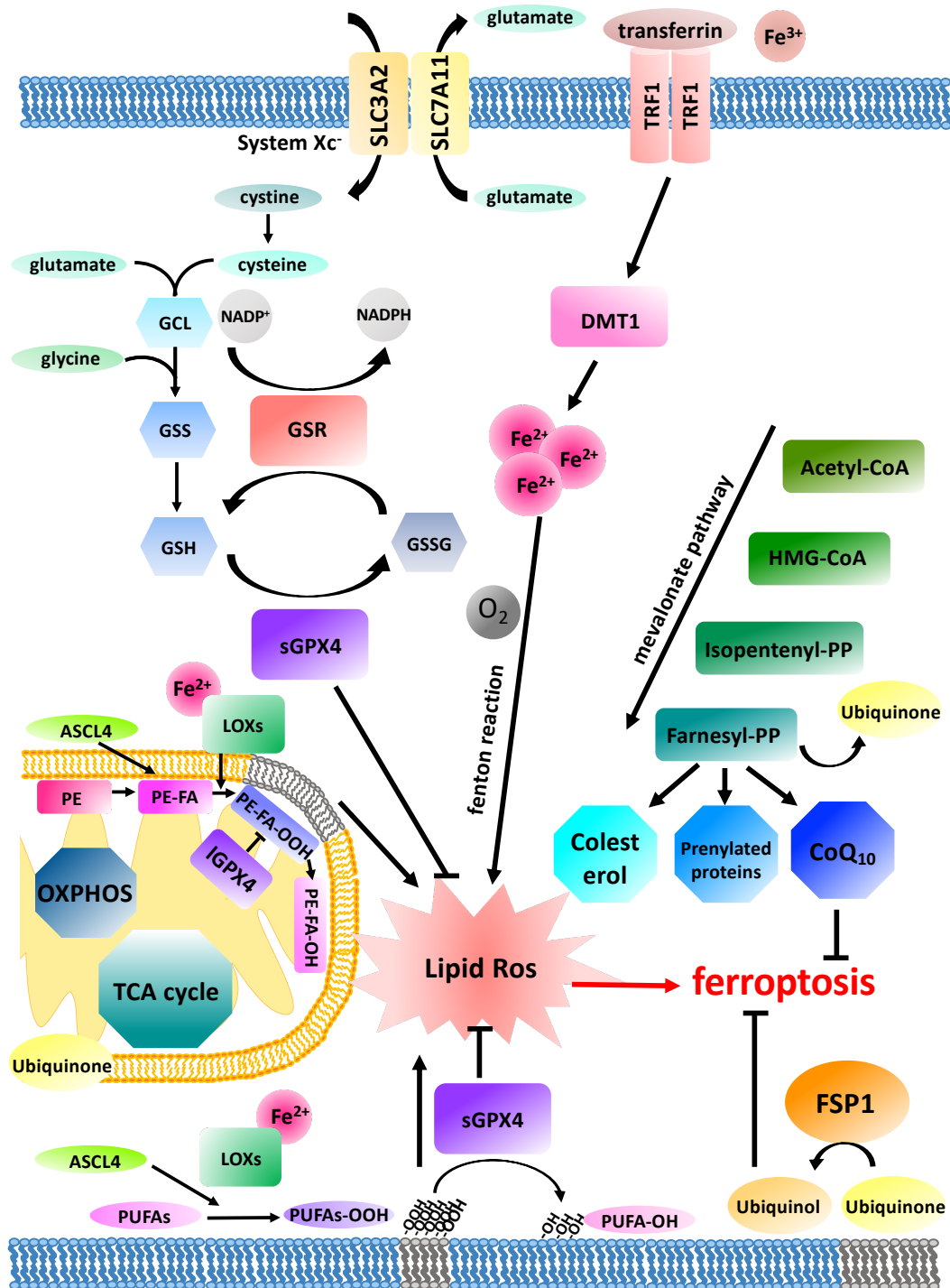


Figure 3 Schematic view of the ferroptosis pathway.

Ferroptosis is induced upon aberrant build-up of lipid reactive oxygen species (ROS) leading to peroxidation (-OOH) of polyunsaturated fatty acids (PUFAs). Main peroxidation target PUFAs are arachidonic acid (AA) phosphatidylethanolamine (PE) lipid species within cellular membranes leading to membrane destabilisation and rupture. Lipid peroxidation can be triggered by cytosolic redox active iron (Fe²⁺) shuttled into cells bound to transferrin via transferrin receptor (TFRC) endocytosis and endosomal release mediated by divalent metal transporter 1 (DMT1). In the presence of H₂O₂, Fe²⁺ catalyses hydroxyl radical (HO·) generation in a Fenton reaction, which sets of a radical lipid peroxidation chain reaction. Lipoxygenase (LOX) can equally catalyse lipid peroxidation using Fe²⁺. Acyl-CoA

synthetase long-chain family member 4 (ACSL4) and lysophosphatidylcholine acyltransferase 3 (LPCAT3) generate the pool of AA-containing target lipids. Glutathione peroxidase 4 (GPX4), in turn, hydrolyses lipid peroxides converting them into their respective non-toxic lipid alcohols (-OH). GPX4 requires glutathione (GSH) as a cofactor which upon its oxidation (GSSG) by GPX4 is reduced to GSH by glutathione reductase (GR). GSH synthesis depends on glutamate cysteine ligase (GCL) and glutathione synthetase (GSS) as well as on intracellular cystine shuttled into the cell in exchange for glutamate mediated by system xc- (SLC3A2 and SCL7A11/xCT). Independently of GSH, ferroptosis suppressor protein 1 (FSP1) generates ubiquinol from ubiquinone which acts as a lipophilic radical trapping agent within membranes thereby protecting from ferroptosis. Oxidative phosphorylation (OXPHOS) and the tricarboxylic acid (TCA) cycle have both been described to be required for ferroptosis triggered by cystine-depletion or system xc- but not GPX4 inhibition. Taken from Bebbber et al., 2020 Cancers ⁹².

1.1.4.1 Thioredoxin redox system

To maintain cell integrity and metabolic competence of cells, maintenance of a reduced intracytoplasmic environment is required. This can be achieved through different antioxidant systems. Controlled oxidation and reduction of proteins is involved in cellular pathways important for proliferation, differentiation and cell death ^{93,94}.

In addition to the GSH-based antioxidant redox system, the thioredoxin-based antioxidant redox system can take over antioxidant defence in cells ⁹⁵. In contrast to the GSH-based system, here, reduced thioredoxin (TXN, protein name: TRX) serves as a redox equivalent for peroxiredoxins (PRDXs) to reduce reactive oxygen species (ROS) and lipid peroxides ⁹³. TRX is a small protein with two redox-active cysteine residues at its active centre either presenting as a dithiol (TRX-SH₂) in the reduced state or a disulphide (TRX-S₂) in the oxidised state (see **Figure 4**) ⁹⁴. An important group of redox regulatory selenoproteins, the thiol-containing thioredoxin reductases (TXNRD, protein name: TRXR) regenerate reduced TRX at the expense of nicotinamide adenine dinucleotide phosphate (NADPH) independently of GSH ^{93,96}. In mammals three isoforms are expressed, cytoplasmic thioredoxin reductase 1 (TXNRD1), mitochondrial TXNRD2 and spermatospecific TXNRD3 ^{93,94}. The thioredoxin interacting protein 1 (TXNIP) acts as a negative regulator of TRX by binding to the reduced form ⁹⁷. TXNIP is upregulated during aging in human cells and *Drosophila melanogaster* leading to accumulation of ROS and oxidative DNA damage ⁹⁸.

The thioredoxin system is essential for embryogenesis. Txnrd1 KO mice die during early embryonic development at E9.5 and display severe growth retardation and impairment in proliferation, yet normal heart development with functional cardiomyocytes ^{99,100}. Mice lacking mitochondrial *Txnrd2* also die during embryogenesis (E13.5) displaying severe anaemia and defective heart development ¹⁰¹ indicating that the two isoforms have non-redundant functions. Given the important role for TXNRD1 and -2 in embryonic

development, it is not surprising that cytosolic TRX1 and mitochondrial TRX2 are also essential for normal embryogenesis^{102,103}. *Txn1^{-/-}* deficiency is lethal at E6.5¹⁰² and *Txn2^{-/-}* mice die at E12.5 showing extensive cell death and exencephaly¹⁰³. Interestingly, mouse embryos start oxidative phosphorylation around E12.5 leading to the production of reactive oxygen species¹⁰³.

A commonly used inhibitor of TXNRD1 and TXNRD2 is Auranofin, a thiol-reactive gold-containing compound that has been used for the treatment of rheumatoid arthritis¹⁰⁴. The role of the thioredoxin system in the ferroptosis pathway has been repeatedly discussed^{105,106}. Interestingly, PRDXs, selenium-independent antioxidant enzymes are capable of using TRX or GSH as a redox equivalent and can protect cells from ferroptosis. PRDXs are classified by harbouring one (PRDX6) or two (PRDX1-5) conserved cysteine residues at the active site. PRDX1-5 use mainly TRX as a redox equivalent whereas PRDX6 mainly uses GSH as an electron donor¹⁰⁷. PRDX1 protects corneal endothelial cells from ferroptosis¹⁰⁵ and PRDX5 inhibits ROS accumulation in erastin treated human liver cancer cells¹⁰⁶. PRDX6 has a crucial function in membrane repair due to its hydroperoxidase activity reducing lipid hydroperoxides to alcohol. Furthermore, Ca^{2+} -independent phospholipase activity of PRDX6 enables hydrolysis of hydroperoxides at their sn-2 fatty acyl ester bond into peroxidised PUFA and lysophospholipid (LPC)^{107,108}. Lu et al described in 2019 that PRDX6 protects cells from ferroptosis¹⁰⁸. Moreover, KO of *TXNRD1* rescues ferroptosis induced by ML210-mediated GPX4 inhibition⁷⁸.

Although these studies might indicate a role of the thioredoxin redox system in suppressing ferroptotic cell death, it remains elusive if the thioredoxin pathway plays an influential part in limiting lipid peroxidation leading to ferroptosis or fulfils a role merely in buffering the general ROS burden of a cell.

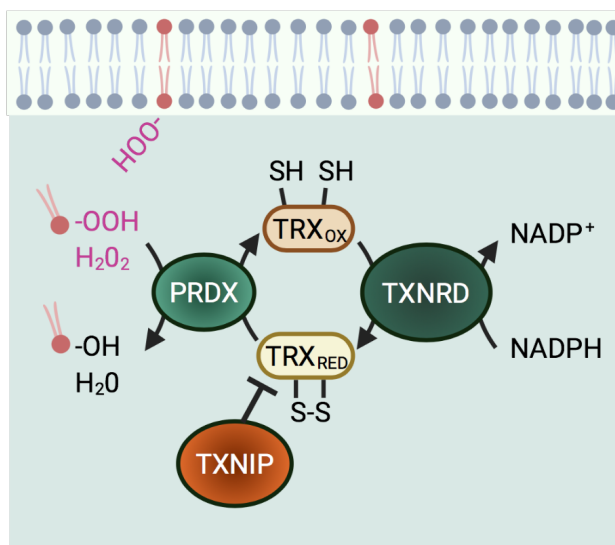


Figure 4 Schematic overview of the thioredoxin pathway.

Peroxiredoxins (PRDXs) reduce reactive oxygen species (ROS) species (lipid peroxides: L-OOH, hydrogen peroxide: H₂O₂) using reduced thioredoxin (TRX) as a redox equivalent which is regenerated by thioredoxin reductase (TXNRD) on the expense of NADPH. Thioredoxin interacting protein 1 (TXNIP) negatively regulates the thioredoxin system by binding reduced TRX. The scheme was drawn using fully licensed biorender.com.

1.1.4.2 Cancer metabolism and ferroptosis

Malignant cellular transformation is often initiated upon mutational activation of a driver oncogene accompanied by inactivation of a tumour suppressor gene together allowing for uncontrolled proliferation at the cost of increased ATP consumption⁶. Increased energy consumption requires higher levels of OXPHOS which, in turn, produces higher levels of ROS. Paradoxically, although OXPHOS is the most efficient way to generate ATP, many cancer cells have undergone metabolic reprogramming wherein they mainly generate ATP from cytosolic aerobic glycolysis coupled to lactate fermentation. This long-term metabolic change was famously discovered by Warburg and Cori in the 1920s and has been suggested as a cancer cell means to evade toxic levels of ROS production^{109,110}. However, switching to the Warburg metabolic state requires higher glucose levels and higher metabolism making tumour cells heavily reliant on the antioxidant machinery and possibly more susceptible to increases in oxidative stress¹¹⁰. This has sparked the discovery of the Crabtree effect describing the short-term effect of glucose-induced suppression of cellular respiration thereby allowing cancer cells to reduce ROS-producing OXPHOS in response to glucose availability¹¹¹.

ROS plays a controversial role in cancer: On the one hand, high levels of ROS are frequently observed in cancer cells and associated with cancer initiation and oncogenic transformation by transcriptional induction of proto-oncogenes like Fos proto-oncogene (c-FOS), Jun proto-oncogene (c-JUN) and MYC proto-oncogene, basic helix-loop-helix (bHLH) transcription factor (MYC)¹¹². Furthermore, many oncogenes like Harvey rat sarcoma viral oncogene homolog (*HRAS*), Kirsten rat sarcoma viral oncogene homolog (*KRAS*) and *MYC* indeed elevate cellular ROS levels arguing against the assumption that ROS mainly originates from OXPHOS^{113–115}. Moreover, ROS released by cells in inflamed tissue are mutagenic for surrounding tumour cells making tumours overall more malignant^{6,116}. Increased levels of ROS have been reported to in fact promote proliferation and survival pathways, such as the phosphoinositide 3 kinase (PI3K) pathway via oxidative inactivation of PTEN and subsequent activation of protein kinase B (AKT)^{117,118}. On the other hand, studies describe that depletion of the ROS scavenger GSH and subsequent increase in ROS levels protect from tumour initiation but not from tumour progression¹¹⁹. It is therefore likely that ROS levels in tumours need to be present at just the right level to be tolerated or even advantageous. This is supported by the finding that

endogenous expression of oncogenic *KRAS* induces the antioxidant transcription factor *NRF2* thereby reducing ROS levels and enhancing tumorigenesis¹²⁰. Interestingly, the same study showed that exogenous expression of high levels of oncogenic *KRAS* rather suppressed activation of *NRF2* which led to very high cellular ROS levels. High oncogenic RAS expression, in turn, is known to trigger cellular senescence¹²¹. Furthermore, it has recently been shown that fibroblasts expressing oncogenic *KRAS*G12V are protected from H₂O₂-induced cell death by up-regulating *SLC7A11*, which allows for *KRAS*-induced tumour growth *in vivo*¹²².

In light of these findings, it is not surprising that recent findings hint at a pivotal role of ferroptosis in cancer cell biology^{123–127}. Interestingly, ferroptosis has been described to be involved in the tumour suppressing function of *TP53* by suppressing the expression of *SLC7A11* on transcriptional level and thereby sensitising cells to ferroptosis¹²³. Moreover, cytosolic accumulation of *TP53* mutants typically found in cancer was shown to bind and thereby sequester *NRF2*, preventing nuclear translocation of *NRF2* and induction of its target genes including *SLC7A11*¹²⁴.

In contrast to the above-mentioned studies, in human colorectal cancer (CRC) cells, p53 was shown to promote *SLC7A11* expression¹²⁵. Furthermore, the same study showed that loss of p53 inhibits accumulation of dipeptidyl-peptidase-4 (DPP4) in the nucleus, which results in enhanced plasma-membrane associated DPP4-dependent lipid peroxidation via ROS-generating NADPH oxidase (NOX) enzymes resulting in ferroptosis¹²⁵. Thereby, loss of p53 may equally sensitise cells to ferroptosis in certain contexts. Interestingly, knockdown of the tumour suppressor gene retinoblastoma-associated protein 1 (*RB1*) in hepatocellular carcinoma (HCC) sensitises cells to ferroptosis induction using sorafenib¹²⁸.

Although these studies propose that there is a relationship between tumour suppression and ferroptosis sensitivity, so far, there is no genetic evidence that p53 expression directly induces ferroptosis and thereby mediates tumour suppression *in vivo*. Future studies will have to unravel whether ferroptosis can suppress tumour growth and to what extent it is part of the constitutive p53-mediated tumour-suppressive machinery.

Interestingly, depletion or inhibition of *SLC7A11* was shown to kill pancreatic and lung adenocarcinoma representing a novel therapeutic vulnerability in these cancers^{129,130}. Considering that components of the ferroptosis pathway are often aberrantly expressed in cancer cells^{52,131,132}, manipulation of the molecular mechanisms in the ferroptosis pathway might be exploited in cancer therapy. However, the two main ferroptosis inducers used *in vitro*, RSL3 and erastin, are not suitable for *in vivo* application due to low water solubility and renal toxicity^{62,133}, but a number of Food and Drug Administration (FDA)-approved drugs have been identified to induce ferroptosis in different cancer cell

lines and entities^{83,126,134,135}. Several efforts are under way to chemically optimise erastin for *in vivo* application, including exosome packaging and administration of metabolically stable derivatives^{47,62,133,136}.

As many cancer cells often present with downregulation of tumour suppressor genes and important pathway components of caspase-dependent PCDs to evade cell death^{6,137}, ferroptosis has recently attracted attention as a potential strategy to kill cancer cells.

1.2 Lung Cancer

Lung Cancer is one of the leading causes of cancer-related deaths worldwide^{138,139}. In 2020, lung cancer was the second most diagnosed cancer after breast cancer in general and the leading cause of malignant cancer-related deaths in male patients¹⁴⁰. In the female population, lung cancer was the second leading cause of cancer-related death after breast cancer¹⁴⁰.

The most common risk factor for lung carcinomas is tobacco smoking, only 10-15% of diagnosed lung carcinoma cases occur in never-smokers¹⁴¹. Based on clinical and histological features, lung carcinomas can be separated into two major groups, small cell lung cancer (SCLC) and non-small cell lung cancer (NSCLC), which account for 15% and 85% of diagnosed cases, respectively¹⁴². NSCLC comprises 85% of lung cancer cases and is characterised by a more heterogeneous phenotype divided into three main groups: adenocarcinomas arising from small airway epithelial, type II alveolar cells (50%)¹⁴³, squamous cell carcinomas arising from squamous cells in bronchial tubes (30%) and other subtypes (20%)^{144,145}.

In lung adenocarcinoma (LUAD), the identification of driver mutations, such as *KRAS* in up to 30% and epidermal growth factor receptor (*EGFR*) in up to 15% of cases led to the development of specific targeted therapies next to chemotherapy^{144,146}. Tyrosine-kinase inhibitors (TKIs) are now used as first-line therapy for NSCLC with activating *EGFR* mutations or rearrangements in anaplastic lymphoma kinase (*ALK*), ROS proto-oncogene 1 (*ROS1*), and rearranged during transfection (*RET*) genes¹⁴⁷. In SCLC, however, such clear targeted approaches have been lacking.

1.2.1 Small Cell Lung Cancer (SCLC)

SCLC is the most aggressive form of lung cancer and affects approximately 200,000 people worldwide every year^{148,149}. SCLC comprises about 15% of all lung cancer cases and is characterised by small cells originating mostly from neuroendocrine (NE) precursor cells within the lung with very high tumour mutational burden (TMB)¹⁵⁰⁻¹⁵².

SCLC cells are phenotypically described as “a malignant epithelial tumour consisting of small cells with scant cytoplasm, ill-defined cell borders, finely granular nuclear chromatin, and absent or inconspicuous nucleoli”¹⁵³. It is staged into limited stage and extensive stage disease, according to the Veterans Administration Lung Study Group system¹⁵³. A considerable fraction of patients (60-70%) is diagnosed at the extensive stage disease, due to rapid growth, early metastatic spread and lack of early detection methods^{153,154}. These patients have a median survival of 7-13 months and an overall five-year survival rate of only 2%^{153,155}. Patients diagnosed at the limited stage disease have a median survival of 23 months and the proportion surviving five years is 12-17%^{153,155}.

Another characteristic of SCLC is the early onset of metastatic spread as SCLC is one of the most metastatic cancer types¹⁵⁶. SCLC typically forms bulky primary tumours in the chest accompanied by mediastinal lymph node metastases¹⁵⁷. The most common additional metastatic sites are bone (19-38%), liver (17-34%), adrenal glands (5-31%), bone marrow (17-23%), brain (0-14%), lymph nodes (7-25%), and soft tissues (3-11%)^{157,158}.

Given that biopsies are rarely taken from metastases of SCLC patients, the extraordinarily high number of circulating tumour cells (CTCs) provides a tool for analysis of metastatic factors as well as to identify expression of marker genes¹⁵⁹⁻¹⁶¹.

The vast majority of SCLC patients are past or current heavy smokers. However, approximately 2% of patients are never-smokers^{155,162,163}. The risk of developing SCLC increases by 12% per year of smoking, compared to 6% per year in the development of adenocarcinomas¹⁶⁴.

In succession to longstanding tobacco exposure, SCLC cells have a highly increased mutational load¹⁶⁵. The mutational burden of SCLC is approximately 7.4 protein-changing mutations per million base pairs, making it the cancer entity with second highest TMB after that of melanoma^{154,165,166}. In rare cases of never-smokers, oncogenesis is mainly associated with exposure to environmental tobacco smoke (ETS) or residential radon^{162,167,168}.

After initial high response rates of up to 80% to chemotherapy, consisting of platinum-based therapy (cisplatin or carboplatin) in combination with a topoisomerase II inhibitor (etoposide), most patients develop relapse¹⁵⁵. At extensive stage and limited stage disease, SCLC relapse rates average approximately 100% and 80% within one year after treatment, respectively, highlighting the urgent need for new treatment strategies^{154,169}. One additional FDA-approved agent used as standard second line therapy for recurrent SCLC is the topoisomerase I inhibitor Topotecan, achieving response rates of 8-20%¹⁷⁰⁻¹⁷².

Due to the fact that high TMB is a marker of potential immunotherapy response¹⁷³, clinical trials involving immune checkpoint blockade have recently been initiated for SCLC recently^{174,175}. As a consequence of neoplastic transformation, neoantigens presented on the major histocompatibility complex (MHC) I on antigen presenting cells (APCs) are recognised by the T cell receptor (TCR) on CD8⁺ cytotoxic T cells¹⁷⁶. This leads to an activation of T cells and further results in immunological elimination of transformed cells presenting antigens on their surface. Ligation of the immune checkpoint receptor programmed cell death protein 1 (PD-1) and programmed death ligand 1 PD-L1 provides a negative modulatory signal to T cell activation that should prevent overstimulation of immune responses^{177,178}. Many cancer tissues are able to express PD-L1 and thereby evade immune surveillance^{179,180}.

Nivolumab, a PD-1 immune checkpoint inhibitor binding to PD-1 and thereby disrupting the interaction with PD-L1 and PD-L2¹⁸¹, was approved for third-line treatment by the FDA in 2018 but does not improve survival significantly¹⁷⁵. In 2019, Atezolizumab, a PD-L1 immune checkpoint inhibitor has been approved by the European Medicines Agency (EMA) as first-line therapy combined with chemotherapy in SCLC patients with extensive stage disease. Yet, this regime only improved median survival by about two months¹⁷⁴ suggesting that despite high TMB SCLC may be difficult to kill by immune effector cells. Taken together, the overall five-year survival rate for SCLC is dramatically low and within the last 30 years the only novel treatment method approved with checkpoint inhibitors in 2018 and 2019 improved median survival only by about two months¹⁷⁵. For this reason, SCLC is yet described to be a “recalcitrant neo-plasm with limited therapeutic options”¹⁸². This highlights the necessity of novel approaches to better understand the biology of SCLC, in order to find features of this disease, which can be targeted therapeutically.

1.2.1.1 Genomic profile of SCLC

In contrast to NSCLC, the majority of SCLC cases do not harbour specific targetable driver mutations. However, whole genome sequencing identified biallelic functional loss of the tumour suppressor genes *RB1* and *TP53* is present in almost 100% of all SCLC cases at the genetic level but this genetic constellation has not been successfully targeted to date^{153,166,183,184}. Thus, there is an urgent need to identify other therapeutically relevant vulnerabilities next to deletions in *TP53* and *RB1*. This is hampered by the rare possibility to obtain samples from SCLC tumours because patients are most often diagnosed at extensive stage disease and hence treated by chemotherapy rather than surgical resection¹⁵³. Furthermore, samples of recurrent SCLC tumours are rarely resected. Consequentially, cohorts for genome analysis in SCLC consist of rather small sample numbers.

Genetically engineered mouse models (GEMM) provide a useful tool to investigate the cellular and molecular mechanisms underlying SCLC development and biology. The Rb1/p53 (RP) mouse model for SCLC carries conditional floxed alleles for *Rb1* and for *Trp53* which are deleted upon intratracheal instillation of adenoviral particles expressing the Cre recombinase (Adeno-Cre) and develop tumours which histopathologically resemble SCLC ¹⁵¹.

In recent studies, the genomic profile of SCLC tumours has been investigated more precisely and the accumulation of certain genomic alterations has been described such as in the MYC amplification, mutations in phosphatase and tensin homolog (PTEN), or tumour protein p73 (TP73) rearrangements. The MYC family members MYC, MYCN proto-oncogene, bHLH transcription factor (MYCN) and MYCL proto-oncogene, bHLH transcription factor (MYCL) encode for transcription factors and participate in many growth-promoting pathways ¹⁸⁵. Particularly, MYC is known to act as a proto-oncogene in a variety of human cancers ¹⁸⁶. In a study from Peifer et al. in 2012, single nucleotide polymorphism (SNP) array analyses on 63 human SCLC tumours was performed identifying focal amplifications in MYCL (5/63 cases), MYCN (4/63 cases) and MYC (1/63 cases) ¹⁶⁶. In further studies, MYC family members are described to be amplified in approximately 16-20% of SCLCs, in most cases they were described to be amplified in a mutually exclusive manner ^{187,188}.

Furthermore, mutations in the tumour suppressor gene *PTEN* are reported to play a role in the development of SCLC ^{184,189}. In 6% of 34 analysed human SCLC cell lines and 10% of primary tumour samples, PTEN was found to be impaired by point mutations, small fragment deletions, and homozygous deletions ^{183,190}. In the RP mouse model for SCLC carrying inactivated *Trp53* and *Rb1*, the additional inactivation of one allele of *Pten* led to accelerated SCLC with frequent metastasis to the liver ¹⁸⁹. This could be confirmed by Peifer et al. in 2012, reporting that in 3 of 29 analysed exomes, mutations in *PTEN* were identified, impairing the phosphatase activity and thereby activating the PI3-kinase pathway ¹⁶⁶.

George et al. recently described somatic genomic rearrangements of the tumour suppressor gene TP73 in their comprehensive genomic profiling study of 110 human SCLC samples. These somatic rearrangements resulted in an oncogenic version TP73 Δ ex2/3 creating a N-terminally truncated TP73 protein which has a dominant negative effect on wildtype p73 and p53 ¹⁸³.

Epigenetic regulators, such as the histone acetyl transferase gene CREB binding protein (*CREBBP*) and other histone modifying enzymes, such as E1A binding protein p300 (*EP300*) were described to be deleted or carry loss-of-function mutations in SCLC ^{166,191}. Further, high expression of the histone methyltransferase enhancer of zeste homolog 2

(*EZH2*) was identified in SCLC¹⁹². *EZH2* expression has been associated with increased chemoresistance by silencing schlafen family member 11 (*SLFN11*) and immune evasion by MHC I silencing¹⁹³. Targeting *EZH2* pharmacologically resulted in reduced tumour growth in SCLC PDX models¹⁹².

Another alteration, the amplification of the gene nuclear factor I/B (*NFIB*), was identified by next generation sequencing in the RP mouse model and human SCLC cell lines¹⁹⁴. Furthermore, elevated *NFIB* levels have been associated with increased metastatic potential in mouse and human models^{195–197}. The transcription factor *NFIB* has been described to promote metastasis in SCLC by increasing chromatin accessibility and induction of genes involved in neuronal differentiation and cell migration and adhesion^{195,198}. Interestingly in terms of cell death regulation, the pro-apoptotic protein BCL-2 has been shown to be upregulated in a fraction of SCLC patients^{199,200}. Venetoclax, a BCL-2 inhibitor, reduces growth in BCL-2 expressing SCLC cell systems *in vitro* and xenograft models *in vivo*²⁰¹.

However, it has been reported repeatedly, that *CASP8*, an essential component of the extrinsic apoptosis pathway is epigenetically silenced by promoter methylation in SCLC cell lines^{202,203}. Also other components such *CASP10* and *CD95* have been observed to be lost in many SCLC cell lines, indicating a strategy for immune escape²⁰⁴.

In general, loss of *RB1* and *TP53* in SCLC tumour samples were frequently confirmed in multiple studies^{183,205,206}. But aside from these two genes, only few genes have been reported to be altered recurrently and to date none of them provides an amenable therapeutic target for most SCLC patients.

1.2.1.2 Cell of origin and SCLC subtypes

Historically, SCLC has been treated as a rather uniform cancer entity without targetable driver mutations and irrespective of SCLC subtype. Due to the fact, that SCLC is not driven by oncogenes, subtypes are categorised by NE status. SCLC tumours predominantly consist of NE cells which mainly arise from pulmonary NE cells (PNECs)²⁰⁷. PNECs are characterised by NE marker expression, such as achaete-scute family bHLH transcription factor 1 (*ASCL1*), synaptophysin (*SYP*), neural cell adhesion molecule (*NCAM1*) and chromogranin A (*CHGA*)²⁰⁸.

The pro-neural bHLH transcription factor *ASCL1* is essential for the development of NE cells in lung and other tissues. Borges et al showed that *Ascl1*^{-/-} mice specifically ablate NE cells in the lung²⁰⁹. Knockdown of *ASCL1* with RNA interference results in growth inhibition and induction of cell death in SCLC cell lines^(210,211). Jiang et al showed that knockdown of *ASCL1* impairs the tumour initiating capacity of *ASCL1* high expressing subpopulation isolated from a xenograft model, indicating the role of *ASCL1* in

maintaining tumorigenicity in SCLC ²¹¹. *In vivo* experiments using the Trp53flox/flox, Rb1flox/flox and p130flox/flox (TCKO) mouse model further confirmed the requirement of ASCL1 for the formation of NE tumour formation in the lung (Borromeo et al., 2016).

In 2019, Rudin et al. defined four different subtypes expressing four different distinguishing transcription factors: NE ASCL1 (**SCLC-A**) and neurogenic differentiation factor 1 (*NEUROD1*) (**SCLC-N**), non-NE POU class 2 homeobox 3 (*POU2F3*) (**SCLC-P**) and yes-associated protein 1 (*YAP1*) (**SCLC-Y**) (see **Figure 5**) ²¹².

Non-NE SCLC cells were characterised by expression of the NE differentiation repressor RE1 Silencing Transcription Factor (*REST1*, also called *NRSF*) ^{213,214}, the negative regulator of ASCL1 and mesenchymal markers, such as CD44 and vimentin (*VIM*) ²⁰⁸. The SCLC-P subtype arises from rare chemosensory tuft cells in the pulmonary epithelium ²¹⁵.

The SCLC-A subtype was further divided into SCLC-A and SCLC-A2 according to low or high expression levels of hairy and enhancer of split-1 (*HES1*), respectively ²¹⁶. Another less NE subtype with high expression of the Atonal BHLH Transcription Factor 1 (*ATOH1*) has been identified recently based on CTC-derived explant models (*CDX*) ¹⁶¹. Recently, expression of an inflamed gene signature was proposed to define another distinct less NE subtype with elevated immunotherapy sensitivity ²¹⁷. However, an exclusively *YAP1*-expressing SCLC-Y subtype could not be confirmed in this study which is in line with previous histochemical analysis ^{217,218}.

Classification into these subtypes is further accompanied by other expression patterns. The SCLC-A subtype is associated with high *MYCL* expression whereas the other subtypes express increased levels of *MYC* rendering them more sensitive to Aurora kinase inhibitors (see **Figure 5**) ^{185,188,219}. Interestingly, Ireland et al. describe the role of *MYC* expression in subtype plasticity as *MYC* expression can lead to dedifferentiation of PNEC cell of origin from SCLC-A subtype to SCLC-N to SCLC-Y via Notch activation ²²⁰.

The Notch signalling pathway is a highly conserved cell signalling pathway and plays an important role in cell-to-cell communication, neuronal development, cell proliferation and cell differentiation ^{221,222}. The Notch signalling pathway is activated by ligation of Notch receptor and its ligands (Delta Like Canonical Notch Ligand (*DLL*) 1, *DLL3*, *DLL4*, *Jagged-1* and *Jagged-2*) resulting in Notch intracellular domain (*NICD*) release ²²². *NICD* then translocates into the nucleus and cooperates with other transcription factors to direct the expression of its target genes such as *HES1*. Notch signalling is involved in both, tumour suppressive and pro-tumorigenic events ²²³. Non-NE SCLC cells present with increased Notch signalling are slowly growing but at the same time also more chemo-resistant and provide trophic support to NE SCLC cells ²²³. *In vivo* experiments with combination of Notch blockage and chemotherapy showed a suppression of tumour growth

and delay in relapse ²²³. However, the mechanism of Notch signalling in mediating chemoresistance is still to be explored in detail.

Interestingly, SCLC NE subtype classification has recently been linked to immune gene signature expression ^{224,225}. NE cells (SCLC-A and SCLC-N) repress expression of immune signature genes especially major MHC I, while MHC I was described to be re-expressed on non-NE chemoresistant relapsed cells (see **Figure 5**) ^{224,225}. Repression of MHC I in SCLC is epigenetically mediated and could be reversed by EZH2 inhibition ²²⁵. MHC I could serve as a biomarker for immune responsiveness in SCLC ^{224,225}.

In conclusion, SCLC is a cancer entity presenting with intratumoural heterogeneity combined with subtype plasticity and consequentially challenging to treat ^{220,223,225,226}.

Further identification of molecular subtypes and their distinct cellular programmes may help identify novel therapeutic targets and respective markers. An important aspect of new therapeutic strategies is to target not only heterogenous subtypes within SCLC tumours but also direct targeting of transdifferentiation between the subtypes to prevent escape mechanisms.

RB1 loss					
TP53 loss					
neuroendocrine			non-neuroendocrine		
SCLC-A2	SCLC-A	SCLC-N	SCLC-P	SCLC-Y	ATOH1
ASCL1		NEUROD1	POU2F3	YAP1	
MYCL high		MYC high			
HES1					REST1/NRSF1
			NOTCH signalling		
low immune gene signature expression			MHC I expression		

Figure 5 Schematic overview of SCLC subtypes.

SCLC is characterised by biallelic RB1 and TP53 loss and is divided into neuroendocrine (NE) and non-NE subtypes. NE subtypes are marked by expression of ASCL1 (SCLC-A) and NEUROD1 (SCLC-N) which present with low immune gene signature expression. Non-NE subtypes express POU2F3 (SCLC-P), YAP1 (SCLC-Y) and ATOH1. Non-NE show increased expression of REST1 and Notch signalling components. SCLC-N and non-NE subtypes are further characterised by high MYC expression whereas SCLC-A expresses high levels of MYCL. Major histocompatibility complex (MHC) I expression is distinctive for non-NE subtypes. SCLC-A2, a variant of SCLC-A is further characterised by HES1 expression. The scheme was drawn using fully licensed biorender.com.

1.2.1.3 The RP mouse model of SCLC

In work undertaken for this thesis, the well-established RP mouse model for SCLC developed by Meuwissen et al., 2003 with a C57BL/6 genetic background was used ¹⁵¹. Here, the tumour suppressor genes *Rb1* and *Trp53* are conditionally deleted, using the

Cre-*loxP* system. The RP mouse model carries conditional alleles for *Rb1* (floxed exon 19) and for *Trp53* (floxed exons 2-10) as presented in **Figure 6**. These are specifically homozygously deleted in the lung epithelium upon intratracheal instillation of replication-deficient Adeno-Cre, which cleaves at *loxP* sites. The RP mice develop multiple neoplasias within six to nine months after inhalation. The formed tumours invade the surrounding lung parenchyma and metastasise to the known metastatic sites mimicking human SCLC (see **Figure 6**). These tumours resemble very closely the histopathological and immunological phenotype of human SCLC^{151,157}.

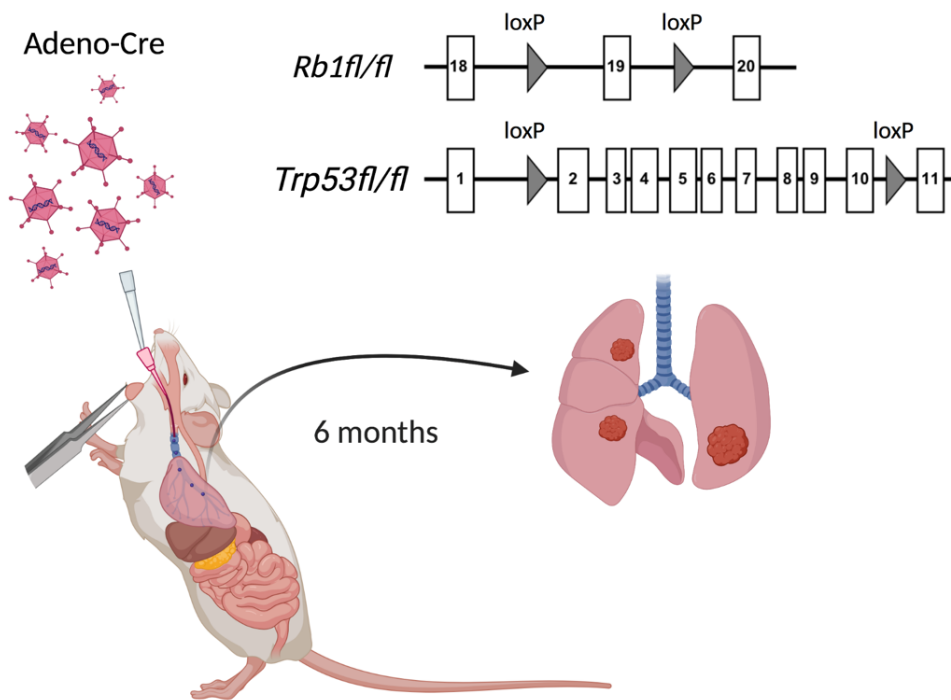


Figure 6 Schematic overview of the SCLC mouse model.

The RP genetically modified mouse model for small cell lung cancer (SCLC) carries homozygous conditional alleles for *Rb1* with *loxP* sites flanking exon 19 and *Trp53* with *loxP* sites flanking exon 2 to 10. Upon intratracheal inhalation of replication-deficient adenoviral particles expressing Cre recombinase (Adeno-Cre), *loxP* sites are cleaved by Cre recombinase and *Rb1* and *Trp53* are deleted. After six months infected cells form neoplasia resembling human SCLC. The scheme was drawn using fully licensed biorender.com.

1.3 Aim of the study

SCLC is one of the most aggressive forms of cancer with dramatically low survival rates and only very few newly approved treatment strategies in the last 30 years^{149,227}. After initial chemotherapy response SCLC almost invariably relapses within a year¹⁵⁵. SCLC often presents with inter- and intratumoural NE subtype heterogeneity as a result of tumorigenesis from different cells-of-origin and subtype plasticity²¹². Recent evidence suggests that MYC-mediated activation of Notch signalling and promotion of a non-NE

cellular state can cause intratumoural heterogeneity in SCLC^{185,220,223}. Furthermore, standard-of-care chemotherapy exacerbates intratumoural heterogeneity suggesting that targeting SCLC plasticity rather than isolated molecular subtypes might be a promising treatment path²²⁸. SCLC is defined by the loss of functioning TP53 and RB1 as well as a significant TMB¹⁶⁶, a marker of potential immunotherapy response¹⁷³, yet clinical trials using immune checkpoint blockade for SCLC underperformed given the high TMB^{174,175}. High TMB may boost constitutive immune editing prior to therapy and hence select against expression of PCD pathway components²²⁹. In addition, CASP8, the essential apical effector enzyme in the extrinsic apoptosis pathway, has been discovered to be epigenetically silenced in SCLC cell lines^{137,203}. Ferroptosis is a recently identified form of cell death, independent from caspases and the necrosome^{47,230}. One important hallmark of ferroptosis is the characteristic iron-dependent accumulation of peroxidised membrane lipids, leading to destabilisation of the lipid bilayer^{47,92}. This fatal accumulation of ROS is counteracted by GPX4, which constitutively reduces accumulating lipid peroxides thereby protecting cells from ferroptosis⁶².

Despite recent advances in understanding SCLC pathogenesis and identification of distinct subtypes, a comprehensive analysis of cell death pathway availability in SCLC has not been pursued yet. Therefore, the following study aims were defined:

1. Systemic analysis of the availability of cell death pathways in RNA-sequencing (RNA-seq) data of treatment-naïve SCLC patient tissue to identify therapeutically targetable vulnerabilities.
2. Characterisation of identified cell death vulnerabilities to elucidate the mechanisms of sensitivity and resistance in SCLC.
3. Identification of markers for sensitivity and resistance in SCLC NE subtypes to possibly target subtype heterogeneity.
4. Validation of identified vulnerabilities in different SCLC mouse models *in vivo*.

Together, the aim of this study is to provide a deeper understanding of NE subtype biology and how heterogeneity can be targeted to contribute to new SCLC treatment avenues.

2 Results

2.1 Treatment naïve SCLC presents with inactivation of important regulated cell death pathways

At time of diagnosis, SCLC tumours are already very aggressive and exhibit a high TMB^{152,165,166}. As a high TMB is correlated with improved immunotherapy response¹⁷³, immune checkpoint inhibition has recently been approved for SCLC treatment but clinical efficacy did not meet expectations^{174,175}. A widely-neglected fact is that high TMB is likely to promote constitutive immune editing prior to treatment and thereby may favour loss of PCD pathway component expression.

Interestingly, treatment-naïve SCLC is characterised by loss of the two tumour suppressor genes *TP53* and *RB1* responsible for cell cycle control and intrinsic apoptosis (George et al., 2015), which further suggests selective pressure to inactivate cell death pathways prior to therapy.

Additionally, *CASP8*, an essential caspase for the execution of extrinsic apoptosis which is triggered by TNF superfamily ligands expressed by immune effector cells¹³, has been shown to be epigenetically silenced in SCLC cell lines^{137,202–204} suggesting this to be a strategy of immune escape in SCLC. Inactive *CASP8* expression would disable the capacity to induce extrinsic apoptosis (see Figure 1). However, genetic downregulation of *CASP8* or its inhibition can enable unrestricted activation of the necroptosis pathway, a non-apoptotic form of cell death driven by RIPK1 and RIPK3^{231–233} (see Figure 2). Importantly, the availability of the necroptosis pathway in SCLC tissue has remained unexplored. In addition, it was shown that immune checkpoint blockade and radiotherapy sensitise cancer cells to the recently described type of regulated necrosis called ferroptosis, a cell death which is completely independent of caspases (see Figure 3)^{84,234}. Therefore, ferroptosis might also be a cell death pathway triggered by tumour-immune cell interaction and selection. Yet, which of these pathways remain available in treatment-naïve SCLC is unknown.

To examine cell death pathway availability in treatment-naïve SCLC, RNA-seq data of important genes involved were analysed in a treatment-naïve SCLC patient cohort¹⁸³ and compared with RNA-seq data of normal lung tissue samples of SCLC patients²³⁵.

2.1.1 Treatment-naïve SCLC presents with inactivation of the extrinsic apoptosis pathway

To analyse gene expression of cell death pathway components log₂-transformed FPKM-normalised RNA-seq data of SCLC primary patient tissue was compared to normal lungs tissue. For computation an R script was used including the R packages *gplots*, *RColorBrewer* and *data.table*. This analysis revealed a strong downregulation of relevant genes involved in the extrinsic apoptosis pathway, such as the two receptor proteins TRAIL (gene name: *TNFSF10*), and CD95L (gene name: *FASLG*)¹³ (Figure 7A). Furthermore, *CASP8* downregulation could be confirmed in the analysis (Figure 7A). Whereas some essential extrinsic apoptosis genes such as the adaptor protein *FADD* were slightly up-regulated in SCLC tissue, potentially facilitating non-apoptotic gene induction^{236,237}, the downstream essential effector *CASP8* was strongly downregulated in approximately 80% of SCLC specimens (Figure 7B). This suggests the extrinsic apoptosis pathway to be incapacitated prior to therapy. The analysis further confirmed overexpression of the anti-apoptotic protein BCL-2 in SCLC tissue in comparison to normal lung tissue as previously described^{199,200}.

Accordingly, a representative panel of prior and post-therapy derived human SCLC cell lines (n=7)^{188,238} was almost uniformly resistant to stimulation with Isoleucine-zipper (iz)-TRAIL used to trigger extrinsic apoptosis. However, iz-TRAIL treatment effectively decreased cell viability in a TRAIL-sensitive control NSCLC cell H460 determined by the cell viability dye Cell Titer Blue (Figure 7C).

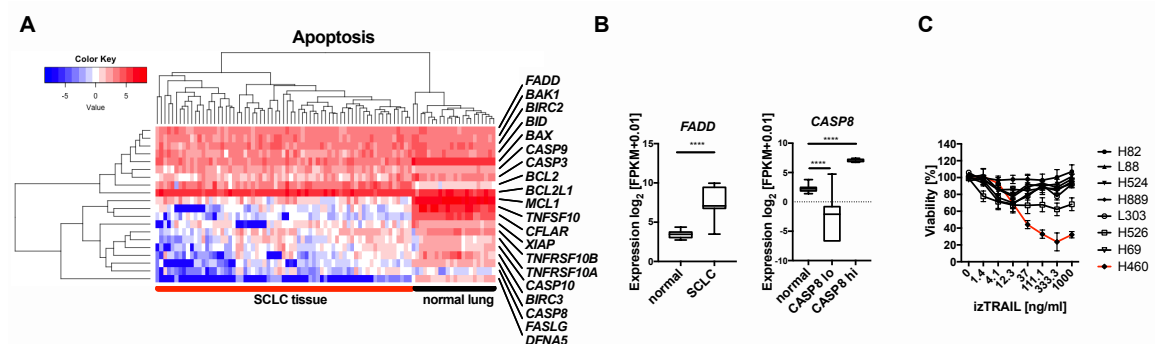


Figure 7 Extrinsic and intrinsic apoptosis pathways are downregulated in treatment-naïve SCLC.

A, B RNA-seq expression data in FPKM (fragments per kilobase of exon model per million reads mapped) from normal lung²³⁵ (n=22) and chemo-naïve SCLC patient samples¹⁸³ (n=67) were log₂ transformed (+0.01) and plotted for relative expression of genes involved in extrinsic apoptosis. boxplot center line, mean; box limits, upper and lower quartile; whiskers min. to max. Heatmap colour code indicates expression levels between each sample and the average of each gene, dendrogram shows distance between sample populations. **C** The indicated seven human SCLC cell lines (n=7) and NSCLC line (H460) were treated with human izTRAIL for 24 h, cell viability was determined by Cell Titer Blue, n(H82)=6, n(L88)=4, n(H524)=4, n(H889)=4, n(L303)=3, n(H526)=3, n(H69)=5, n(H460)=3.

Data are means +/- SEM of three independent experiments wherever not indicated otherwise. Two-tailed unpaired *t* tests, *****p*<0.0001. R script for analysis (A) was adapted from Emily Thomas. Viability assay (C) was contributed by Emily Thomas. Figure adapted from Bebbber et al., 2021, Nature Communications.

2.1.2 Treatment-naïve SCLC presents with inactivation of the necroptosis pathway

Under conditions of genetic or chemical inhibition of CASP8 or destabilisation of complex I through deubiquitination of RIPK1 by CYLD, TNFR1 ligation can also activate the formation of the necrosome, a multiprotein complex leading to necroptosis (see Figure 2)
37,40,239

Therefore, expression of necroptosis pathway components was analysed next as described and revealed a downregulation of relevant genes such as *RIPK3* and *MLKL* (Figure 8A). While *RIPK3* was only slightly downregulated, expression of the downstream essential necroptosis effector *MLKL*^{240–242} was strongly downregulated in SCLC tissue compared to normal lung tissue (Figure 8B).

As expected based on this observation, tested SCLC cell lines were resistant to treatment with a combination commonly used to induce necroptosis, namely of TNF (T), the pan-caspase inhibitor z-VAD-fmk (Z) and the SMAC mimetic (S) compound Birinapant, an inhibitor of cIAP1/2 (=TZS) (Figure 8C). In contrast, MEFs used as a positive control, readily underwent necroptosis upon TZS stimulation (Figure 8C). Cell death was determined by propidium iodide (PI) incorporation into dead cells with damaged cell membrane and quantified by flow cytometry (Figure 8D). Importantly, TZS-induced cell death was blocked by co-treatment with the RIPK1 inhibitor Necrostatin-1 (Nec-1) thereby confirming the specific induction of necroptotic cell death in MEFs (Figure 8C).

These results might suggest that strong selective pressure already incapacitates both, the extrinsic apoptosis and necroptosis pathways in SCLC prior to diagnosis and therapy.

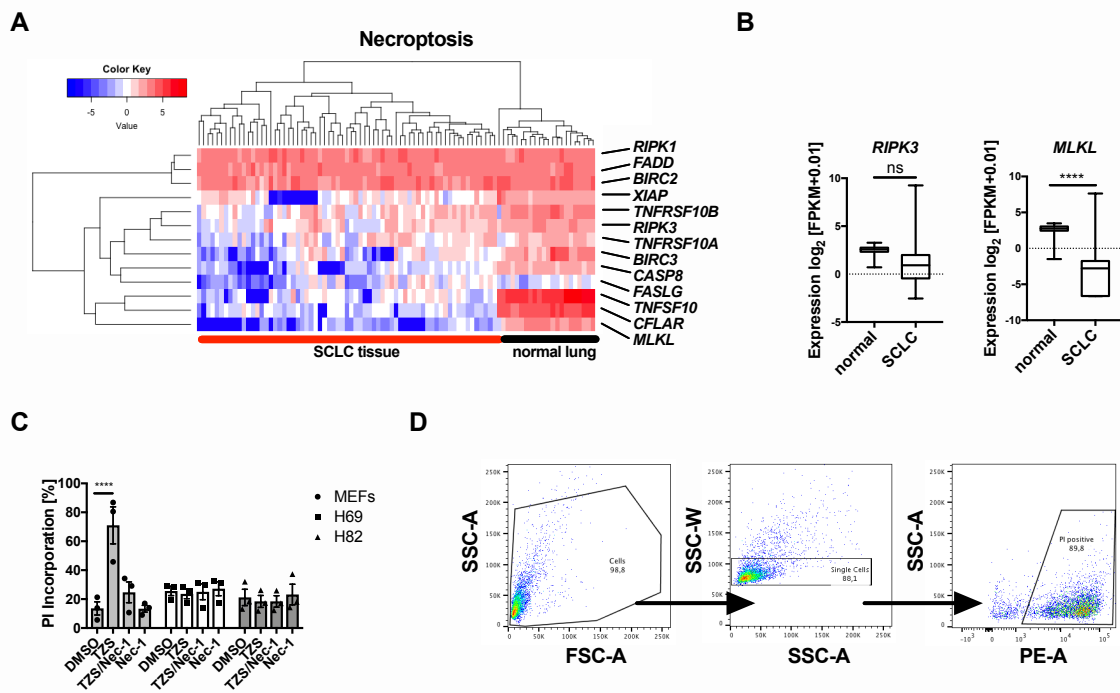


Figure 8 The necroptosis pathway is downregulated in treatment-naïve SCLC.

A, B RNA-seq expression data in FPKM (fragments per kilobase of exon model per million reads mapped) from normal lung²³⁵ (n=22) and chemo-naïve SCLC patient samples¹⁸³ (n=67) were log₂ transformed (+0.01) and plotted for relative expression of genes involved in necroptosis. boxplot center line, mean; box limits, upper and lower quartile; whiskers min. to max. Heatmap colour code indicates expression levels between each sample and the average of each gene, dendrogram shows distance between sample populations. **C** Cells were treated with TNF (T) [10 ng/ml], zVAD (Z) [20 μM], SMAC mimetic (S) Birinapant [1 μM] in combination with Nec-1 [10 μM] for 24 h, cell death was quantified by propidium iodide (PI) uptake and flow cytometry. **D** Flow cytometry gating strategy to quantify % propidium iodide (PI) positive cells. Representative plots out of three independent experiments are shown. FSC-H, forward scatter-heights, SSC-A, side scatter-area, SSC-W, side scatter-width. Data are means ± SEM of three independent experiments wherever not indicated otherwise. Two-way ANOVA + Tukey's multiple comparison test (C) and two-tailed unpaired t tests for all others, ****p<0.0001, ns p>0.05. R script for analysis (A) was adapted from Emily Thomas. Viability assay (C) was contributed by Emily Thomas. Figure adapted from Bebbler et al., 2021, Nature Communications.

2.2 SCLC presents with high vulnerability for ferroptosis

2.2.1 Treatment-naïve SCLC presents with upregulation of ferroptosis protective genes

Ferroptosis is an iron-dependent form of regulated necrosis, which is independent of the molecular machinery driving apoptosis or necroptosis (see Figure 3)^{47,92,243}. Recently, it was shown that immune checkpoint blockade sensitises cancer cells to ferroptosis

redefining it as a potential cell death pathway triggered by tumour-immune cell interaction and selection⁸⁴.

Therefore, to assess the availability of the ferroptosis pathway, expression of ferroptosis genes in SCLC patient samples was analysed as described. While some genes protecting from ferroptosis such as *NFS1*⁵² and *AIFM2* (= *FSP1*)^{89,90} were decreased in SCLC tissue in comparison to normal lung tissue (Figure 9A), an important gene protecting from ferroptosis, *SLC7A11*⁴⁷ was strongly upregulated in SCLC and only expressed at very low levels in normal lung (Figure 9A). *SLC7A11* is the crucial subunit of system xc-, a glutamate/cysteine antiporter important for cystine import and thereby linked to GSH synthesis. Also, *GPX4*⁴⁷, a ferroptosis-protective gene acting downstream of *SLC7A11*, was highly expressed in SCLC and normal lung suggesting an increased dependency on escaping ferroptosis (Figure 9A).

Moreover, protein expression of both, *SLC7A11* and *GPX4* could be validated by Western Blot analysis in human SCLC cell lines (Figure 9C).

Based on the observation that *SLC7A11* expression was elevated in SCLC tumour tissue, next, cytotoxicity of *SLC7A11* inhibition was assessed in SCLC cell lines. Treatment of human SCLC cell lines with erastin, an *SLC7A11* inhibitor, indeed demonstrated dose-dependent cytotoxicity determined by Cell Titer Blue assays, which was less pronounced in the tested NSCLC cell lines (Figure 9D).

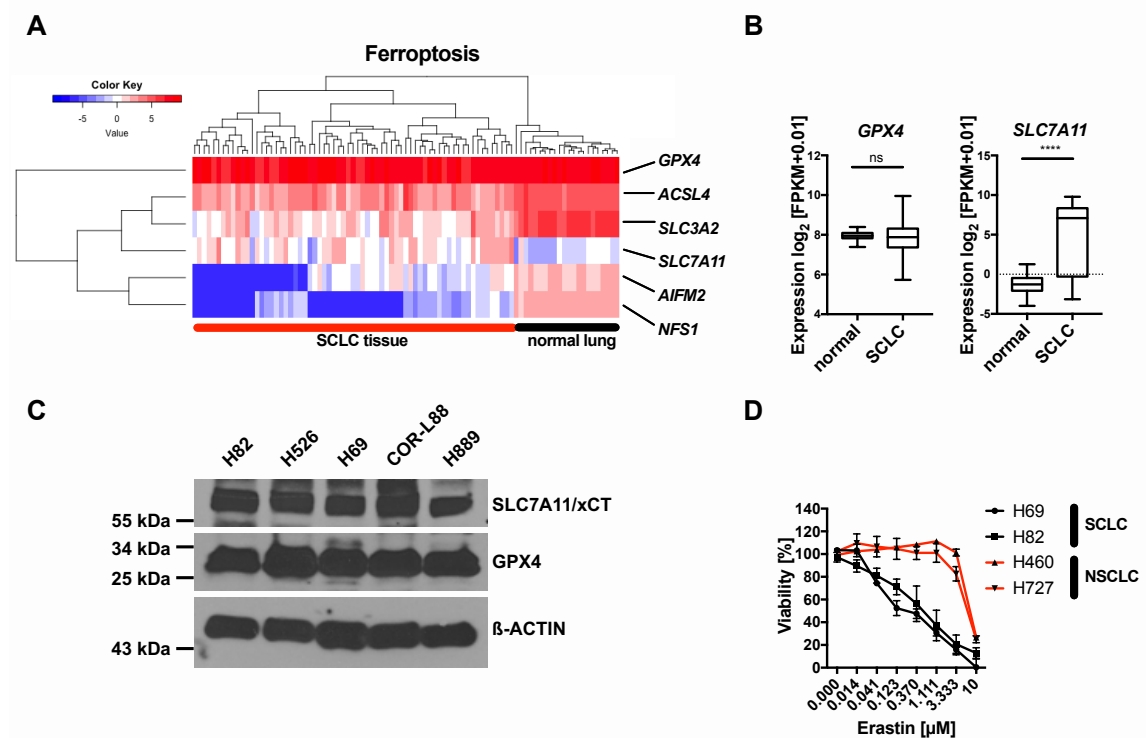


Figure 9 Ferroptosis pathway components are upregulated in treatment-naïve SCLC.

A, B RNA-seq expression data in FPKM (fragments per kilobase of exon model per million reads mapped) from normal lung²³⁵ (n=22) and chemo-naïve SCLC patient samples¹⁸³ (n=67) were log2

transformed (+0.01) and plotted for relative expression of genes involved in ferroptosis. boxplot center line, mean; box limits, upper and lower quartile; whiskers min. to max. Heatmap colour code indicates expression levels between each sample and the average of each gene, dendrogram shows distance between sample populations. **C** Western Blot of ferroptosis pathway component expression in representative human SCLC cell lines indicated. Representative Western Blots are shown. **D** Cells were treated with erastin at indicated concentrations for 24 h, cell viability was determined by Cell Titer Blue. Data are means \pm SEM of three independent experiments if not indicated otherwise. Two-tailed unpaired *t* tests, **** $p < 0.0001$, ns $p > 0.05$. R script for analysis (A) was adapted from Emily Thomas. Viability assay and Western Blot (C, D) were contributed by Emily Thomas. Figure adapted from Beber et al., 2021, Nature Communications.

2.2.2 SCLC is more sensitive to ferroptosis induction than NSCLC

In line with our observation that SCLC cell lines seemed to be more sensitive to erastin than the NSCLC cell lines tested, SCLC lines from a panel of 117 human cancer cell lines⁶² also showed increased erastin sensitivity (Figure 10A). Furthermore, data from 101 human NSCLC cell lines and 33 human SCLC cell lines^{244,245} tested for sensitivity to ML162, which is a GPX4 small molecule inhibitor⁷⁵ confirmed increased ferroptosis sensitivity of SCLC over NSCLC cell lines (Figure 10B).

Next, murine cell lines derived from GEMMs for SCLC (RP)¹⁵¹ and NSCLC (KP)²⁴⁶ both on the C57BL/6 strain background were tested for their respective sensitivity to RSL3, another small molecule inhibitor of GPX4 known to trigger ferroptosis⁶². Again, a higher cytotoxicity in SCLC as compared to NSCLC cells measured by Cell Titer Blue could be observed (Figure 10C).

While Western Blot analysis revealed comparable protein levels of GPX4, xCT (=SLC7A11) and ACSL4 between SCLC and NSCLC cells, interestingly, transferrin receptor (CD71) expression was elevated in all SCLC cell lines as compared to two out of three NSCLC lines (Figure 10D). Furthermore, expression of FSP1 (=AIFM2), recently demonstrated to render cells more resistant to ferroptosis^{89,90}, was elevated specifically in NSCLC (Figure 10D) cells on protein level (Figure 10D). Moreover, RNA-seq data of human NSCLC and SCLC cell lines plotted for *FSP1* log₂-transformed (transcripts per million (TPM)-normalised expression²⁴⁷ confirmed increased *FSP1* expression in NSCLC over SCLC cells (Figure 10E). Together this suggests that elevated TFRC/CD71 expression combined with low FSP1 expression may specifically prime SCLC for ferroptosis induction.

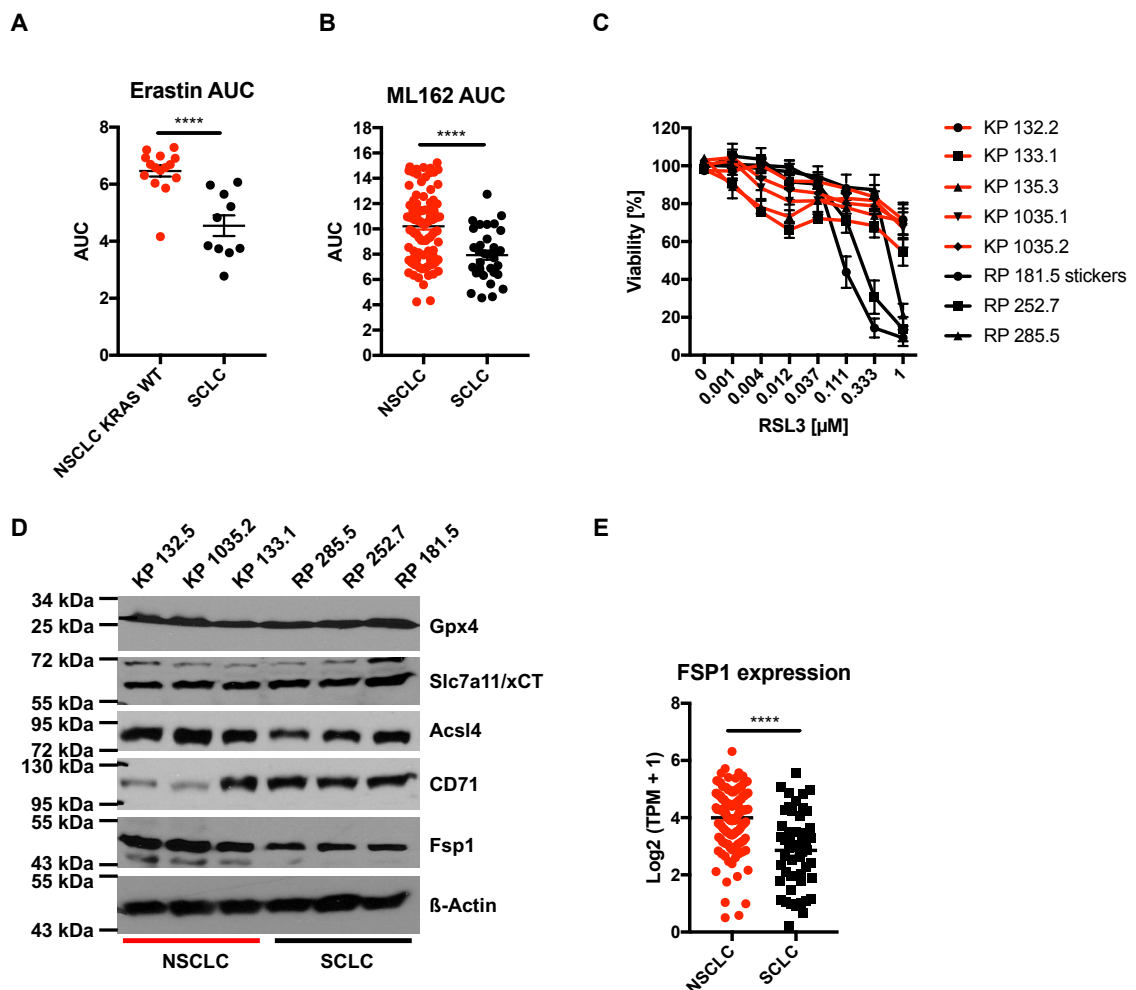


Figure 10 SCLC cells are more susceptible to ferroptosis induction than NSCLC cells.

A Erastin-treated human SCLC (n=10) and KRAS wild type NSCLC cells (n=15) were plotted for area under the curve (AUC). Source data can be found in Yang et al.⁶² **B** ML162-treated human NSCLC (n=101) and SCLC (n=33) cells were plotted for area under the curve (AUC). Source data were obtained from depmap²⁴⁷ and can be found in Rees et al. and Seashore-Ludlow et al.^{244,245}. **C** The indicated three murine SCLC (black; n=6) and five NSCLC (red; n=5) cell lines were treated as indicated with RSL3 for 24 h, cell viability was determined by Cell Titer Blue. **D** Western Blot of ferroptosis pathway component expression in representative three murine SCLC cell lines (RP) and three murine NSCLC (KP). Representative Western Blots are shown. **E** NSCLC and SCLC cell lines were plotted for FSP1 expression as log₂ of transcript per million (TPM)+1²⁴⁷. Data are means +/- SEM of three or more independent experiments for each cell line wherever not indicated otherwise. Representative blots are shown. Two-tailed unpaired *t* test, **** p<0.0001. Figure adapted from Bebbler et al., 2021, Nature Communications.

Collectively, we found that SCLC presents with resistance to cell death (extrinsic apoptosis, necroptosis) prior to treatment. While extrinsic apoptosis and necroptosis escape was rather defined by downregulation of important agonists, ferroptosis escape in SCLC involved the upregulation of protective and targetable proteins. Hence, ferroptosis induction was further analysed aiming to mechanistically validate its role in SCLC.

2.2.3 Human and mouse SCLC cell lines are vulnerable to ferroptotic cell death

To validate whether SCLC was generally vulnerable to ferroptotic cell death, murine SCLC cells were stimulated with the GPX4 small molecule inhibitor RSL3 in absence and presence of the lipophilic radical scavenger Fer-1 which is known to specifically block ferroptosis ⁴⁷.

Indeed, a clonogenic survival assay of adherent murine SCLC lines using crystal violet showed that RSL3 and erastin effectively decreased survival (Figure 11A). This could be fully rescued with co-treatment of Fer-1 in the case of RSL3 treatment and partially restored in the case of erastin which induces ferroptosis by depletion of GSH (Figure 11A).

Moreover, in human suspension SCLC cells, cell death induced by erastin or the GPX4 small molecule inhibitor RSL3 ⁴⁶ could be rescued by co-incubation with Fer-1 (Figure 11B, C). Co-treatment with the iron-scavenger DFO equally rescued cell death induced by erastin or RSL3 in human SCLC cells (Figure 11D, E). Using the fluorescent probe Calcein-AM in a fluorescence-activated cell sorting (FACS) assay, which allows for relative quantification of the intracellular labile iron pool through the principle of fluorescent quenching ²⁴⁸, DFO mediated depletion of iron which led to reduced fluorescent quenching could be further confirmed (Figure 11F). Finally, cell death induced by erastin or RSL3 in more murine SCLC cell lines could also be restored by co-incubation with Fer-1 (Figure 11G, H).

Collectively, these data indicate that RSL3 and erastin induce lipid ROS- and iron-dependent cell death in human and murine SCLC cells.

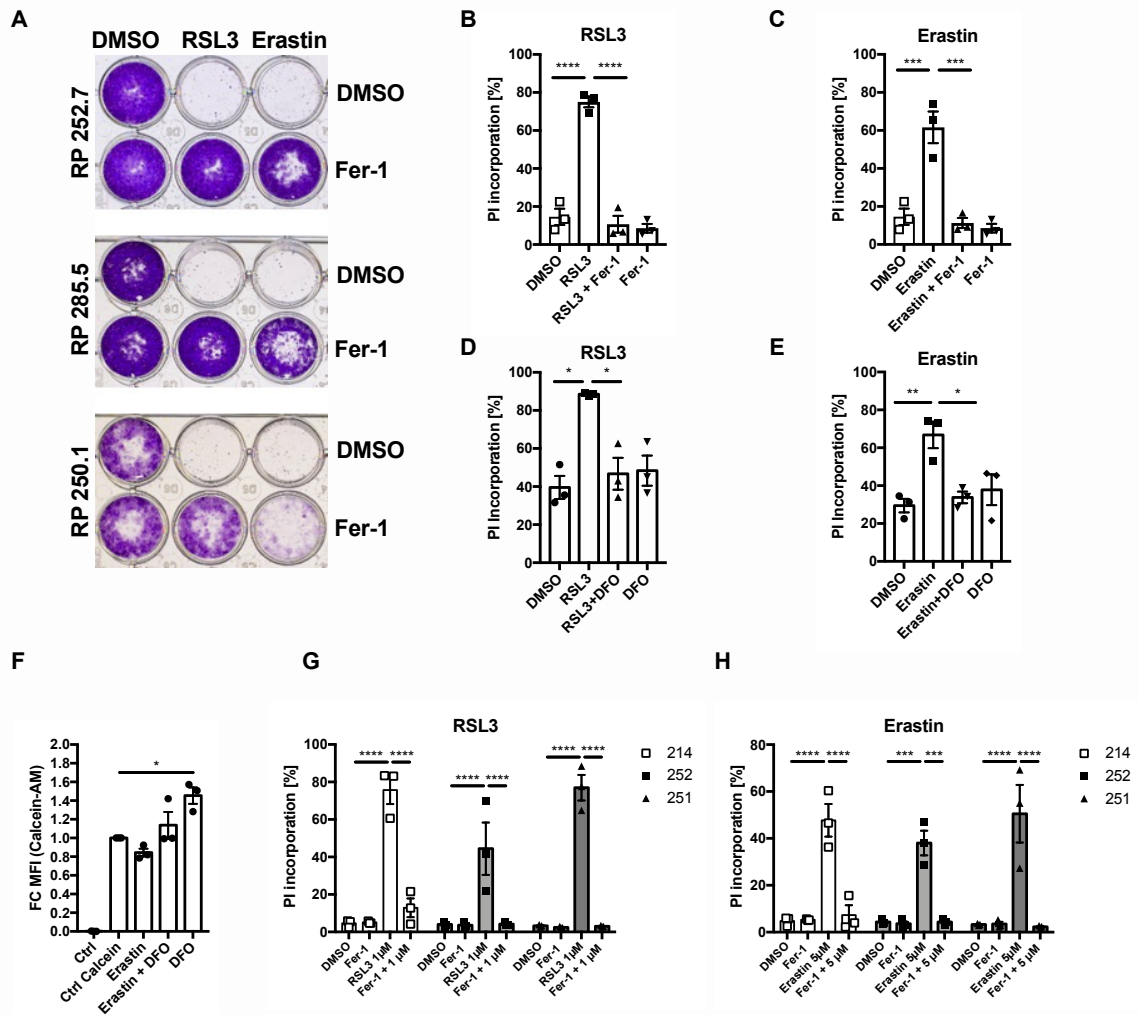


Figure 11 Human and mouse SCLC cell lines are sensitive to ferroptosis induction.

A The indicated murine SCLC lines (n=3) were treated either with DMSO, RSL3 [1 μ M], erastin [10 μ M] alone or in combination with Ferrostatin-1 (Fer-1) [5 μ M] for 24 h. Cells were washed, cultured for 5 days for recovery and stained with crystal violet. **B, C, D, E** Human H82 SCLC cells were treated as indicated: erastin [10 μ M] +/- Fer-1 [5 μ M] +/- Deferoxamine (DFO) [100 μ M], RSL3 [1 μ M] +/- Fer-1 +/- DFO for 24 h. Cell death was determined by propidium iodide (PI) uptake and flow cytometry. **F** RP181.5 sticker cells were treated with erastin [10 μ M] +/- DFO [100 μ M], for 3 h. Labile iron pools were quantified by Calcein-AM staining and flow cytometry. FC (fold change) MFI (mean fluorescence intensity), n=3 biological replicates. **G, H** The indicated murine SCLC cells were treated as indicated +/- Fer-1 [5 μ M] for 24 h and quantified as in (B, C, D, E), n=3 biological replicates. Data are means +/- SEM of three independent experiments in each individual cell line or representative images or histograms were applicable. One-way ANOVA + Tukey's multiple comparison test (B-E) Two-way ANOVA + Tukey's multiple comparison test, **** p<0.0001, *** p<0.001, ** p<0.01, * p<0.05. FACS assay (H) was contributed by Emily Thomas. Figure adapted from Bebbler et al., 2021, Nature Communications.

2.2.4 Gpx4 expression is sufficient to protect SCLC cells from ferroptosis

GPX4 plays a central role in protecting cells from ferroptosis by directly reducing harmful lipid peroxides to their respective harmless lipid alcohol⁶². While GPX4 protects cells

from ferroptosis in a variety of cells, *GPX4* deletion is not sufficient to induce ferroptosis in lung adenocarcinoma cells⁸⁹. To examine whether *GPX4* is sufficient to protect SCLC from ferroptosis, CRISPR/Cas9-mediated KO SCLC cell lines were generated using three different *GPX4*-targeting single guide (sg) RNAs. Western Blot analysis confirmed *GPX4* KO on protein level in the presence of Fer-1 (Figure 12A). These KO cells could only be generated and cultured in the presence of Fer-1 in the media, which supports that *GPX4* is critical for survival of these cells. Upon Fer-1 withdrawal, *GPX4* KO cells underwent cell death which was measured by PI incorporation (Figure 12B, C). In addition, *GPX4* KO SCLC cells presented with lipid ROS accumulation upon Fer-1 withdrawal measured by FACS analysis using the fluorescent dye BODIPY C11, indicating again the induction of ferroptotic cell death²⁴³ (Figure 12D, E, F).

In conclusion, these data support a requirement for lipid radicals in cell death execution upon pharmacological induction of ferroptosis and identify *GPX4* as the central player sufficient to prevent lipid peroxidation and ferroptosis in SCLC.

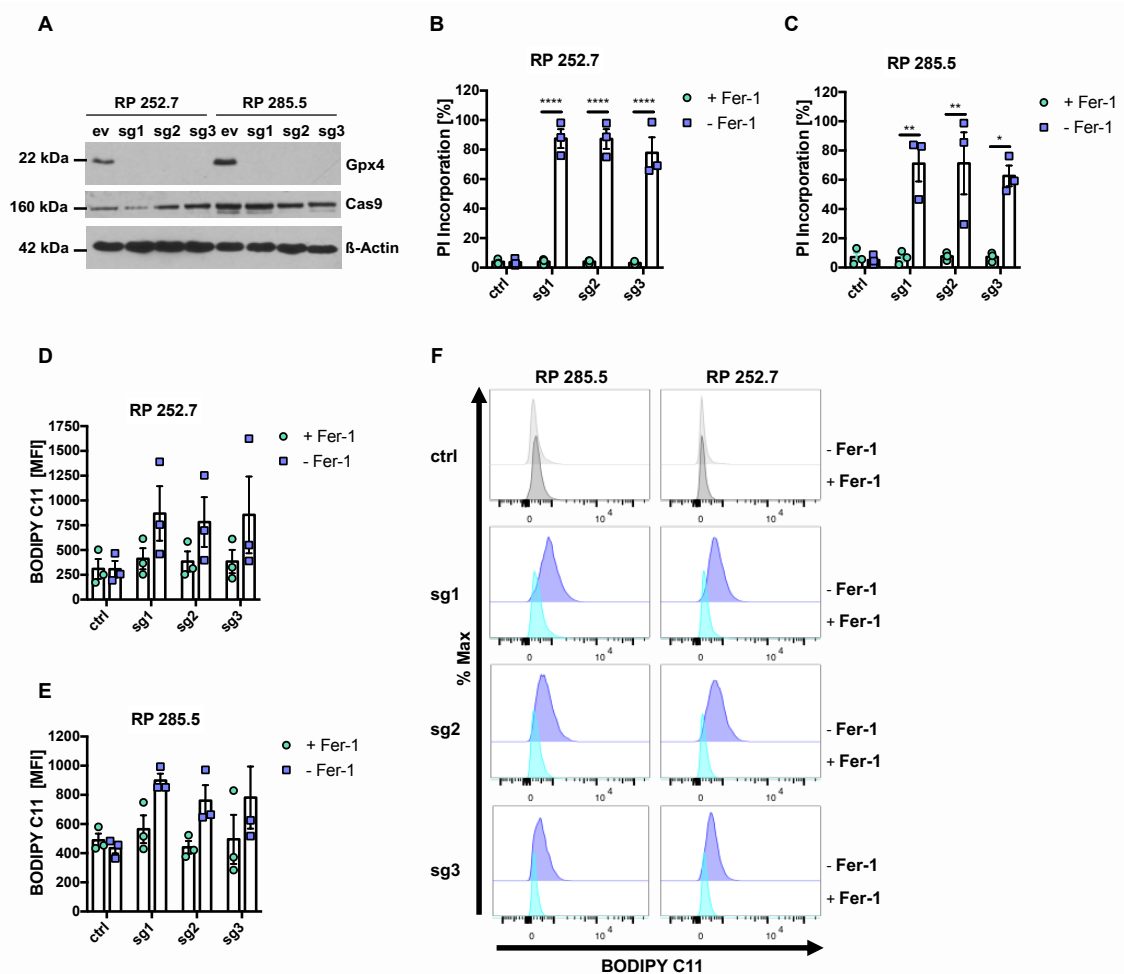


Figure 12 *GPX4* expression is sufficient to protect SCLC from ferroptosis.

A Protein extracts lines were obtained from indicated cell lines cultured in the presence of Fer-1 [5 μ M]. Representative Western Blot is shown **B**, **C** RP252.7 and RP285.5 murine SCLC cells stably

expressing Cas9 and the indicated control or sgRNAs targeting *GPX4* were cultured with or without Ferrostatin-1 (Fer-1) for 24 h. Cell death was quantified by propidium iodide (PI) uptake and flow cytometry. **D, E, F** RP252.7 and RP285.5 murine SCLC cells as in **(A, B)** were cultured in the presence or absence of Fer-1 [5 μ M] for 5 h and stained for lipid ROS accumulation using BODIPY C11. Cells were analysed by flow cytometry and mean fluorescent intensity (MFI) was quantified. Cells were analysed by flow cytometry. Grey=control cell lines, violet=sgRNA, -Fer-1, turquoise=sgRNA, +Fer-1. Data are means \pm SEM of three independent experiments in each individual cell line or representative Western Blot images or histograms were applicable. One-way ANOVA + Tukey's multiple comparison test (B, C) Two-way ANOVA + Tukey's multiple comparison test **** $p < 0.0001$, ** $p < 0.01$, * $p < 0.05$. Figure adapted from Bebbber et al., 2021, Nature Communications.

2.3 SCLC cell lines are segregated by ferroptosis response

When testing a larger panel of human SCLC cell lines for response to ferroptotic stimuli it was revealed that they divided into subsets of responders (black) and non-responders (grey) equally upon stimulation with erastin and RSL3 (Figure 13A, B). Furthermore, upon *GPX4* inhibition in representative cell lines from each subset, responders (H82) accumulated lipid ROS but non-responders (H2171) failed to accumulate lipid ROS using BODIPY C11 for FACS analysis (Figure 13C, D). However, human non-responders were still capable to accumulate total ROS upon RSL3-induced ferroptosis measured by the fluorescent dye H2DCFDA for FACS analysis (Figure 13E).

Moreover, while responders showed decreased levels of GSH upon *SLC7A11* inhibition by erastin, non-responders did not reveal a difference in GSH level upon erastin treatment measured using the fluorescent dye monochlorobimane (MCB) for FACS analysis (Figure 13F).

In conclusion, a panel of human SCLC cell lines divided into ferroptosis non-responders and responders, equally separated by erastin and RSL3 treatment. Furthermore, ferroptosis induction failed to accumulate lipid ROS in non-responders as well as a reduction in GSH levels.

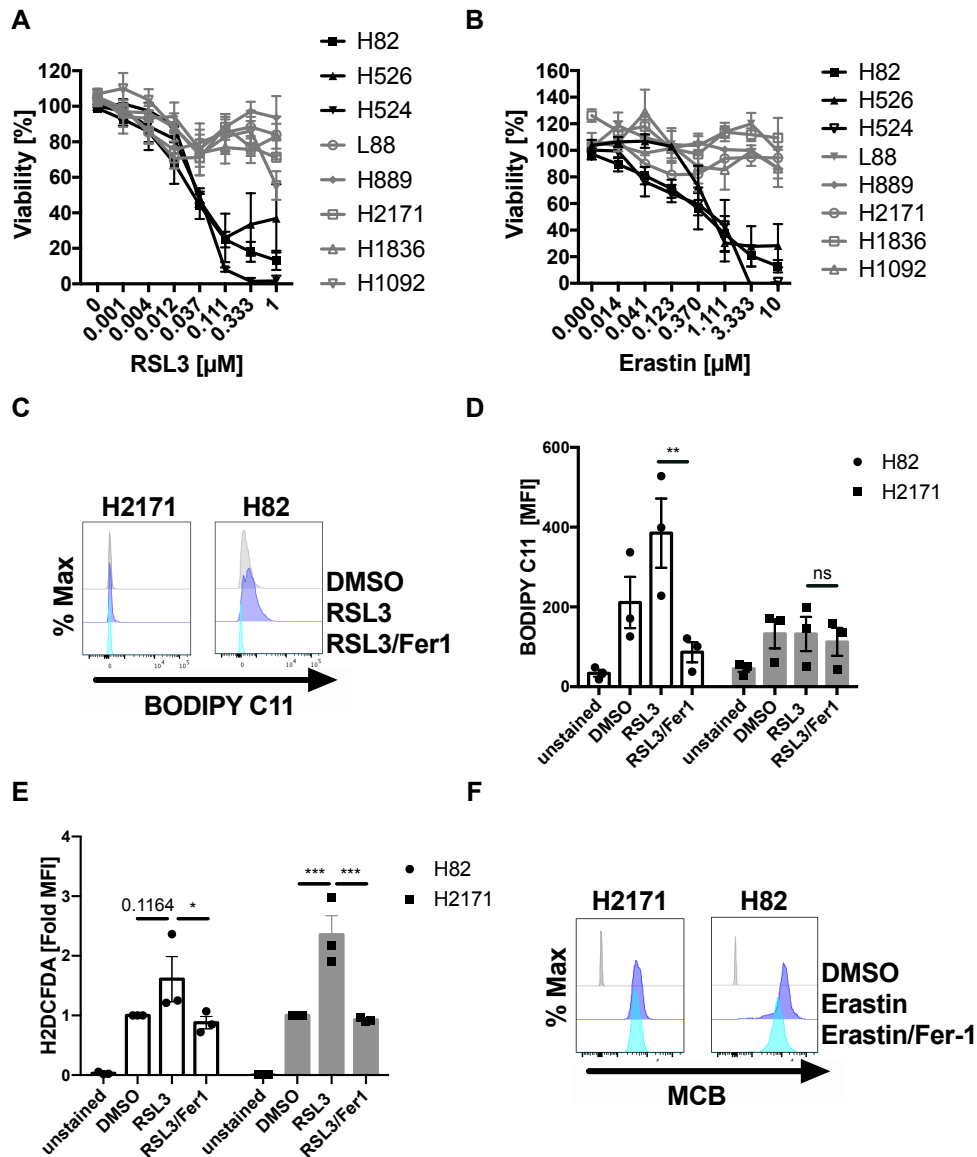


Figure 13 SCLC cell lines segregate by ferroptosis response.

A, B Eight human SCLC cell lines were treated as indicated for 24 h, cell viability was determined by Cell Titer Blue. **C** The indicated human SCLC cells were treated with DMSO, RSL3 [100 nM] or RSL3/Fer-1 [5 μM] for 5 h and stained for lipid ROS accumulation using BODIPY C11. **D, F** the indicated human SCLC cells lines were treated with DMSO, RSL3 [1 μM] or RSL3/Fer-1 [5 μM] for 5 h and stained for lipid ROS accumulation using BODIPY C11 and for general ROS accumulation using H2DCFDA. Fold change (FC) mean fluorescence intensity (MFI) was quantified, $n=4$ biological replicates. **E** the indicated cell lines were treated with erastin [10 μM] or erastin/Fer-1 [5 μM] and stained for GSH levels using MCB. Cells were analysed by flow cytometry. Grey=DMSO treated, violet=RSL3 or erastin treated, turquoise=RSL3 or erastin/Fer-1 treated. Data are means \pm SEM of three independent experiments in each individual cell line or histograms were applicable. One-way ANOVA + Tukey's multiple comparison test, *** $p<0.001$, ** $p<0.01$, * $p<0.05$, $ns>0.05$. Viability assays (A, B) were contributed by Emily Thomas and Zhiyi Chen. Figure adapted from Bebbber et al., 2021, Nature Communications.

2.4 SCLC ferroptosis response and neuroendocrine subtypes

SCLC is not a uniform disease but consists of several molecular subtypes characterised by the expression of NE differentiation markers, which differ in cell signalling^{223,249}, cell of origin²¹⁵ or arise as a consequence of intratumoural plasticity^{185,220}. Hence, next it was assessed whether ferroptosis sensitivity was a common feature of all molecular subtypes of SCLC. To test a variety of SCLC subtypes, a larger panel of human (n=8) SCLC lines representative of different SCLC molecular subtypes was used²¹².

2.4.1 SCLC ferroptosis response separates neuroendocrine subtypes

To identify markers of ferroptosis sensitivity and resistance in SCLC, differential expression analysis of RNA-seq data in human SCLC cells¹⁸⁵ was performed comparing three ferroptosis responder and five non-responder cell lines. Analysis of log2-transformed FPKM-normalised of RNA-seq data of the 50 most differentially expressed genes revealed increased expression of the important transcription factor for neuroendocrine differentiation ASCL1 in non-responders (Figure 14A). For computation an R script was used including the R packages *gplots* and *RColorBrewer*.

Interestingly, expression levels of the important ferroptosis genes such as *SLC7A11*, *GPX4*, *ACSL4*, *TFRC* and *FSP1* did not differ substantially between non-responders and responders (Figure 14B). However, non-responders showed increased expression of *ASCL1*, responders instead expressed elevated mRNA levels of *REST1* (also called neuron-restrictive silencing factor *NRSF*) (Figure 14B). Western Blot analysis of a sensitive and resistant cell line confirmed similar expression level of *GPX4* and an increased expression of *REST1* together with decreased expression of *ASCL1* in responders (Figure 14C).

Consistently, gene set enrichment analysis (GSEA) analysis confirmed that a gene set representing upregulated ASCL1 target genes²⁵⁰ was enriched in non-responders while a REST1 signature gene set was enriched in ferroptosis sensitive cells (Figure 14D). While ASCL1 is known to promote NE differentiation, REST1 suppresses NE differentiation in SCLC^{213,214}. Moreover, RNA-seq data of human SCLC cell lines plotted for area under the curve (AUC) data of a drug sensitivity screen for the *GPX4* small molecule ML210 separated by high and low ASCL1 expression²⁴⁷ revealed a correlation of high ASCL1 expression and low ML210 sensitivity (Figure 14E).

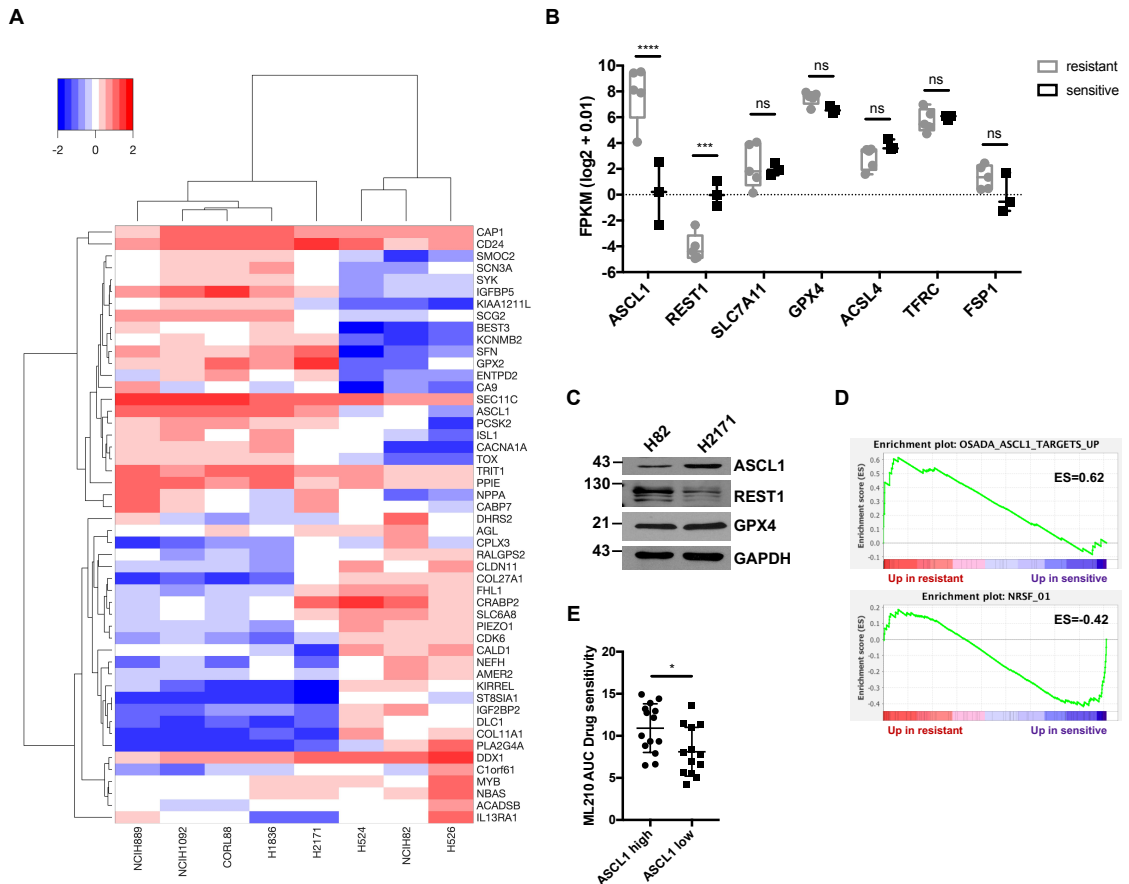


Figure 14 SCLC neuroendocrine subtypes segregate by ferroptosis response.

A RNA-seq data¹⁸⁵ of human SCLC lines (sensitive n=3 cell lines, H524, NCIH82, H526; resistant n=5 cell lines, NCIH889, NCIH1092, CORL88, H1836, H2171) were analysed for differential expression between responders and non-responders, heatmap represents hierarchical clustering of FPKM ($\log_2 + 0.01$) of the 50 most differentially expressed genes. Heatmap colour code indicates expression levels between each sample and the average of each gene, dendrogram shows distance between sample populations. **B** *ASCL1* and *REST1* expression (FPKM ($\log_2 + 0.01$)) comparing three sensitive and five resistant cells is plotted, boxplot center line, mean; box limits, upper and lower quartile; whiskers min. to max. Two-way ANOVA + Tukey's multiple comparison test, **** $p < 0.0001$, *** $p < 0.001$, ns > 0.05 . **C** Protein extracts were obtained from sensitive cells (H82) and resistant cells (H2171). Representative Western Blot is shown. **D** Gene set enrichment analysis (GSEA) of a ranked list of differentially expressed genes from human ferroptosis sensitive and resistant cells (A) was performed for *ASCL1* targets (Enrichment score (ES)=0.62, $p < 0.01$) and *REST1* targets (ES=-0.42, $p < 0.01$)^{251,252}. **E** Area under the curve (AUC) ML210 drug response in *ASCL1* high (n=14) and *ASCL1* low (n=13) expressing human SCLC cell lines²⁴⁷ and can be found in Rees et al. and Seashore-Ludlow et al.^{244,245}. Bioinformatic analysis (A) was contributed by Dr. Armin Khonsari. Figure adapted from Bebbler et al., 2021, Nature Communications.

2.4.2 Mouse SCLC cell lines segregate by ferroptosis response

Interestingly, mouse SCLC cells can spontaneously transdifferentiate from non-NE state marked by REST1 expression to an NE state marked by ASCL1 expression, a transition phenotypically manifested by adherent growth (“sticker”) and growth in suspension (“floaters”), respectively^{208,223}. Hence, murine SCLC cell lines from three different tumour-bearing RP-mice (RP181, RP246 and BYC5) were generated next and validated for isogenic spontaneous transition between the stickers and floaters state in these cells (Figure 15A). Isogenic spontaneous NE differentiation could be validated by Western Blot analysis revealing distinct protein expression of non-NE markers, such as REST1 (in RP181.5 and RP246.7), YAP1 and VIM in sticker cells and protein expression of NE markers, such as ASCL1 and SYP in floater cells (Figure 15B).

Confirming the observations made in human SCLC cell lines, all isogenic NE floater cells were indeed more resistant to ferroptotic stimulation with RSL3 or erastin, while non-NE sticker cells were highly sensitive analysed using IncuCyte real-time live cell imaging (Figure 15C, D). Furthermore, floater unlike sticker cells showed impaired accumulation of lipid ROS and total ROS upon GPX4 inhibition monitored by BODIPY C11 and H2DCFDA staining and analysed by FACS (Figure 15 E, F). Importantly, ferroptosis sensitivity or resistance was not determined by cell adherent or non-adherent states, as all human responder and non-responder cell lines grow in suspension (Figure 13A, B).

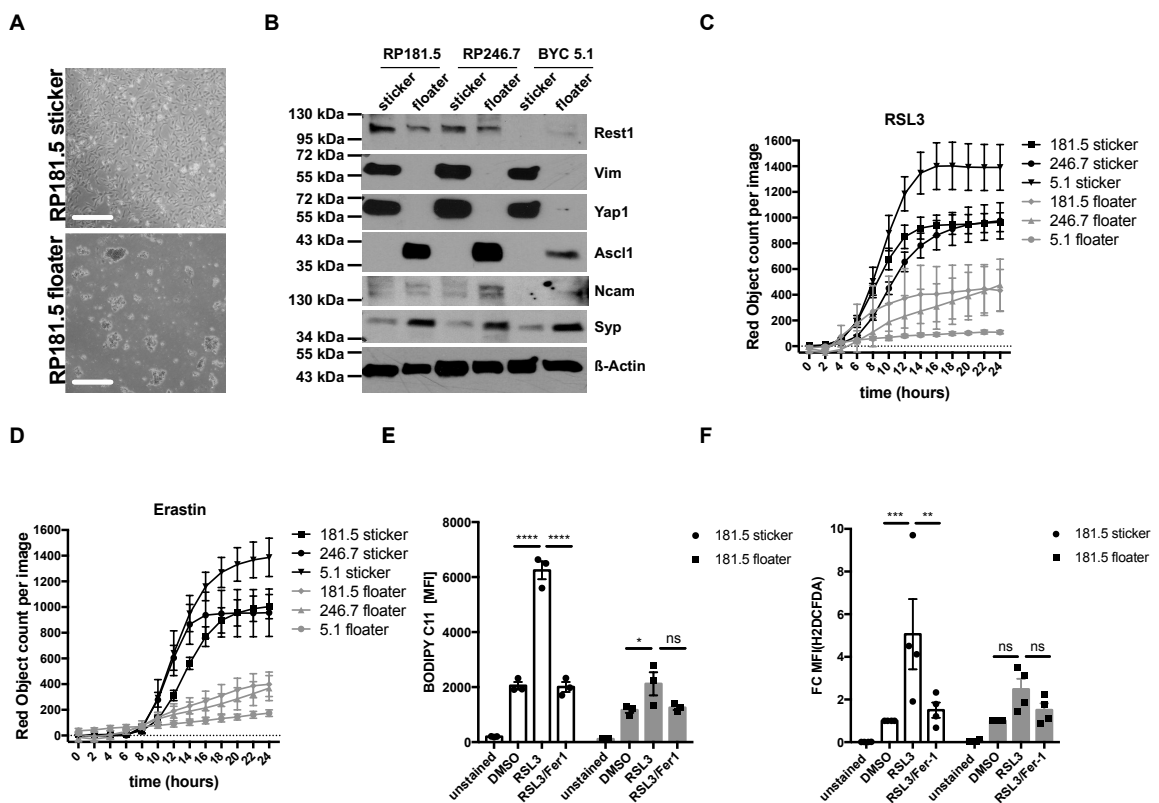


Figure 15 Murine SCLC neuroendocrine subtypes segregate by ferroptosis response.

A Representative images of 181.5 sticker and floater cells out of at least three independent biological experiments, scale bar=400 μm . **B** Protein extracts were obtained from three different sticker and floater cell lines. Western Blot of SCLC NE subtype marker expression in the indicated manually separated stickers and floaters lines (n=3). **C, D** Manually separated stickers and floaters lines (n=3) were treated with RSL3 [1 μM] (B) and erastin [10 μM] (C) for 24 h, DRAQ7 [0.1 μM] was added to all wells and cell death was quantified using IncuCyte real-time live cell imaging. **E, F** indicated murine SCLC cells were treated with RSL3 [1 μM] and RSL3/Fer-1 [5 μM] for 6 h. Total ROS was determined by H2DCFDA staining. Fold change (FC) mean fluorescence intensity (MFI) was quantified, n=3 biological replicates. Data are means \pm SEM of three or more independent experiments or representative images if not indicated otherwise. Data are means \pm SEM of three or more independent experiments or representative Western Blots or images where applicable. One-way ANOVA + Tukey's multiple comparison test, ****p<0.0001, *** p<0.001, ** p<0.01, * p<0.05. Figure adapted from Bebber et al., 2021, Nature Communications.

2.4.3 Neuroendocrine subtypes do not segregate by chemotherapy response

To test whether division of tested cell lines into responders and non-responders was unique to ferroptosis, cell lines were tested for chemotherapy response using the standard-of-care cytostatics cisplatin and etoposide¹⁵⁵. Stimulation with increasing concentrations of cisplatin and etoposide did not show the same segregated response pattern as for ferroptosis treatment but all tested human cell lines responded equally (Figure 16A, B). Moreover, tested murine sticker and floater cells responded equally to cisplatin or etoposide treatment (Figure 16C, D).

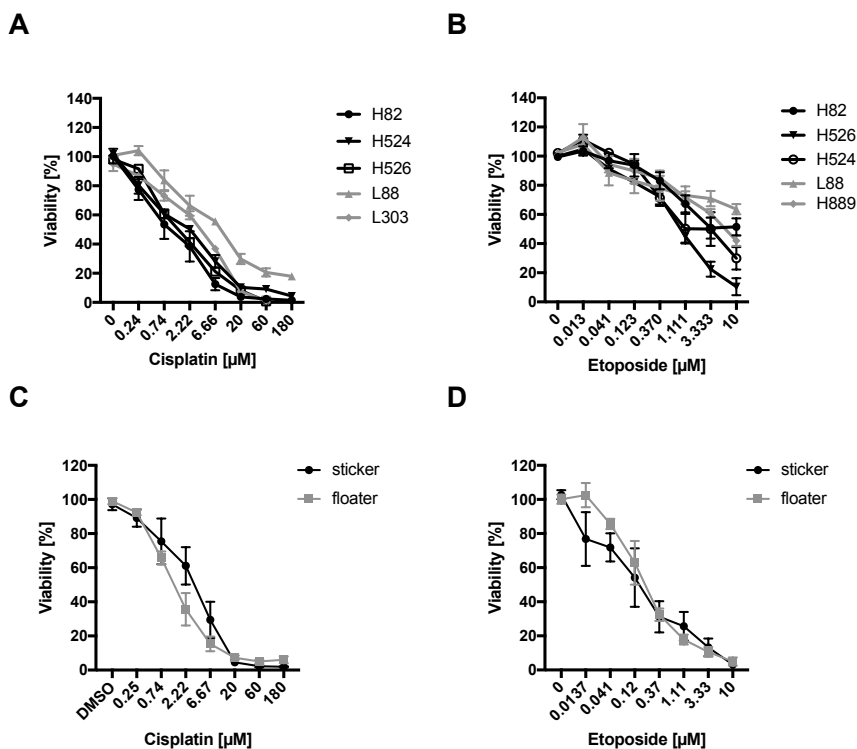
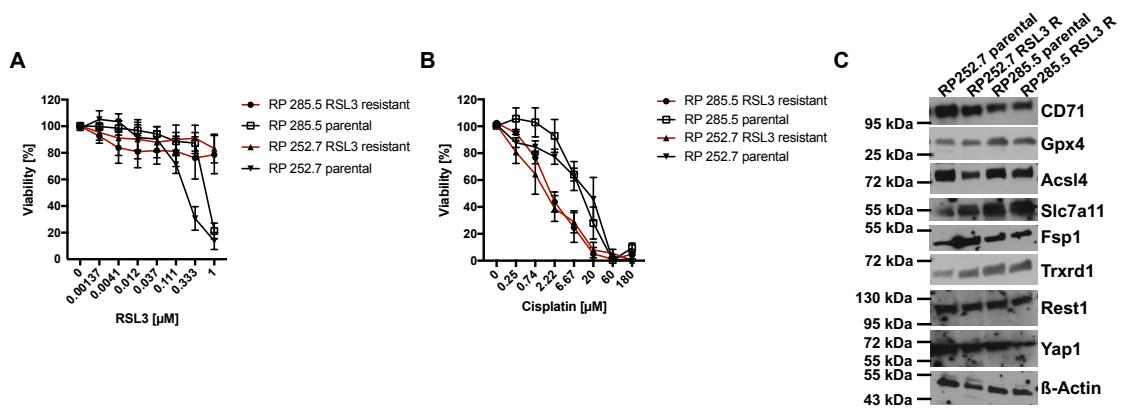


Figure 16 SCLC neuroendocrine subtypes do not segregate by chemotherapy response.

A, B The indicated five human SCLC lines were treated with indicated rising concentrations of cisplatin (A) or etoposide (B) for 72 h, cell viability was determined by Cell Titer Blue. For each cell line $n=3$ biological replicates. **C, D** RP 181.5 sticker and floater were treated with indicated rising concentrations of cisplatin (C) or etoposide (D) for 72 h, cell viability was determined by Cell Titer Blue. For each cell line $n=3$ biological replicates. Data are means \pm SEM of three or more independent experiments. Figure adapted from Bebbler et al., 2021, Nature Communications.

2.4.4 Cells with acquired ferroptosis resistance are more sensitive to chemotherapy

To test whether cells with acquired ferroptosis develop collateral sensitivity or resistance to chemotherapy, SCLC cells were treated with rising concentrations of RSL3 for three months to render them resistant (Figure 17A). Strikingly, ferroptosis resistant cells were indeed more sensitive to cisplatin (Figure 17B). Interestingly, a slight decrease in *Acs14* expression could be observed in RSL3-resistant made cells but expression levels of other important ferroptosis pathway components and NE markers were comparable between parental and RSL3 resistant cells (Figure 17C).



To further examine the role of NE differentiation in ferroptosis response segregation in a genetically-defined experimental set-up, mouse SCLC cells (RP) were compared to cells derived from the RPM GEMM, here expression of constitutively active cMyc T58A in which threonine 58 has been exchanged by alanine in addition to Rb1 and Tp53 KO leads to largely non-NE differentiated tumours¹⁸⁵. Strikingly, RPM cells were more sensitive to ferroptosis induced by erastin and RSL3 treatment than RP cells monitored by Cell Titer Blue cell viability assay (Figure 18A, B). Western Blot analysis could indeed confirm slightly increased expression of the non-NE markers REST1 and VIM but did not reveal a difference in YAP1 expression (Figure 18A, B, C). Additionally, confirming that different ferroptosis sensitivity does not stem from cell adhesion or suspension state, RP and RPM cells all grow under adherent conditions.

Interestingly, it was shown that cMyc T58A expression promotes Ne to non-NE differentiation in SCLC by upregulating the non-NE marker YAP1 in the RPM mouse model²²⁰. Additionally, YAP1 was recently shown to promote ferroptosis sensitivity of cells cultured at low confluence^{253,254}. Therefore, non-NE sticker cell were transduced with a constitutively active mutant of YAP1 in which all five serines haven been mutated to alanines (YAP1 5SA)^{255,256} to test whether YAP1 was sufficient to render cells even more ferroptosis sensitive. Indeed, sticker cells overexpressing YAP1 5SA displayed an increased ferroptosis sensitivity accompanied by slightly increased REST1 expression (Figure 18D, E, F).

Taken together, this suggests that ferroptosis sensitivity further increases along with differentiation from NE to non-NE cellular states.

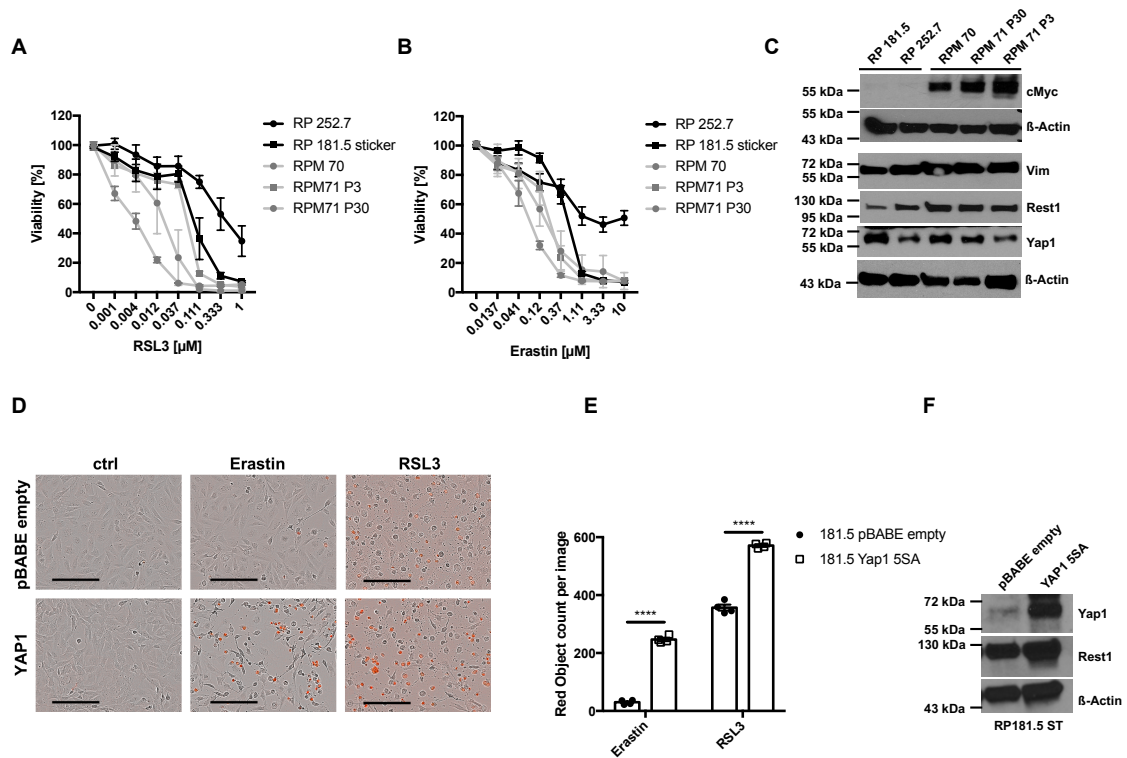


Figure 18 Non-ne SCLC cells are more sensitive to ferroptosis.

A, B The indicated mouse RP and RPM (RPM mouse model) cell lines were treated with increasing concentrations of RSL3 (A) or erastin (B) for 24 h, cell viability was determined by Cell Titer Blue. **C** Cells as in (A) were analysed for protein expression by Western Blotting. **D, E** 181.5 stickers expressing either vector control or YAP1 5SA-YFP were treated with RSL3 [1 μ M] or erastin [10 μ M] for 24 h DRAQ7 [0.1 μ M] was added to all wells to visualise dead cells (red colour in image). Images were acquired every 2 h using the IncuCyte S3 bioimaging platform, n=4 biological replicates. Images shown are acquired after 10 h. Scale bar = 200 μ m. Representative images out of four independent biological replicates are shown. **F** Cells as in (D, E) were analysed for protein expression by Western Blotting. Representative Western Blot images are shown. Data are means \pm SEM of three or more independent experiments or representative images if not indicated otherwise. Two-tailed unpaired *t* tests, *****p*<0.0001. Figure adapted from Bebbber et al., 2021, Nature Communications.

Due to the fact, that SCLC subtypes are not only characterised by ASCL1 and REST1, expression of all described NE subtype markers ASCL1, NEUROD1, YAP-1, POU2F3, REST1, ATOH1 and NE subtype-related markers, such as MYC, MYCL, HES1 (see **Figure 5**)²²⁷ was analysed and compared using RNA-seq data murine and human cells. This analysis confirmed that human non-responders belong to the SCLC-A subtype expressing high levels of ASCL1 and very low levels of REST1 (Figure 19A). All three human responder cell lines express increased REST1 levels and belong either to the SCLC-N subtype expressing NEUROD1 (H82, H524) or the SCLC-P subtype expressing POU2F3 (H526). None of the tested human SCLC cell lines belongs to the SCLC-Y subtype.

Murine non-responder floater cells (181.5) and a mixed population of sticker and floater cells (246.7) were characterised by high *Ascl1* expression (Figure 19B). Murine responder sticker cells were characterised by increased *Rest1* and *Yap1* expression and low *Ascl1* expression which could also be confirmed on protein level (see Figure 13B). All murine cell lines presented with low *Neurod1* and low *Pou2f3* expression. The newly identified non-NE marker *ATOH1*¹⁶¹ was expressed generally at very low levels in all human and murine cell lines analysed.

In conclusion, ferroptosis responders and non-responders are mainly characterised by high *ASCL1* and high *REST1* expression, respectively. While *NEUROD1* and *HES1* expression does not correlate with ferroptosis sensitivity in human SCLC cells and expressed only at very low levels in murine SCLC cells, non-NE markers *POU2F3* and *YAP1* were expressed at higher levels in responders.

While *Myc* and *Mycl* expression levels segregate murine responders and non-responders, this segregation could not be confirmed in human responders and non-responders. Taken together, this analysis revealed that human and murine responders and non-responders show a clear segregation of responders and non-responders by high *ASCL1* and *REST1* expression, respectively, but do not show identical expression patterns of all described NE and non-NE markers.

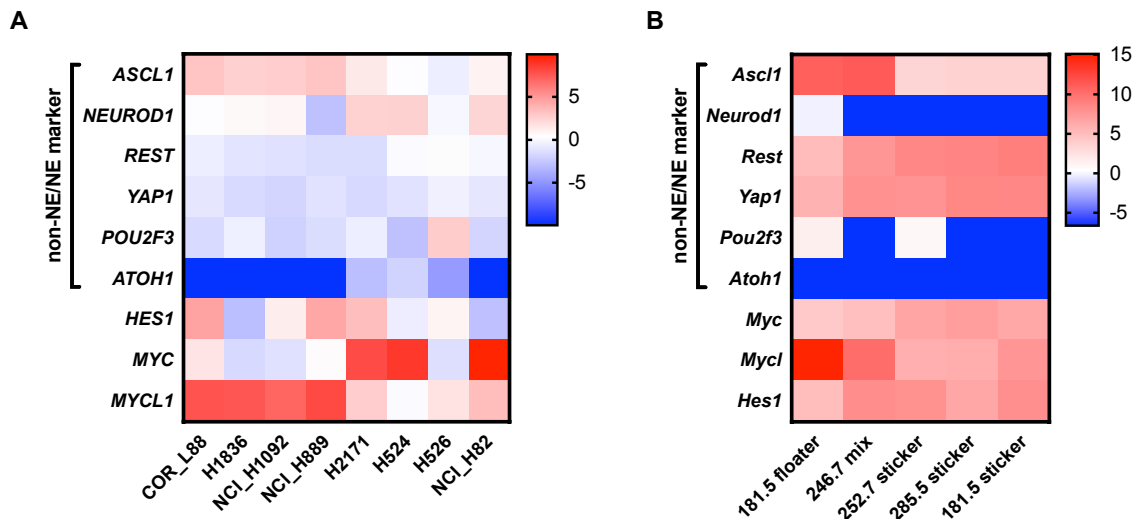


Figure 19 NE marker expression in human and mouse SCLC cell lines.

A, B RNA-sequencing of indicated human (A) and murine (B) SCLC cell lines. FPKM data were log₂ transformed (+0.01) and plotted for expression of non-NE/NE marker genes. Heatmap colour code indicates expression levels.

2.5 Ferroptosis responders are characterised by a ferroptosis-prone lipidome

The accumulation of peroxidised membrane lipids is the crucial hallmark of ferroptosis which allows for membrane pore formation and destabilisation of the lipid bilayer^{56,257}. Within the plasma membrane, PUFAs are especially sensitive to lipid peroxidation²⁵⁸. Within this PUFA pool, AA- and AdA-containing PE species were identified as ferroptosis-specific peroxidation targets which are by orders of magnitude less peroxidised during other types of PCD^{55,56}. Recently, ether-linked phospholipids synthesised in peroxisome and ER were identified to be specifically peroxidised during ferroptosis and thereby contribute to the lipid peroxide pool and drive ferroptosis (Zou et al., 2020).

ACSL4 was identified as one of the first proteins genetically required for cells to undergo ferroptosis⁷². ACSL4 mediates esterification of AA and AdA with CoA forming Acyl-CoA which can then be used for anabolic PUFA biosynthesis thereby generating the lipid peroxidation target pool. Similarly, LPCAT3 contributes to ferroptosis by incorporation of AA into phospholipids of cellular membranes^{72,75,76}.

2.5.1 Ferroptosis sensitive SCLC presents with increased fatty acid metabolism

To analyse gene expression of ferroptosis regulators log₂-transformed TPM-normalised RNA-seq data of RP 181.5 sticker to floater cells was compared. For computation an R script was used including the R packages *gplots* and *RColorBrewer*. While expression patterns of the important ferroptosis regulators GPX4, SLC7A11, FSP1 (=AIFM2), and TFRC/CD71 could not explain increased ferroptosis sensitivity of non-NE stickers, ACSL4 and LPCAT3 were indeed expressed at slightly elevated levels (Figure 20A). Furthermore, GSEA analysis revealed an enrichment of a fatty acid metabolism gene set including genes, such as ACSL4 and the important fatty acid synthesis enzyme fatty acid synthase (FASN)²⁶⁰ in ferroptosis sensitive human SCLC cells (Figure 20B). Expression data of an NIH SCLC cell line panel independently confirmed an inverse correlation of ASCL1 and ACSL4 expression (Figure 20C).

Together these data indicated increased availability of phospholipids as targets of lipid peroxidation during ferroptosis in non-NE SCLC.

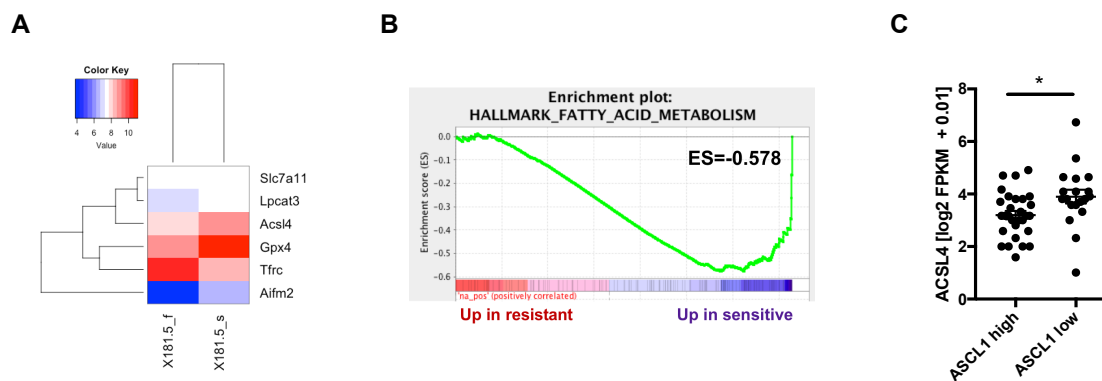


Figure 20 non-NE SCLC presents with increased levels of ACSL4 and upregulated lipid metabolism.

A 181.5 sticker and floater cells were subjected to RNA-sequencing. TPM data were log₂ transformed (+0.01) and plotted for relative expression of genes involved in ferroptosis. Heatmap colour code indicates expression levels between each sample and the average of each gene, dendrogram shows distance between sample populations. **B** Gene set enrichment analysis (GSEA) of a ranked list of differentially expressed genes from human ferroptosis sensitive and resistant cells was performed for fatty acid metabolism genes (Enrichment score (ES)=-0.578, $p < 0.001$ ^{251,252}). **C** The NIH SCLC cell line panel (n=48 cell lines) was segregated by ASCL1 expression (high= log₂ (FPKM +0,01)> 3) (low= log₂ FPKM +0,01< 3) and ACSL4 mRNA expression is plotted. Two-tailed unpaired *t* tests. * $p < 0.05$ Cell line panel expression data are available at Expression Atlas <https://www.ebi.ac.uk/gxa/home>.

2.5.2 Ferroptosis sensitive SCLC presents with increased basal levels of peroxidised lipids

To further analyse differences in lipid metabolism in SCLC NE subtypes the oxidised lipidome was analysed in isogenic sticker and floater cells upon RSL3-induced ferroptosis using Liquid Chromatography coupled to Electrospray Ionisation Tandem Mass Spectrometry (LC-ESI-MS/MS). Comparison of the amounts of phospholipid peroxidation products such as oxidised PUFA-PE species revealed already highly increased basal levels in sticker cells compared to floater cells (Figure 21A). Cells were treated with RSL3 for a sublethal period which further increased amount oxidised phospholipids in sticker cells but not in floater cells (Figure 21A). Due to the fact, that already basal levels of oxidised PUFA species were strongly increased in sticker as compared to floater cells, it was tempting to hypothesise that non-NE/NE transdifferentiation may affect the metabolism of PUFA-containing phospholipids. To examine this, Nano-Electrospray Ionisation Tandem Mass Spectrometry (Nano-ESI-MS/MS) of total amounts of unoxidised phospholipids in extracted lipids from stickers and floaters was performed and revealed that the majority of diacylglycerol (DAG) PUFA levels detected were either comparable or elevated in ferroptosis resistant floaters (Figure 21B, C).

precursor 1-O-alkyl-glycerol-3-phosphate (AGP), which is then acylated at the sn-2 position in the ER²⁶¹. Although the exact mechanism of ether-linked phospholipid synthesis in the ER is not fully elucidated yet, depletion of the ER-resident enzymes 1-Acylglycerol-3-Phosphate O-Acyltransferase (AGPAT) and plasmanylethanolamine desaturase 1 (PEDS1) were identified to cause reduced ether-linked phospholipid synthesis^{262,263}.

Interestingly, expression of several enzymes involved in ether-linked phospholipids was overall elevated in murine non-NE SCLC sticker cells analysed by qRT-PCR (Figure 22B). Furthermore, *Lpcat3* and *Acs14*, two enzymes specifically involved in AA and Ada containing phospholipid synthesis were upregulated in all three sticker cell lines (Figure 22B). Since ether-linked PUFAs and their synthesis were recently shown to promote ferroptosis sensitivity⁵⁷, next it was assessed whether knockdown of responsible enzymes would render sticker cells more resistant to ferroptosis. Indeed, upon siRNA mediated silencing of *Agpat2* or *Agpat3*, non-NE 181.5 and 246.7 SCLC sticker cells were less sensitive to ferroptosis (Figure 22C, D, E, F).

Together these data showed that lipid metabolism remodelling during non-NE/NE trans-differentiation contributes to their ferroptosis sensitivity and resistance, respectively.

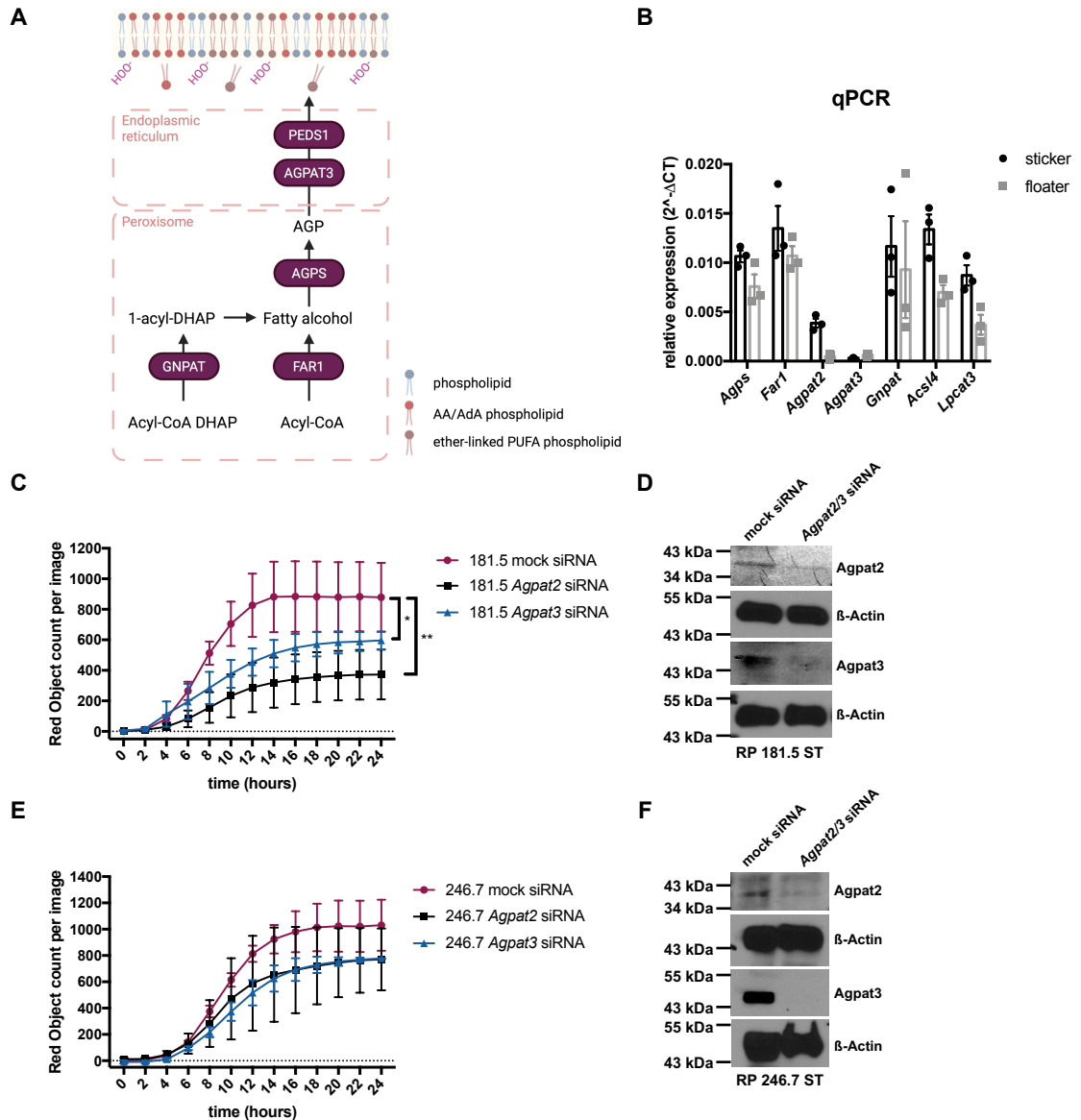


Figure 22 Non-NE SCLC subtype presents with increased ether-lipid synthesis.

A In the peroxisome, ether-linked phospholipid synthesis begins with synthesis of fatty alcohol from Acyl-CoA DHAP mediated by glyceronephosphate O-acyltransferase (GNPAT) or directly from Acyl-CoA mediated by fatty acyl-CoA reductase 1 (FAR1). Fatty alcohol is converted into the ether lipid precursor 1-O-alkyl-glycerol-3-phosphate (AGP) by alkylglycerone phosphate synthase (AGPS). In the endoplasmic reticulum (ER), AGP is then acylated at the sn-2 position enzymes under involvement of the enzymes 1-Acylglycerol-3-Phosphate O-Acyltransferase (AGPAT) and plasmanylethanolamine desaturase 1 (PEDS1) but the exact mechanism is not yet fully elucidated. Scheme was created with Biorender.com and adapted from Tang and Kroemer, 2020²⁵⁹. **B** RNA was isolated from three sticker floater cell lines (RP181.5; RP246.7; BYC5.1), respective cDNA was transcribed and qPCR performed for the indicated transcripts. **C, E** RP181.5 (C) and RP246.7 (E) sticker cells were subjected to the indicated siRNA-mediated knockdown of *Agpat2* and *Agpat3* for 72 h and then treated with RSL3 [1 μ M] for an additional 24 h. DRAQ7 [0.1 μ M] was added to all wells to visualise dead cells. Images were acquired every 2 h using the IncuCyte S3 bioimaging platform. For each condition n=3 biological replicates. Dead cells/image are normalised to cell confluence at the beginning of RSL3 treatment. **D, F** Representative Western Blots of cells as in (C, E) are shown. Data are means \pm SEM of three

independent experiments or representative images where applicable. One-way ANOVA + Tukey's multiple comparison test, ** $p < 0.01$, * $p < 0.05$, ns > 0.05 . Scheme was drawn with fully licensed Biorender.com. Figure adapted from Bebbber et al., 2021, Nature Communications.

2.5.4 SCLC patient data confirm altered lipid metabolism in ASCL1-low patients

To determine the levels of expression of ether-linked phospholipid synthesis pathway components in non-NE SCLC in treatment naïve patients, RNA expression data were firstly analysed for *ASCL1* expression, revealing a fraction of ten *ASCL1*-low expressing patients (Figure 23). In these patients, low *ASCL1* expression indeed correlated with increased expression of *GNPAT*, *ACSL4* and, slightly increased *AGPAT3* expression (Figure 23).

Taken together, we have shown that increased lipid metabolism and upregulation of ether lipid metabolism is a hallmark of non-NE SCLC and thereby promotes ferroptosis sensitivity. Moreover, non-NE to NE transdifferentiation involves downregulation of ether-linked phospholipid synthesis resulting in a lipidome which is less prone for lipid peroxidation.

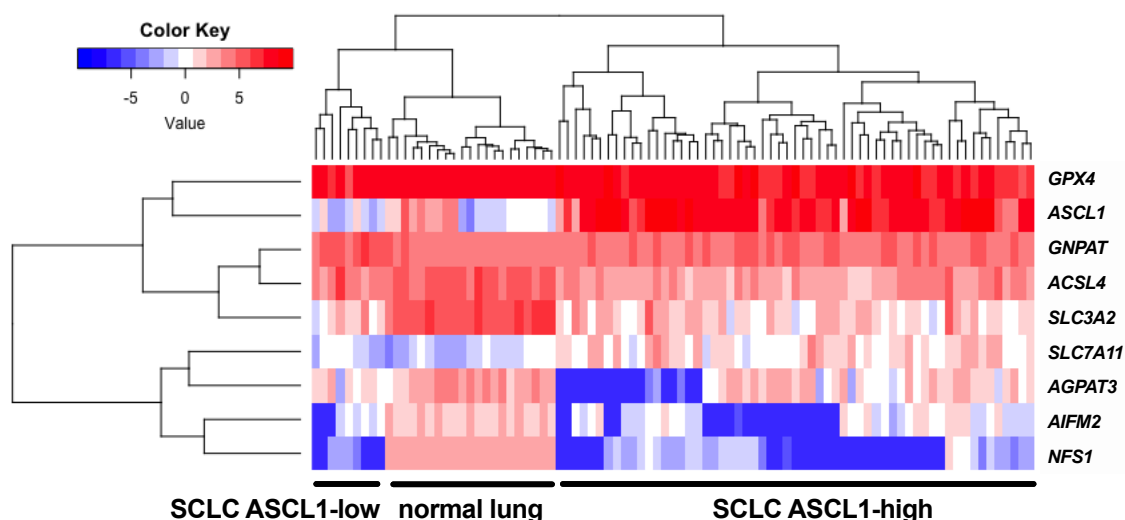


Figure 23 ASCL1^{low} SCLC express higher levels of lipid ether metabolism genes.

RNA-seq expression data in FPKM (fragments per kilobase of exon model per million reads mapped) from normal lung²³⁵ (n=22) and chemo-naïve SCLC patient samples¹⁸³ (n=67) were log₂ transformed (+0.01) and plotted for relative expression of the indicated genes. Heatmap colour code indicates expression levels between each sample and the average of each gene, dendrogram shows distance between sample populations. Figure adapted from Bebbber et al., 2021, Nature Communications.

2.6 SCLC subtypes divide by two distinct redox pathway dependencies

2.6.1 Non-NE SCLC is dependent on the GSH-based anti-oxidant redox pathway

ASCL1-low expressing human and murine SCLC cells were identified to be ferroptosis sensitive due to upregulated lipid metabolism and specifically increased ether lipid synthesis, whereas ASCL1-high expressing SCLC cells were highly resistant. To now investigate why ASCL1-high SCLC can cope with ferroptotic stimulation, concentrations of the major cellular antioxidant GSH and its oxidised form GSSG were examined in these cells using a GSH/GSSG kit and by FACS analysis using a fluorescent dye as specific read-outs. Contrary to expectations, human and murine ASCL1-high ferroptosis-resistant SCLC cells in fact presented with lower basal levels of GSH whilst levels of reduced GSSG were comparable with those in ferroptosis-sensitive cells (Figure 24A, B). These observations indicated GSH synthesis to be specifically repressed in ASCL1-high expressing NE SCLC cells but not its recovery. In line with this, doxycycline (dox) inducible overexpression of ASCL1 in two murine non-NE SCLC cell lines (RP285.5, RP252.7) resulted in decreased expression of GCLC an essential enzyme for GSH synthesis (Figure 24C) and consequentially in decreased cellular amounts of GSH (Figure 24D).

However, inducible overexpression of ASCL1 in non-NE SCLC sticker cells was insufficient to induce an NE differentiated floater phenotype in line with prior observations in SCLC non-NE/NE transition²²³. Therefore, inducible ASCL1-expression in sticker cells was also insufficient to render cells more resistant to ferroptosis induction (Figure 24E).

In conclusion, ASCL1 expression status can serve as a marker of ferroptosis resistance in fully NE differentiated SCLC cell lines, but its induced expression is insufficient to drive NE switch in the cellular system as well as ferroptosis resistance.

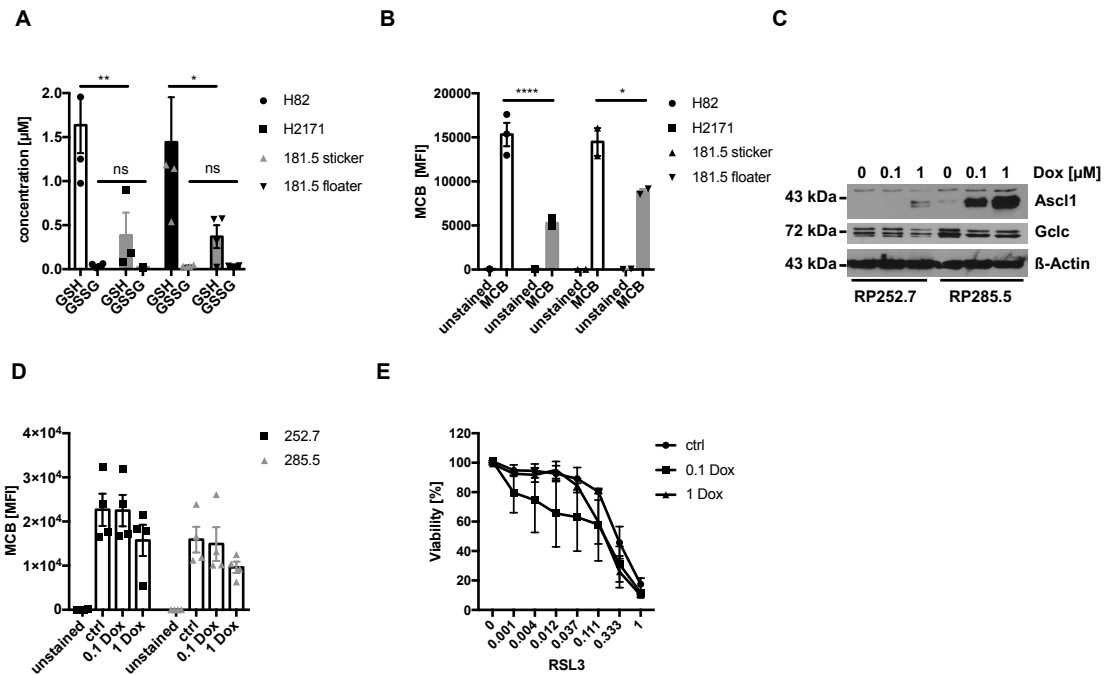


Figure 24 SCLC-A cells presents with low GSH levels.

A Cellular GSH concentrations were quantified by GSH/GSSG Glo Assay (Promega) in the indicated cell lines, n(H82, 181.5 stickers, 181.5 floaters)=4, n(H2171)=3 biological replicates. **B** cellular GSH levels were determined by monochlorobimane (MCB) staining and flow cytometry (MFI- mean fluorescent intensity) in the indicated murine SCLC cell lines, n=3 biological replicates. **C** the indicated ASCL1-inducible cell lines were treated as indicated for 24 h. Representative Western Blots are shown. **D** cellular GSH levels were determined by MCB staining and flow cytometry (MFI- mean fluorescent intensity) in the indicated murine SCLC cell lines upon 24h of doxycycline induction, n=4 biological replicates. **E** RP285.5 cells were pre-treated with 0.1 and 1 µM Doxycycline for 48 h and treated with RSL3 as indicated for 24 h, cell viability was determined by Cell Titer Blue, n=3 biological replicates. Data are means +/- SEM of three or more independent experiments or representative Western Blots where applicable. One-way ANOVA + Tukey's multiple comparison test, ****p<0.0001, ** p<0.01, * p<0.05, ns>0.05. Figure adapted from Bebbler et al., 2021, Nature Communications.

At the same time, inducible as well as fully established ASCL1 expression in NE SCLC cells decreased cellular GSH levels and thereby cellular redox potential. Still, all fully NE differentiated SCLC cells tested were more resistant to ferroptosis induced by RSL3 and erastin (see Figure 15C, D). Further confirming independence of human and murine ASCL1-high expressing NE SCLC cell lines on GSH levels, they were resistant to ferroptosis induced by the GCLC inhibitor BSO (Figure 25A, B) albeit clearly reduced GSH levels while ASCL1-low expressing SCLC cells were sensitive (Figure 25C). Importantly, BSO treatment induced lipid ROS accumulation which could be blocked by co-incubation with Fer-1 in murine non-NE SCLC (Figure 25D). Furthermore, ferroptosis could be

induced in ASCL1-low expressing sticker cells but not in ASCL1-high floater cells upon cystine starvation resulting in GSH depletion which was rescued with Fer-1 (Figure 25E).

Together, these data suggested that the initial decrease in GSH levels and thereby anti-oxidant defence upon ASCL1 expression must drive a switch to usage of a compensatory anti-oxidant defence system which is entirely independent of GSH in ASCL1-expressing NE SCLC cells.

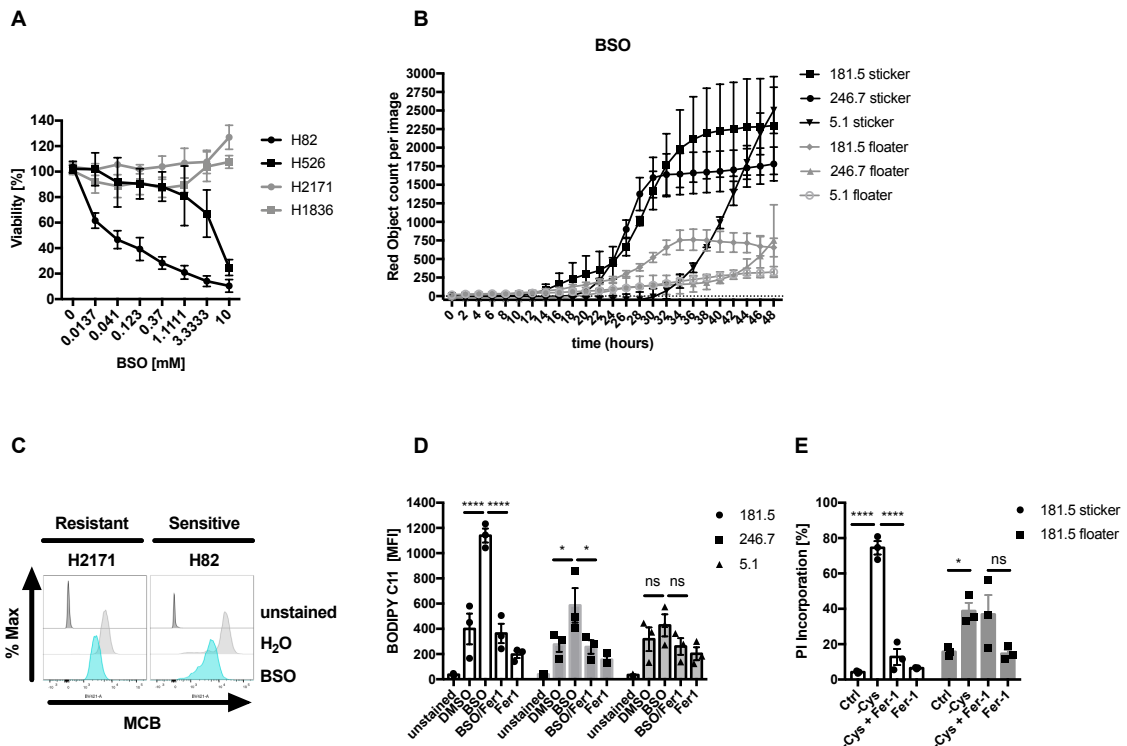


Figure 25 ASCL1-low expressing SCLC cells are sensitive to GSH depletion.

A The indicated human SCLC cell lines were treated with indicated concentrations of BSO for 24 h, cell viability was determined by Cell Titer Blue, $n=3$ biological replicates. **B** The indicated murine SCLC cell lines were treated with BSO [10 mM] for 48 h in the presence of DRAQ7 [0.1 μ M] to visualise dead cells. Images were acquired every 2 h using the IncuCyte S3 bioimaging platform. For each cell line $n=3$ biological replicates. **C** The indicated human cell lines were treated for 8 h with BSO [10 mM] and stained for GSH levels using MCB. Cells were analysed by flow cytometry. Grey=untreated, blue=BSO treated. **D** The indicated sticker cells were treated with DMSO, BSO [10 mM] +/- Fer-1 [5 μ M] for 5 h and stained for lipid ROS accumulation using BODIPY C11 and analysed by flow cytometry; mean fluorescent intensity (MFI) was quantified, $n=3$ biological replicates. **E** 181.5 sticker and floater cells were cultured in normal (Ctrl) or cystine-free medium (-Cys) +/- Fer-1 [5 μ M] for 24 h, cell death was quantified by propidium iodide (PI) uptake and flow cytometry, $n=3$ biological replicates. Data are means +/- SEM of three or more independent experiments. One-way ANOVA + Tukey's multiple comparison test, **** $p<0.0001$, ** $p<0.01$, * $p<0.05$, ns >0.05 . Figure adapted from Bebbber et al., 2021, Nature Communications.

2.6.2 Neuroendocrine SCLC is characterised by TRX pathway addiction

Besides the GSH-based antioxidant redox system, the thioredoxin-based antioxidant redox system can take over antioxidant defence in cells and compensate for GSH-deficiency and vice versa^{95,96,119}. Here, reduced TRX serves as a redox equivalent for PRDXs to reduce ROS species and lipid peroxides⁹³. The TXNRDs reduce TRX at the expense of NADPH which can then function as a redox equivalent to reduce other oxidised cellular substrates.^{93,94,96} TXNIP limits TRX availability for antioxidant defence by binding reduced TRX (Figure 26A).

Based on the result, that ASCL1 expression suppresses GCLC in NE SCLC, it was tempting to hypothesise that anti-oxidant defence in NE SCLC may be dependent on the alternative TRX pathway. Thus, expression of important proteins of the TRX pathway was examined in human ASCL1-low expressing non-NE compared to ASCL1-high expressing NE cells as well as murine sticker with floater cells. Western Blot analysis revealed that TRXR1/TRXR2 were upregulated in human ASCL1-high SCLC cells and slightly upregulated in murine ASCL1-high SCLC cells, as well as expression of TXNIP, the negative regulator of TRX, was consistently increased in human and murine ASCL1-high cells suggesting an increased activity of the TRX-pathway for antioxidant defence (Figure 26B, C).

Indeed, treatment with the commonly used inhibitor of TXNRD1 and TXNRD2 Auranofin, a thiol-reactive gold-containing compound clinically used for treatment of rheumatoid arthritis¹⁰⁴, led to a quicker time-dependent loss of fully-reduced TRX in ASCL1-high as compared to ASCL1-low SCLC cells in redox shift assays supporting increased sensitivity of the TRX pathway in ASCL1-high expressing NE SCLC (Figure 26D, E).

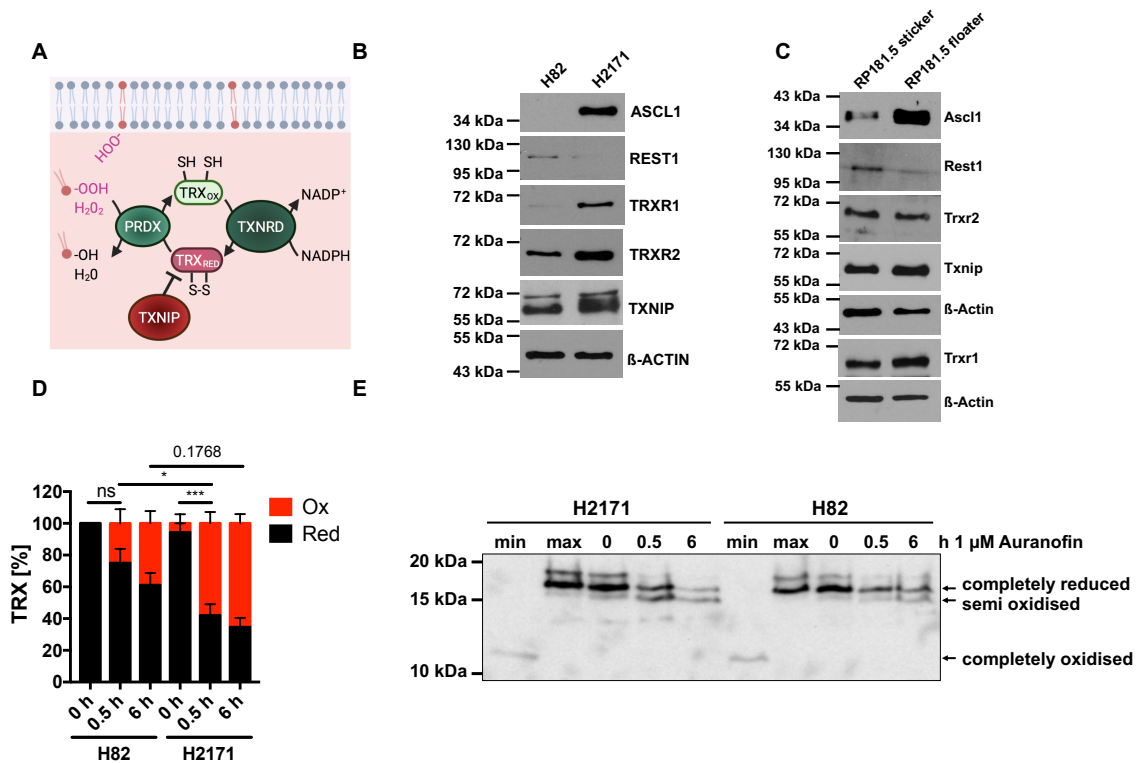


Figure 26 SCLC-A cells present with increased TRX pathway activity.

A Schematic view of genes involved in the TRX antioxidant pathway. **B, C** human (B) and murine (C) cells were lysed and TRX pathway component expression was detected by Western Blot. Representative Western Blots are shown. **D** Indicated cells were treated with Auranofin [1 μ M] for the indicated times and subjected to redox shift assays. Densitometrical quantification of TRX redox forms is shown. **E** 1.5×10^6 (H82) and 1×10^6 (H2171) cells were treated with Auranofin [1 μ M] for the indicated times, cells were lysed with 8% (w/v) TCA. TRX shift was analysed by Western Blot. Representative Western Blots are shown. Data are means \pm SEM of three independent experiments or representative images out of at least three independent experiments are shown. Two-way ANOVA + Tukey's multiple comparison test, *** $p < 0.001$, * $p < 0.05$, ns > 0.05 . Redox shift assays (D, E) were contributed by Dr. Michaela Höhne. Scheme was drawn with fully licensed Biorender.com. Figure adapted from Bebbler et al., 2021, Nature Communications.

Strikingly, human and murine SCLC cells treated with Auranofin revealed that NE SCLC cell lines are selectively sensitive to Auranofin-induced cell death while non-NE SCLC were resistant (Figure 27A, B). Stimulation with two other structurally distinct inhibitors of TRXR1 (PX-12 and D9) confirmed sensitivity to TRX antioxidant pathway inhibition (Figure 27C, D). Furthermore, Western Blot analysis could confirm increased expression of Trx1 and Trxr1 in all floater cells as compared to sticker cells (Figure 27E).

In conclusion, results show that ASCL1-high expressing NE SCLC cells are selectively dependent on the TRX anti-oxidant pathway while ASCL1-low expressing SCLC cells are sensitive to ferroptosis.

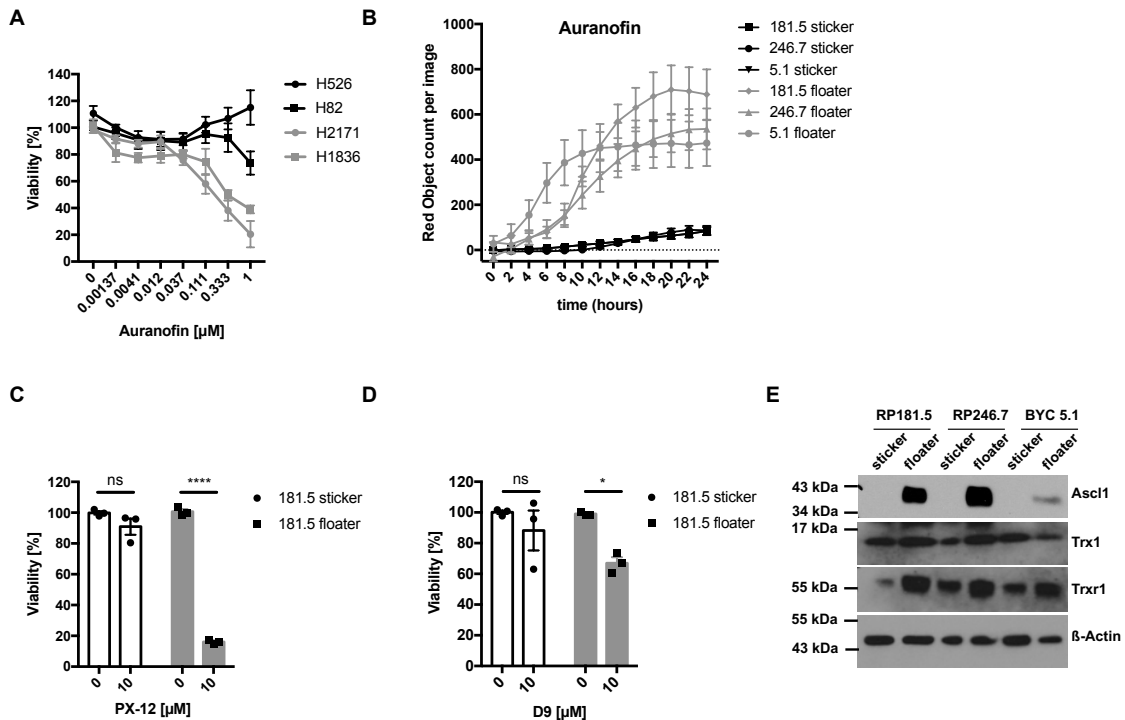


Figure 27 Neuroendocrine SCLC presents with TRX pathway addiction.

A Indicated cells were treated with Auranofin for 24 h, cell viability was determined by Cell Titer Blue. **B** The indicated sticker and floater isogenic cell lines (n=3) were cultured separately and treated with Auranofin [1 µM] for 24 h in the presence of DRAQ7 [0.1 µM] to visualise dead cells. Images were acquired every 2 h using the IncuCyte S3 bioimaging platform. For each cell line n=3 biological replicates. **C, D** 181.5 stickers and floaters were cultured separately and treated as indicated for 48 h. Cell viability was determined by Cell Titer Blue, n=3 biological replicates. Data are means +/- SEM of three or more independent experiments. One-way ANOVA + Tukey's multiple comparison test, ****p<0.0001, * p<0.05, ns>0.05. Figure adapted from Bebbler et al., 2021, Nature Communications.

2.6.3 TXNRD1 inhibition does not induce ferroptotic cell

To determine, which type of cell death was induced by TRX pathway inhibition, sticker and floater cells were stimulated with BSO and Auranofin, respectively and co-incubated with different cell death inhibitors. BSO-induced cell death could be rescued by co-incubation with Fer-1, DFO and by co-incubation with the general antioxidant N-acetylcysteine (NAC) described to partially rescue ferroptosis⁷⁵, but not by co-incubation with the pan-caspase inhibitor zVAD or the RIPK1 inhibitor Necrostatin-1s (Nec-1s), specifically confirming ferroptotic cell death to be induced by BSO (Figure 28). Auranofin-induced cell death in floater cells was ROS induced and could be partially rescued by NAC co-incubation, but could not be rescued by Fer-1, DFO, zVAD and Nec-1s (Figure 28).

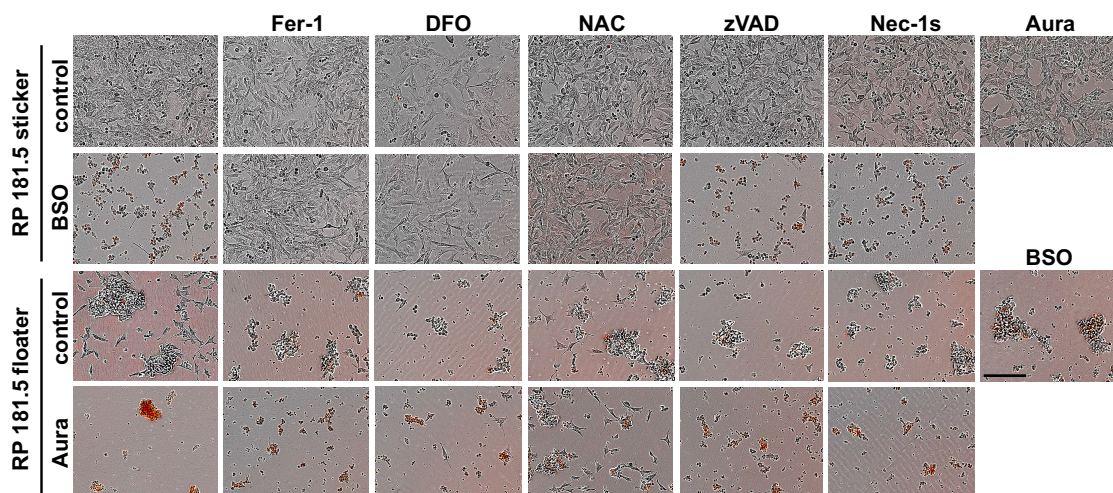


Figure 28 Auranofin induced cell death is not rescued with Fer-1 co-incubation.

RP181.5 sticker and floater cells were treated with DMSO, BSO [10 mM] or Auranofin [1 μ M] in combination with Fer-1 [1 μ M], DFO [100 μ M], NAC [3 mM], zVAD [20 μ M] or Nec-1s [10 μ M] for 24 h. DRAQ7 [0.1 μ M] (red colour in image) was added to all wells to visualise dead cells. Images were acquired every 5 h using the IncuCyte S3 bioimaging platform. Scale bar=200 μ m. Representative images out of three independent experiments are shown.

2.7 SCLC subtype plasticity is defined by redox pathway compensation

SCLC tumours are known to present with intratumoural NE subtype heterogeneity^{208,223,249} which can stem from differences in their cell of origin, cell signalling but also plasticity between subtypes^{185,220}. Hence, next it was examined how induction of either ferroptosis or TRX pathway inhibition would affect subtype heterogeneity. To create an *in vitro* scenario of NE intratumoural heterogeneity, manually separated sticker cells were used, utilising the fact that they already contain a subpopulation of cells in the process of NE transdifferentiation with high expression of ASCL1 resulting in an isogenic mixed ASCL1-high/ASCL1-low culture. Interestingly, while a morphologically distinct subpopulation of SCLC cells with a suspension-like shape and a bright nuclear ASCL1 staining could be observed in DMSO-treated cells, this population was selectively depleted upon Auranofin treatment which did not affect the total numbers of ASCL1-low expressing sticker cells as visualised by DAPI (Figure 29). Induction of ferroptosis using BSO, albeit reducing the amount of ASCL1-low expressing cells indicated by DAPI staining, led to a strong relative enrichment in ASCL1-high expressing cells (Figure 29).

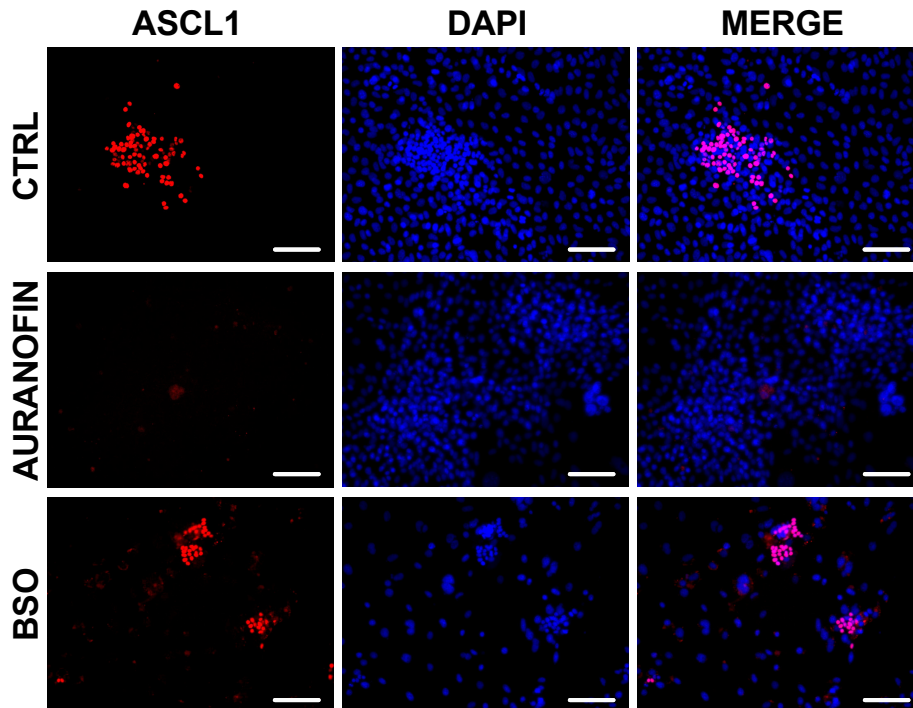


Figure 29 Single treatment regime selectively depletes ASCL1-low or ASCL1-high population. RP181.5 sticker cells were treated with either DMSO (ctrl), Auranofin [500 nM] or BSO [500 μ M] for 96 h and then fixed and stained for ASCL1 (red) and counterstained with the DNA-stain DAPI (blue). Scale bar = 100 μ m. Representative images out of three independent experiments are shown. Figure adapted from Bebbber et al., 2021, Nature Communications.

Interestingly, when analysing mixed sticker and floater cell populations by FACS analysis and gating on live cells, a proportion of these sticker cells transdifferentiated under BSO treatment to the NE SCLC subtype marked by acquired ASCL1 expression (Figure 30). In a manually separated floater cell population instead ASCL1 expression was lost in 13.2% of live cells under Auranofin treatment revealing a proportion of non-NE/NE plasticity to depend on cellular redox signalling in SCLC (Figure 30).

Together, these observations suggest that in heterogeneous non-NE/NE SCLC tumours, ferroptosis treatment may select for ASCL1-high NE cells over time while, *vice versa*, TRX pathway inhibition might enrich tumours for ASCL1-low SCLC cells. Moreover, single pathway targeted treatment may induce non-NE/NE plasticity which might promote escape of SCLC subtypes by transdifferentiation.

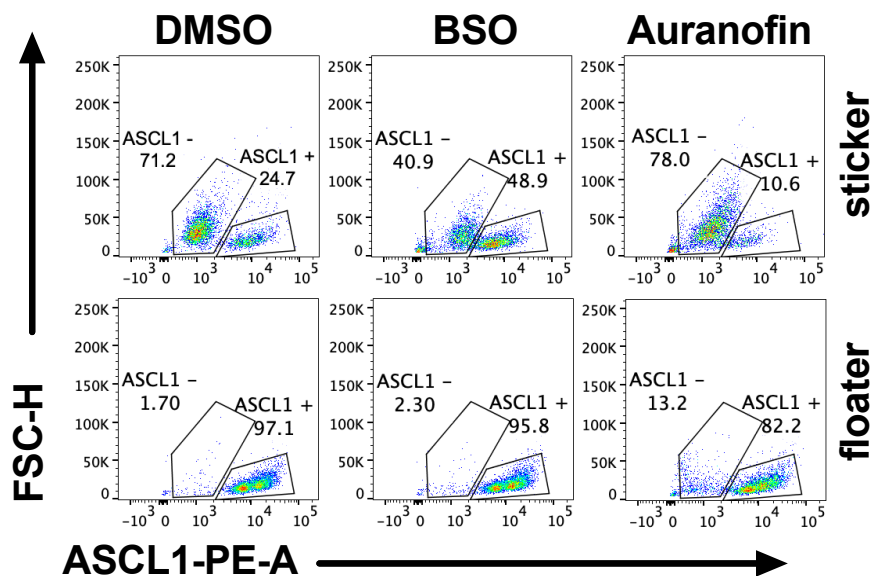


Figure 30 Single treatment regime promotes subtype plasticity.

Manually separated stickers and floaters were treated with either DMSO, BSO [10 mM] or Auranofin [1 μ M] for 24 h. Cells were gated on live cells and analysed for ASCL1 expression by flow cytometry. FSC-H, forward scatter-heights. Representative FACS data out of three independent experiments are shown. FACS experiment in this figure was contributed by Dr. Ariadne Androulidaki. Figure adapted from Bebbler et al., 2021, Nature Communications.

To prevent single therapy induced selection and subtype plasticity, ferroptosis inducing treatment combined with TRX-pathway inhibition was examined. In fact, combined BSO and Auranofin treatment (combo) induced synergistic cell death in both subtypes in human and murine SCLC cells (Figure 31A, B). Cell death induced by a combination of sublethal doses of Auranofin with BSO (combo), could not be rescued by single Fer-1 or NAC co-incubation but by combined Fer-1 and NAC treatment (Figure 31B, C). This indicated that combo-induced cell death was partially dependent on ferroptosis upon lipid ROS generation (Fer-1 rescued) and partially dependent on general ROS generation (NAC rescued).

To confirm specificity of the combo treatment, siRNA mediated knockdown experiments of the drug targets of BSO (*Gclc*), and Auranofin (*Trxr1* and *Trxr2*) were performed. Indeed, only combined targeting of all three genes induced synergistic cell death induction in sticker and floater cells while knockdown targeting only one of the genes resulted in low cell death rates (Figure 31D, E). In general, knockdown efficiency achieved in suspension cells (floater) was in general lower than in adherent cells (sticker) (Figure 31E). Accordingly, knockdown targeting *Slc7a11* alone was insufficient to kill non-NE SCLC, while co-stimulation with Auranofin slightly reduced cell viability (Figure 31F, G). Together, these data revealed highly synergistic effects of combo treatment in all SCLC subtypes and indicated a very rapid redox pathway plasticity in these cells enabling

escape from ROS-induced stress within the 48 h knockdown experiments via use of the alternative TRX pathway for anti-oxidant defence.

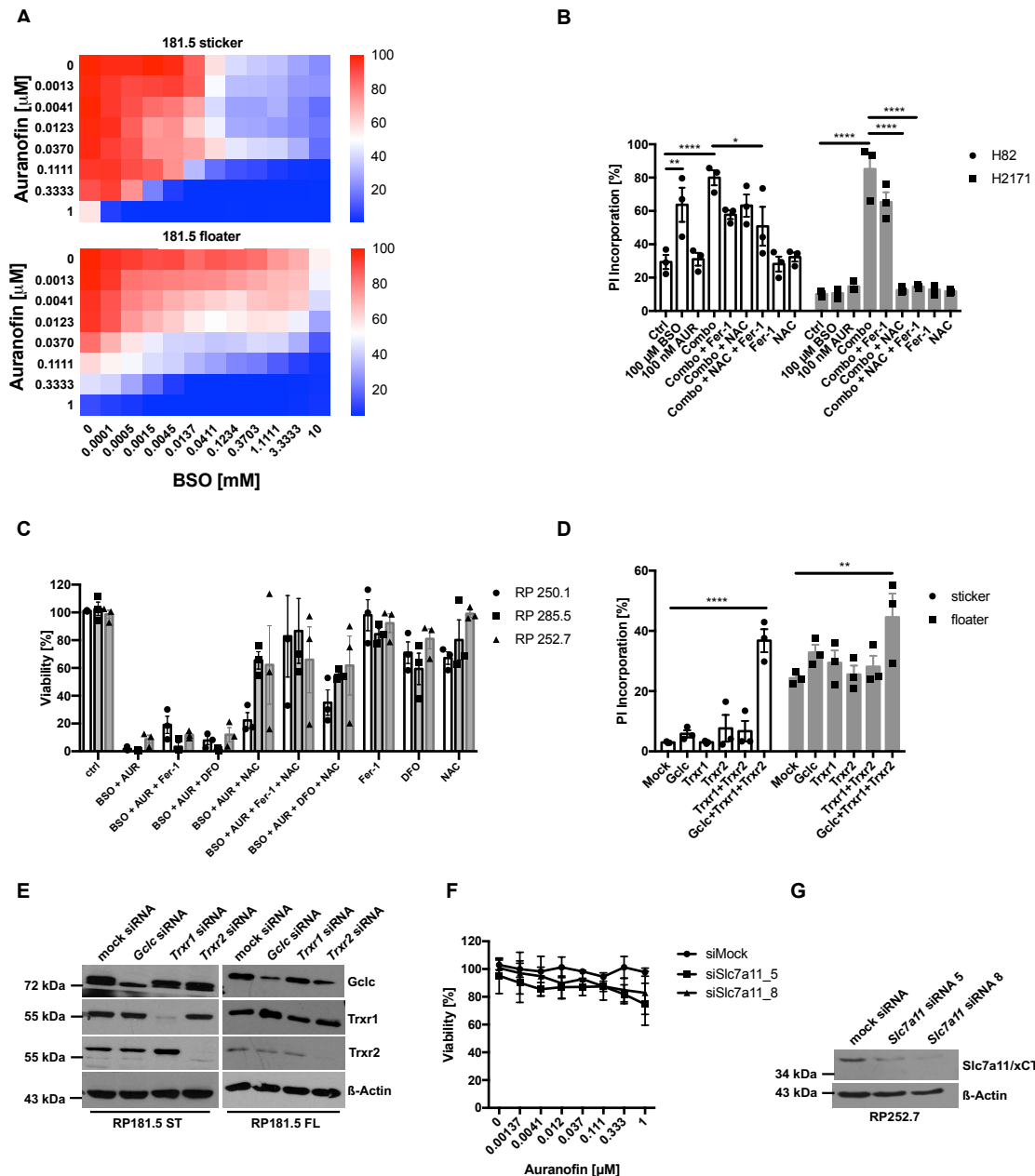


Figure 31 BSO/Auranofin-induced cell death is partially ferroptotic and partially dependent on ROS.

A 181.5 stickers and floaters were subjected to the indicated cross titrations for 48 h and cell viability was determined by Cell Titer Blue. For each cell line $n=3$ biological replicates. **C** The indicated human SCLC cell lines were treated with the indicated combinations of BSO [10 mM], Auranofin (AUR) [1 μ M], N-Acetyl Cysteine (NAC) [3 mM], Ferrostatin-1 (Fer-1) [5 μ M] for 24 h. Cell death was quantified by propidium iodide (PI) uptake and flow cytometry. For each cell line $n=3$ biological replicates. **D** the indicated murine SCLC cell lines were either left untreated (ctrl), or treated as indicated: BSO [10 mM], Auranofin (AUR) [1 μ M], Deferoxamine (DFO) [100 μ M], N-Acetyl Cysteine (NAC) [3 mM], Fer-1 [5 μ M] for 24 h. Cell viability was determined by Cell Titer Blue. For each cell line $n=3$ biological replicates. **E** 181.5 stickers and floaters were subjected to siRNA-mediated knockdown targeting the indicated

genes for 72 h. Spontaneous cell death was quantified by propidium iodide (PI) uptake and flow cytometry. For each cell line n=3 biological replicates. **F** Representative cells as in **(E)** were subjected to Western Blot analysis. Representative Western Blots are shown. **G** RP252.7 cells were subjected to siRNA-mediated knockdown targeting the indicated gene for 72 h. Cell viability was determined by Cell Titer Blue. For each condition n=3 biological replicates. **H** representative cells as in **(h)** were subjected to Western Blot analysis. Representative Western Blots are shown. Data are means +/- SEM of three independent experiments or representative FACS plots where applicable. One-way ANOVA + Tukey's multiple comparison test, ****p<0.0001, ** p<0.01, * p<0.05. Knockdown experiments (D-G) were contributed by Jenny Stroh and Zhiyi Chen. Figure adapted from Bebber et al., 2021, Nature Communications.

2.8 *In vivo* treatment response

Since ferroptosis has been implicated in different types of cancer, several efforts are presently underway to develop selective GPX4 inhibitors with increased bioavailability for clinical use, however these have yet to fulfil pharmacokinetic requirements^{92,264}. Therefore, the clinically progressed GCLC inhibitor BSO was used to assess *in vivo* lipid ROS-dependent ferroptosis response (Figure 24, 25). Moreover, to repurpose a clinically applied TRX pathway inhibitor for the treatment of SCLC, Auranofin was used for *in vivo* treatment to allow for a more rapid clinical translation.

2.8.1 Combined inhibition of GCL and TXNRD1 reduces SCLC tumour growth *in vivo*

As combined treatment using BSO and Auranofin has not yet been described in literature, first an applicable non-toxic dose had to be determined. However, the combination of the published single maximal tolerated treatment doses (20 mM BSO²⁶⁵, 10 mg/kg Auranofin²⁶⁶) led to severe toxicity after 3 days of treatment (Figure 32A). Therefore, doses were decreased to reduce toxicity resulting in a well-tolerated combination of 5 mM BSO and 2.5 mg/kg Auranofin three times a week (7.5 mg/kg/week) monitored by daily weight measurement (Figure 32B).

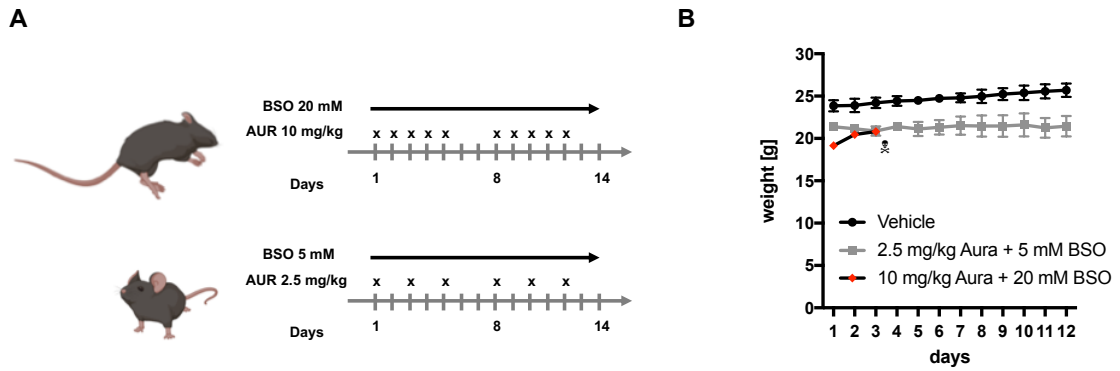


Figure 32 Dose titration.

A Treatment scheme of tested treatments. **B** Weights of mice were monitored over the treatment course.

To now test SCLC *in vivo* sensitivity, human representative ferroptosis responder cells (H82) and non-responder cells (H2171) were subcutaneously injected into both flanks of immunodeficient NMRI-Foxn1 nu/nu mice as a xenograft model. Upon detection of palpable tumours, mice were randomised by tumour volume into two treatment groups receiving either vehicle or the combination of Auranofin and BSO (combo) to avoid subtype plasticity for two consecutive weeks monitoring toxicity by daily weight control (Figure 33 A-D).

Strikingly, a very clear and significant response was observed in established human ASCL1-low responder cells and ASCL1-high non-responder cells xenograft tumours *in vivo* (Figure 33E, F). Confirming ferroptosis induction *in vivo*, histological analysis of combo-treated tumours of both subtypes revealed an increase of the end product of lipid ROS generation malondialdehyde (MDA) which was recently validated as a specific *in vivo* ferroptosis marker²⁶⁷ (Figure 33G).

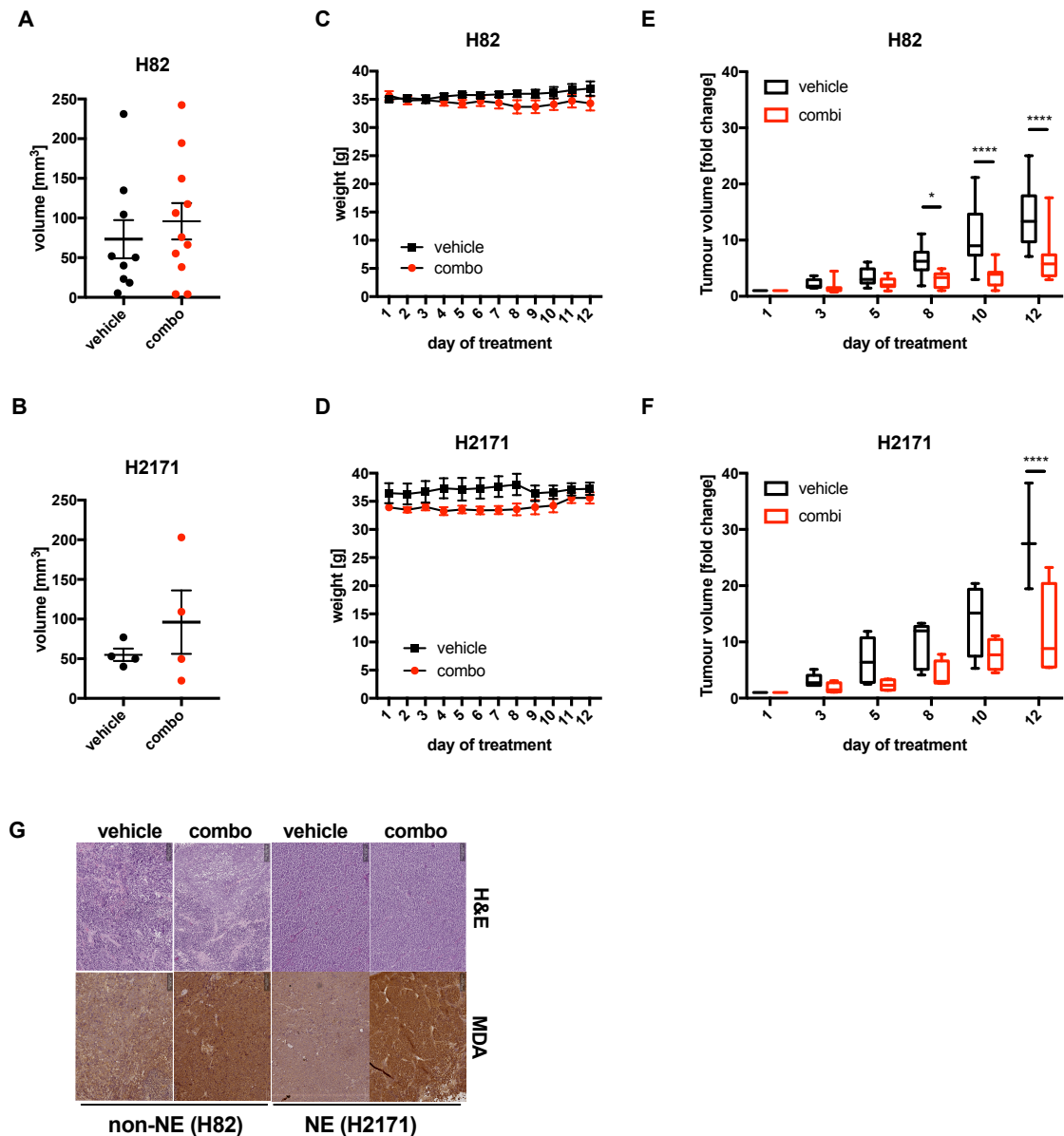


Figure 33 Combined ferroptosis induction and TRX pathway inhibition demonstrates broad anti-tumour activity in human SCLC xenograft model *in vivo*.

A, B 8-weeks old male nude mice were injected s. c. with 1.5×10^6 H82 (n=20 tumours) or H2171 (n=8 tumours) cells into flanks. Once measurable, tumours were randomised for the indicated treatment groups, n(H82 vehicle)=9, n(H82 combo)=11, n(H2171 vehicle)=4, n(H2171 combo)=4 biologically independent tumour samples. **C, D** Weights were monitored daily to control for toxicity effects. **E, F** 8-weeks old male nude mice were injected with 1.5×10^6 H82 (E) and H2171 (F) cells into flanks. Once palpable, tumours were treated either with vehicle (H82, n=9; H2171 n=4) or combined BSO [5 mM] in the drinking water and Auranofin 3x per week i.p. [2.5 mg/kg] (H82, n=11, H2171 n=4) for two consecutive weeks. Fold change of initial tumour size is shown. Boxplot center line, mean; box limits, upper and lower quartile; whiskers min. to max. **G** Sections from paraffin-embedded tumours of vehicle or combo-treated mice (E, F) were stained by H&E or for MDA. Representative images are shown, scale bar=200 μ m. Significance was tested by two-way ANOVA + Tukey's multiple comparison test, ****p<0.0001, * p<0.05. Figure adapted from Bebbler et al., 2021, Nature Communications.

To better mimic non-NE/NE intratumoural heterogeneity in SCLC patients, murine non-NE sticker and NE floater cells containing 50% ASCL1⁻ cells and 50% ASCL1⁺ cells were co-transplanted subcutaneously into both flanks of immunodeficient NMRI-Foxn1^{nu/nu} mice (Figure 34A). Upon palpable tumour detection, mice were randomised according to the tumour volume into four treatment groups receiving either vehicle, BSO, Auranofin or combo for two consecutive weeks and toxicity was monitored by weighing (Figure 34B-D).

Notably, only combo treatment achieved a significant anti-tumour response, whereas both single treatments slowed early tumour growth, this trend was reversed in later assessments, implying that NE/non-NE plasticity under single arm therapy might compensate for SCLC tumour growth *in vivo* (Figure 34E). Indeed, immunohistochemical ASCL1 stainings of tumours after therapy that were manually quantified by H score quantification as described in 4.2.10.3^{220,268} revealed that ASCL1 histology scores of vehicle and combo-treated tumours were comparable in bigger and smaller tumours, respectively (Figure 34F). Unlike BSO-treated tumours, which only showed a trend toward enrichment of ASCL1⁺ cells, Auranofin-treated tumours had a considerably lower ASCL1 score (Figure 34G).

As a result, only combined treatment can effectively overcome non-NE/NE plasticity in heterogeneous SCLC under single drug treatment, resulting in a considerable anti-tumour effect. Since we found SCLC NE subtypes to be addicted to mutually exclusive antioxidant pathways, SCLC might be a particularly vulnerable entity for this combination treatment strategy.

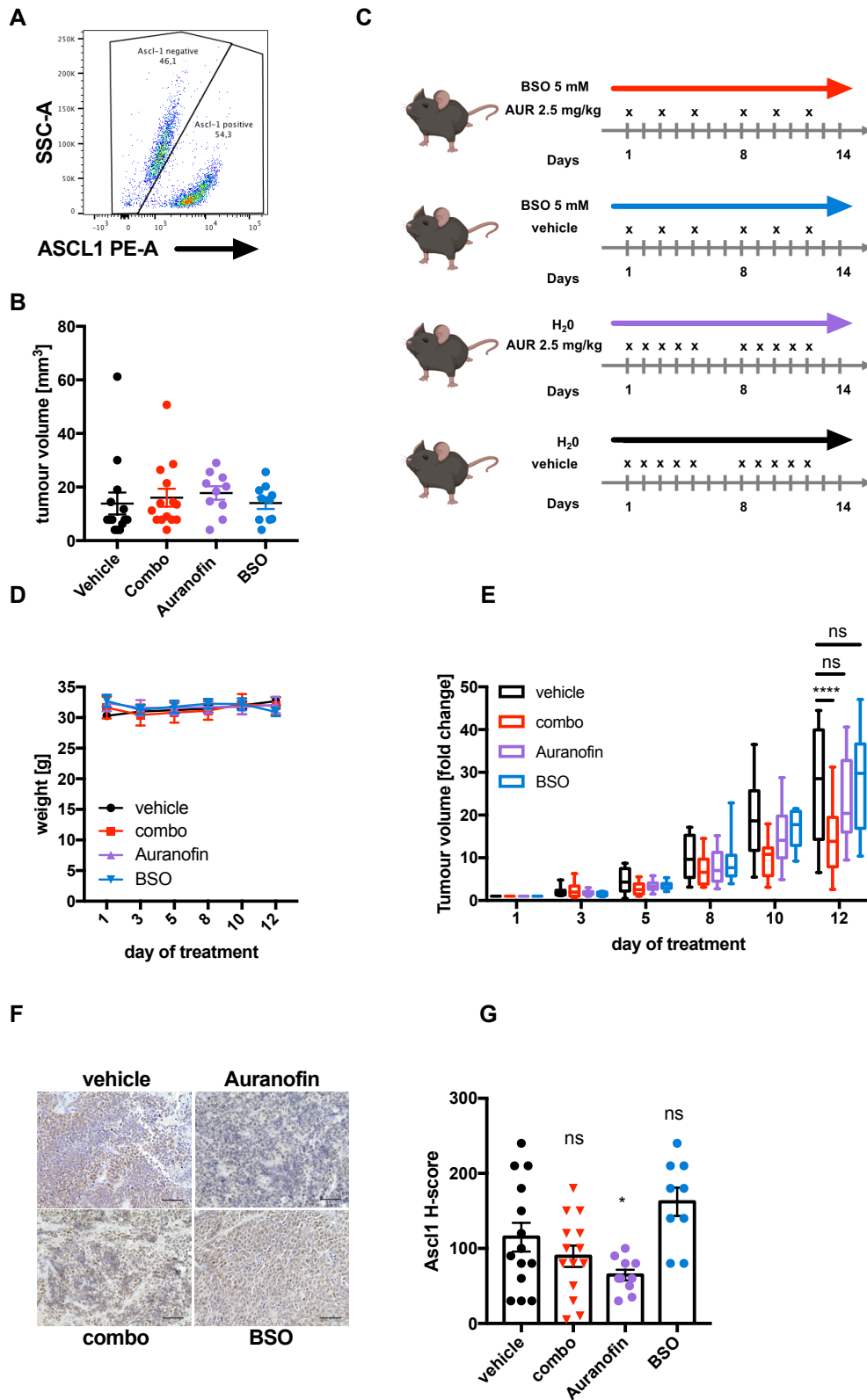


Figure 34 Combined ferroptosis induction and TRX pathway inhibition demonstrates broad anti-tumour activity murine in a SCLC allograft model for subtype heterogeneity *in vivo*.

A 181.5 stickers and floaters were mixed 50:50 and percentage of ASCL1+ cells was validated by flow cytometry before subcutaneous injection. **B** 8-weeks old male nude mice were injected with 1.5×10^6 RP181.5 mixed sticker/floater cells as shown in (Figure 34A) into flanks. Upon detection of palpable tumours, mice were randomised into four different treatment groups as indicated (A) and treated as

described in B for two consecutive weeks. **C** Scheme of different treatment groups. **D** Mouse weights were monitored during treatment. **E** 8-weeks old male nude mice were injected with 50:50 mixed 181.5 stickers and floaters (B) at a total of 1.5×10^6 cells into both flanks. Once palpable, tumours were treated either with vehicle (n=14), Auranofin [2.5 mg/kg] (n=10) 3x per week i.p., BSO [5 mM] (n=10) in the drinking water or the combination (combo) (n=14) for two consecutive weeks. Fold change of initial tumour size is shown. Boxplot center line, mean; box limits, upper and lower quartile; whiskers min. to max. **F** Sections from paraffin-embedded tumours stained for ASCL1. Representative images are shown, scale bar=100 μm . **G** ASCL1 H-score was quantified, n(vehicle)=14, n(BSO)=9, n(Aura)=10, n(combo)=14. Significance was tested by two-tailed unpaired t-test (E, G), ****p<0.0001, * p<0.05, ns>0.05. H score analysis (H, G) was contributed by Prof. Dr. Silvia von Karstedt. Figure adapted from Bebbler et al., 2021, Nature Communications.

To further validate efficacy of combo treatment in an immune-competent autochthonous mouse model, an established GEMM for SCLC was used¹⁵¹. In these mice, SCLC develops as a consequence of Rb1 and Trp53 co-deletion (RP-mice) upon lung-specific inhalation of Adeno-Cre within 6 months (Figure 36A). Moreover, intratumoural heterogeneity is observed in SCLC tumours in this GEMM as they contain both ASCL1-high and ASCL1-low cells^{151,208}. Once a tumour with a mean volume of 15-30 mm³ was detected by MRI analysis, mice were randomised into two treatment groups and treated with vehicle or combo for two consecutive weeks (Figure 35B). During time of treatment, weights were assessed daily to monitor changes indicating toxicity (Figure 35C). Whereas, tumour growth in all vehicle control mice progressed, tumour growth in 4 out of 7 mice receiving combo treatment significantly regressed within two weeks monitored by MRI analysis while weights remained stable (Figure 35D, E).

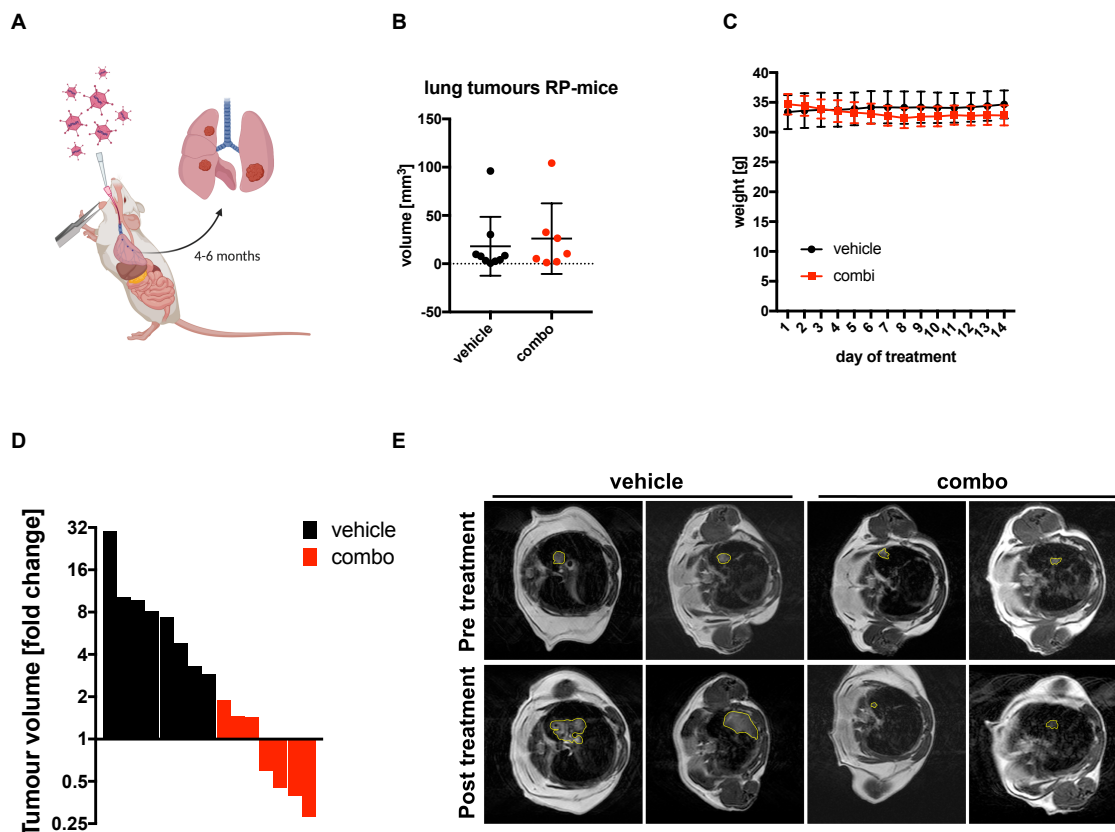


Figure 35 Combined ferroptosis induction and TRX pathway inhibition demonstrates broad anti-tumour activity in a SCLC GEMM *in vivo*.

A 8-12-week-old RP mice were inhaled intratracheally with 2.5×10^7 plaque-forming units (PFU) Adeno-Cre virus to initiate SCLC development. **B** Tumour bearing RP-mice were randomised into two treatment groups (vehicle, combo) upon tumour development. **C** Mouse weights were monitored during treatment. **D** Tumour-bearing RP-mice were treated either with vehicle ($n=8$) or combined BSO [5 mM] in the drinking water and Auranofin 3x per week i.p. [2.5 mg/kg] ($n=7$) for two consecutive weeks. Fold change in tumour volumes was determined by quantifying initial tumour volume from MRI scans as compared to tumour volume at the end of the treatment cycle using Horos software. **E** Representative MRI images pre and post treatment of mice as in (D). Scheme was drawn with fully licensed Biorender.com. Figure adapted from Bebbler et al., 2021, Nature Communications.²⁶⁹

2.9 Combined inhibition of GCL and TXNRD1 kills chemo-naive and relapse SCLC CDXs *ex vivo*

Since CTCs and CTC-derived xenotransplants (CDXs) from SCLC patients have proven to be a reliable tool for accurately predicting patient response to chemotherapy^{160,270} CDXs from a treatment-naive and a post-chemotherapy relapse SCLC patient were used to investigate a potential response to combo therapy in this human SCLC patient model system (Figure 36A, B).

In line with both CDX lines expressing the NE marker ASCL1, they were sensitive to Auranofin treatment and combo treatment but not BSO-induced ferroptosis. Tested peripheral blood monocytes (PBMCs) though were relatively resistant to stimulation with BSO, Auranofin and the combination (Figure 36C) confirming prior data on resistance to erastin-induced ferroptosis in PBCMs²⁷¹ and suggesting potentially low levels of toxicity. Importantly, combo treatment induced similar efficacy in chemotherapy-naïve and relapse CDXs (Figure 36C) indicating that response to combo treatment is not influenced by prior treatments or relapse state.

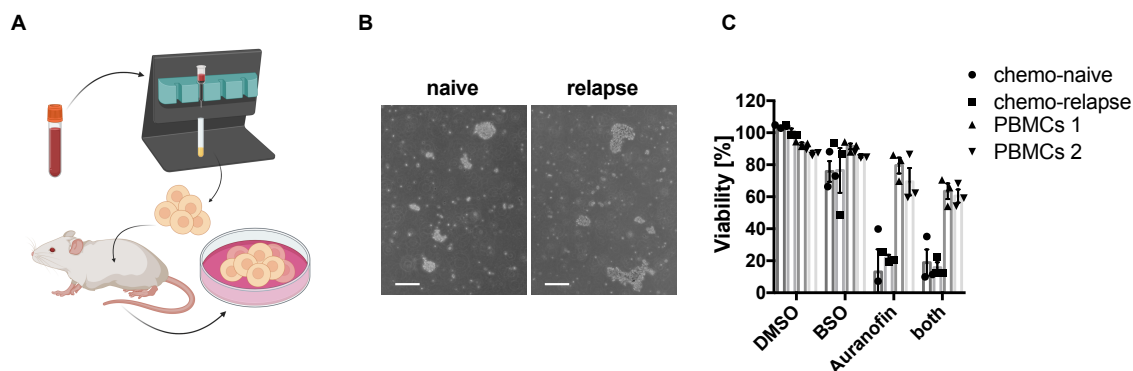


Figure 36 Combined inhibition of GCL and TXNRD1 kills chemo-naive and relapse SCLC CDXs ex vivo.

A Isolation scheme of human CDXs. **B** Cellular morphology of human CDXs, scale bar=400 μm. **C** Two CDXs or two healthy donor PBMCs were treated with DMSO, BSO [PBMCs, 500 μM; CDXs, 50 μM], Auranofin [250 nM] or BSO [PBMCs, 500 μM; CDXs, 50 μM] /Auranofin [250 nM] for 24 h, cell viability was quantified by Cell Titer Blue (CDXs) or flow cytometric quantification of propidium iodide (PI)-negative cells (PBMCs). Scheme was drawn with fully licensed Biorender.com. Figure adapted from Bebbler et al., 2021, Nature Communications.

2.10 Low expression of GPX4 and TXNRD1 is a marker for improved outcome in SCLC patients

To determine whether expression of genes crucial for protection from ferroptosis (*GPX4*) or cell death induced by TRX-pathway inhibition (*TXNRD1*) can serve as a prognostic marker in SCLC patients, overall survival data of patients who had undergone surgical resection¹⁸³ was analysed. Strikingly, low *GPX4* as well as low *TXNRD1* expression, independently correlated with improved overall patient survival (Figure 37A, B). Furthermore, when genetically mimicking the tested combination treatment, by analysing combined low expression of both *GPX4* and *TXNRD1*, a small group of SCLC patients was identified with drastically improved median survival time of 43.5 months as compared to 16 months median survival in patients with high *GPX4* and *TXNRD1* expression (Figure 37C). The expression of *TXNRD1* and *GPX4* in these patients did not correlate with

chemotherapy or radiation treatment these patients received post-surgery and diagnosed stage IV patients were excluded from the analysis to avoid survival bias originating from advanced tumour stage at diagnosis and stage III patients were equally present in both groups (n=4 in high/high; n=3 in low/low)¹⁸³.

To test whether, the prognostic use of these markers was unique to SCLC patients, survival data of LUAD patients were analysed but did not significantly segregate by low *GPX4*, *TXNRD1* or combined *GPX4* and *TXNRD1* expression (Figure 37D-F). This further suggests low combined *GPX4* and *TXNRD1* expression to be a specific prognostic marker of drastically improved overall survival in SCLC.

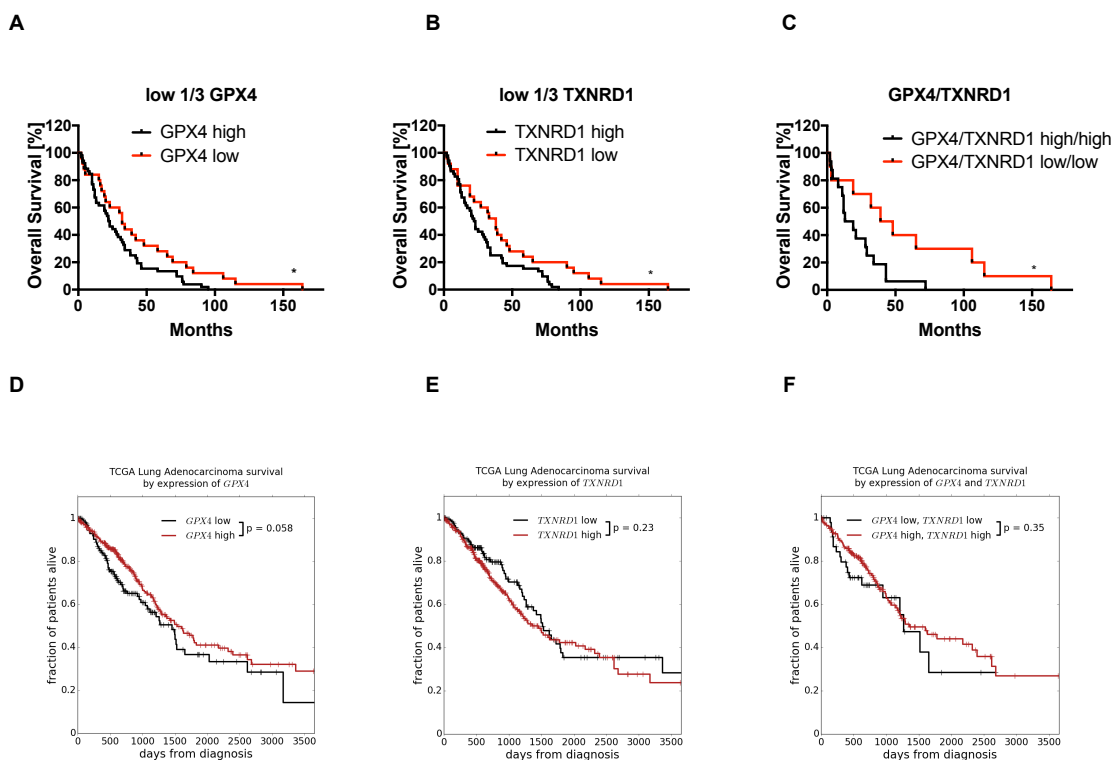


Figure 37 Low expression of *GPX4* and *TXNRD1* serves as prognostic marker set for improved survival in SCLC patients.

A Kaplan-Meier survival curves for SCLC patients (n=77)¹⁸³ containing low (low 1/3 n=25, median survival 33 months) or high (high 2/3 n=52, median survival 22.5 months) expression of *GPX4* mRNA. **B** As in (A) expression of *TXNRD1* mRNA was correlated using the same cut-off (low=1/3, median survival 38 months; high 2/3, median survival 22.5 months). **C** Kaplan-Meier survival curves for SCLC patients with combined low or high *GPX4* and *TXNRD1* mRNA expression (low/low n=10, median survival 43.5 months; high/high n=16, median survival 16 months). Two-sided log-rank (Mantel Cox) test (A-C), * p < 0.05. **D** Kaplan-Meier survival curves for LUAD patients from TCGA (n=503) containing low (low 1/3 n=167, median survival 48.5 months) or high (high 2/3 n=336, median survival 51 months) expression of *GPX4* mRNA. **E** as in D, expression of *TXNRD1* mRNA was correlated using the same cut-off (low=1/3, median survival 50.5 months; high 2/3, median survival 45.2 months). **F** Kaplan-Meier survival curves for LUAD patients from TCGA with combined low or high *GPX4* and *TXNRD1* mRNA expression (low/low n=49, median survival 42.2 months; high/high n=218, median

survival 45.2 months). Bioinformatic analysis data (D, E, F) were contributed by Dr. Filippo Beleggia. Figure adapted from Bebbber et al., 2021, Nature Communications.

In summary, data obtained in this study show for the first time that treatment-naïve SCLC exhibits signs of selection against extrinsic apoptosis and necroptosis and upregulates SLC7A11, a gene protecting from ferroptosis. While the ASCL1-low expressing non-NE SCLC subtype was identified to be exquisitely ferroptosis sensitive and to present with increased lipid metabolism and a ferroptosis-prone lipidome, we find the ASCL1-high expressing NE SCLC subtype to be resistant to ferroptosis but selectively vulnerable to TRX pathway inhibition. Thereby, this study identified that SCLC ASCL1-low and high expressing subtypes mechanistically segregate by ferroptosis sensitivity or resistance. Importantly, heterogeneous SCLC cultures selectively deplete non-NE or NE subpopulations upon single pathway targeting and demonstrate plasticity under treatment. Due to subtype heterogeneity and plasticity of SCLC, combining ferroptosis induction with TRX pathway inhibition demonstrates high therapeutic efficacy in SCLC xenografts, allografts, GEMMs, patient-derived CDXs and moreover serves as prognostic marker set in SCLC patients identifying a subset with drastically improved prognosis. These data propose that combining ferroptosis induction with TRX pathway inhibition may specifically tackle the problem of intratumoural NE/non-NE heterogeneity and plasticity in SCLC.

2.11 Data contribution

In this thesis, other researchers have contributed by generating/analysing some of the data presented in the results section. The contributions of external researchers (Emily Thomas (CECAD/von Karstedt laboratory), Zhiyi Chen (CECAD/von Karstedt laboratory), Jenny Stroh (CECAD/von Karstedt laboratory), Dr. Michaela Höhne (Biochemistry Department/Riemer laboratory), Dr. Armin Khonsari (Translational Genomics/Sos laboratory), Dr. Filippo Beleggia (CECAD/Reinhardt laboratory), Prof. Dr. Silvia von Karstedt) were clarified in the figure legends of the respective figure. Jenny Stroh contributed with experimental repeats and technical assistance.

3 Discussion

In this study, it has been identified for the first time, through systematic analysis of cell death pathway availabilities in treatment-naïve SCLC, that ASCL1-low expressing non-NE SCLC is vulnerable to ferroptosis through subtype-specific lipidome remodelling. ASCL1-high expressing NE SCLC, on the other hand, could be identified as ferroptosis resistant and instead acquires selective addiction to the TRX anti-oxidant pathway. In experimental settings of non-NE/NE intratumoural heterogeneity, non-NE or NE populations were selectively depleted by ferroptosis or TRX pathway inhibition, respectively. Moreover, subtype plasticity observed under single redox-pathway targeting was prevented by combined treatment of ferroptosis induction and TRX-pathway inhibition which targets established non-NE and NE tumours in xenografts, genetically engineered mouse models of SCLC, patient-derived cells and identifies a patient subset with drastically improved overall survival.

3.1 Cell death pathways in SCLC

SCLC is one of the most aggressive cancer entities and accounts for 15% of all lung cancer cases worldwide^{149,150}. Although up to 80% of SCLC patients initially respond to standard-of-care chemotherapy, most patients develop relapse within one year after treatment^{149,155}. In the last 30 years, only few new treatment methods were approved with minor effects on median survival resulting in very low overall five-year survival rate for SCLC of 5-7% and emphasising the need to identify novel vulnerabilities in the biology of SCLC^{149,175}.

Evasion of regulated cell death is one of the most important hallmarks of cancer⁶. SCLC is genetically defined by biallelic loss of the two tumour suppressor genes *TP53* and *RB1*^{153,183}, which are responsible for cell cycle control and can thereby induce cell cycle arrest or intrinsic apoptosis upon cellular stress such as DNA-damage²⁷². Loss of *TP53* and *RB1* suggests that the intrinsic apoptosis pathway might be disabled in SCLC tumours.

In addition, *CASP8*, the essential apical effector enzyme in the extrinsic apoptosis pathway, has been shown to be downregulated in SCLC through methylation likely making these cells resistant against apoptosis induction through the extrinsic and intrinsic pathway^{137,204}. Thereby, SCLC provides a highly interesting disease model system for the investigation of alternative, necrosis-like regulated cell death pathways.

A comprehensive analysis of cell death pathway availability in SCLC is lacking to date. In this study, through systematic characterisation of regulated cell death pathway

availability in RNA-seq data of human treatment-naïve SCLC patient tissue, downregulation of essential extrinsic apoptosis genes including *CASP8* could be confirmed. As in the absence of *CASP8* necroptosis is enabled, data were also analysed for expression of the crucial necroptosis genes. Strikingly, *RIPK3* and *MLKL* expression was downregulated in SCLC but not in normal lung tissue, incapacitating SCLC for extrinsic apoptosis as well as necroptosis. These data hint that SCLC undergoes stringent selection against PCD pathways already at diagnosis. Consistently, SCLC is known to present with high TMB^{165,166}, therefore, selection pressure may stem from CD8⁺ T cells trying to target tumour cells with high TMB^{173,229}.

Interestingly, the NE status of SCLC cells has recently been linked to the expression of immune gene signatures^{224,225}. Immune signature genes, particularly MHC I, are suppressed in NE SCLC cells via methylation which could be reversed by EZH2 inhibition²²⁵ indicating immune evasion, however MHC I proteins have been found to be re-expressed on non-NE chemoresistant relapsed SCLC cells.

Importantly, in this study, key components involved in preventing a newly discovered form of regulated cell death termed ferroptosis (*SLC7A11* and *GPX4*), were identified to be highly expressed in SCLC suggesting an increased dependency on preventing ferroptosis⁴⁷. Interestingly, *TP53*, which is mostly absent in SCLC, suppresses the expression of *SLC7A11*^{123,183}. Moreover, the tumour suppressor gene *RB1*, which is widely absent in SCLC¹⁸³, was associated with ferroptosis sensitivity as its knockdown in HCC sensitises cells to ferroptosis induction using sorafenib¹²⁸.

Ferroptosis is a recently described form of regulated cell death characterised by an iron-dependent accumulation of fatal lipid-peroxides resulting in destabilisation of the lipid bilayer and membrane rupture independent of caspases and the necrosome but rather induced upon inhibition of ferroptosis antagonists^{47,92,273}.

Importantly, we found SCLC cell lines to be more prone to ferroptosis induction than NSCLC cell lines, this observation correlated with increased expression of the ferroptosis regulator FSP1^{89,90} in NSCLC cell lines, suggesting them to be more protected from ferroptosis. Together, this indicated a specific ferroptosis vulnerability in SCLC.

3.2 Ferroptosis sensitivity in ASCL1-low non-NE SCLC

To date, SCLC has been treated as a fairly uniform cancer entity with no targetable driver mutations and irrespective of subtypes. SCLC tumours predominantly consist of NE cells arising from PNECs marked by ASCL1 expression^{207,274}. However, SCLC tumours often present with inter- and intratumoural subtype heterogeneity characterised by expression

of the molecular markers ASCL1, NEUROD1, YAP1 and POU2F3^{208,212,223,226,228}. In human SCLC patient tissue the SCLC-A subtype comprises ~70% of tumours accompanied by MYCL amplification or elevated expression and ~30% of SCLC-N (11%), SCLC-P (16%), SCLC-Y (2%) accompanied by MYC amplification or overexpression²¹². This tumour heterogeneity is further promoted by standard-of-care chemotherapy in SCLC²²⁸ highlighting clinical importance of elucidating subtype biology. Recent studies have suggested therapeutic vulnerabilities in different SCLC subtypes^{185,219,275–278}.

In our study, the ASCL1-low expressing mostly non-NE SCLC subtype was identified to be exquisitely sensitive to ferroptosis. Ferroptosis induction using small-molecule inhibitors (RSL3, erastin) and CRISPR-Cas9-mediated *GPX4* KO resulted in a lipid ROS and iron-dependent cell death in human and murine SCLC cell lines with low ASCL1 expression and elevated REST1 expression. We identified ferroptosis responders to be ASCL1-low/REST1-high expressing SCLC cells belonging to the SCLC-Y (RP181.5 sticker, RP246.7 sticker, BYC5.1 sticker, RP285.5, RP252.7), the SCLC-P (H526) or the SCLC-N subtype (H524, H82). While in the human SCLC cell lines YAP1 expression was less frequently observed than in murine SCLC cell lines, tested murine cell lines derived from the RP mouse model mostly represented the ASCL1-high expressing NE cells or YAP1-high expressing non-NE cells.

We identified NE-differentiation marked by ASCL1 expression to determine ferroptosis resistance. ASCL1-low expressing cells present with elevated levels of the important ferroptosis promoting enzymes ACSL4 and LPCAT3 on protein and mRNA level, which generate AA-CoA for lysophospholipid acylation and thereby the PUFA lipid target pool for lipid peroxidation. ACSL4 and LPCAT3 are essential ferroptosis enzymes, as KO experiments have demonstrated in several studies^{56,72,74,75}. Using mass spectrometry analysis, we also found that PUFA-containing ether lipid species were enriched in ASCL1-low SCLC while the majority of PUFA-containing DAG phospholipids were not elevated. Furthermore, expression of ether lipid synthesis enzymes, such as AGPS and AGPAT2 was elevated in non-NE SCLC. Intriguingly, it was recently identified, that ether-linked phospholipids synthesised in peroxisome and ER are specifically peroxidised during ferroptosis and thereby contribute to the lipid peroxide pool and drive ferroptosis (Zou et al., 2020). Moreover, we could show that suppression of ether lipid synthesis enzymes rendered non-NE cells more ferroptosis resistant. Together, these data suggested that a ferroptosis promoting function of ACSL4 and LPCAT3 in non-NE SCLC may stem from incorporation of AA-CoA into ether lysolipids. Interestingly, LPCAT3 has been shown to be able to use lyso-ether lipids as substrates for acylation by AA-CoA²⁷⁹ thereby promoting phospholipid recovery via the Lands cycle²⁸⁰. The Lands cycle is a conserved process remodelling phospholipids within cellular membranes by controlling the release

and incorporation of PUFAs such as AA ²⁸¹. Based on our findings, we hypothesise that upregulated ether lipid synthesis in non-NE SCLC feeds into the ferroptosis vulnerable membrane lipid pool generated and re-generated by ACSL4 and LPCAT3, resulting in a “ferroptosis-prone” membrane enriched for ether-linked PUFAs (Figure 38).

Interestingly, NE to non-NE subtype differentiation in SCLC is associated with chemotherapy resistance upon relapse ^{223,224}. Metabolic remodelling is one of the hallmarks of cancer and changes in lipid metabolism have been described to fuel cancer progression and proliferation ⁶. Moreover, ACSL4 has been reported to increase chemoresistance in breast cancer by regulating ATP binding cassette (ABC) transporter expression ²⁸² implying that acquired metabolic changes in NE to non-NE plasticity could play a role in chemotherapy resistance of non-NE SCLC. In SCLC, increased low-density lipoprotein receptor (LDLR) expression prominently involved in cholesterol import ²⁸³ has been shown to be correlated with poor prognosis in SCLC patients ²⁸⁴. LDLR expression is correlated with increased lipid metabolism and accumulation of lipid droplets (LDs) which is frequently observed combined with chemoresistance, hinting that metabolic changes in NE to non-NE differentiation may further fuel chemotherapy resistance ^{285–287}. However, the exact mechanism by which increased lipid metabolism might support chemoresistance in non-NE SCLC remains to be further elucidated. Based on our finding that non-NE SCLC is particularly susceptible to ferroptosis as a result of elevated ether lipid synthesis, ferroptosis induction could serve as alternative treatment strategy specifically targeting non-NE chemoresistant tumours upon relapse.

Although ferroptosis sensitivity did not correlate with chemotherapy sensitivity in our tested SCLC cell line panel, intriguingly, we could show that SCLC cells with acquired ferroptosis resistance in fact presented with decreased cell viability upon cisplatin treatment accompanied by a slight decrease in ACSL4 protein levels, further indicating a role of lipid metabolism in ferroptosis and possibly chemotherapy response in SCLC.

Interestingly, non-NE SCLC cells are characterised by a mesenchymal phenotype and expression profile ²⁰⁸. Of note, it was shown by Hangauer et al., that so called cancer persister cells with a high mesenchymal state, were selectively sensitised to the induction of ferroptosis ¹²⁷. Furthermore, a signature of EMT was predictive of ferroptosis sensitivity ¹²⁶. Moreover, remodelling of the plasma membrane during EMT leads to an increase in biosynthesis of PUFAs which are the main target of lipid peroxidation, the fatal event in the execution of ferroptosis ²⁸⁸. In line with this, we identified non-NE SCLC to be exquisitely ferroptosis sensitive and to express EMT signature genes such as *VIM*. Moreover, GSEA analysis revealed enrichment of an EMT gene set in human ferroptosis sensitive cells (Figure 41A). Furthermore, Notch signalling has repeatedly been shown to promote

expression of an EMT signature in various cancers²⁸⁹. In SCLC, non-NE cells present with increased Notch signalling via activation of REST1 and are slowly growing but at the same time also more chemoresistant and provide trophic support to NE SCLC cells²²³. In our experiments, expression of constitutively active cMyc T58A in RPM derived murine cell lines was sufficient to sensitise SCLC cells to ferroptosis. Notch pathway activation by cMyc might be responsible for this. Therefore, it is tempting to speculate whether Notch pathway activation and a consequent EMT could make these intrinsically chemotherapy resistant cells vulnerable to ferroptosis induction.

Recently, it was shown that expression of cMyc T58A expression drives subtype plasticity from SCLC-A subtype to SCLC-N to SCLC-Y marked by YAP1 expression via Notch activation²²⁰. Interestingly, YAP1 was recently shown to promote ferroptosis sensitivity of cells cultured at low confluence²⁵³. Overexpression of constitutively active YAP1 5SA further sensitised murine non-NE SCLC cells to ferroptosis induction in our experiments, suggesting a ferroptosis promoting role during non-NE differentiation. However, the percentage of SCLC-Y subtype in human samples is really low and whether YAP1 is a transcriptional driver in SCLC or a subtype-specific correlate has not been determined. The existence of a SCLC-Y subtype remains a controversial topic in the field^{217,218}.

It will be important to further investigate how Notch signalling and EMT might influence the lipidome of non-NE SCLC and its effect on chemotherapy response and potentially metastasis formation.

MYC signalling has also been described to promote GSH synthesis by transcriptional activation of the GCL²⁹⁰. In line with this, we identified ASCL1-low expressing SCLC to present with increased GSH levels. Moreover, GSEA analysis revealed enrichment of MYC target genes in ferroptosis sensitive human cell lines (Figure 41B, C). Therefore, MYC activation during NE to non-NE transdifferentiation might induce metabolic rewiring and increased dependency on the GSH pathway for antioxidant defence.

Interestingly, MYC expressing ASCL1-low expressing SCLC subtypes (SCLC-N, -Y, -P) have been identified to be vulnerable to arginine depletion²⁷⁵. Additionally, GSEA analysis revealed enrichment of arginine and proline metabolism genes in ferroptosis sensitive human cell lines (Figure 41D). Supplementation with L-Arginine induces GSH synthesis and activation of the antioxidant-transcription factor NRF2²⁹¹. Therefore, an interesting hypothesis to test would be whether depletion of arginine further sensitises ASCL1-low SCLC cells to ferroptotic cell death.

Hence, further studies should unravel the impact of MYC signalling in GSH synthesis and lipid metabolism in the non-NE SCLC subtype to better understand the biology of heterogenous tumours allowing for plasticity and treatment escape.

Furthermore, the mevalonate and lipid synthesis pathway controlled by mitogen-activated protein kinase 5/extracellular signal-regulated kinase 5 (MEK5/ERK5) was recently shown to be required for optimal survival and expansion of SCLC cell lines *in vitro* and *in vivo*²⁹². Of note, the mevalonate pathway plays a crucial role in the ferroptosis pathway being involved in the synthesis of coenzyme Q10, which is reduced to ubiquinol by the newly identified factor FSP1 and acts as a radical trapping agent preventing ferroptosis^{89,90}. Given our finding that ASCL1-low expressing non-NE SCLC presents with elevated ACSL4 expression and a ferroptosis-prone lipidome, it is tempting to speculate whether targeting of MEK5/ERK5 or the mevalonate pathway might sensitise non-NE SCLC to ferroptosis.

Moreover, the mevalonate pathway regulates selenoprotein synthesis^{293,294}. Amongst the small group of selenoproteins are the important redox-active proteins GPX4 and TXNRD1²⁹³. Hence, inhibiting MEK5-ERK5 kinase axis might hamper antioxidant defence and increase sensitivity to ROS-induced cell death and might thereby prevent optimal growth and expansion in SCLC irrespective of subtypes.

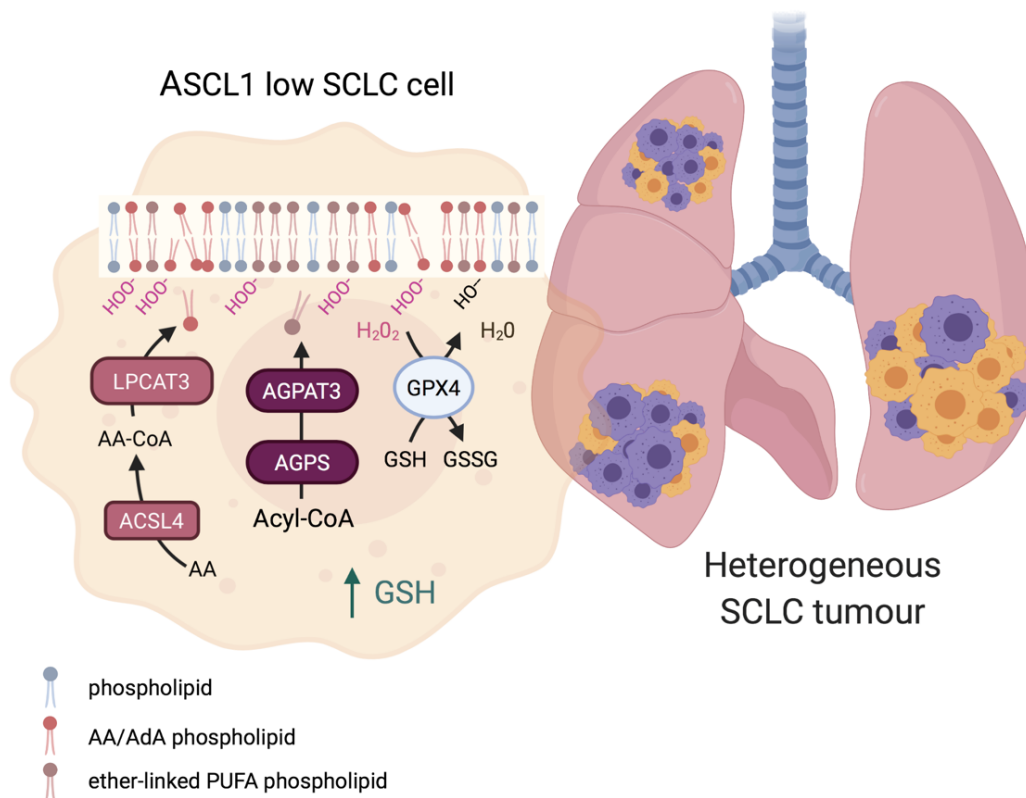


Figure 38 ASCL1-low non-NE SCLC is characterised by ferroptosis sensitivity due to a ferroptosis-prone lipidome.

Heterogenous SCLC tumours contain non-neuroendocrine (non-NE) and neuroendocrine (NE) cells. Cell membranes of ASCL1-low expressing non-NE cells are characterised by a high arachidonic acid (AA) and adrenic acid (AdA) phospholipid and ether-linked polyunsaturated fatty acid (PUFA) phospholipid content prone to be peroxidised during ferroptosis. Acyl-CoA synthetase long-chain family member 4 (ACSL4) and lysophosphatidylcholine acyltransferase 3 (LPCAT3) are crucial for the synthesis of AA and AdA containing phospholipids and alkylglycerone phosphate synthase (AGPS) and 1-acylglycerol-3-phosphate O-acyltransferase 3 (AGPAT3) catalyse ether phospholipid synthesis from Acyl-Coenzyme A (Acyl-CoA) and are highly expressed in non-NE SCLC cells. Peroxidation of membrane lipids is counteracted by glutathione peroxidase 4 (GPX4) reducing lipid peroxides (L-OOH) to their respective lipid alcohol (L-OH) while oxidising glutathione (GSH) to glutathione disulfide (GSSG) thereby preventing ferroptosis. The scheme was drawn using fully licensed Biorender.com. Figure adapted from Bebbler and von Karstedt 2021, Molecular and Cellular Oncology.

3.3 TRX pathway dependency in ASCL1-high NE SCLC

Of note, our study could show that NE SCLC did not present with elevated ether lipid synthesis and was resistant to ferroptosis. Instead, by performing redox shift assays and Western Blot analysis, we identified an increased activity of the TRX pathway for antioxidant defence in ASCL1-high expressing NE SCLC cells whereas they are independent on GSH. Accordingly, Auranofin, a thioredoxin reductase inhibitor, which is already clinically approved for the treatment of rheumatoid arthritis, was highly and selectively active against ASCL1-high NE SCLC cells. Consequently, we identified a novel treatment vulnerability of the NE ASCL1 positive SCLC subtype (Figure 39).

The fact that we identified both SCLC subtypes investigated to be vulnerable to two distinct types of anti-oxidant defence suggests that SCLC might experience elevated oxidative stress through elevated generation of ROS species. The lung is an organ specialised in handling oxygen. Within lungs, oxygen handling is further compartmentalised through alveoli at the end of bronchi which are essential for respiration. Hence, the lung specifically requires a sensitive network regulating the amount of oxygen uptake and sensing cellular oxygen load. This is regulated by PNECs, which are located at bronchial branch points either as single cells or in neuroepithelial bodies (NEBs)²⁹⁵. PNECs are the main cell-of-origin for SCLC²⁰⁷. Interestingly, under normoxia, at the molecular level, membranous NOX in PNECs generate ROS from extracellular O₂ and thereby keep K⁺ channels in an oxidised open state²⁹⁶. Upon hypoxia, ROS levels decrease and cysteine-residues of K⁺ channels sense the changed redox-state and switch to a closed conformation causing membrane depolarisation and activation of voltage-gated Ca²⁺ channels causing Ca²⁺ influx which in turn triggers exocytosis of neurotransmitter as serotonin and

neuropeptides such as SYP^{297,298}. Neurotransmitters released by PNECs are then sensed by nearby neurons which in turn induce an elevated respiratory reflex response to reload oxygen levels by increasing the breathing frequency^{299,300}. This inert function in regulating oxygen uptake indicates a high activity of redox-regulatory systems in PNECs and may hint why SCLC stemming from this cell type may be particularly dependent on antioxidant defence.

NOXs are one of the main sources for ROS production in cells next to OXPHOS³⁰¹. By oxidizing intracellular NADPH to NADP⁺ and the transfer of electrons through membranes they reduce molecular oxygen and generate the superoxide anion as a primary product and H₂O₂ as the end product³⁰¹.

High levels of ROS can cause cellular damage and oxidative stress causing cell death³⁰². Yet, balanced levels of ROS can serve as signalling molecules involved in regulation of processes, such as proliferation and differentiation^{303,304}. Several studies describe the role of ROS in neural development and neurogenesis, specifically the role of NOX2 in regulating ROS levels^{305,306}. Changes in ROS levels induce changes in the redox state of proteins and thereby control proliferation and differentiation by cell signalling and transcriptional regulation³⁰⁴. In early phases of neuronal differentiation oxidising species accumulate, but terminally differentiated neural cells maintain a reductive environment³⁰⁷.

ASCL1 expression does not only drive NE differentiation in SCLC cells but also has an important function in neuronal reprogramming^{308,309}. GSEA analysis revealed that gene sets for neuronal differentiation are enriched in human ferroptosis resistant SCLC cell lines (Figure 41E, F). During neuronal differentiation, cells have to overcome a period of enhanced sensitivity to ferroptosis upon ASCL1 expression to fully transdifferentiate into neurons³¹⁰. Moreover, Gascon et al. described that supplementation with antioxidants as well as overexpression of BCL-2 decreased ROS levels and promoted neuronal maturation³¹⁰. This indicates that cells must acquire ferroptosis resistance through selection and adaption rather than through direct ASCL1-mediated ferroptosis resistance to tolerate ASCL1 expression induced ferroptosis sensitivity. In support of this idea, ASCL1-high expressing SCLC has been described to present with increased levels of BCL-2^{200,311,312}. In our study, we identified that overexpression of ASCL1 alone in murine non-NE SCLC cells was neither sufficient to render cells more ferroptosis resistant nor to induce transition from sticker to floater cell state. Therefore, it is tempting to speculate whether combined overexpression of ASCL1 and BCL-2 in non-NE SCLC cells would induce full transdifferentiation into the SCLC-A subtype and render cells ferroptosis resistant.

Upon genetic deletion of GCLC, TXNRD1 can compensate anti-oxidant defence in cells¹¹⁹. Vice versa, TXNRD1 deficiency is compensated by upregulation of GSH synthesis pathway enzymes⁹⁶. In our study, we identified that acute overexpression of ASCL1 in non-NE SCLC cells does not render cells ferroptosis resistant, but all ferroptosis resistant cell lines present with high ASCL1 expression and decreased GSH levels. Moreover, acute ASCL1 expression caused decreased GCLC expression which resulted in lower GSH levels in these cells. We propose that this reduced cellular redox potential through decreased GSH levels imposed by ASCL1 expression may force NE SCLC into a selective dependency on the TRX antioxidant pathway, as the TRX system and the GSH-based system can compensate for each other^{96,119}.

We identified selective addiction to the TRX-pathway to be a mechanistic feature of the NE SCLC subtype that shows similarities to neuronal differentiation. TRX upregulation is frequently observed in different cancer entities^{313,314}. Hence, it will be interesting to determine whether this principle extends to other NE cancers.

Another source of high ROS levels in cancer cells is due to increased cell proliferation and increased OXPHOS, a process recently shown to promote ferroptosis³¹⁵. Interestingly, increased MYC expression in SCLC has been shown to elevate cellular OXPHOS and glycolytic metabolism, resulting in increased ROS generation³¹⁶. While MYC amplification is very uncommon in NSCLC (about 5%), it has been detected in 20% of SCLC cases¹⁶⁶. Increased MYC activity has repeatedly been described to correlate in ASCL1-low expressing SCLC subtypes^{219,275,317}. Recently, it has been shown that, MYC expression promotes differentiation of a non-NE phenotype in SCLC mouse models^{185,220}, providing an explanation for why non-NE SCLC experiences oxidative stress from ROS.

Importantly, we discovered that NE SCLC relies on the TRX pathway for anti-oxidant defence, implying that increased ROS is a concern in this subtype as well. Intriguingly, OXPHOS was shown to be upregulation during neuronal differentiation^{318,319}. Moreover, MYC and MYCN are decreased during neuronal differentiation indicating again their involvement in differentiation³¹⁹. Although NE differentiation in SCLC is not identical with neuronal differentiation, they share several transcriptional processes including those initiated by the neuronal transcription factor ASCL1. Together this shows that transcriptional programs elevating OXPHOS and ROS levels are found in both non-NE and NE SCLC subtypes.

Thus, it is of major interest to decipher the delicate role of ROS signalling and its underlying metabolic changes in non-NE/NE transdifferentiation causing heterogeneity in SCLC tumours.

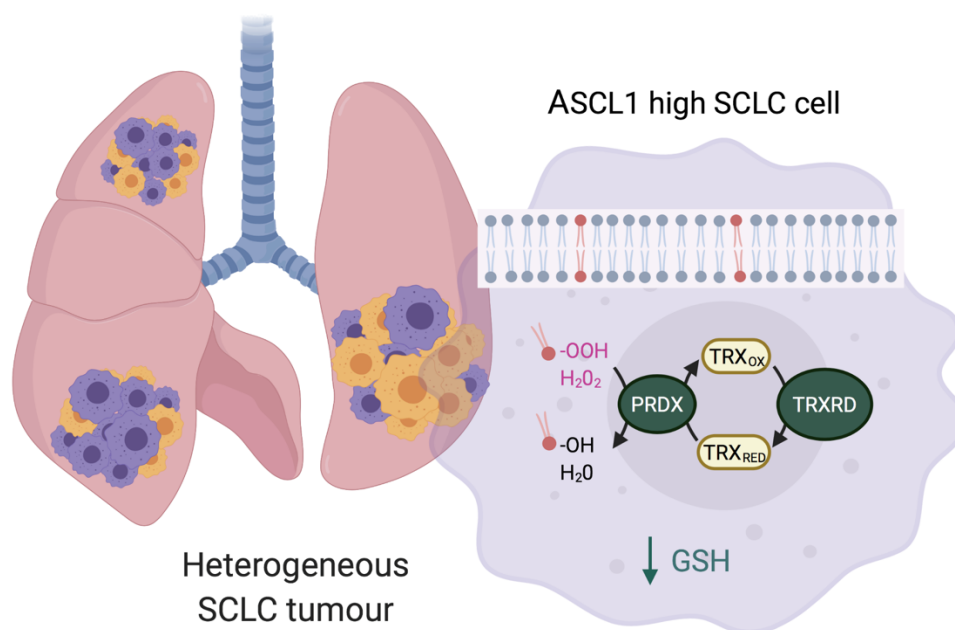


Figure 39 ASCL1-high NE SCLC is characterised by TRX pathway dependency.

NE SCLC cells present with a lipidome less prone to ferroptosis-induced lipid peroxidation and are highly dependent on the thioredoxin (TRX) redox pathway. Here, reactive oxygen (ROS) species such as hydrogen peroxide (H_2O_2) as well as lipid peroxides are reduced respectively by peroxiredoxins (PRDX) using TRX as a redox equivalent, which is restored by thioredoxin reductases (TRXRD). Inhibition of the thioredoxin pathways results in ROS-dependent cell death in NE SCLC. The scheme was drawn using fully licensed Biorender.com. Figure adapted from Bebbler and von Karstedt 2021, Molecular and Cellular Oncology.

3.4 Combined ferroptosis induction and TRX pathway inhibition targets SCLC subtype plasticity

Non-NE cells in SCLC tumours can arise from the same cell-of-origin as NE cells, implying a high degree of plasticity in SCLC tumours²⁰⁸. Importantly, we discovered that ASCL1-marked non-NE/NE subtype plasticity is driven by compensation between both the GSH- and TRX-based redox pathways, revealing their combined targeting as a plasticity-directed vulnerability. We also identified that under single redox pathway targeting, non-NE and NE SCLC subpopulations can transdifferentiate and so escape treatment, whereas dual targeting precludes this plasticity (Figure 40).

Our data indicate that non-NE/NE transdifferentiation involves ROS signalling at a certain level but both subtypes are sensitive to antioxidant pathway inhibition and subsequent excessive generation of ROS species. Our observations in isogenic cell lines shows that spontaneous transdifferentiation between NE subtypes in 2D cell culture is

promoted by an increased cell density. Several studies link increased cell density with a decrease in ROS levels^{320–322}. Moreover, several studies identified an increase in ferroptosis resistance *in vitro* in high cell density in cell culture (Wu et al., 2019; W.-H. Yang et al., 2019, own observation unpublished). Therefore, it is tempting to speculate that spontaneous transdifferentiation might be enabled by a short decrease in ROS levels but further studies are needed to further establish this theory.

While dual targeting of the TRX and GSH synthesis pathways has previously been identified as a synergistic killing strategy against a variety of cancers^{119,323}, more research is needed to determine what the nature of the synergy is in regard to plasticity and cellular redox compensation and which patient groups may benefit from this treatment in clinical trials.

Our study findings propose that while part of the synergy in tumours without plasticity may come from compensatory overexpression of the other redox pathway, exquisite treatment response in SCLC to combined GSH- and TRX-pathway targeting may stem from preventing treatment escape through transdifferentiation induced by higher ROS. Thereby, a proportion of the synergy might be caused by subpopulation coping with the applied oxidative stress by NE transdifferentiation and upregulating the respective compensatory redox-pathway rather than intracellular compensation mechanism.

Our data from isogenic non-NE/NE cell lines demonstrate that, following ASCL1-mediated reduction of GSH synthesis, SCLC cells may spontaneously switch from a GSH-dependent non-NE state to use of the TRX anti-oxidant pathway. This SCLC-specific trait of NE/non-NE plasticity could explain why the *in vivo* combination of BSO with Auranofin and Carboplatin has only shown limited efficacy in lung cancer without NE/non-NE plasticity²⁶⁷. Low expression of both GPX4 and TXNRD1 was found to be significantly associated with increased overall survival in SCLC patients, but not in LUAD patients, supporting this theory.

Importantly, the combined therapy of ferroptosis induction and targeting the thioredoxin pathway allows to target heterogenous SCLC tumours and subtype plasticity oppressing escape mechanisms. These findings reveal cell death pathway mining as a means to identify rational combination therapies for SCLC.

For future work, it will be important to identify in a clinical trial effectiveness of combined ferroptosis induction and TRX-pathway inhibition using BSO and Auranofin, respectively. Clinical trials using a combination of BSO and the cytostatic melphalan in different cancer patients including neuroblastoma patients show good tolerance and low toxicity^{324,325}.

Due to the fact, that Auranofin is clinically applied for the treatment of rheumatoid arthritis since the 1980s^{104,326} doses have been well defined in toxicity studies. Auranofin has recently gained attention in drug repurposing studies and is tested in several clinical trials for cancer³²⁷. Our data indicate that PBMCs are less sensitive to combined inhibition of the GSH- and TRX-based pathway as compared to SCLC patient derived CTCs but due to its high synergy it will be important to closely monitor toxicity in patients.

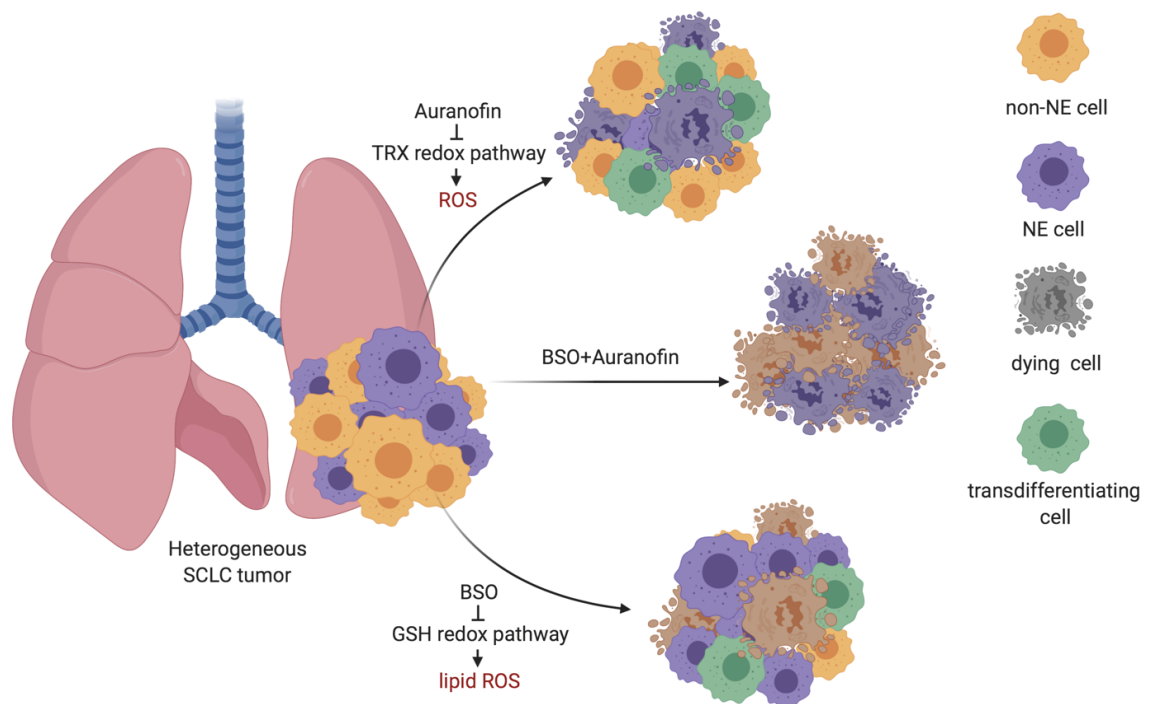


Figure 40 SCLC non-NE/NE subtypes segregate by lipid ROS/ROS vulnerability.

Heterogeneous SCLC tumours contain ASCL1-high expressing and REST1-low expressing NE cells and non-NE cells with an inverse expression pattern. Upon induction of ferroptosis by BSO, non-NE cells die due to excessive lipid ROS accumulation. NE cells in turn, undergo ROS-dependent cell death upon TRX pathway inhibition. Surviving cellular fractions in both single treatment arms can transdifferentiate under treatment thereby escaping therapy. Dual targeting prevents selection and plasticity in SCLC. NE, neuroendocrine, ROS, reactive oxygen species, GSH, glutathione, TRX, thioredoxin. The scheme was drawn using fully licensed Biorender.com. Figure taken from Bebbler et al., 2021, Nature communications.

3.5 Concluding remarks

In conclusion, we identified that treatment-naïve SCLC exhibits signs of selection against extrinsic apoptosis and necroptosis and upregulates SLC7A11 for ferroptosis protection. We identify the ASCL1-low expressing non-NE SCLC subtype to be exquisitely ferroptosis sensitive and present with high ACSL4 expression and a ferroptosis-prone lipidome. On the other hand, we find the ASCL1-high expressing NE SCLC to be resistant to

ferroptosis, but dependent on the TRX pathway to compensate for low cellular GSH levels. Importantly, we identify that SCLC NE subtypes are defined by alternate redox pathway usage and targeting of heterogeneous population with single pathway targeting treatment results in depletion of only subpopulations and cells exhibit subtype plasticity.

Our study could show that NE subtypes in SCLC present with differences in metabolism likely to fuel plasticity and subsequently heterogeneity in SCLC tumours, a circumstance which is further enhanced by currently approved chemotherapy and immunotherapy and complicates treatment in this cancer entity. Combined ferroptosis induction and TRX-pathway inhibition prevents this adaptable redox pathway plasticity defined by NE differentiation in SCLC, and results in synergistic killing in SCLC xenografts, GEMMs, patient-derived SCLC CDXs. Moreover, combined low expression of GPX4 and TXNRD1 identifies a unique SCLC patient subset with improved prognosis. In our study, we identified new insights into the biology of SCLC NE subtype heterogeneity and plasticity allowing for more informed treatment approaches that consider the availability of selective cell death pathways in SCLC NE subtypes and also enable patient stratification. Therefore, we propose that targeting redox pathway plasticity may represent a novel therapeutic vulnerability in SCLC targeting heterogeneity and plasticity, which, due to its inherent quality of being a caspase-independent cell death, should be available in chemotherapy-naïve and -relapsed SCLC, irrespective of prior selection against other regulated cell death pathways.

4 Material and Methods

4.1 Materials used in this study

Reagents

Isoleucine zipper-(iz) TRAIL was kindly provided by Prof. Dr. Henning Walczak and TNF was kindly provided by Prof. Dr. Manolis Pasparakis. Lipid standards (made by Avanti Polar lipids) were purchased from Sigma.

Table 4-1 Reagents used in this study

Name	Company	Catalogue #
AACOCF3	Tocris Bioscience	1462/5
Auranofin	Cayman Chemicals	Cay15316-25
Birinapant	Bertin Pharma	19699.1 mg
BODIPY C11	Invitrogen	D3861
BSO	Sigma	B2515-5G
Calcein-AM	Abcam	ab141420
Cisplatin	Merck	232120-50MG
D9	Sigma	5329100001
DFO	TargetMol	T1637.10 mg
Dharmafect I	Dharmacon	T-2001-01
Doxycycline	VWR	J63805.06
DRAQ7	Biologend	424001
erastin	Biomol	cay17754-5
Etoposide	Merck	341205-25MG
Ferostatin-1	Sigma	SML0583-5MG
H2DCFDA	Invitrogen	D399
ISOFLURAN (Forene 100% (v/v))	Baxter AG	103058
Ketaset	ZOETIS	116810
MCB	Sigma	69899-5MG
NAC	BIOTREND Chemicals AG	A9165-5G
Necrostatin-1s	Abcam	ab221984
Polybrene	Merck	TR-1003-G
Proteinase K	VWR	1245680100
Puromycin	Sigma	P8833-10MG
PX-12	Hözel	S7947-10

Rompun	Provet AG	QN05CM92
RSL3	Selleckchem	S8155
SYBR safe	Thermo Fisher	S33102
zVad-FMK	Enzo	BML-P416-0001

Table 4-2 Chemicals used in this study

Name	Company	Catalogue #
Acrylamide	Roth	A124.2
Agarose	Roth	3810.2
Ammonium persulfate	Sigma	431532
CaCl ₂	Roth	A119.1
DTT	VWR	441496P
EDTA	VWR	1,084,520,250
Ethanol	VWR	20,821,330
HEPES	Roth	HN78.2
Isopropanol	Roth	CP41.3
Potassium chloride EMSURE®	VWR	1,049,361,000
KH ₂ PO ₄	VWR	1,048,730,250
MgCl ₂	Sigma	M8266-100G
MnCl ₂	Sigma	244589-50G
Na ₂ HPO ₄	VWR	1,065,861,000
NaCl	VWR	1,064,045,000
SDS	Sigma	L3771-100G
Tris	VWR	1083872500
Tris-HCl	VWR	648313-250
Triton x100	VWR	1,086,031,000
Tryptone	VWR	J859-500G
Tween 20	VWR	0777-1L
Yeast extract	VWR	J850-500G

4.2 Molecular biological techniques

4.2.1 Nucleic acid techniques

4.2.1.1 Preparation of Plasmid DNA

For isolation of plasmid DNA from *Escherichia coli* (*E. coli*), bacteria were cultured overnight in a shaking incubator at 37 °C and 150 RPM in 5 ml lysogeny broth (LB) medium

(1% tryptone, 0.5% yeast extract, 1% NaCl, pH 7) supplemented with appropriate antibiotics when required (50 µg/ml Ampicillin (Sigma, A0166-5G)).

Plasmid DNA was isolated using PureYield Plasmid Miniprep System (Promega, A1223) according to the manufacturer's instructions.

For purification of DNA at higher grade and yield, maxi preparations were performed with the help of PureYield Midiprep system (Promega, A2492). Therefore, 3 ml pre-cultured cells were added to 300 ml LB medium supplemented with the appropriate antibiotic in a 1000 ml Erlenmeyer flask. Cells were incubated overnight in a shaking incubator at 37 °C and 150 RPM. DNA isolation was then performed according to the protocol provided by the manufacturer.

4.2.1.2 Preparation of genomic DNA for genotyping

For genotyping analysis, genomic DNA was isolated from ear punch samples of mice. To dissolve the tissue, samples were incubated overnight in 200 µl tail lysis buffer (100 mM Tris-HCl pH 8.5, 5 mM EDTA, 200 mM NaCl, 0.2% SDS) and 2 µl freshly added Proteinase-K (Stock 10 mg/ml in H₂O) at 56 °C. The next day, 200 µl of isopropanol were added for DNA precipitation followed by centrifugation at 13,000 RPM for 1 min. Supernatant was discarded and DNA pellet was washed with 200 µl 75% ethanol. After centrifugation pellet was dried to remove ethanol and DNA was dissolved in 200 µl TE buffer (10 mM Tris-HCl, 1 mM EDTA).

Table 4-3 Primers used in genotyping

Name	Sequence	Annealing Temp.	Expected sizes
p53 1	CAC AAA AAC AGG TTA AAC CCA G	60.5	FL = 370 bp
p53 2	AGC ACA TAG GAG GCA GAG AC		WT = 288 bp
RB1 1	CTCATGGACTAGGTTAAGTTGTGG	65	FL = 201 bp
RB1 2	GCATTTAATTGTCCCCTAATCC		WT = 163 bp

4.2.1.3 Polymerase chain reaction (PCR)

To control genotype polymerase chain reaction (PCR) was performed using Red Taq DNA Polymerase Master Mix 2x (VWR, 733-2546). To perform PCR reaction T100 Thermal cycler (Biorad) was used. The melting temperature of oligonucleotides was adapted for each primer pair. For standard Red Taq polymerase PCR conditions are listed in **Table 4-4** and **Table 4-5**.

Table 4-4 Components used for PCR.

Component	Amount
2x Red Taq DNA Polymerase Master Mix	5 μ l
Forward primer	1 μ l
Reverse primer	1 μ l
DNA template	2 μ l
Nuclease-free water	ad 20 μ l

Table 4-5 PCR program for amplification of DNA fragments using Red Taq polymerase.

Step	Time [sec]	Temp. [°C]	Cycle
Initial denaturation	120	94	1
Denaturation	30	94	30-40
Annealing	30	Primer specific	
Elongation	30	72	
Final elongation	300	72	1

Duration of elongation was adapted to the size of the PCR product (20 sec/kb).

4.2.1.4 Detection and purification of nucleic acids by agarose gel electrophoresis

For purification of DNA fragments along with size determination of PCR products, samples were applied onto agarose gels for gel electrophoresis. Gels were produced by mixing agarose with 1x TAE buffer (40 mM Tris-Base, 19 mM Glacial acetic acid, 1 mM EDTA) and warmed using microwaves until a homogenous mixture formed and the agarose was completely dissolved. SYBR safe was added to each gel prior pouring. The specific length of single DNA fragments was identified due to a standard DNA marker (100bp DNA ladder, NEB, N3231S). DNA fragments smaller than 500 bp were analysed using 2% agarose gels while 1% gels were used for fragments larger than 500 bp. Gel pictures were recorded using ChemiDoc XRS+ Molecular Imager (BioRad).

4.2.1.4.1 RNA Isolation and cDNA synthesis

For isolation of total RNA from cells and tissue, the NucleoSpin RNA kit (Macherey-Nagel, 740955.250) was used according to the manufacturer's protocol. The isolated RNA was reverse transcribed into cDNA using the LunaScript RT SuperMix Kit (NEB, E3010L) following the protocol provided by the manufacturer.

4.2.1.4.2 Determination of nucleic acid concentration

To determine the concentration of nucleic acids, the Nanodrop 8000 spectrophotometer by Thermo Fisher Scientific was used in a range of 240 nm to 300 nm with absorption maxima of 260 nm for DNA and 280 nm for aromatic amino acid residues of proteins.

The purity of DNA and RNA is reported by the ratio of absorbance at 260 nm to 280 nm. A ratio of OD₂₆₀/OD₂₈₀ about 1.8 was considered as sufficiently purified DNA samples. A ratio of OD₂₆₀/OD₂₈₀ of 2 was considered as sufficiently purified RNA samples.

4.2.1.4.3 Quantitative real-time PCR analysis

For quantitative real-time PCR (qRT-PCR) analysis, the Power SYBR Green PCR Master Mix (Thermo Fisher, 4368702) was used according to the manufacturer's protocol. Here, Power SYBR Green PCR Master Mix (Thermo Fisher, 4368702) was mixed with nuclease-free water (NEB, B1500L), forward and reverse primers (Thermo Fisher) reconstituted in nuclease free water (NEB, B1500L) respectively (Table 2-3) and cDNA according to table 2-2. Real-time qPCR was performed in triplicates on the Quant Studio5 qRT PCR machine. Relative expression of gene transcripts was analysed via the 2- Δ CT method and are presented in dot plot graphs as mRNA expression values relative to the reference gene Glyceraldehyd-3-phosphat-Dehydrogenase (GAPDH)³²⁸.

Table-4-6 qPCR components.

Name	Amount (μ l)	Concentration	Final concentration in 10 μ l
cDNA	2	5 ng/ μ l	10 ng
Fw and rv primer mix	1	10 μ M	100 nM
H ₂ O	2		
Power SYBR Green PCR Master Mix	5	2x	1x

Table 4-7 Primer sequences used for qPCR analysis.

Primer	Sequence (5' > 3')	Species	Exon spanning	Source
Gapdh fw	CTCCCACCTCTCCACCTTCG	<i>M. musculus</i>	no	NCBI Primer Blast
Gapdh rv	GCCTCTCTTGCTCAGTGTC			
Agps fw	TACTGTTCGAGGGAGACCGT	<i>M. musculus</i>	yes	NCBI Primer Blast
Agps rv	CAGCAGCCAGACCACCAAAT			
Far1 fw	TAGTGGTCAACACGAGCCTTG	<i>M. musculus</i>	no	Harvard primer bank
Far1 rv	GGCTTACAGCAATCCAGTAATGA			
Lpcat3 fw	ACTGAAGCTAATTGGGCTGTGT	<i>M. musculus</i>	yes	NCBI Primer Blast
Lpcat3 rv	TCCAGCAATGAAGGGACACC			
Acs14 fw	CTTCCTCTTAAGGCCGGGAC	<i>M. musculus</i>	yes	NCBI Primer Blast
Acs14 rv	TGCCATAGCGTTTTTCTTAGATTT			

Agpat2 fw	CACCGTGGATAACATGAGCATC	<i>M. musculus</i>	yes	NCBI Primer Blast
Agpat2 rv	ATTGTCGTTGCGTGACCCT			
Agpat3 fw	AGGAAAACACCTGTCCACGG	<i>M. musculus</i>	yes	NCBI Primer Blast
Agpat3 rv	ACTGAGAACAGCCGTCCAAG			
Gnpat fw	ATGGACGTTCTAGCTCCTCC	<i>M. musculus</i>	no	Harvard primer bank
Gnpat rv	CGGGGTGTAGCACTTCATTG			
Agpat4 fw	ATGTCACCTGGTCTTCTGCTA	<i>M. musculus</i>	no	Harvard primer bank
Agpat4 rv	TTCGGGTCGGTGTAGATGGTA			

4.2.2 Cell culture techniques

Table 4-8 Cell lines used in this work.

Cell line	Organism	Tissue	Source
RP252.7	<i>M. musculus</i>	SCLC tumour	RP mouse 252
RP285.5	<i>M. musculus</i>	SCLC tumour	RP mouse 285
RP246.7	<i>M. musculus</i>	SCLC tumour	RP mouse 246
RP181.5	<i>M. musculus</i>	SCLC tumour	RP mouse 181
BYC5.1	<i>M. musculus</i>	SCLC tumour	RP mouse 5
MEF	<i>M. musculus</i>	Mouse embryonic tissue	
RPM70	<i>M. musculus</i>	SCLC tumour	RPM mouse 70
RPM71	<i>M. musculus</i>	SCLC tumour	RPM mouse 71
H82	<i>H. sapiens</i>	SCLC tumour	ATCC
COR-L88	<i>H. sapiens</i>	SCLC tumour	ATCC
H524	<i>H. sapiens</i>	SCLC tumour	ATCC
H889	<i>H. sapiens</i>	SCLC tumour	ATCC
L303	<i>H. sapiens</i>	SCLC tumour	ATCC
H526	<i>H. sapiens</i>	SCLC tumour	ATCC
H2171	<i>H. sapiens</i>	SCLC tumour	ATCC
H1836	<i>H. sapiens</i>	SCLC tumour	ATCC
H1092	<i>H. sapiens</i>	SCLC tumour	ATCC
NCI-H460	<i>H. sapiens</i>	NSCLC tumour	ATCC
NCI-H727	<i>H. sapiens</i>	NSCLC tumour	ATCC
HEK-293T	<i>H. sapiens</i>	kidney	ATCC
HEK Phoenix	<i>H. sapiens</i>	kidney	ATCC

Table 4-9 Cell culture reagents.

Name	Company	Catalogue #
RPMI 1640 medium	Thermo Fisher	765656
Opti-MEM medium	Thermo Fisher	31985062
DMEM medium	Lifetechnologies	61965059
Fetal calf serum (FCS)	Sigma	10500064
Penicillium Streptomycin (PS)	Sigma	P4333-100ML
Trypsin-EDTA (1x)	Thermo Fisher	745065
Trypsin-EDTA (10x)	Thermo Fisher	15090046
PBS	Thermo Fisher	10010056
Reagent Reservoirs	VWR	613-1174
75 cm ² Cell Culture Flask	Greiner	658175
175 cm ² Cell Culture Flask	Greiner	660 160
6 Well Cell Culture Plate	Greiner	657160
24 Well Cell Culture Plate	Greiner	662160
96 Well Cell Culture Plate	Greiner	655180
5 mL Serological pipettes	3D Biotek	GSP010005
10 mL Serological pipettes	3D Biotek	GSP010010

Table 4-10 Antibiotics used in cell culture

Name	Company	Catalogue #
Blasticidin	AppliChem GmbH	A3784,0025
Puromycin	Sigma	P8833-10MG

4.2.2.1 Generation of mouse SCLC cell lines

Sticker and floater isogenic cell lines were isolated freshly from the RP mouse model. Whole solid lung tumours were obtained from mouse lungs which were inhaled with Adeno-Cre virus (see 4.2.9.1), washed twice in ice cold PBS, and cut into small pieces, followed by 20 min digestion with 10x trypsin (Thermo Fisher, 15090046) at 37 °C. To stop trypsin digestion 10 ml of RPMI medium supplemented with 10% fetal calf serum (FCS) and 1% Penicillin-Streptomycin (PS) was added. The next day, cells were washed in PBS and seeded again in RPMI on the same plate. Cells were continuously cultured keeping adherent and suspension cells together in RPMI medium and passaged until they formed a uniform SCLC cell line characterised by expressing non-NE or NE markers of SCLC cells.

4.2.2.2 Cell lines and culture conditions

Human SCLC cell lines (H82, COR-L88, H524, H889, L303, H526, H2171, H1836, H1092) were grown in suspension in RPMI (GIBCO) and were obtained from ATCC (https://www.lgcstandards-atcc.org/?geo_country=de). Murine SCLC cell lines (RP252.7, RP214, RP181.5, RP285.5, RP251, RP250.1, RP246.7) were previously derived from lung tumours of the RP GEMM for SCLC driven by loss of *Trp53* and *Rb1* by the laboratory of H. Christian Reinhardt as described in 4.2.2.1. All SCLC cell lines were grown in RPMI medium. Mouse embryonic fibroblasts (MEFs) were kindly provided by Prof. Dr. Manolis Pasparakis and kept in DMEM medium (GIBCO), human NSCLC cell lines NCI-H460 and NCI-H727 were kindly provided by Julian Downward and kept in DMEM medium (GIBCO). CDXs and PBMCs were grown in RPMI medium. All cells were kept at 37 °C with 5% CO₂ and all media were supplemented with 10% FCS and 1% PS. All cell lines were tested for mycoplasma at regular intervals (mycoplasma barcodes, Eurofins Genomics) and human SCLC have been validated by a cell line validation service provided by Eurofins Genomics.

4.2.2.3 Generation of human SCLC CDXs

CTCs were isolated from blood of two patients diagnosed with SCLC following previously described protocols^{160,270}. After tumour development in immunocompromised NSG mice, cells were dissociated, expanded and maintained in cell culture in HITES media. At least 90% of cells were confirmed to be tumour cells with NE marker expression (ASCL1, chromogranin A (CHGA), CD56 (also called NCAM) and SYP) as determined by RNA analysis and immunohistochemistry (IHC). Use of patient material was approved by the institutional review board of the University of Cologne following written informed consent. We have complied with all relevant ethical regulations pertaining to the use of human patient material.

4.2.2.4 PBMC isolation

PBMCs (kindly provided by Dr. Johannes Kühle) were isolated from buffy coats from two healthy donors under an existing ethics approval at the University Hospital Cologne (01-090) following written informed consent. We have complied with all relevant ethical regulations pertaining to the use of human patient material.

4.2.2.5 Plasmid construction for CRISPR sgRNAs

4.2.2.5.1 Phosphorylation and Annealing of oligonucleotide duplexes

The lyophilised oligonucleotides (Thermo Fisher, see Table 4-11) were dissolved in autoclaved, distilled water to a concentration of 100 µM and 1 µl of each oligonucleotide

was mixed with 1 μ l 10x T4 ligation buffer (NEB), 0.5 μ l (5 units) of T4 PNK (NEB) and 6.5 μ l distilled water in a 200 μ l centrifuge tube. The oligonucleotide mixture was incubated for 30 minutes at 37 °C, followed by an incubation for 5 minutes at 95 °C and then slowly cooled (5 °C/min) down to room temperature.

Table 4-11 CRISPR gRNA sequences.

Name	Sequence	CRISPR design tool
Gpx4_sg1_F	CACCG GACGATGCACACGAAACCCC	CRISPick (Broad institute)
Gpx4_sg1_R	AAAC GGGGTTTCGTGTGCATCGTCC	CRISPick (Broad institute)
Gpx4_sg2_F	CACCG ACGATGCACACGAAACCCCT	CRISPick (Broad institute)
Gpx4_sg2_R	AAAC AGGGGTTTCGTGTGCATCGT C	CRISPick (Broad institute)
Gpx4_sg3_F	CACCG CGTGTGCATCGTCACCAACG	CRISPick (Broad institute)
Gpx4_sg3_R	AAAC CGTTGGTGACGATGCACACG C	CRISPick (Broad institute)

4.2.2.5.2 Backbone digest and ligation of DNA (Golden Gate reaction) for sgRNA

For cloning of sgRNAs restriction digest of the plasmid backbone and ligation was performed in one reaction according to the Golden Gate cloning method^{329,330}.

Table-4-12 Components used for Golden Gate reaction

Component	Amount [μ L]
2X quick ligase buffer (NEB)	12.5
BSA [20 mg/ml] (NEB)	0.125
Restriction enzyme	1
Quick ligase (NEB)	0.125
Diluted oligonucleotides annealing (1:10)	1
Backbone Vector [25 ng/ μ l]	1
Distilled water	9.25

4.2.2.5.3 Sanger sequencing

DNA Sanger sequencing was carried out by the sequencing service group of GATCBI-OTEC AG.

4.2.2.5.4 Preparation of chemo competent *E. coli*

For preparation of chemo competent cells, first, bacteria were streak on a LB agar plate without antibiotics and let it grow over night at 37°C. The next day, one single clone was

picked and grown overnight in 5 mL SOB medium (2% Tryptone, 0.5% yeast extract, 0.05% NaCl, 250 μ M KCl, pH to 7.0, freshly add 25 mM MgCl₂) at 37 °C and 150 RPM. Next days, 240 ml of SOB medium were inoculated with 1 ml overnight culture and grown at 18 °C until OD₆₀₀ of 0.6 was reached. Culture was cooled for 10 min on ice, centrifuged at 3,000 RPM for 10 min at 4 °C and pellet was resuspended in 10 ml cold transformation buffer (10 mM PIPES, 15 mM CaCl₂, 250 mM KCl, pH 6.7, 55 mM MnCl₂). After adding 7% DMSO bacteria were aliquoted in 100 μ l into 1.5 ml tubes and stored at -80 °C.

4.2.2.5.5 Transformation of *E. coli*

Transformation of *E. coli* DH5 α (F⁻ ϕ 80lacZ Δ M15 Δ (lacZYA-argF)U169 recA1 endA1 hsdR17(rK⁻, mK⁺) phoA supE44 λ ⁻ thi-1 gyrA96 relA1) cells was performed using pre-made chemically competent cells. Stocks of chemically competent cells were stored at -80 °C. After thawing cells on ice, 1 μ l plasmid DNA was added to 50 μ l cells. The suspension was incubated for 5 minutes on ice, the transformed cells were plated onto pre-warmed LB agar plates containing ampicillin (100 μ g/ml) and incubated overnight at 37 °C.

4.2.2.6 Production of viral vectors

4.2.2.6.1 Production of lentiviral particles in HEK293T cells

For stable transduction of cells, viral particles were produced. For virus production, HEK293T cells were transfected using the CaCl₂ method³³¹. HEK293T cells were plated one day prior transfection to achieve a confluence of 70-80% at the day of transfection. Lentiviral particles were produced using the following packaging plasmids of the third generation pCMV-VSV-G (#8454) from Bob Weinberg, and pRSV-Rev (#12253) and pMDLg/pRRE (#12251) by Didier Trono (Stewart, 2003). As transfer for CRISPR mediated KO as transfer plasmid lentiGuide-Puro (#52963) was used carrying the sgRNA sequence. For CRISPR-Cas system mediated KO of genes first stably Cas9-expressing cells were produced using the second-generation packaging plasmids pSPAX2 (#12260) and pMD2.G (#12259) in combination with the lentiCas9-Blast (#52962) plasmid for the expression of Cas9.

For transfection of a 10 cm cell dish, 10 μ g of the transfer plasmid and 5 μ g of each lentiviral packaging plasmid were prepared together with 400 μ l of 250 mM CaCl₂. Under constant vortex 400 μ l of 2x HEBS buffer was added in drops to enable the formation of fine calcium-phosphate-DNA co-precipitate. The transfection mix was then added drop-wise under constant circular movement to the cell dish. Six hours post transfection cell culture medium was replaced with RPMI supplemented with 20% FCS and 1% P/S. The

following three days virus-containing supernatant was harvested in the morning and centrifuged at 300 g for 5 min in a 50 ml centrifuge tube and filtered using a 0.45 µm sterile syringe filter to remove residual HEK293T cells.

4.2.2.6.2 Production of retroviral particles in HEK Phoenix Eco cells

Retroviral particles were produced using the second generation retrovirus producer HEK Phoenix Eco cells (Dull et al., 1998). HEK Phoenix cells were plated one day prior in 10 cm cell culture dish at a confluence of 70-80% at the day of transfection. For transfection of a 10 cm dish, 10 µg of pBABE empty vector or pBABE YAP 5SA-YFP (kindly provided by Dr. Erik Sahai) were prepared in 400 µl 250 mM CaCl₂. For the formation of calcium-phosphate-DNA co-precipitate, the 400 µl of 2x HEBS buffer was added drop by drop to the CaCl₂-DNA mixture under constant vortex. The mixture was then added drop-wise to the cells. After 8 hours transfection, cell culture medium was replaced with RPMI with 20% FCS and 1% P/S. The following three days virus containing supernatant was harvested and filtered with 0.45 µm sterile syringe filter.

Table 4-13 Plasmids

Gene name	Selection resistance	Identifier
pBABE empty vector	Puromycin	#1764
pBABE YAP 5SA-YFP	Puromycin	kindly provided by Dr. Erik Sahai
pCMV-VSV-G	-	#8454
pRSV-Rev	-	#12253
pMDLg/pRRE	-	#12251
lentiGuide-Puro	Puromycin	#52963
lentiCas9-Blast	Blasticidin	#52962
pSPAX2	-	#12260
pMD2.G	-	#12259
pCW-Cas9	Blasticidin	#50661

4.2.2.6.3 Transduction of target cells

Target cells were transduced using the sterile filtered virus-containing supernatant of transfected HEK293T or HEK phoenix cells. Therefore, cells were plated at a confluence of 30% and virus-containing supernatant was added on three consecutive days. To enhance transduction efficiency by dampening the repulsion of charges on cell surface and virions 8 µg/ml polybrene (Hexadimethrine bromide) was added to the virus suspension

Cells were selected for successful transduction using previously tested concentration (2.5-10 $\mu\text{g/ml}$) of puromycin (Sigma, P8833-10MG) or blasticidin (10 $\mu\text{g}/\mu\text{l}$) for 5 days.

4.2.2.6.4 Generation of inducible Ascl1 overexpressing cells

For stable transduction of cells, viral particles were produced in HEK293T cells as described in 4.2.2.6.1. As transfer plasmid containing the ASCL1 cDNA, pCW-Cas9 (#50661) from Eric Lander & David Sabatini, was used³³⁴. The Cas9 fragment was firstly replaced with ASCL1 cDNA. Target cells for transduction were plated at a confluence of 30% and virus-containing supernatant with 6 $\mu\text{g/ml}$ polybrene was added on three consecutive days.

4.2.2.7 Transfection of target cells

For siRNA mediated knockdowns, 200 μl Opti-MEM and 1.5 μl Dharmafect Reagent I (Dharmacon, T-2001-02) were mixed per single 6-well and incubated for 10 min at room temperature (RT). Subsequently, 2.2 μl small interfering (si) RNA (stock 20 mM) were added to 200 μl Opti-MEM mixture and incubated for 30 min at RT. 200 μl of the mixture were added to each well of a 6-well plate and cells were plated on top in 1 ml media. Knockdowns were incubated for 48–72 h, as indicated.

Table 4-14 siRNA sequences

Gene name	siRNA sequences	Source
Agpat2	CAGCCAGGUUCUACGCCAA, GGGUA-CACGCAACGACAAU, GCUUUGAGGUCAGCGGACA, CCGUG-GAUAACAUGAGCAU	ON-TARGETplus Smartpool
Agpat3	CUUCGUGGUGAGCGGGUUA, CCA-GAUGGGAAGACCGCAU, CUGAUGCGGUAUCCAAUUA, GAUAG-GAGUGACUGAGUA	ON-TARGETplus Smartpool
Gclc	GCGAUGAGGUGGAAUACAU, UAACAGACUUUGAGAACUC, UGGCAG-ACAAUGAGAUUUA, CCAUCUCCAU-UUAUAGAAA	ON-TARGETplus Smartpool
Txnrd2	GACAAAGGCGGGAAGGCGA, GGGAUGCAUCACAGUGCUA, GACUGGUUGCUGAGGCUAA, GGGAAUCCUCAACCUUAA	ON-TARGETplus Smartpool
Txnrd1	GCAUCAAGUUUAUAAGACA, GCGAUUAUUGGAGGAUAA,	ON-TARGETplus Smartpool

	CUAAGGAGGCAGCCCAAUA, GGACAG-CACAAUUGGAAUC	
Slc7a11	CAACGUUGAUGAUGGACUAT; GAUUUAUCUUCGAUACAAATT	Qiagen

4.2.3 Protein analysis techniques

4.2.3.1 Protein extraction from cultured cells

To enable the analysis the level of specific protein in different cell lines, cells were washed once with PBS and lysed in IP-lysis buffer (30 mM Tris-HCl, 120 mM NaCl, 2 mM EDTA, 2 mM KCl, 1% Triton-X-100, pH 7.4, Protease and Phosphatase inhibitor (Roche)) on ice or overnight at -20 °C. Lysed cells were collected using a cell scraper (Roth, EKX9.1) and centrifuged at 14,000 RPM for 20 minutes at 4 °C.

The supernatant containing the whole protein fraction was then transferred into a new reaction tube. Protein concentration was determined using the well-established ³³⁵ bicinchoninic acid (BCA) protein assay (Biorad, 774985) according to the manufacturer's instructions. The absorbance of each sample was measured at 750 nm with Multimode Plate Reader by Enspire.

Gel electrophoresis of proteins was performed using the Mini-PROTEAN® Tetra Cell System by Biorad. To resolve the proteins, sodium dodecyl sulfate polyacrylamide gel electrophoresis (SDS-PAGE) consisting of a stacking gel with a polyacrylamide percentage of 4% followed by a 10% separation gel (see table 2 18) were used. Equal amounts of protein were mixed to a final concentration of 1x reducing sample buffer (Thermo Fisher, NP0008) containing 200 mM dithiothreitol (DTT). Samples were heated to 90 °C for 10 minutes to denature proteins and loaded onto the gel. Proteins were separated via gel electrophoresis at 80 V for 15 minutes followed by 150 V for 2 hours in 1x Tris-Glycine SDS Running buffer (Biorad, 1610772).

Table 4-15 SDS Page composition

Components	10%	12.5%	4%
	Separating gel	Separating gel	Stacking gel
	Volume (ml) for 4 gels (30 ml total)		10 ml total
Distilled H2O	12.2	9.7	6
30% Acrylamide	10	12.5	1.35
1.5 M Tris, 0.4% SDS, pH 8.8	7.5	7.5	-
1.0 M Tris, 0.4% SDS, pH 6.8	-	-	2.5

10% (w/v) Ammonium persulfate	0.15	0.15	0.066
TEMED	0.015	0.015	0.001

4.2.3.2 Protein extraction from fresh frozen tissue

For protein isolation, 20-30 mg of fresh frozen tumour tissue were mixed in a peqlab vial with the adequate number of ceramic beads and 500 μ l IP-lysis buffer. For lysis, samples were homogenised for 2 x 30 sec using the Precellys 24-dual homogeniser (Peqlab). Samples were further processed as described before in 4.2.3.1.

4.2.3.3 Western Blot analysis

After separation of protein samples via gel electrophoresis, they were transferred to a 0.2 μ m nitrocellulose membranes using the Trans-Blot Turbo Transfer system (Bio-Rad, 1704270). Depending on acrylamide percentage, gels were transferred at 1.3 A, 25 V for 7 min (10% gel) or 12 min (12.5% gel). After protein transfer, membranes were blocked in PBS with 0.1% Tween 20 (PBS-T) with 5% (w/v) non-fat dried milk powder (ITW reagents, A0830) for at least 30 minutes. Subsequently, membranes were incubated with primary antibody (see **Table 4-16**) overnight at 4 °C. The next day, membranes were washed three times with PBS-T for 10 minutes, respectively. Afterwards they were incubated with secondary antibody conjugated with horse radish peroxidase (HRP) in 5% non-fat dried milk powder in PBST (see **Table 4-17**) for 1 h at RT. Another three washing steps for 10 minutes with PBS-T were performed and membranes were developed using chemiluminescent substrate Immobilon Luminata Classico (Millipore, WBLUC0500) or SuperSignal™ West Femto chemiluminescence substrate (Thermo Fisher, 34095) and X-ray films (VWR, PIER34089).

Table 4-16 Primary antibodies used for Western Blot analysis

Description	Supplier/Catalogue#	Dilution in 5% BSA in PBST
Anti-AcsI4	Santa Cruz Biotechnology, sc-271800	1:2,000
Anti-AGPAT2	Thermo Fisher, PA5-76010	1:2,000
Anti-AGPAT3	Thermo Fisher, PA5-101343	1:2,000
Anti-Ascl1	BD Pharmingen, 556604	1:1,000
Anti-Cas9	Cell signaling, 14697	1:1,000
Anti-CD71	Santa Cruz, sc-65882	1:2,000
Anti-cMyc	Abcam, ab32072	1:2,000
Anti-FSP1	previously described ⁹⁰ , kindly provided by M. Conrad	undiluted hybridoma supernatant

Anti-GAPDH	Cell signaling, 97166S	1:2,000
Anti-GCLC	Santa Cruz, sc-166345	1:1,000
Anti-Gpx4	Abcam, ab41787	1:2,000
Anti-NCAM	Invitrogen, PA5-79717	1:1,000
Anti-REST1	Abcam, ab21635	1:1,000
Anti-REST1	Thermo Fisher, BS-2590R	1:1,000
Anti- β -Actin	Sigma, A1978	1:10,000
Anti-Synaptophysin	Invitrogen, MA5-14532	1:1,000
Anti-Txn1	Cell signaling, 2429S	1:1,000
Anti-TXNIP	Cell signaling, 14715S	1:1,000
Anti-Txnrd1	Cell signaling, 15140S	1:1,000
Anti-Txnrd2	Cell signaling, 12029	1:1,000
Anti-Vimentin	Abcam, ab137321	1:1,000
Anti-xCT	Abcam, ab37185	1:2,000
Anti-YAP1	Cell signaling, 4912	1:1,000

Table 4-17 Secondary antibodies used for Western Blot analysis

Description	Supplier/Cat. #	Dilution in 5% milk powder in PBST
anti-mouse HRP	Biotium/20400	1:20,000
anti-rabbit HRP	Biotium/20402	1:20,000
anti-rat HRP	Sigma/A9037	1:20,000

4.2.4 Redox shift assays

1.5×10^6 cells (H82, RP181.5 floaters) and 1×10^6 cells (H2171, RP181.5 stickers) were seeded in 6-well plates and treated the next day for 0.5 or 6 h with 1 μ M Auranofin. Cells were then harvested, washed in PBS and lysed in 1 ml 8% (w/v) trichloroacetic acid (TCA) on ice and frozen at -20 °C. Samples were thawed and centrifuged for 15 min at 20,000 g at 4 °C. TCA supernatant was removed, pellets were centrifuged for 5 min at 20,000 g at 4 °C and residual TCA was removed. 20 μ l of alkylation buffer (6 M urea, 0.2 M Tris-HCl, pH 7.5, 0.2 M EDTA, 2% SDS, bromophenol blue) was added and samples were sonicated for 10 cycles at an amplitude of 60% to dissolve pellets (UP50H, Hielscher). For minimum and maximum samples, tris(2-carboxyethyl)phosphine (TCEP) was added (10 μ M final concentration) followed by incubation for 10 min at 50 °C. For the minimum shift sample, N-ethyl maleimide (NEM) was added (15 mM final concentration) and to all other samples, methyl-polyethylenglycol-maleimide (mmPEG24, 15 mM final concentration) was added. Samples were incubated for 1 h in the dark at RT, then

20 μ l of 2x Laemmli buffer was added. Samples were loaded on tris-tricine gels and run overnight at constant 130 V at 4 °C.

4.2.5 Quantification of oxidised glycerophospholipids via lipidomics

Mass spectrometry was conducted by the Lipidomics/Metabolomics Core Facility of CECAD led by Dr. Susanne Brodesser. Levels of oxidised PC and PE species were determined by Liquid Chromatography coupled to Electrospray Ionisation Tandem Mass Spectrometry (LC-ESI-MS/MS) using a procedure described in Doll et al. 2019⁹⁰ with several modifications: 2.5×10^6 cells were resuspended in 250 μ l of an ice-cold 2:5 (v/v) mixture of 100 μ M diethylenetriaminepentaacetic acid (DTPA) in PBS, pH 7.4, and 40 μ M butylated hydroxytoluene (BHT) in methanol. To 100 μ l of the cell suspension another 3.4 ml of the above-mentioned PBS/methanol mixture, 1.25 ml of ice-cold chloroform and internal standards (10 pmol 1,2-dimyristoyl-*sn*-glycero-3-phosphocholine (DMPC) and 10 pmol 1,2-dimyristoyl-*sn*-glycero-3-phosphoethanolamine (DMPE)) were added. The samples were vortexed for 1 min and incubated at -20 °C for 15 min. After adding 1.25 ml of chloroform and 1.25 ml of water, the mixture was vortexed vigorously for 30 sec and then centrifuged ($4,000 \times g$, 5 min, 4 °C) to separate phases. The lower (organic) phase was transferred to a new tube and dried under a stream of nitrogen. The residues were dissolved in 150 μ l of methanol and transferred to autoinjector vials. LC-MS/MS analysis was performed by injecting 20 μ l of sample onto a Core-Shell Kinetex C18 column (150 mm \times 2.1 mm ID, 2.6 μ m particle size, 100 Å pore size, Phenomenex) at 30 °C and with detection using a QTRAP 6500 triple quadrupole/linear ion trap mass spectrometer (SCIEX). The LC (Nexera X2 UHPLC System, Shimadzu) was operated at a flow rate of 200 μ l/min. The mobile phase system, gradient program and source- and compound-dependent parameters of the mass spectrometer were set as previously described⁹⁰. Oxidised PC and PE species and the internal standards were monitored in the negative ion mode using their specific Multiple Reaction Monitoring (MRM) transitions⁹⁰. The LC chromatogram peaks were integrated using the MultiQuant 3.0.2 software (SCIEX). Oxidised PC and PE species were quantified by normalising their peak areas to those of the internal standards. The normalised peak areas were related to the mean values of the floater cells + DMSO cell samples.

In the MRM analyses, specific precursor ions – here: molecular ions ($[M-H]^-$) of the different PE species - were selected in the first quadrupole (Q1). These PE species were fragmented in the second quadrupole (Q2), which serves as collision cell. Simultaneously, the third quadrupole (Q3) was set to let pass only a characteristic PE fragment ion. The advantage of MRM analyses is that only ions, which fit both, the selected precursor and the characteristic fragment ions, can reach the detector whereas all other

(lipid) species in the LC eluate are ignored. To enable the selective detection of only those PE species, which are acylated by oxidised fatty acids, and the differentiation of these oxidised from non-oxidised PE species (including plasmalogens), we chose the oxidised fatty acyl chains as characteristic fragment ions in Q3.

4.2.6 Quantification of Glycerophospholipid via lipidomics

Mass spectrometry was conducted by the Lipidomics/Metabolomics Core Facility of CECAD led by Dr. Susanne Brodesser. Glycerophospholipids (PC and PE, including ether-linked species) in cells were analysed by Nano-Electrospray Ionisation Tandem Mass Spectrometry (Nano-ESI-MS/MS) with direct infusion of the lipid extract (Shotgun Lipidomics): 3×10^6 cells were homogenised in 300 μ l of Milli-Q water using the Precellys 24 Homogenisator (Peqlab) at 6,500 RPM for 30 sec. The protein content of the homogenate was determined using BCA. To 30 μ l of the homogenate, 470 μ l of Milli-Q water, 1.875 ml of methanol/chloroform 2:1 (v/v) and internal standards (187 pmol PC 17:0-20:4 and 198 pmol PE 17:0-20:4, Avanti Polar Lipids) were added. Lipid extraction and Nano-ESI-MS/MS analysis were performed as previously described (Doll et al., 2019). Endogenous glycerophospholipids were quantified by referring their peak areas to those of the internal standards. The calculated glycerophospholipid amounts were normalised to the protein content of the cell homogenate.

4.2.7 Fluorescence activated Cell Sorting (FACS)

To quantify stainings using fluorescent probes in cells FACS analysis was used. Quantification was done using an LSR-FACS Fortessa (BD Bioscience) counting 5,000 cells per sample.

4.2.7.1 ASCL1-staining for Flow Cytometry

RP181.5 stickers or floaters (1×10^5 cells) were seeded in 12-well plates (Greiner, 665180) a day in advance and then treated with different compounds for 24 h. Cells were harvested, washed with PBS and stained for live/dead cells using the viability dye eFluor780 (eBioscience, 65-0865-14), 1:1,000, for 30 min at 4 °C. Cells were then washed twice with FACS buffer (PBS, 2% FCS) and cell pellets were resuspended in 200 μ l Fixation/Permeabilisation buffer (eBioscience, 00-5523-00) (overnight incubation at 4 °C). The next day, cells were washed with 1x Permeabilisation buffer (eBioscience, 00-5523-00) and incubated for 15 min in FACS buffer before adding the primary MASH-1 antibody (BD Biosciences, 556604), 1:250, for 30 min at 4 °C in 1x Permeabilisation buffer. After washing cells twice with 1x Permeabilisation buffer, pellets were resuspended in the secondary antibody (Cy3, Jackson Laboratories) 1:500 for 30 min at 4 °C

in 1x Permeabilisation buffer. Cells were again washed twice with 1x Permeabilisation buffer and resuspended in FACS buffer. Measurements were acquired using a BD LSR Fortessa flow cytometer and data were analysed with the FlowJo software. For sorting experiments cells were resuspended in PBS with 2% FCS and 25 mM Hepes and passed through a BD FACS sorter (Influx).

4.2.7.2 Lipid ROS quantification by BODIPY C11 staining

For lipid ROS quantification, 50,000 cells were seeded in 500 μ l respective medium in 24-well plates (Greiner, 662160). The next day, cells were treated with DMSO, 100 nM RSL3 or 100 nM RSL3/5 μ M Fer-1 for 5 h. During the last 30 minutes of incubation, BODIPY C11 was added at 5 μ M to each well. Cells were then washed, detached and fold increased green fluorescence over baseline (stained but untreated) was determined by flow cytometry (excitation 520 nm) counting 5,000 cells per sample.

4.2.7.3 General ROS quantification by H2DCFDA staining

To stain cells, cells were treated as for BODIPY C11 staining but instead H2DCFDA was added to wells during the last 30 minutes treatment incubation at 20 μ M/well. Cells were then washed and detached using trypsin. Fold increased green fluorescence over baseline (stained but untreated) was determined by flow cytometry (excitation 496 nm) counting 5,000 cells per sample.

4.2.7.4 Labile iron quantification by Calcein-AM staining

For quantification of labile iron in cells, cells were seeded one day in advance. The next day cells were washed three times with PBS to remove residual FCS containing free iron. Cells were incubated for 20 min with 500 nM Calcein-AM in PBS. Cells were detached using trypsin and washed. Fold increased green fluorescence over baseline (stained but untreated) was determined by flow cytometry (excitation 496 nm) counting 5,000 cells per sample.

4.2.7.5 Cellular GSH quantification

To determine relative levels of GSH in ferroptosis responder and non-responder cell lines, the thiol-reactive dye MCB was added to cells seeded a day in advance (50,000 cells per well in 24-well plates) at a concentration of 50 μ M for 30 minutes. Cells were then washed, detached and analysed by flow cytometry (405 nm excitation) counting 5,000 cells per sample. To quantify concentrations of cellular GSH and GSSG, the GSH/GSSG Glo Assay (Promega, V6611) was used according to the manufacturer's instructions using 75,000 (H82 and H2171) or 50,000 (RP) cells.

4.2.8 Cell viability and cell death assays

Cell viability was determined by different types of cell death assays monitoring metabolic activity of cells or cell membrane integrity by incorporation of intercalating agents into dsDNA.

4.2.8.1 Cell Titer Blue assay

Cell viability was determined by Cell Titer Blue assay (Promega, G8081) following the manufacturer's instructions. For this assay, cells were plated at 10,000 or 5,000 cells per 96-well in 100 μ l media. During this assay metabolic activity of cells is measured. Viable cells are converting the redox dye resazurin into fluorescent resorufin emitting at 590 nm.

4.2.8.2 IncuCyte cell imaging

Cells were plated in 96-well plates (Greiner, 655180) (5,000 for 72 h, 10,000 for 24 h) and stimulated with different drug combinations. Dead cells were stained by adding 100 nM DRAQ7 to all wells. Cells were imaged for 24 h every 2 or 4 h and 4 images per well on a 96-well plate were captured.

4.2.8.3 PI staining in FACS

For FACS analysis of dead cells, cells were trypsinised, washed and harvested by centrifugation for 5 min at 1,500 RPM. To quantify cell death by damaged cell membrane, the cell pellet was then resuspended in 400 μ l of PBS with 2% FCS and 1 μ g/ml propidium iodide (PI).

4.2.8.4 Clonogenic survival assay

Adherent murine SCLC cells were plated at 2,500 cells/24-well in 500 μ l medium a day in advance. The next day they were treated with DMSO, RSL3 or erastin with or without Fer-1 (5 μ M) for 24 h after which wells were washed with PBS and replenished with fresh media for incubation for another six days. On day seven, cells were washed with PBS, fixed and stained for 30 minutes using crystal violet solution (0.05% (w/v) crystal violet, 1% Formaldehyde, 1% methanol in PBS). After washing with H₂O, plates were dried and cell clones were quantified.

4.2.9 Mouse experiments

All animal procedures and experiments were conducted in accordance with an Institutional Animal Care and Use Committee (IACUC). All people involved in animal experiments received prior training and have passed the additionally required personal

licensing course (FELASA B). All animal experiments were approved by the local government authorities (Landesamt für Natur, Umwelt und Verbraucherschutz Nordrhein-Westfalen, Germany (LANUV), North-Rhine-Westphalia, Germany) and performed under license number 81-02.04.2017.A477.

Mice were maintained in a conventional animal facility in individually ventilated cages (IVC) in a specific pathogen free (SPF) mouse facility in the CECAD Research Center, University of Cologne. Mice were housed at 22-24°C, under a 12 hours (h) light/dark cycle, given acidified water and a regular chow diet (Teklad Global Rodent 2018, Harlan) *ad libitum*. For breeding, male and female mice were placed together at an age of 8 weeks minimum. Litters were marked with ear marks at minimum age of 2 weeks which were taken for genotyping at that time and litters were weaned at the age of 3 weeks.

4.2.9.1 Autochthonous SCLC Mouse Model

In this project, the well-established GEMM recapitulating SCLC harbours a Rb1flox/flox (Rb1fl/fl) allele in which exons 18 and 19 are flanked by loxP sites as well as a Trp53flox/flox (Trp53fl/fl) allele in which exons 2-10 are flanked by loxP sites (RP model) for Small Cell Lung Cancer was used (Kumar et al., 2015). In order to induce lung tumour formation, 8-12 weeks old mice were anaesthetised with Ketaset (100 mg/kg) and Rompun (20 mg/kg) by intraperitoneal injection followed by intratracheal instillation of replication-deficient Adeno-Cre (2.5×10^7 PFU) as described in (Meuwissen et al., 2003b) see **Figure 6**.

4.2.9.2 MRI analysis

Five months after tumour induction, tumour formation was monitored bi-weekly by magnetic resonance imaging (MRI) (A 3.0 T Philips Achieva clinical MRI (Philips Best, the Netherlands)) in combination with a dedicated mouse solenoid coil (Philips Hamburg, Germany), were used for imaging. T2-weighted MR images were acquired in the axial plane using turbo-spin echo (TSE) sequence [repetition time (TR)=3819 ms, echo time (TE)=60 ms, field of view (FOV)=40x40x20 mm³, reconstructed voxel size=0.13x0.13x1.0 mm³, number of average=1) under isoflurane (2.5%) anaesthesia. MR images (DICOM files) were analysed by determining and calculating region of interests (ROIs) using Horos software. Once tumours reached a mean volume of 15-30 mm³, mice were randomised into groups and treated.

4.2.9.3 Tumour xenograft studies

Human SCLC cell lines (1.5×10^6 cells either H82 or H2171) were injected in 200 µl PBS into both flanks of 8-10 weeks old male NMRI-Foxn1 nu/nu mice (Janvier). For that, cells were harvested from plates using trypsin and washed three times with PBS to remove

residual FCS to avoid rejection. Mice were assigned to either vehicle or combination treatment groups once tumours reached a minimum size of 2.5 x 2.5 mm. For two consecutive weeks mice were injected either with vehicle (PBS with 2% DMSO, 8.5% ethanol and 5% polyethylene glycol 400) and received normal drinking water or were injected with Auranofin (2.5 mg/kg) three times a week and received BSO (5 mM) in the drinking water *ad libitum*. Tumour size was tracked by calliper measurements and volume was calculated as (length x width x width)/2. Mice were sacrificed at the end of the treatment. Due to variance in tumour size at the start of the experiment, fold change of tumour volume upon treatment was calculated.

4.2.9.4 Tumour allograft studies

RP 181.5 sticker and floater cells were injected at a 1:1 ratio (1.5×10^6 cells in total) into both flanks of 8-10 weeks old male NMRI-Foxn1 nu/nu mice (Janvier) in 200 μ l PBS. For that, cells were harvested from plates using trypsin and washed three times with PBS to remove residual FCS to avoid rejection. Mice were assigned to either vehicle, BSO, Auranofin or combination treatment groups once tumours reached a minimum size of 2.5 x 2.5 mm. For two consecutive weeks, mice were injected either with vehicle (PBS with 2% DMSO, 8.5% ethanol and 5% polyethylene glycol 400), received BSO (5 mM) in the drinking water *ad libitum*, were i.p. injected with Auranofin (2.5 mg/kg) three times a week or received combined BSO/Auranofin. Tumour size was tracked by calliper measurements and volume was calculated as (length x width x width)/2. Mice were sacrificed at the end of the treatment. Due to variance in tumour size at the start of the experiment, fold change of tumour volume upon treatment was calculated.

4.2.10 Staining

4.2.10.1 ASCL1-staining for immunofluorescence microscopy

RP181.5 stickers (5,000 cells) were seeded in 24-well plates. The following day, they were treated with 500 nM Auranofin and 500 μ M BSO for 96 h. For staining, cells were washed with PBS followed by incubation in 200 μ l Fixation/Permeabilisation buffer (eBioscience, 00-5523-00) overnight at 4 °C. The next day, cells were washed with 1x Permeabilisation buffer (eBioscience, 00-5523-00) and incubated for 15 min in FACS buffer (PBS, 2% FCS) before adding the primary MASH-1 antibody (BD Biosciences, 556604), 1:250, for 30 min at 4 °C in 1x Permeabilisation buffer. After washing cells twice with 1x Permeabilisation buffer, cells were incubated in the secondary antibody (Cy3, Jackson Laboratories) 1:500 for 30 min at 4 °C in 1x Permeabilisation buffer. Cells were again washed twice with 1x Permeabilisation buffer and subsequently incubated in PBS for

microscopy. Microscopy was performed using a Leica DMI 6000B microscope (20x objective).

4.2.10.2 Immunohistochemistry

For immunohistochemistry, tissues were fixed in 4% Formaldehyde solution (VWR, 1039992500), dehydrated and subsequently embedded in paraffin. After sectioning tissue (4 μ m) it was deparaffinised by incubating in Xylol for 20 min and rehydrated in decreasing EtOH-concentrated solutions. For antigen retrieval, samples were heated in a citrate-based buffer (Vector Laboratories, H-3300) for anti-MDA staining to 100 °C for 30 min or in a TE-based buffer (10 mM Trizma Base, 1 mM EDTA, pH=9) in a pressure cooker for anti-ASCL1 staining. Firstly, endogenous peroxidases on samples were blocked for 15 min (BLOXALL Endogenous Peroxidase and Alkaline Phosphatase Blocking Solution, Vector Laboratories, SP-6000). For anti-MDA staining, this was followed by blocking of unspecific binding for 1 h (5% bovine serum albumin (BSA), 5% normal goat serum (NGS) in PBST) and Avidin/Biotin blocking for 15 min (Avidin/Biotin Blocking Kit, Vector Laboratories, SP-2001). For anti-ASCL1 staining, blocking step was performed using mouse-on-mouse blocking buffer (Abcam, ab269452) 30 min. Samples were incubated overnight at 4 °C with anti-MDA antibody (Abcam, ab6463) 1:250 in blocking buffer (PBS, 1% BSA, 0.003% NaN₃, 0.05% Tween20) and for anti-ASCL1 (BD Pharmingen, 556604) 1:300 in blocking buffer (TBS 1% BSA). The following day, samples were washed three times in PBS-T and incubated with secondary antibody (Perkin Elmer, NEF813) 1:1,000 in respective blocking buffer for 1 h (anti-MDA staining) or HRP polymer detector for 15 min for anti-ASCL1 (Abcam, mouse on mouse kit) and washed as before. For staining anti-MDA, samples were incubated with PBS + 1/60 Biotin + 1/60 Avidin (VECTASTAIN® Elite® ABC HRP Kit, Vector Laboratories, PK-6100) for 30 min. Both stainings were developed using DAB chromogen (Abcam, ab6423) according to the manufacturer's instructions and counterstained using Hematoxylin.

4.2.10.3 ASCL1 histology scoring

ASCL1 staining was manually quantified by H-score quantification on a scale of 0-300 as described^{220,268}. In brief, the H-score was calculated from % of positive cells multiplied by intensity score of 0-3. Tumours were first categorised into intensities followed by an estimation of % of positive cells.

4.2.11 Human SCLC RNA-seq data ethical approval

All SCLC and normal lung patient datasets and human SCLC cell line data used in this study have been previously published and, as such, are appropriately referenced, have

previously obtained the appropriate ethics approvals and are online available for George et al. 2015 (SCLC data) under (George et al., 2015) , for Rudin et al. 2012 (normal lung data) under (Rudin et al., 2012) and for Mollaoglu et al. 2017 (human SCLC cell line RNA-seq data) under ¹⁸⁵. Raw sequencing data were analysed with TRUP (Mollaoglu et al., 2017) and gene expression was quantified as FPKM.

4.2.12 Analysis software and bioinformatic analysis

Heatmaps visualising cell death pathway component expression were generated using RStudio version 1.1.456 and *gplots*, *data.table* and *RColorBrewer* packages. A ranked list of fold differential expression was generated for human cell line RNA-seq data using Excel and analysed for enrichment of gene sets by GSEA Desktop v3.0 ²³⁵ and <https://doi.org/10.1038/ng1180>). FACS data were analysed and quantified using FlowJo 10.4.2. Cell Titer Blue viability assays were analysed using Excel. MRI scans were quantified using Horos v3.3.5. Lipidomics measurements were analysed by MultiQuant 3.0.2 software (SCIEX). Figures were assembled and data plotted and analysed using GraphPad Prism 7 for Mac OS X. All figures were drawn using fully licensed biorender.com. IncuCyte images were analysed using the IncuCyte software (Sartorius).

4.2.13 Data presentation and statistical analysis

Data shown in graphs are presented as mean +/- SEM of at least three independent experiments unless stated otherwise. Thereby, the mean is calculated and plotted from at least three means from three independent experiments (each one performed in duplicates or triplicate experimental replicates). Two-tailed p values with a cut-off of $\alpha=0.05$ are calculated for the comparison between two conditions/groups. For comparison of multiple conditions/groups adjusted p values (cut off $\alpha=0.05$) were determined by ANOVA and Tukey's post-test. All statistical analysis was performed using GraphPad Prism 7 for Mac OS X. * $p<0.05$, ** $p<0.01$, *** $p<0.005$, **** $p<0.0001$ for all figures.

5 References

1. Galluzzi, L. *et al.* Essential versus accessory aspects of cell death: recommendations of the NCCD 2015. *Cell Death Differ.* **22**, 58–73 (2015).
2. Galluzzi, L. *et al.* Molecular mechanisms of cell death: recommendations of the Nomenclature Committee on Cell Death 2018. *Cell Death Differ.* **25**, 486 (2018).
3. Green, D. R. The Coming Decade of Cell Death Research: Five Riddles. *Cell* **177**, 1094–1107 (2019).
4. Fuchs, Y. & Steller, H. Programmed cell death in animal development and disease. *Cell* **147**, 742–758 (2011).
5. Kroemer, G. *et al.* Classification of cell death: recommendations of the Nomenclature Committee on Cell Death. *Cell Death Differ.* **12**, 1463–1467 (2005).
6. Hanahan, D. & Weinberg, R. A. Hallmarks of Cancer: The Next Generation. *Cell* **144**, 646–674 (2011).
7. Ashkenazi, A. Targeting death and decoy receptors of the tumour-necrosis factor superfamily. *Nat. Rev. Cancer* **2**, 420–430 (2002).
8. Delbridge, A. R. D., Grabow, S., Strasser, A. & Vaux, D. L. Thirty years of BCL-2: translating cell death discoveries into novel cancer therapies. *Nat. Rev. Cancer* **16**, 99–109 (2016).
9. Ravi, R. *et al.* Elimination of Hepatic Metastases of Colon Cancer Cells via p53-Independent Cross-Talk between Irinotecan and Apo2 Ligand/TRAIL. *Cancer Res.* **64**, 9105–9114 (2004).
10. Walczak, H. *et al.* Tumoricidal activity of tumor necrosis factor-related apoptosis-inducing ligand in vivo. *Nat. Med.* **5**, 157–163 (1999).
11. Adkins, I., Fucikova, J., Garg, A. D., Agostinis, P. & Špišek, R. Physical modalities inducing immunogenic tumor cell death for cancer immunotherapy. *OncolImmunology* **3**, e968434 (2014).

12. Hitomi, J. *et al.* Identification of a Molecular Signaling Network that Regulates a Cellular Necrotic Cell Death Pathway. *Cell* **135**, 1311–1323 (2008).
13. von Karstedt, S., Montinaro, A. & Walczak, H. Exploring the TRAILs less travelled: TRAIL in cancer biology and therapy. *Nat. Rev. Cancer* **17**, 352–366 (2017).
14. Kerr, J. F. R., Wyllie, A. H. & Currie, A. R. Apoptosis: A Basic Biological Phenomenon with Wideranging Implications in Tissue Kinetics. *Br. J. Cancer* **26**, 239–257 (1972).
15. Wyllie, A. H., Kerr, J. F. R. & Currie, A. R. Cell Death: The Significance of Apoptosis. in *International Review of Cytology* vol. 68 251–306 (Elsevier, 1980).
16. Vaseva, A. V. & Moll, U. M. The mitochondrial p53 pathway. *Biochim. Biophys. Acta BBA - Bioenerg.* **1787**, 414–420 (2009).
17. Mihara, M. *et al.* p53 Has a Direct Apoptogenic Role at the Mitochondria. *Mol. Cell* **11**, 577–590 (2003).
18. Dai, H., Pang, Y.-P., Ramirez-Alvarado, M. & Kaufmann, S. H. Evaluation of the BH3-only Protein Puma as a Direct Bak Activator. *J. Biol. Chem.* **289**, 89–99 (2014).
19. Villunger, A. p53- and Drug-Induced Apoptotic Responses Mediated by BH3-Only Proteins Puma and Noxa. *Science* **302**, 1036–1038 (2003).
20. Bouillet, P. *et al.* BH3-only Bcl-2 family member Bim is required for apoptosis of autoreactive thymocytes. *Nature* **415**, 922–926 (2002).
21. Ren, X. *et al.* Redox Signaling Mediated by Thioredoxin and Glutathione Systems in the Central Nervous System. *Antioxid. Redox Signal.* **27**, 989–1010 (2017).
22. Antonsson, B. Inhibition of Bax Channel-Forming Activity by Bcl-2. *Science* **277**, 370–372 (1997).
23. Edlich, F. *et al.* Bcl-xL Retrotranslocates Bax from the Mitochondria into the Cytosol. *Cell* **145**, 104–116 (2011).
24. Moldoveanu, T., Follis, A. V., Kriwacki, R. W. & Green, D. R. Many players in BCL-2 family affairs. *Trends Biochem. Sci.* **39**, 101–111 (2014).

25. Shamas-Din, A., Kale, J., Leber, B. & Andrews, D. W. Mechanisms of Action of Bcl-2 Family Proteins. *Cold Spring Harb. Perspect. Biol.* **5**, a008714–a008714 (2013).
26. Wei, M. C. Proapoptotic BAX and BAK: A Requisite Gateway to Mitochondrial Dysfunction and Death. *Science* **292**, 727–730 (2001).
27. Wolter, K. G. *et al.* Movement of Bax from the Cytosol to Mitochondria during Apoptosis. *J. Cell Biol.* **139**, 1281–1292 (1997).
28. Tait, S. W. G. & Green, D. R. Mitochondria and cell death: outer membrane permeabilization and beyond. *Nat. Rev. Mol. Cell Biol.* **11**, 621–632 (2010).
29. García Sáez, A. J. & Villunger, A. MOMP in the absence of BH3-only proteins. *Genes Dev.* **30**, 878–880 (2016).
30. Pan, G., O'Rourke, K. & Dixit, V. M. Caspase-9, Bcl-XL, and Apaf-1 Form a Ternary Complex. *J. Biol. Chem.* **273**, 5841–5845 (1998).
31. Zhou, M. *et al.* Atomic structure of the apoptosome: mechanism of cytochrome c - and dATP-mediated activation of Apaf-1. *Genes Dev.* **29**, 2349–2361 (2015).
32. Wajant, H. The Fas Signaling Pathway: More Than a Paradigm. *Science* **296**, 1635–1636 (2002).
33. Chinnaiyan, A. M., O'Rourke, K., Tewari, M. & Dixit, V. M. FADD, a novel death domain-containing protein, interacts with the death domain of fas and initiates apoptosis. *Cell* **81**, 505–512 (1995).
34. Schug, Z. T., Gonzalez, F., Houtkooper, R. H., Vaz, F. M. & Gottlieb, E. BID is cleaved by caspase-8 within a native complex on the mitochondrial membrane. *Cell Death Differ.* **18**, 538–548 (2011).
35. Jost, P. J. *et al.* XIAP discriminates between type I and type II FAS-induced apoptosis. *Nature* **460**, 1035–1039 (2009).
36. Wei, M. C. *et al.* tBID, a membrane-targeted death ligand, oligomerizes BAK to release cytochrome c. *Genes Dev.* **14**, 2060–2071 (2000).

37. Pasparakis, M. & Vandenabeele, P. Necroptosis and its role in inflammation. *Nature* **517**, 311–320 (2015).
38. Kaczmarek, A., Vandenabeele, P. & Krysko, D. V. Necroptosis: The Release of Damage-Associated Molecular Patterns and Its Physiological Relevance. *Immunity* **38**, 209–223 (2013).
39. Berghe, T. V., Linkermann, A., Jouan-Lanhouet, S., Walczak, H. & Vandenabeele, P. Regulated necrosis: the expanding network of non-apoptotic cell death pathways. *Nat. Rev. Mol. Cell Biol.* **15**, 135–147 (2014).
40. O'Donnell, M. A. *et al.* Caspase 8 inhibits programmed necrosis by processing CYLD. *Nat. Cell Biol.* **13**, 1437–1442 (2011).
41. Vandenabeele, P., Declercq, W., Van Herreweghe, F. & Vanden Berghe, T. The Role of the Kinases RIP1 and RIP3 in TNF-Induced Necrosis. *Sci. Signal.* **3**, re4–re4 (2010).
42. Jiao, H. *et al.* Z-nucleic-acid sensing triggers ZBP1-dependent necroptosis and inflammation. *Nature* **580**, 391–395 (2020).
43. Murphy, J. M. *et al.* The Pseudokinase MLKL Mediates Necroptosis via a Molecular Switch Mechanism. *Immunity* **39**, 443–453 (2013).
44. Dolma, S., Lessnick, S. L., Hahn, W. C. & Stockwell, B. R. Identification of genotype-selective antitumor agents using synthetic lethal chemical screening in engineered human tumor cells. *Cancer Cell* **3**, 285–296 (2003).
45. Yagoda, N. *et al.* RAS-RAF-MEK-dependent oxidative cell death involving voltage-dependent anion channels. *Nature* **447**, 864–868 (2007).
46. Yang, W. S. & Stockwell, B. R. Synthetic lethal screening identifies compounds activating iron-dependent, nonapoptotic cell death in oncogenic-RAS-harboring cancer cells. *Chem. Biol.* **15**, 234–245 (2008).
47. Dixon, S. J. *et al.* Ferroptosis: An Iron-Dependent Form of Non-Apoptotic Cell Death. *Cell* **149**, 1060–1072 (2012).

48. Gao, M., Monian, P., Quadri, N., Ramasamy, R. & Jiang, X. Glutaminolysis and Transferrin Regulate Ferroptosis. *Mol. Cell* **59**, 298–308 (2015).
49. Clemente, L. P. *et al.* Dynasore Blocks Ferroptosis through Combined Modulation of Iron Uptake and Inhibition of Mitochondrial Respiration. *Cells* **9**, 2259 (2020).
50. Ohgami, R. S., Campagna, D. R., McDonald, A. & Fleming, M. D. The Steap proteins are metalloreductases. *Blood* **108**, 1388–1394 (2006).
51. Yu, H. *et al.* Sulfasalazine-induced ferroptosis in breast cancer cells is reduced by the inhibitory effect of estrogen receptor on the transferrin receptor. *Oncol. Rep.* **42**, 826–838 (2019).
52. Alvarez, S. W. *et al.* NFS1 undergoes positive selection in lung tumours and protects cells from ferroptosis. *Nature* **551**, 639–643 (2017).
53. Casey, J. *et al.* Iron-responsive elements: regulatory RNA sequences that control mRNA levels and translation. *Science* **240**, 924–928 (1988).
54. Agmon, E., Solon, J., Bassereau, P. & Stockwell, B. R. Modeling the effects of lipid peroxidation during ferroptosis on membrane properties. *Sci. Rep.* **8**, 5155 (2018).
55. Wiernicki, B. *et al.* Excessive phospholipid peroxidation distinguishes ferroptosis from other cell death modes including pyroptosis. *Cell Death Dis.* **11**, 922 (2020).
56. Kagan, V. E. *et al.* Oxidized Arachidonic/Adrenic Phosphatidylethanolamines Navigate Cells to Ferroptosis. *Nat. Chem. Biol.* **13**, 81–90 (2017).
57. Zou, Y. *et al.* Plasticity of ether lipids promotes ferroptosis susceptibility and evasion. *Nature* **585**, 603–608 (2020).
58. Cheng, Z. & Li, Y. What Is Responsible for the Initiating Chemistry of Iron-Mediated Lipid Peroxidation: An Update. *Chem. Rev.* **107**, 748–766 (2007).
59. Yang, W. S. *et al.* Peroxidation of polyunsaturated fatty acids by lipoxygenases drives ferroptosis. *Proc. Natl. Acad. Sci. U. S. A.* **113**, E4966–4975 (2016).
60. Halliwell, B. & Gutteridge, J. M. C. *Free Radicals in Biology and Medicine*. (Oxford University Press, 2015).

61. Repetto, M., Semprine, J. & Boveris, A. Lipid Peroxidation: Chemical Mechanism, Biological Implications and Analytical Determination. in *Lipid Peroxidation* (ed. Catala, A.) (InTech, 2012). doi:10.5772/45943.
62. Yang, W. S. *et al.* Regulation of Ferroptotic Cancer Cell Death by GPX4. *Cell* **156**, 317–331 (2014).
63. Feng, H. *et al.* Transferrin Receptor Is a Specific Ferroptosis Marker. *Cell Rep.* **30**, 3411-3423.e7 (2020).
64. Papa, S. *et al.* The oxidative phosphorylation system in mammalian mitochondria. *Adv. Exp. Med. Biol.* **942**, 3–37 (2012).
65. Sullivan, L. B. & Chandel, N. S. Mitochondrial reactive oxygen species and cancer. *Cancer Metab.* **2**, (2014).
66. Brigelius-Flohé, R. & Maiorino, M. Glutathione peroxidases. *Biochim. Biophys. Acta* **1830**, 3289–3303 (2013).
67. Anandhan, A., Dodson, M., Schmidlin, C. J., Liu, P. & Zhang, D. D. Breakdown of an Ironclad Defense System: The Critical Role of NRF2 in Mediating Ferroptosis. *Cell Chem. Biol.* **27**, 436–447 (2020).
68. Itoh, K. *et al.* An Nrf2/Small Maf Heterodimer Mediates the Induction of Phase II Detoxifying Enzyme Genes through Antioxidant Response Elements. *Biochem. Biophys. Res. Commun.* **236**, 313–322 (1997).
69. Abdalkader, M., Lampinen, R., Kanninen, K. M., Malm, T. M. & Liddell, J. R. Targeting Nrf2 to Suppress Ferroptosis and Mitochondrial Dysfunction in Neurodegeneration. *Front. Neurosci.* **12**, (2018).
70. Dixon, S. J. & Stockwell, B. R. The role of iron and reactive oxygen species in cell death. *Nat. Chem. Biol.* **10**, 9–17 (2014).
71. Angeli, J. P. F., Krysko, D. V. & Conrad, M. Ferroptosis at the crossroads of cancer-acquired drug resistance and immune evasion. *Nat. Rev. Cancer* **19**, 405–414 (2019).

72. Doll, S. *et al.* ACSL4 dictates ferroptosis sensitivity by shaping cellular lipid composition. *Nat. Chem. Biol.* **13**, 91–98 (2017).
73. Tang, Y., Zhou, J., Hooi, S. C., Jiang, Y.-M. & Lu, G.-D. Fatty acid activation in carcinogenesis and cancer development: Essential roles of long-chain acyl-CoA synthetases. *Oncol. Lett.* **16**, 1390–1396 (2018).
74. Yuan, H., Li, X., Zhang, X., Kang, R. & Tang, D. Identification of ACSL4 as a biomarker and contributor of ferroptosis. *Biochem. Biophys. Res. Commun.* **478**, 1338–1343 (2016).
75. Dixon, S. J. *et al.* Human Haploid Cell Genetics Reveals Roles for Lipid Metabolism Genes in Nonapoptotic Cell Death. *ACS Chem. Biol.* **10**, 1604–1609 (2015).
76. Hashidate-Yoshida, T. *et al.* Fatty acid remodeling by LPCAT3 enriches arachidonate in phospholipid membranes and regulates triglyceride transport. *eLife* **4**, e06328 (2015).
77. Forman, H. J., Zhang, H. & Rinna, A. Glutathione: Overview of its protective roles, measurement, and biosynthesis. *Mol. Aspects Med.* **30**, 1–12 (2009).
78. Eaton, J. K. *et al.* Selective covalent targeting of GPX4 using masked nitrile-oxide electrophiles. *Nat. Chem. Biol.* **16**, 497–506 (2020).
79. Weiwler, M. *et al.* Development of small-molecule probes that selectively kill cells induced to express mutant RAS. *Bioorg. Med. Chem. Lett.* **22**, 1822–1826 (2012).
80. Meister, A. Selective modification of glutathione metabolism. *Science* **220**, 472–477 (1983).
81. Proneth, B. & Conrad, M. Ferroptosis and necroinflammation, a yet poorly explored link. *Cell Death Differ.* **26**, 14–24 (2019).
82. Burdo, J., Dargusch, R. & Schubert, D. Distribution of the cystine/glutamate antiporter system xc⁻ in the brain, kidney, and duodenum. *J. Histochem. Cytochem. Off. J. Histochem. Soc.* **54**, 549–557 (2006).

83. Dixon, S. J. *et al.* Pharmacological inhibition of cystine–glutamate exchange induces endoplasmic reticulum stress and ferroptosis. *eLife* **3**, (2014).
84. Wang, W. *et al.* CD8⁺ T cells regulate tumour ferroptosis during cancer immunotherapy. *Nature* (2019) doi:10.1038/s41586-019-1170-y.
85. Conrad, M. & Sato, H. The oxidative stress-inducible cystine/glutamate antiporter, system xc⁻: cystine supplier and beyond. *Amino Acids* **42**, 231–246 (2012).
86. McBean, G. J. The transsulfuration pathway: a source of cysteine for glutathione in astrocytes. *Amino Acids* **42**, 199–205 (2012).
87. Wang, L. *et al.* A pharmacological probe identifies cystathionine β-synthase as a new negative regulator for ferroptosis. *Cell Death Dis.* **9**, 1–17 (2018).
88. Lu, S. C. GLUTATHIONE SYNTHESIS. *Biochim. Biophys. Acta* **1830**, 3143–3153 (2013).
89. Bersuker, K. *et al.* The CoQ oxidoreductase FSP1 acts parallel to GPX4 to inhibit ferroptosis. *Nature* (2019) doi:10.1038/s41586-019-1705-2.
90. Doll, S. *et al.* FSP1 is a glutathione-independent ferroptosis suppressor. *Nature* (2019) doi:10.1038/s41586-019-1707-0.
91. Friedmann Angeli, J. P. *et al.* Inactivation of the ferroptosis regulator Gpx4 triggers acute renal failure in mice. *Nat. Cell Biol.* **16**, 1180–1191 (2014).
92. Bebbber, C. M., Müller, F., Clemente, L. P. & Weber, J. Ferroptosis in Cancer Cell Biology. **24** (2020).
93. Nordberg, J. & Arnér, E. S. Reactive oxygen species, antioxidants, and the mammalian thioredoxin system. *Free Radic. Biol. Med.* **31**, 1287–1312 (2001).
94. Holmgren, A. Thioredoxin. *Annu. Rev. Biochem.* **54**, 237–271 (1985).
95. Lu, J. & Holmgren, A. The thioredoxin antioxidant system. *Free Radic. Biol. Med.* **66**, 75–87 (2014).
96. Mandal, P. K. *et al.* System xc⁻ and Thioredoxin Reductase 1 Cooperatively Rescue Glutathione Deficiency. *J. Biol. Chem.* **285**, 22244 (2010).

97. Nishiyama, A. *et al.* Identification of Thioredoxin-binding Protein-2/Vitamin D3 Up-regulated Protein 1 as a Negative Regulator of Thioredoxin Function and Expression. *J. Biol. Chem.* **274**, 21645–21650 (1999).
98. Oberacker, T. *et al.* Enhanced expression of thioredoxin-interacting-protein regulates oxidative DNA damage and aging. *FEBS Lett.* **592**, 2297–2307 (2018).
99. Bondareva, A. A. *et al.* Effects of thioredoxin reductase-1 deletion on embryogenesis and transcriptome. *Free Radic. Biol. Med.* **43**, 911–923 (2007).
100. Jakupoglu, C. *et al.* Cytoplasmic thioredoxin reductase is essential for embryogenesis but dispensable for cardiac development. *Mol. Cell. Biol.* **25**, 1980–1988 (2005).
101. Conrad, M. *et al.* The nuclear form of phospholipid hydroperoxide glutathione peroxidase is a protein thiol peroxidase contributing to sperm chromatin stability. *Mol. Cell. Biol.* **25**, 7637–7644 (2005).
102. Matsui, M. *et al.* Early embryonic lethality caused by targeted disruption of the mouse thioredoxin gene. *Dev. Biol.* **178**, 179–185 (1996).
103. Nonn, L., Williams, R. R., Erickson, R. P. & Powis, G. The absence of mitochondrial thioredoxin 2 causes massive apoptosis, exencephaly, and early embryonic lethality in homozygous mice. *Mol. Cell. Biol.* **23**, 916–922 (2003).
104. Roder, C. & Thomson, M. J. Auranofin: Repurposing an Old Drug for a Golden New Age. *Drugs RD* **15**, 13–20 (2015).
105. Lovatt, M. *et al.* Peroxiredoxin-1 regulates lipid peroxidation in corneal endothelial cells. *Redox Biol.* **30**, 101417 (2020).
106. Qi, W. *et al.* LncRNA GABPB1-AS1 and GABPB1 regulate oxidative stress during erastin-induced ferroptosis in HepG2 hepatocellular carcinoma cells. *Sci. Rep.* **9**, 16185 (2019).

107. Rhee, S. G., Kang, S. W., Chang, T.-S., Jeong, W. & Kim, K. Peroxiredoxin, a Novel Family of Peroxidases. *IUBMB Life Int. Union Biochem. Mol. Biol. Life* **52**, 35–41 (2001).
108. Lu, B. *et al.* Identification of PRDX6 as a regulator of ferroptosis. *Acta Pharmacol. Sin.* (2019) doi:10.1038/s41401-019-0233-9.
109. Cori, C. F. & Cori, G. T. The Carbohydrate Metabolism of Tumors II. Changes in the Sugar, Lactic Acid, and CO₂-Combining Power of Blood Passing Through a Tumor. *J. Biol. Chem.* **65**, 397–405 (1925).
110. Warburg, O. & Minami, S. Versuche an Überlebendem Carcinom-gewebe. *Klin. Wochenschr.* **2**, 776–777 (1923).
111. Crabtree, H. G. Observations on the carbohydrate metabolism of tumours. *Biochem. J.* **23**, 536–545 (1929).
112. Cerutti, P. A. & Trump, B. F. Inflammation and oxidative stress in carcinogenesis. *Cancer Cells Cold Spring Harb. N* 1989 **3**, 1–7 (1991).
113. Irani, K. *et al.* Mitogenic signaling mediated by oxidants in Ras-transformed fibroblasts. *Science* **275**, 1649–1652 (1997).
114. Tanaka, H. *et al.* E2F1 and c-Myc potentiate apoptosis through inhibition of NF- κ B activity that facilitates MnSOD-mediated ROS elimination. *Mol. Cell* **9**, 1017–1029 (2002).
115. Vafa, O. *et al.* c-Myc can induce DNA damage, increase reactive oxygen species, and mitigate p53 function: a mechanism for oncogene-induced genetic instability. *Mol. Cell* **9**, 1031–1044 (2002).
116. Hussain, S. P., Hofseth, L. J. & Harris, C. C. Radical causes of cancer. *Nat. Rev. Cancer* **3**, 276–285 (2003).
117. Lee, S.-R. *et al.* Reversible inactivation of the tumor suppressor PTEN by H₂O₂. *J. Biol. Chem.* **277**, 20336–20342 (2002).

118. Leslie, N. R. *et al.* Redox regulation of PI 3-kinase signalling via inactivation of PTEN. *EMBO J.* **22**, 5501–5510 (2003).
119. Harris, I. S. *et al.* Glutathione and thioredoxin antioxidant pathways synergize to drive cancer initiation and progression. *Cancer Cell* **27**, 211–222 (2015).
120. DeNicola, G. M. *et al.* Oncogene-induced Nrf2 transcription promotes ROS detoxification and tumorigenesis. *Nature* **475**, 106–109 (2011).
121. Deng, Q., Liao, R., Wu, B.-L. & Sun, P. High intensity ras signaling induces premature senescence by activating p38 pathway in primary human fibroblasts. *J. Biol. Chem.* **279**, 1050–1059 (2004).
122. Lim, J. K. M. *et al.* Cystine/glutamate antiporter xCT (SLC7A11) facilitates oncogenic RAS transformation by preserving intracellular redox balance. *Proc. Natl. Acad. Sci. U. S. A.* **116**, 9433–9442 (2019).
123. Jiang, L. *et al.* Ferroptosis as a p53-mediated activity during tumour suppression. *Nature* **520**, 57–62 (2015).
124. Liu, D. S. *et al.* Inhibiting the system xC⁻/glutathione axis selectively targets cancers with mutant-p53 accumulation. *Nat. Commun.* **8**, 14844 (2017).
125. Xie, Y. *et al.* Ferroptosis: process and function. *Cell Death Differ.* **23**, 369–379 (2016).
126. Viswanathan, V. S. *et al.* Dependency of a therapy-resistant state of cancer cells on a lipid peroxidase pathway. *Nature* **547**, 453–457 (2017).
127. Hangauer, M. J. *et al.* Drug-tolerant persister cancer cells are vulnerable to GPX4 inhibition. *Nature* **551**, 247–250 (2017).
128. Louandre, C. *et al.* The retinoblastoma (Rb) protein regulates ferroptosis induced by sorafenib in human hepatocellular carcinoma cells. *Cancer Lett.* **356**, 971–977 (2015).
129. Badgley, M. A. *et al.* Cysteine depletion induces pancreatic tumor ferroptosis in mice. *Science* **368**, 85–89 (2020).

130. Hu, K. *et al.* Suppression of the SLC7A11/glutathione axis causes synthetic lethality in KRAS-mutant lung adenocarcinoma. *J. Clin. Invest.* **130**, 1752–1766 (2020).
131. Ji, X. *et al.* xCT (SLC7A11)-mediated metabolic reprogramming promotes non-small cell lung cancer progression. *Oncogene* **37**, 5007–5019 (2018).
132. Timmerman, L. A. *et al.* Glutamine Sensitivity Analysis Identifies the xCT Antiporter as a Common Triple-Negative Breast Tumor Therapeutic Target. *Cancer Cell* **24**, 450–465 (2013).
133. Yu, M. *et al.* Targeted exosomes-encapsulated erastin induced ferroptosis in the triple negative breast cancer cells. *Cancer Sci.* (2019) doi:10.1111/cas.14181.
134. Gout, P. W., Buckley, A. R., Simms, C. R. & Bruchovsky, N. Sulfasalazine, a potent suppressor of lymphoma growth by inhibition of the x(c)- cystine transporter: a new action for an old drug. *Leukemia* **15**, 1633–1640 (2001).
135. Louandre, C. *et al.* Iron-dependent cell death of hepatocellular carcinoma cells exposed to sorafenib. *Int. J. Cancer* **133**, 1732–1742 (2013).
136. Zhang, Y. *et al.* Imidazole Ketone Erastin Induces Ferroptosis and Slows Tumor Growth in a Mouse Lymphoma Model. *Cell Chem. Biol.* **26**, 623-633.e9 (2019).
137. Hopkins-Donaldson, S. *et al.* Silencing of death receptor and caspase-8 expression in small cell lung carcinoma cell lines and tumors by DNA methylation. *Cell Death Differ.* **10**, 356–364 (2003).
138. Torre, L. A. *et al.* Global cancer statistics, 2012: Global Cancer Statistics, 2012. *CA. Cancer J. Clin.* **65**, 87–108 (2015).
139. Jemal, A. *et al.* Cancer Statistics, 2007. *CA. Cancer J. Clin.* **57**, 43–66 (2007).
140. Sung, H. *et al.* Global Cancer Statistics 2020: GLOBOCAN Estimates of Incidence and Mortality Worldwide for 36 Cancers in 185 Countries. *CA. Cancer J. Clin.* **71**, 209–249 (2021).
141. Alberg, A. J. & Samet, J. M. Epidemiology of Lung Cancer*. *Chest* **123**, 21S-49S (2003).

142. Lemjabbar-Alaoui, H., Hassan, O. U., Yang, Y.-W. & Buchanan, P. Lung cancer: Biology and treatment options. *Biochim. Biophys. Acta BBA - Rev. Cancer* **1856**, 189–210 (2015).
143. Noguchi, M. *et al.* Small adenocarcinoma of the lung. Histologic characteristics and prognosis. *Cancer* **75**, 2844–2852 (1995).
144. Chan, B. A. & Hughes, B. G. M. Targeted therapy for non-small cell lung cancer: current standards and the promise of the future. *Transl. Lung Cancer Res.* **4**, 36–54 (2015).
145. Zappa, C. & Mousa, S. A. Non-small cell lung cancer: current treatment and future advances. *Transl. Lung Cancer Res.* **5**, 288–300 (2016).
146. Riely, G. J. & Ladanyi, M. KRAS Mutations. *J. Mol. Diagn.* **10**, 493–495 (2008).
147. Paez, J. G. EGFR Mutations in Lung Cancer: Correlation with Clinical Response to Gefitinib Therapy. *Science* **304**, 1497–1500 (2004).
148. Park, K.-S. *et al.* Characterization of the cell of origin for small cell lung cancer. *Cell Cycle* **10**, 2806–2815 (2011).
149. Gazdar, A. F., Bunn, P. A. & Minna, J. D. Small-cell lung cancer: what we know, what we need to know and the path forward. *Nat. Rev. Cancer* **17**, 725–737 (2017).
150. Früh, M. *et al.* Small-cell lung cancer (SCLC): ESMO Clinical Practice Guidelines for diagnosis, treatment and follow-up. *Ann. Oncol.* **24**, vi99–vi105 (2013).
151. Meuwissen, R. *et al.* Induction of small cell lung cancer by somatic inactivation of both Trp53 and Rb1 in a conditional mouse model. *Cancer Cell* **4**, 181–189 (2003).
152. Australian Pancreatic Cancer Genome Initiative *et al.* Signatures of mutational processes in human cancer. *Nature* **500**, 415–421 (2013).
153. Jackman, D. M. & Johnson, B. E. Small-cell lung cancer. *The Lancet* **366**, 1385–1396 (2005).

154. Pietanza, M. C., Byers, L. A., Minna, J. D. & Rudin, C. M. Small cell lung cancer: will recent progress lead to improved outcomes? *Clin. Cancer Res. Off. J. Am. Assoc. Cancer Res.* **21**, 2244–2255 (2015).
155. van Meerbeeck, J. P., Fennell, D. A. & De Ruyscher, D. K. Small-cell lung cancer. *The Lancet* **378**, 1741–1755 (2011).
156. Junker, K., Wiethage, Th. & Müller, K.-M. Pathology of small-cell lung cancer. *J. Cancer Res. Clin. Oncol.* **126**, 361–368 (2000).
157. Minna, J. D., Kurie, J. M. & Jacks, T. A big step in the study of small cell lung cancer. *Cancer Cell* **4**, 163–166 (2003).
158. Simon, G. R. & Wagner, H. Small Cell Lung Cancer*. *Chest* **123**, 259S-271S (2003).
159. Carter, L. *et al.* Molecular analysis of circulating tumor cells identifies distinct copy-number profiles in patients with chemosensitive and chemorefractory small-cell lung cancer. *Nat. Med.* **23**, 114–119 (2017).
160. Hodgkinson, C. L. *et al.* Tumorigenicity and genetic profiling of circulating tumor cells in small-cell lung cancer. *Nat. Med.* **20**, 897–903 (2014).
161. Simpson, K. L. *et al.* A biobank of small cell lung cancer CDX models elucidates inter- and intratumoral phenotypic heterogeneity. *Nat. Cancer* **1**, 437–451 (2020).
162. Torres-Durán, M. *et al.* Small cell lung cancer in never-smokers. *Eur. Respir. J.* **47**, 947–953 (2016).
163. Varghese, A. M. *et al.* Small-Cell Lung Cancers in Patients Who Never Smoked Cigarettes. *J. Thorac. Oncol.* **9**, 892–896 (2014).
164. Kenfield, S. A., Wei, E. K., Stampfer, M. J., Rosner, B. A. & Colditz, G. A. Comparison of aspects of smoking among the four histological types of lung cancer. *Tob. Control* **17**, 198–204 (2008).
165. Plesance, E. D. *et al.* A small-cell lung cancer genome with complex signatures of tobacco exposure. *Nature* **463**, 184–190 (2010).

166. Peifer, M. *et al.* Integrative genome analyses identify key somatic driver mutations of small-cell lung cancer. *Nat. Genet.* **44**, 1104–1110 (2012).
167. Kreuzer, M., Gerken, M., Kreienbrock, L., Wellmann, J. & Wichmann, H. E. Lung cancer in lifetime nonsmoking men – results of a case-control study in Germany. *Br. J. Cancer* **84**, 134–140 (2001).
168. Kreuzer, M. *et al.* Risk factors for lung cancer among nonsmoking women. *Int. J. Cancer* **100**, 706–713 (2002).
169. Simon, G. R. & Turrisi, A. Management of Small Cell Lung Cancer. *Chest* **132**, 324S-339S (2007).
170. Eckardt, J. R. *et al.* Phase III Study of Oral Compared With Intravenous Topotecan As Second-Line Therapy in Small-Cell Lung Cancer. *J. Clin. Oncol.* **25**, 2086–2092 (2007).
171. O'Brien, M. E. R. *et al.* Phase III Trial Comparing Supportive Care Alone With Supportive Care With Oral Topotecan in Patients With Relapsed Small-Cell Lung Cancer. *J. Clin. Oncol.* **24**, 5441–5447 (2006).
172. von Pawel, J. *et al.* Topotecan Versus Cyclophosphamide, Doxorubicin, and Vincristine for the Treatment of Recurrent Small-Cell Lung Cancer. *J. Clin. Oncol.* **17**, 658–658 (1999).
173. McGranahan, N. *et al.* Clonal neoantigens elicit T cell immunoreactivity and sensitivity to immune checkpoint blockade. *Science* **351**, 1463–1469 (2016).
174. Horn, L. *et al.* First-Line Atezolizumab plus Chemotherapy in Extensive-Stage Small-Cell Lung Cancer. *N. Engl. J. Med.* **379**, 2220–2229 (2018).
175. Antonia, S. J. *et al.* Checkmate 032: Nivolumab (N) alone or in combination with ipilimumab (I) for the treatment of recurrent small cell lung cancer (SCLC). *J. Clin. Oncol.* **34**, 100–100 (2016).
176. Heemels, M.-T. & Ploegh, H. Generation, Translocation, and Presentation of MHC Class I-Restricted Peptides. *Annu. Rev. Biochem.* **64**, 463–491 (1995).

177. Freeman, G. J. *et al.* Engagement of the Pd-1 Immunoinhibitory Receptor by a Novel B7 Family Member Leads to Negative Regulation of Lymphocyte Activation. *J. Exp. Med.* **192**, 1027–1034 (2000).
178. Keir, M. E. *et al.* Tissue expression of PD-L1 mediates peripheral T cell tolerance. *J. Exp. Med.* **203**, 883–895 (2006).
179. Zou, W. & Chen, L. Inhibitory B7-family molecules in the tumour microenvironment. *Nat. Rev. Immunol.* **8**, 467–477 (2008).
180. Tumeh, P. C. *et al.* PD-1 blockade induces responses by inhibiting adaptive immune resistance. *Nature* **515**, 568–571 (2014).
181. Brahmer, J. R. *et al.* Phase I Study of Single-Agent Anti-Programmed Death-1 (MDX-1106) in Refractory Solid Tumors: Safety, Clinical Activity, Pharmacodynamics, and Immunologic Correlates. *J. Clin. Oncol.* **28**, 3167–3175 (2010).
182. *H.R. 733 - Recalcitrant Cancer Research Act of 2012.*
183. George, J. *et al.* Comprehensive genomic profiles of small cell lung cancer. *Nature* **524**, 47–53 (2015).
184. McFadden, D. G. *et al.* Genetic and Clonal Dissection of Murine Small Cell Lung Carcinoma Progression by Genome Sequencing. *Cell* **156**, 1298–1311 (2014).
185. Mollaoglu, G. *et al.* MYC Drives Progression of Small Cell Lung Cancer to a Variant Neuroendocrine Subtype with Vulnerability to Aurora Kinase Inhibition. *Cancer Cell* **31**, 270–285 (2017).
186. Dang, C. V. MYC on the Path to Cancer. *Cell* **149**, 22–35 (2012).
187. Hwang, D. H., Sun, H., Rodig, S. J., Hornick, J. L. & Sholl, L. M. Myc protein expression correlates with MYC amplification in small-cell lung carcinoma. *Histopathology* **67**, 81–89 (2015).
188. Sos, M. L. *et al.* A framework for identification of actionable cancer genome dependencies in small cell lung cancer. *Proc. Natl. Acad. Sci.* **109**, 17034–17039 (2012).

189. Cui, M. *et al.* PTEN Is a Potent Suppressor of Small Cell Lung Cancer. *Mol. Cancer Res.* **12**, 654–659 (2014).
190. Yokomizo, A. *et al.* PTEN/MMAC1 mutations identified in small cell, but not in non-small cell lung cancers. *Oncogene* **17**, 475–479 (1998).
191. Jia, D. *et al.* *Crebbp* Loss Drives Small Cell Lung Cancer and Increases Sensitivity to HDAC Inhibition. *Cancer Discov.* **8**, 1422–1437 (2018).
192. Poirier, J. T. *et al.* DNA methylation in small cell lung cancer defines distinct disease subtypes and correlates with high expression of EZH2. *Oncogene* **34**, 5869–5878 (2015).
193. Burr, M. L. *et al.* An Evolutionarily Conserved Function of Polycomb Silences the MHC Class I Antigen Presentation Pathway and Enables Immune Evasion in Cancer. *Cancer Cell* **36**, 385–401.e8 (2019).
194. Dooley, A. L. *et al.* Nuclear factor I/B is an oncogene in small cell lung cancer. *Genes Dev.* **25**, 1470–1475 (2011).
195. Denny, S. K. *et al.* Nfib Promotes Metastasis through a Widespread Increase in Chromatin Accessibility. *Cell* **166**, 328–342 (2016).
196. Semenova, E. A. *et al.* Transcription Factor NFIB Is a Driver of Small Cell Lung Cancer Progression in Mice and Marks Metastatic Disease in Patients. *Cell Rep.* **16**, 631–643 (2016).
197. Wu, N. *et al.* NFIB overexpression cooperates with *Rb/p53* deletion to promote small cell lung cancer. *Oncotarget* **7**, 57514–57524 (2016).
198. Yang, D. *et al.* Axon-like protrusions promote small cell lung cancer migration and metastasis. *eLife* **8**, e50616 (2019).
199. Ben-Ezra, J. M., Kornstein, M. J., Grimes, M. M. & Krystal, G. Small cell carcinomas of the lung express the Bcl-2 protein. *Am. J. Pathol.* **145**, 1036–1040 (1994).
200. Ikegaki, N., Katsumata, M., Minna, J. & Tsujimoto, Y. Expression of bcl-2 in small cell lung carcinoma cells. *Cancer Res.* **54**, 6–8 (1994).

201. Lochmann, T. L. *et al.* Venetoclax Is Effective in Small-Cell Lung Cancers with High BCL-2 Expression. *Clin. Cancer Res. Off. J. Am. Assoc. Cancer Res.* **24**, 360–369 (2018).
202. Belyanskaya, L. L. *et al.* TRAIL-induced survival and proliferation of SCLC cells is mediated by ERK and dependent on TRAIL-R2/DR5 expression in the absence of caspase-8. *Lung Cancer* **60**, 355–365 (2008).
203. Shivapurkar, N. *et al.* Differential inactivation of caspase-8 in lung cancers. *Cancer Biol. Ther.* **1**, 65–69 (2002).
204. Shivapurkar, N. *et al.* Loss of expression of death-inducing signaling complex (DISC) components in lung cancer cell lines and the influence of MYC amplification. *Oncogene* **21**, 8510–8514 (2002).
205. Gouyer, V. *et al.* Mechanism of Retinoblastoma Gene Inactivation in the Spectrum of Neuroendocrine Lung Tumors. *Am. J. Respir. Cell Mol. Biol.* **18**, 188–196 (1998).
206. Sherr, C. J. & McCormick, F. The RB and p53 pathways in cancer. *Cancer Cell* **2**, 103–112 (2002).
207. Meuwissen, R., Linn, S. C., Valk, M. van der, Mooi, W. J. & Berns, A. Mouse model for lung tumorigenesis through Cre/lox controlled sporadic activation of the K-Ras oncogene. *Oncogene* **20**, 6551 (2001).
208. Calbo, J. *et al.* A Functional Role for Tumor Cell Heterogeneity in a Mouse Model of Small Cell Lung Cancer. *Cancer Cell* **19**, 244–256 (2011).
209. Borges, M. *et al.* An achaete-scute homologue essential for neuroendocrine differentiation in the lung. *Nature* **386**, 852–855 (1997).
210. Osada, H., Tatematsu, Y., Yatabe, Y., Horio, Y. & Takahashi, T. *ASH1* Gene Is a Specific Therapeutic Target for Lung Cancers with Neuroendocrine Features. *Cancer Res.* **65**, 10680–10685 (2005).
211. Jiang, T. *et al.* Achaete-Scute Complex Homologue 1 Regulates Tumor-Initiating Capacity in Human Small Cell Lung Cancer. *Cancer Res.* **69**, 845–854 (2009).

212. Rudin, C. M. *et al.* Molecular subtypes of small cell lung cancer: a synthesis of human and mouse model data. *Nat. Rev. Cancer* **19**, 289 (2019).
213. Ballas, N. & Mandel, G. The many faces of REST oversee epigenetic programming of neuronal genes. *Curr. Opin. Neurobiol.* **15**, 500–506 (2005).
214. Chong, J. A. *et al.* REST: a mammalian silencer protein that restricts sodium channel gene expression to neurons. *Cell* **80**, 949–957 (1995).
215. Huang, Y.-H. *et al.* POU2F3 is a master regulator of a tuft cell-like variant of small cell lung cancer. *Genes Dev.* **32**, 915–928 (2018).
216. Wooten, D. J. *et al.* Systems-level network modeling of Small Cell Lung Cancer subtypes identifies master regulators and destabilizers. *PLOS Comput. Biol.* **15**, e1007343 (2019).
217. Gay, C. M. *et al.* Patterns of transcription factor programs and immune pathway activation define four major subtypes of SCLC with distinct therapeutic vulnerabilities. *Cancer Cell* **39**, 346-360.e7 (2021).
218. Baine, M. K. *et al.* SCLC Subtypes Defined by ASCL1, NEUROD1, POU2F3, and YAP1: A Comprehensive Immunohistochemical and Histopathologic Characterization. *J. Thorac. Oncol.* **15**, 1823–1835 (2020).
219. Cardnell, R. J. *et al.* Protein expression of TTF1 and cMYC define distinct molecular subgroups of small cell lung cancer with unique vulnerabilities to aurora kinase inhibition, DLL3 targeting, and other targeted therapies. *Oncotarget* **8**, 73419–73432 (2017).
220. Ireland, A. S. *et al.* MYC Drives Temporal Evolution of Small Cell Lung Cancer Subtypes by Reprogramming Neuroendocrine Fate. *Cancer Cell* **38**, 60-78.e12 (2020).
221. Koch, U. & Radtke, F. Notch and cancer: a double-edged sword. *Cell. Mol. Life Sci.* **64**, 2746–2762 (2007).

222. Hori, K., Sen, A. & Artavanis-Tsakonas, S. Notch signaling at a glance. *J. Cell Sci.* jcs.127308 (2013) doi:10.1242/jcs.127308.
223. Lim, J. S. *et al.* Intratumoural heterogeneity generated by Notch signalling promotes small-cell lung cancer. *Nature* **545**, 360–364 (2017).
224. Cai, L. *et al.* Cell-autonomous immune gene expression is repressed in pulmonary neuroendocrine cells and small cell lung cancer. *Commun. Biol.* **4**, 314 (2021).
225. Mahadevan, N. R. *et al.* Intrinsic immunogenicity of small cell lung carcinoma revealed by its cellular plasticity. *Cancer Discov.* candisc.0913.2020 (2021) doi:10.1158/2159-8290.CD-20-0913.
226. Yang, D. *et al.* Intertumoral Heterogeneity in SCLC Is Influenced by the Cell Type of Origin. *Cancer Discov.* **8**, 1316–1331 (2018).
227. Rudin, C. M., Brambilla, E., Faivre-Finn, C. & Sage, J. Small-cell lung cancer. *Nat. Rev. Dis. Primer* **7**, 3 (2021).
228. Stewart, C. A. *et al.* Single-cell analyses reveal increased intratumoral heterogeneity after the onset of therapy resistance in small-cell lung cancer. *Nat. Cancer* **1**, 423–436 (2020).
229. Bruttel, V. S. & Wischhusen, J. Cancer Stem Cell Immunology: Key to Understanding Tumorigenesis and Tumor Immune Escape? *Front. Immunol.* **5**, (2014).
230. Cao, J. Y. & Dixon, S. J. Mechanisms of ferroptosis. *Cell. Mol. Life Sci. CMLS* **73**, 2195–2209 (2016).
231. Degterev, A. *et al.* Identification of RIP1 kinase as a specific cellular target of necrostatins. *Nat. Chem. Biol.* **4**, 313–321 (2008).
232. Kaiser, W. J. *et al.* RIP3 mediates the embryonic lethality of caspase-8-deficient mice. *Nature* **471**, 368–372 (2011).
233. Oberst, A. *et al.* Catalytic activity of the caspase-8–FLIPL complex inhibits RIPK3-dependent necrosis. *Nature* **471**, 363–367 (2011).

234. Lang, X. *et al.* Radiotherapy and Immunotherapy Promote Tumoral Lipid Oxidation and Ferroptosis via Synergistic Repression of SLC7A11. *Cancer Discov.* **9**, 1673–1685 (2019).
235. Rudin, C. M. *et al.* Comprehensive genomic analysis identifies SOX2 as a frequently amplified gene in small-cell lung cancer. *Nat. Genet.* **44**, 1111–1116 (2012).
236. Hartwig, T. *et al.* The TRAIL-Induced Cancer Secretome Promotes a Tumor-Supportive Immune Microenvironment via CCR2. *Mol. Cell* **65**, 730-742.e5 (2017).
237. Henry, C. M. & Martin, S. J. Caspase-8 Acts in a Non-enzymatic Role as a Scaffold for Assembly of a Pro-inflammatory “FADDosome” Complex upon TRAIL Stimulation. *Mol. Cell* **65**, 715-729.e5 (2017).
238. Christensen, C. L. *et al.* Targeting Transcriptional Addictions in Small Cell Lung Cancer with a Covalent CDK7 Inhibitor. *Cancer Cell* **26**, 909–922 (2014).
239. Moquin, D. M., McQuade, T. & Chan, F. K.-M. CYLD Deubiquitinates RIP1 in the TNF α -Induced Necrosome to Facilitate Kinase Activation and Programmed Necrosis. *PLoS ONE* **8**, e76841 (2013).
240. Dondelinger, Y. *et al.* MLKL Compromises Plasma Membrane Integrity by Binding to Phosphatidylinositol Phosphates. *Cell Rep.* **7**, 971–981 (2014).
241. Sun, L. *et al.* Mixed Lineage Kinase Domain-like Protein Mediates Necrosis Signaling Downstream of RIP3 Kinase. *Cell* **148**, 213–227 (2012).
242. Zhao, J. *et al.* Mixed lineage kinase domain-like is a key receptor interacting protein 3 downstream component of TNF-induced necrosis. *Proc. Natl. Acad. Sci.* **109**, 5322–5327 (2012).
243. Seiler, A. *et al.* Glutathione Peroxidase 4 Senses and Translates Oxidative Stress into 12/15-Lipoxygenase Dependent- and AIF-Mediated Cell Death. *Cell Metab.* **8**, 237–248 (2008).
244. Rees, M. G. *et al.* Correlating chemical sensitivity and basal gene expression reveals mechanism of action. *Nat. Chem. Biol.* **12**, 109–116 (2016).

245. Seashore-Ludlow, B. *et al.* Harnessing Connectivity in a Large-Scale Small-Molecule Sensitivity Dataset. *Cancer Discov.* **5**, 1210–1223 (2015).
246. DuPage, M., Dooley, A. L. & Jacks, T. Conditional mouse lung cancer models using adenoviral or lentiviral delivery of Cre recombinase. *Nat. Protoc.* **4**, 1064–1072 (2009).
247. DepMap, Broad. DepMap 21Q3 Public. 14529771955 Bytes (2021) doi:10.6084/M9.FIGSHARE.15160110.V2.
248. Prus, E. & Fibach, E. Flow cytometry measurement of the labile iron pool in human hematopoietic cells. *Cytometry A* **73A**, 22–27 (2008).
249. Borromeo, M. D. *et al.* ASCL1 and NEUROD1 Reveal Heterogeneity in Pulmonary Neuroendocrine Tumors and Regulate Distinct Genetic Programs. *Cell Rep.* **16**, 1259–1272 (2016).
250. Osada, H. *et al.* Roles of Achaete-Scute Homologue 1 in DKK1 and E-cadherin Repression and Neuroendocrine Differentiation in Lung Cancer. *Cancer Res.* **68**, 1647–1655 (2008).
251. Mootha, V. K. *et al.* PGC-1 α -responsive genes involved in oxidative phosphorylation are coordinately downregulated in human diabetes. *Nat. Genet.* **34**, 267–273 (2003).
252. Subramanian, A. *et al.* Gene set enrichment analysis: A knowledge-based approach for interpreting genome-wide expression profiles. *Proc. Natl. Acad. Sci.* **102**, 15545–15550 (2005).
253. Wu, J. *et al.* Intercellular interaction dictates cancer cell ferroptosis via NF2–YAP signalling. *Nature* **572**, 402–406 (2019).
254. Yang, W.-H. *et al.* The Hippo Pathway Effector TAZ Regulates Ferroptosis in Renal Cell Carcinoma. *Cell Rep.* **28**, 2501-2508.e4 (2019).
255. Dai, X. *et al.* YAP activates the Hippo pathway in a negative feedback loop. *Cell Res.* **25**, 1175–1178 (2015).

256. Dowbaj, A. M. *et al.* An optogenetic method for interrogating YAP1 and TAZ nuclear–cytoplasmic shuttling. *J. Cell Sci.* **134**, jcs253484 (2021).
257. Pedrera, L. *et al.* Ferroptotic pores induce Ca²⁺ fluxes and ESCRT-III activation to modulate cell death kinetics. *Cell Death Differ.* (2020) doi:10.1038/s41418-020-00691-x.
258. Conrad, M. & Pratt, D. A. The chemical basis of ferroptosis. *Nat. Chem. Biol.* **15**, 1137–1147 (2019).
259. Tang, D. & Kroemer, G. Peroxisome: the new player in ferroptosis. *Signal Transduct. Target. Ther.* **5**, 273 (2020).
260. Chirala, S. S. & Wakil, S. J. Structure and function of animal fatty acid synthase. *Lipids* **39**, 1045–1053 (2004).
261. Lodhi, I. J. & Semenkovich, C. F. Peroxisomes: A Nexus for Lipid Metabolism and Cellular Signaling. *Cell Metab.* **19**, 380–392 (2014).
262. Dean, J. M. & Lodhi, I. J. Structural and functional roles of ether lipids. *Protein Cell* **9**, 196–206 (2018).
263. Honsho, M. & Fujiki, Y. Plasmalogen homeostasis – regulation of plasmalogen biosynthesis and its physiological consequence in mammals. *FEBS Lett.* **591**, 2720–2729 (2017).
264. Hassannia, B., Vandenabeele, P. & Vanden Berghe, T. Targeting Ferroptosis to Iron Out Cancer. *Cancer Cell* **35**, 830–849 (2019).
265. Reliene, R. & Schiestl, R. H. Glutathione depletion by buthionine sulfoximine induces DNA deletions in mice. *Carcinogenesis* **27**, 240–244 (2006).
266. Li, H. *et al.* Auranofin-mediated inhibition of PI3K/AKT/mTOR axis and anticancer activity in non-small cell lung cancer cells. *Oncotarget* **7**, 3548–3558 (2015).
267. Fath, M. A., Ahmad, I. M., Smith, C. J., Spence, J. & Spitz, D. R. Enhancement of carboplatin-mediated lung cancer cell killing by simultaneous disruption of

- glutathione and thioredoxin metabolism. *Clin. Cancer Res. Off. J. Am. Assoc. Cancer Res.* **17**, 6206–6217 (2011).
268. Flowers, J. L. *et al.* Use of Monoclonal Antiestrogen Receptor Antibody to Evaluate Estrogen Receptor Content in Fine Needle Aspiration Breast Biopsies: *Ann. Surg.* **203**, 250–254 (1986).
269. Bebbler, C. M. *et al.* Ferroptosis response segregates small cell lung cancer (SCLC) neuroendocrine subtypes. *Nat. Commun.* **12**, 2048 (2021).
270. Drapkin, B. J. *et al.* Genomic and Functional Fidelity of Small Cell Lung Cancer Patient-Derived Xenografts. *Cancer Discov.* **8**, 600–615 (2018).
271. Wang, D., Xie, N., Gao, W., Kang, R. & Tang, D. The ferroptosis inducer erastin promotes proliferation and differentiation in human peripheral blood mononuclear cells. *Biochem. Biophys. Res. Commun.* **503**, 1689–1695 (2018).
272. Junttila, M. R. & Evan, G. I. p53 — a Jack of all trades but master of none. *Nat. Rev. Cancer* **9**, 821–829 (2009).
273. Xie, Y. *et al.* Ferroptosis: process and function. *Cell Death Differ.* **23**, 369–379 (2016).
274. Gazdar, A. F., Carney, D. N., Nau, M. M. & Minna, J. D. Characterization of variant subclasses of cell lines derived from small cell lung cancer having distinctive biochemical, morphological, and growth properties. *Cancer Res.* **45**, 2924–2930 (1985).
275. Chalishazar, M. D. *et al.* MYC-Driven Small-Cell Lung Cancer is Metabolically Distinct and Vulnerable to Arginine Depletion. *Clin. Cancer Res.* **25**, 5107–5121 (2019).
276. Dammert, M. A. *et al.* MYC paralog-dependent apoptotic priming orchestrates a spectrum of vulnerabilities in small cell lung cancer. *Nat. Commun.* **10**, 3485 (2019).
277. Huang, F. *et al.* Inosine Monophosphate Dehydrogenase Dependence in a Subset of Small Cell Lung Cancers. *Cell Metab.* **28**, 369–382.e5 (2018).

278. Owonikoko, T. K. *et al.* YAP1 Expression in SCLC Defines a Distinct Subtype With T-cell–Inflamed Phenotype. *J. Thorac. Oncol.* **16**, 464–476 (2021).
279. Kazachkov, M., Chen, Q., Wang, L. & Zou, J. Substrate Preferences of a Lysophosphatidylcholine Acyltransferase Highlight Its Role in Phospholipid Remodeling. *Lipids* **43**, 895–902 (2008).
280. Lands, W. E. Metabolism of glycerolipides; a comparison of lecithin and triglyceride synthesis. *J. Biol. Chem.* **231**, 883–888 (1958).
281. Wang, B. & Tontonoz, P. Phospholipid Remodeling in Physiology and Disease. *Annu. Rev. Physiol.* **81**, 165–188 (2019).
282. Orlando, U. D. *et al.* Acyl-CoA synthetase-4, a new regulator of mTOR and a potential therapeutic target for enhanced estrogen receptor function in receptor-positive and -negative breast cancer. *Oncotarget* **6**, 42632–42650 (2015).
283. Goldstein, J. L. & Brown, M. S. The LDL Receptor. *Arterioscler. Thromb. Vasc. Biol.* **29**, 431–438 (2009).
284. Zhou, T. *et al.* Serum low-density lipoprotein and low-density lipoprotein expression level at diagnosis are favorable prognostic factors in patients with small-cell lung cancer (SCLC). *BMC Cancer* **17**, 269 (2017).
285. Al-Bahlani, S. *et al.* Fatty acid synthase regulates the chemosensitivity of breast cancer cells to cisplatin-induced apoptosis. *Apoptosis* **22**, 865–876 (2017).
286. Cotte, A. K. *et al.* Lysophosphatidylcholine acyltransferase 2-mediated lipid droplet production supports colorectal cancer chemoresistance. *Nat. Commun.* **9**, 322 (2018).
287. Liu, H., Liu, Y. & Zhang, J.-T. A new mechanism of drug resistance in breast cancer cells: fatty acid synthase overexpression-mediated palmitate overproduction. *Mol. Cancer Ther.* **7**, 263–270 (2008).

288. Liu, H., Schreiber, S. L. & Stockwell, B. R. Targeting Dependency on the GPX4 Lipid Peroxide Repair Pathway for Cancer Therapy. *Biochemistry* **57**, 2059–2060 (2018).
289. Wang, Z., Li, Y., Kong, D. & Sarkar, F. H. The role of Notch signaling pathway in epithelial-mesenchymal transition (EMT) during development and tumor aggressiveness. *Curr. Drug Targets* **11**, 745–751 (2010).
290. Benassi, B. *et al.* c-Myc Phosphorylation Is Required for Cellular Response to Oxidative Stress. *Mol. Cell* **21**, 509–519 (2006).
291. Liang, M. *et al.* L-Arginine induces antioxidant response to prevent oxidative stress via stimulation of glutathione synthesis and activation of Nrf2 pathway. *Food Chem. Toxicol.* **115**, 315–328 (2018).
292. Cristea, S. *et al.* The MEK5–ERK5 Kinase Axis Controls Lipid Metabolism in Small-Cell Lung Cancer. *Cancer Res.* **80**, 1293–1303 (2020).
293. Kryukov, G. V. Characterization of Mammalian Selenoproteomes. *Science* **300**, 1439–1443 (2003).
294. Warner, G. J. *et al.* Inhibition of Selenoprotein Synthesis by Selenocysteine tRNA[Ser]^{Sec} Lacking Isopentenyladenosine. *J. Biol. Chem.* **275**, 28110–28119 (2000).
295. Cutz, E. & Jackson, A. Neuroepithelial bodies as airway oxygen sensors. *Respir. Physiol.* **115**, 201–214 (1999).
296. Cutz, E., Pan, J. & Yeger, H. The role of NOX2 and ‘novel oxidases’ in airway chemoreceptor O₂ sensing. *Adv. Exp. Med. Biol.* **648**, 427–438 (2009).
297. Cutz, E., Pan, J., Yeger, H., Domnik, N. J. & Fisher, J. T. Recent advances and controversies on the role of pulmonary neuroepithelial bodies as airway sensors. *Semin. Cell Dev. Biol.* **24**, 40–50 (2013).
298. Wang, D. *et al.* NADPH-oxidase and a hydrogen peroxide-sensitive K⁺ channel may function as an oxygen sensor complex in airway chemoreceptors and small

- cell lung carcinoma cell lines. *Proc. Natl. Acad. Sci. U. S. A.* **93**, 13182–13187 (1996).
299. Hockman, D. *et al.* Evolution of the hypoxia-sensitive cells involved in amniote respiratory reflexes. *eLife* **6**, e21231 (2017).
300. Stupnikov, M. R. & Cardoso, W. V. Evolutionary Developmental Biology: Sensing oxygen inside and out. *eLife* <https://elifesciences.org/articles/27467> (2017) doi:10.7554/eLife.27467.
301. Lambeth, J. D. NOX enzymes and the biology of reactive oxygen. *Nat. Rev. Immunol.* **4**, 181–189 (2004).
302. Trachootham, D., Alexandre, J. & Huang, P. Targeting cancer cells by ROS-mediated mechanisms: a radical therapeutic approach? *Nat. Rev. Drug Discov.* **8**, 579–591 (2009).
303. Oshikawa, J. *et al.* Novel role of p66Shc in ROS-dependent VEGF signaling and angiogenesis in endothelial cells. *Am. J. Physiol. Heart Circ. Physiol.* **302**, H724–732 (2012).
304. Sena, L. A. & Chandel, N. S. Physiological Roles of Mitochondrial Reactive Oxygen Species. *Mol. Cell* **48**, 158–167 (2012).
305. Dickinson, B. C., Peltier, J., Stone, D., Schaffer, D. V. & Chang, C. J. Nox2 redox signaling maintains essential cell populations in the brain. *Nat. Chem. Biol.* **7**, 106–112 (2011).
306. Prozorovski, T., Schneider, R., Berndt, C., Hartung, H.-P. & Aktas, O. Redox-regulated fate of neural stem progenitor cells. *Biochim. Biophys. Acta BBA - Gen. Subj.* **1850**, 1543–1554 (2015).
307. Le Belle, J. E. *et al.* Proliferative Neural Stem Cells Have High Endogenous ROS Levels that Regulate Self-Renewal and Neurogenesis in a PI3K/Akt-Dependent Manner. *Cell Stem Cell* **8**, 59–71 (2011).

308. Raposo, A. A. S. F. *et al.* Ascl1 Coordinately Regulates Gene Expression and the Chromatin Landscape during Neurogenesis. *Cell Rep.* **10**, 1544–1556 (2015).
309. Vasconcelos, F. F. & Castro, D. S. Transcriptional control of vertebrate neurogenesis by the proneural factor Ascl1. *Front. Cell. Neurosci.* **8**, (2014).
310. Gascón, S. *et al.* Identification and Successful Negotiation of a Metabolic Checkpoint in Direct Neuronal Reprogramming. *Cell Stem Cell* **18**, 396–409 (2016).
311. Augustyn, A. *et al.* ASCL1 is a lineage oncogene providing therapeutic targets for high-grade neuroendocrine lung cancers. *Proc. Natl. Acad. Sci.* **111**, 14788–14793 (2014).
312. Niehans, G. A. *et al.* Human lung carcinomas express Fas ligand. *Cancer Res.* **57**, 1007–1012 (1997).
313. Powis, G., Mustacich, D. & Coon, A. The role of the redox protein thioredoxin in cell growth and cancer. *Free Radic. Biol. Med.* **29**, 312–322 (2000).
314. Yoo, M.-H. *et al.* Targeting Thioredoxin Reductase 1 Reduction in Cancer Cells Inhibits Self-Sufficient Growth and DNA Replication. *PLoS ONE* **2**, e1112 (2007).
315. Gao, M. *et al.* Role of Mitochondria in Ferroptosis. *Mol. Cell* **73**, 354–363.e3 (2019).
316. Prieto, J. *et al.* MYC Induces a Hybrid Energetics Program Early in Cell Reprogramming. *Stem Cell Rep.* **11**, 1479–1492 (2018).
317. Johnson, B. E. *et al.* MYC family DNA amplification in 126 tumor cell lines from patients with small cell lung cancer. *J. Cell. Biochem.* **63**, 210–217 (1996).
318. Agathocleous, M. *et al.* Metabolic differentiation in the embryonic retina. *Nat. Cell Biol.* **14**, 859–864 (2012).
319. Zheng, X. *et al.* Metabolic reprogramming during neuronal differentiation from aerobic glycolysis to neuronal oxidative phosphorylation. *eLife* **5**, e13374 (2016).
320. Kim, D. P. *et al.* High cell density attenuates reactive oxygen species: Implications for in vitro assays: High cell density attenuates oxidative stress. *Wound Repair Regen.* **20**, 74–82 (2012).

321. Limoli, C. L. *et al.* Cell-density-dependent regulation of neural precursor cell function. *Proc. Natl. Acad. Sci.* **101**, 16052–16057 (2004).
322. Pani, G. *et al.* A Redox Signaling Mechanism for Density-dependent Inhibition of Cell Growth. *J. Biol. Chem.* **275**, 38891–38899 (2000).
323. Roh, J.-L., Jang, H., Kim, E. H. & Shin, D. Targeting of the Glutathione, Thioredoxin, and Nrf2 Antioxidant Systems in Head and Neck Cancer. *Antioxid. Redox Signal.* **27**, 106–114 (2017).
324. O'Dwyer, P. J. *et al.* Phase I trial of buthionine sulfoximine in combination with melphalan in patients with cancer. *J. Clin. Oncol.* **14**, 249–256 (1996).
325. Villablanca, J. G. *et al.* A Phase I New Approaches to Neuroblastoma Therapy Study of Buthionine Sulfoximine and Melphalan With Autologous Stem Cells for Recurrent/Refractory High-Risk Neuroblastoma: Phase I BSO-Melphalan in Neuroblastoma. *Pediatr. Blood Cancer* **63**, 1349–1356 (2016).
326. Sutton, B. M., McGusty, E., Walz, D. T. & DiMartino, M. J. Oral gold. Antiarthritic properties of alkylphosphinegold coordination complexes. *J. Med. Chem.* **15**, 1095–1098 (1972).
327. Onodera, T., Momose, I. & Kawada, M. Potential Anticancer Activity of Auranofin. *Chem. Pharm. Bull. (Tokyo)* **67**, 186–191 (2019).
328. Livak, K. J. & Schmittgen, T. D. Analysis of Relative Gene Expression Data Using Real-Time Quantitative PCR and the $2^{-\Delta\Delta CT}$ Method. *Methods* **25**, 402–408 (2001).
329. Weber, E., Engler, C., Gruetzner, R., Werner, S. & Marillonnet, S. A Modular Cloning System for Standardized Assembly of Multigene Constructs. *PLoS ONE* **6**, (2011).
330. Engler, C. & Marillonnet, S. Golden Gate cloning. *Methods Mol. Biol. Clifton NJ* **1116**, 119–131 (2014).

331. Swift, S., Lorens, J., Achacoso, P. & Nolan, G. P. Rapid Production of Retroviruses for Efficient Gene Delivery to Mammalian Cells Using 293 T Cell–Based Systems. *Curr. Protoc. Immunol.* **31**, (1999).
332. Dull, T. *et al.* A Third-Generation Lentivirus Vector with a Conditional Packaging System. *J. Virol.* **72**, 8463–8471 (1998).
333. Davis, H. E., Rosinski, M., Morgan, J. R. & Yarmush, M. L. Charged Polymers Modulate Retrovirus Transduction via Membrane Charge Neutralization and Virus Aggregation. *Biophys. J.* **86**, 1234–1242 (2004).
334. Wang, T., Wei, J. J., Sabatini, D. M. & Lander, E. S. Genetic Screens in Human Cells Using the CRISPR-Cas9 System. *Science* **343**, 80–84 (2014).
335. Lowry, Oliver H., Rosebrough, Nira J., Farr, A. L. & Randall, Rose J. PROTEIN MEASUREMENT WITH THE FOLIN PHENOL REAGENT. *J. Biol. Chem.* **193**, 265–275 (1951).
336. Kumar, V. *et al.* A keratin scaffold regulates epidermal barrier formation, mitochondrial lipid composition, and activity. *J. Cell Biol.* **211**, 1057–1075 (2015).
337. Meuwissen, R. *et al.* Induction of small cell lung cancer by somatic inactivation of both Trp53 and Rb1 in a conditional mouse model. *Cancer Cell* **4**, 181–189 (2003).
338. Meuwissen, R., Linn, S. C., van der Valk, M., Mooi, W. J. & Berns, A. Mouse model for lung tumorigenesis through Cre/lox controlled sporadic activation of the K-Ras oncogene. *Oncogene* **20**, 6551–6558 (2001).
339. Fernandez-Cuesta, L. *et al.* Identification of novel fusion genes in lung cancer using breakpoint assembly of transcriptome sequencing data. *Genome Biol.* **16**, 7 (2015).

6 Publications

Teilpublikation:

Bebber CM, Thomas ES, Stroh J, Chen Z, Androulidaki A, Schmitt A, Höhne MN, Stüker L, de Pádua Alves C, Khonsari A, Dammert MA, Parmaksiz F, Tumbrink HL, Beleggia F, Sos ML, Riemer J, George J, Brodesser S, Thomas RK, Reinhardt HC, von Karstedt S. Ferroptosis response segregates small cell lung cancer (SCLC) neuroendocrine subtypes. *Nat Commun.* 2021 Apr 6;12(1):2048. doi: 10.1038/s41467-021-22336-4. PMID: 33824345; PMCID: PMC8024350.

Literature reviews:

Bebber, CM, and von Karstedt, S. (2021). Non-neuroendocrine differentiation generates a ferroptosis-prone lipidome in small cell lung cancer (SCLC). *Mol. Cell. Oncol.* 1933871. doi: 10.1080/23723556.2021.1933871.

Bebber CM, Müller F, Prieto Clemente L, Weber J, von Karstedt S. Ferroptosis in Cancer Cell Biology. *Cancers (Basel).* 2020 Jan 9;12(1):164. doi: 10.3390/cancers12010164. PMID: 31936571; PMCID: PMC7016816.

7 Acknowledgements

Foremost, I want to thank my supervisor Prof. Dr. Silvia von Karstedt for giving me the opportunity to work on this very exciting PhD project. I highly appreciate your scientific guidance, constant encouragement and great interest in my work during that time. I am grateful for your excellent support and mentorship, especially, but not only, in scientific questions helping me to develop as a scientist.

I want to thank Prof. Dr. H. Christian Reinhardt for his constant support and scientific guidance during my PhD thesis. Moreover, I want to thank Prof. Dr. Jan Riemer for his feedback as a member of my thesis advisory committee. I want to thank Prof. Dr. Günter Schwarz and Prof. Dr. Ana J. García-Sáez who kindly agreed to take part in my dissertation defense.

I would like to thank Jenny Stroh for her big contributions to this PhD thesis and together with Laura Prieto Clemente and Isil Yapici for their support, friendship and listening to all the problems that I encountered during my PhD.

I would like to thank Dr. Eric Seidel for helpful discussions and proofreading my PhD thesis.

I want to specially thank Emily Thomas, Zhiyi Chen, Ariadne Androulidaki, Lukas Stüker and Fanyu Liu for their contribution to this work but also all former and current members of the von Karstedt laboratory for the great working atmosphere and scientific discussions.

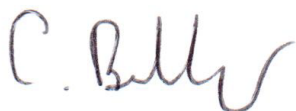
Abschließend würde ich gerne Marten, meiner Familie und meinen Freunden danken für die bedingungslose, großartige Unterstützung während dieser Promotion und der gesamten Zeit meines Studiums! Ohne das viele Zuhören, Euren stetigen Zuspruch und Eurer Hilfe bei allen Problemen die mir während der Zeit begegnet sind wäre diese Arbeit nicht möglich gewesen!

8 Eidesstattliche Erklärung

Hiermit versichere ich an Eides statt, dass ich die vorliegende Dissertation selbstständig und ohne Benutzung anderer Hilfsmittel und Literatur angefertigt habe. Alle Stellen, die wörtlich oder sinngemäß aus veröffentlichten und nicht veröffentlichten Werken dem Wortlaut oder dem Sinn nach entnommen wurden, sind als solche kenntlich gemacht. Ich versichere an Eides statt, dass diese Dissertation noch keiner anderen Fakultät oder Universität zur Prüfung vorgelegen hat; dass sie - abgesehen von unten angegebenen Teilpublikationen und eingebundenen Artikeln und Manuskripten - noch nicht veröffentlicht worden ist sowie, dass ich eine Veröffentlichung der Promotion nicht ohne Genehmigung des Promotionsausschusses vornehmen werde. Die Bestimmungen dieser Ordnung sind mir bekannt. Darüber hinaus erkläre ich hiermit, dass ich die Ordnung zur Sicherung guter wissenschaftlicher Praxis und zum Umgang mit wissenschaftlichem Fehlverhalten der Universität zu Köln gelesen und sie bei der Durchführung der Dissertation zugrundeliegenden Arbeiten und der schriftlich verfassten Dissertation beachtet habe und verpflichte mich hiermit, die dort genannten Vorgaben bei allen wissenschaftlichen Tätigkeiten zu beachten und umzusetzen. Ich versichere, dass die eingereichte elektronische Fassung der eingereichten Druckfassung vollständig entspricht. Die von mir vorgelegte Dissertation ist von Prof. Dr. Silvia von Karstedt betreut worden.

Teilpublikation:

Bebber CM, Thomas ES, Stroh J, Chen Z, Androulidaki A, Schmitt A, Höhne MN, Stüker L, de Pádua Alves C, Khonsari A, Dammert MA, Parmaksiz F, Tumbrink HL, Beleggia F, Sos ML, Riemer J, George J, Brodesser S, Thomas RK, Reinhardt HC, von Karstedt S. Ferroptosis response segregates small cell lung cancer (SCLC) neuroendocrine subtypes. Nat Commun. 2021 Apr 6;12(1):2048. doi: 10.1038/s41467-021-22336-4. PMID: 33824345; PMCID: PMC8024350.



Christina Bebber

Köln, 20.09.2021

9 Appendix

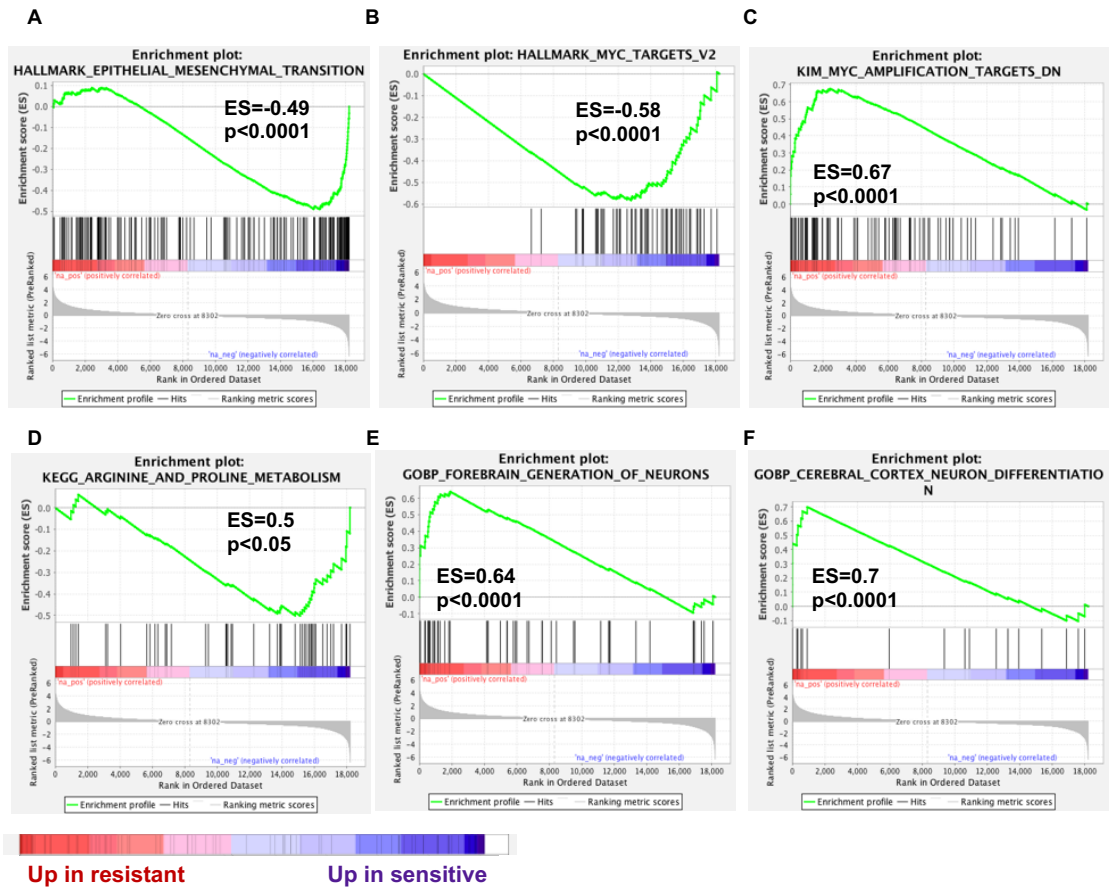


Figure 41 GSEA analysis.

Gene set enrichment analysis (GSEA) of a ranked list of differentially expressed genes from human ferroptosis sensitive and resistant cells was performed, ES=enrichment score and p value are indicated. A positive ES indicates enrichment of a gene set in ferroptosis resistant cells, a negative ES indicates enrichment of a gene set in ferroptosis sensitive cells^{251,252}.